NANYANG
TECHNOLOGICAL
UNIVERSITY
SINGAPORE

SEMICONDUCTING COVALENT ORGANIC FRAMEWORKS FOR PEROVSKITE SOLAR CELLS

HESHAM RASHED ABUZEID MAHMOUD

SCHOOL OF MATERIALS SCIENCE AND ENGINEERING

2024

SEMICONDUCTING COVALENT ORGANIC FRAMEWORKS FOR PEROVSKITE SOLAR CELLS

HESHAM RASHED ABUZEID MAHMOUD

SCHOOL OF MATERIALS SCIENCE AND ENGINEERING

A thesis submitted to the Nanyang Technological University
in partial fulfilment of the requirement for the degree of
Doctor of Philosophy

2024

Statement of Originality

I hereby certify that the work embodied in this thesis is the result of original research, is free of plagiarised materials, and has not been submitted for a higher degree to any other University or Institution.

21-Aug-2024 Hesham Rashed

. . . .

Date Hesham Rashed Abuzeid Mahmoud

Supervisor Declaration Statement

I have reviewed the content and presentation style of this thesis and declare it is free of plagiarism and of sufficient grammatical clarity to be examined. To the best of my knowledge, the research and writing are those of the candidate except as acknowledged in the Author Attribution Statement. I confirm that the investigations were conducted in accord with the ethics policies and integrity standards of Nanyang Technological University and that the research data are presented honestly and without prejudice.

21-Aug-2024

. . . .
Date

. . . .
Prof. Nripan Mathews

Authorship Attribution Statement

This thesis contains material from one paper accepted in the following peer-reviewed journal in which I am listed as an author.

A portion of Chapter 4 and 5 has been published as H. R. Abuzeid, D. J. J. Tay, B. Febriansyah, A. Kanwat, T. Salim, A. A. Zhumekenov, S. A. Pullarkat, and N. Mathews. Functionalized sp^2 Carbon-Conjugated Covalent Organic Frameworks for Interfacial Modulation of Inverted Perovskite Solar Cells. *Small Methods*, **2025**, 9, 2400666.
DOI: 10.1002/smtd.202400666.

The contributions of the co-authors are as follows:

- Prof N. Mathews provided the initial project direction, solar cells devices fabrication and characterization facilities and revised the collected data and revised the manuscript drafts.
- Dr S. A. Pullarkat provided the laboratory facilities for synthesis and characterization of covalent organic frameworks materials.
- I co-designed the study with Prof N. Mathews and Dr. S. A. Pullarkat and performed all the laboratory work at the School of Materials Science and Engineering (MSE), Energy Research Institute at Nanyang Technological University (ERI@N) and the School of Chemistry, Chemical Engineering and Biotechnology (CCEB).
- I synthesized and characterized the COFs, performed simulations, and analyzed the data. Additionally, I conducted data collection and analysis on crystallinity, surface area, thermal stability, morphology, optical, and electronic properties. I also carried out thin-film fabrication and device characterization, along with data interpretation.
- I prepared the manuscript drafts. Revisions and advice were also taken from Prof. N. Mathews, Dr. S. A. Pullarkat and Dr. A. A. Zhumekenov.
- D. J. J. Tay fabricated CsFA-based devices and conducted performance measurements, including current-voltage (J-V) analysis and light intensity dependence of V_{oc}.

- B. Febriansyah performed ^{1}H-NMR for TFFPy and provided guidance on materials characterization, device fabrication, and data interpretation.
- Dr A. Kanwat carried out time-resolved photoluminescence (TRPL) measurements.
- Dr T. Salim performed X-ray photoelectron spectroscopy (XPS) measurements.
- Dr A. A. Zhumekenov assisted in the data interpretation and manuscript revision.

21-Aug-2024

Hesham Rashed

. . . .
Date

. . . .
Hesham Rashed Abuzeid Mahmoud

Abstract

The development of efficient, stable, and cost-effective photovoltaic technologies is critical to addressing the global energy crisis and reducing reliance on fossil fuels. Perovskite solar cells (PSCs) have gained attention as a viable alternative to conventional silicon-based solar cells, offering high power conversion efficiency (PCE) and cost-effective manufacturing processes. Despite their advantages, PSCs are hindered by significant challenges, including environmental instability and the presence of defects at material interfaces and within the bulk perovskite layers. These defects lead to non-radiative recombination, reduced charge carrier lifetimes, and ultimately, lower device efficiency and shorter operational lifetimes. This thesis explores the novel incorporation of covalent organic frameworks (COFs) into PSCs as a means of addressing these issues. The use of COFs in PSCs is driven by their highly tunable structures, excellent stability, and ability to passivate defects effectively. COFs can be engineered to improve both interfacial and bulk properties, thereby enhancing charge transport and reducing non-radiative recombination, which ultimately leads to increased PCE and improved stability in PSCs.

The primary aim of the research is to enhance the efficiency of PSCs by mitigating interfacial and bulk defects. Specifically, the research investigates the use of sp^2 carbon-conjugated COF (sp^2c-COF) as interfacial passivation layers and pyrene-based COFs (ILCOF-1 and SH-COF) as bulk dopants in perovskite films. The dual approach of using COFs both at the interfaces and within the perovskite bulk is designed to reduce the density of trap states and enhance the overall crystallinity of the films. By addressing both surface and internal defects, the research aims to achieve an improvement in PCE of the devices.

The scope of the thesis includes the synthesis and characterization of COFs, their integration into PSCs, and the evaluation of their impact on device performance. Several key methods are employed to analyse the materials and devices, including X-ray diffraction (XRD), scanning electron microscopy (SEM), time-resolved photoluminescence (TRPL), X-ray photoelectron spectroscopy (XPS), and current-voltage (J-V) measurements. These characterization techniques provide insights into the structural, optical, and electrical properties of the COF-modified perovskite films and allow for a detailed analysis of the improvements in device performance.

The major findings of the research demonstrate that the incorporation of COFs leads to significant improvements in the efficiency of PSCs. The use of sp^2c-COFs as interfacial layers successfully passivates surface defects at the NiO_x/perovskite interface, reducing non-radiative recombination and enhancing charge extraction. This results in a notable increase in PCE, with COF-treated devices achieving PCE values of up to 17.65%, compared to 15.82% in untreated devices. Furthermore, the integration of pyrene-based COFs as bulk dopants improves the crystallinity of perovskite films, reducing the density of trap states and improving charge carrier mobility. Devices doped with SH-COF show even greater improvements, achieving PCE values of 19.49%. These findings are supported by TRPL measurements, which indicate longer carrier lifetimes in COF-doped films compared to controls.

While the research primarily focuses on enhancing performance, it also highlights the potential of COFs to improve the long-term stability of PSCs. The hydrophobic nature of COFs, combined with their defect passivation capabilities, suggests that they could contribute to the development of more durable PSCs. However, further studies will be required to fully explore their effects on long-term operational stability under real-world conditions.

In conclusion, this thesis demonstrates the successful application of COFs in improving the performance of PSCs. The use of COFs, both as interfacial layers and bulk dopants, has been shown to address key limitations in PSC technology, leading to significant improvements in PCE and perovskite crystallinity. These findings suggest that COFs represent a promising avenue for advancing perovskite solar cell technology and, more broadly, for contributing to the ongoing development of renewable energy solutions. Future research is recommended to further explore the scalability of COF integration in large-area solar modules, as well as their potential applications in other optoelectronic devices.

Lay Summary

Solar energy is globally considered as one of the promising renewable energy sources for decreasing the dependence on fossil fuels that contribute to climate change. Despite its potential, solar power has not yet been fully optimized for widespread use, particularly due to the limitations of solar panel materials. Perovskite solar cells (PSCs), a promising class of materials with a distinctive crystal structure—typically composed of a metal cation, a halide anion, and an organic or inorganic component in a ABX_3 framework—have demonstrated higher efficiency and lower manufacturing costs compared to traditional silicon-based solar cells. However, PSCs have been found to degrade quickly when exposed to sunlight, moisture, and heat, limiting their long-term performance. This instability has delayed the broader adoption of PSCs, prompting researchers to search for new solutions to enhance their durability and efficiency.

This research explores the utilizing of covalent organic frameworks (COFs) to improve the performance of PSCs. COFs are lightweight, highly porous materials made from organic molecules linked by strong covalent bonds, forming stable and customizable network structures. These materials can be precisely designed at the molecular level, making them promising for addressing instability issues in PSCs. It has been hypothesized that COFs can mitigate the defects in perovskite materials that cause energy loss over time. Two approaches were investigated in this study: first, COFs were introduced as interfacial layers between different components of the PSCs to reduce surface defects; second, they were incorporated into the perovskite material itself to improve internal structure and reduce defect density.

The aim of the research was to increase both the efficiency and lifespan of PSCs, making solar energy a more reliable and cost-effective option. By introducing COFs into the solar cell architecture, defects in the perovskite material were passivated, reducing energy loss and improving the performance of the cells. The novel integration of COFs allowed both surface and internal defects to be addressed, resulting in more stable and efficient PSCs. The potential impact of this research extends to the broader renewable energy landscape.

The development of more efficient and durable solar panels could lead to significant reductions in energy costs and environmental impact. With improved stability, solar panels could generate electricity for longer periods and require less frequent replacements, which would lower costs for consumers and make solar energy a more attractive option. Additionally, by increasing the efficiency of solar panels, less space and fewer materials would be needed to generate the same amount of energy, reducing the overall environmental footprint of solar energy production. In the long term, this research could help to reduce global reliance on fossil fuels and contribute to efforts to reduce carbon emissions.

The novelty of this research lies in the application of COFs in PSCs, an approach that has not been extensively explored. While COFs have been used in other areas of research, their potential for improving the performance and stability of PSCs has only recently been recognized. This research demonstrated that COFs can be tailored to interact with and passivate defects in the perovskite material, resulting in measurable improvements in efficiency and stability. The findings of this research have the potential to influence further exploration of COFs in renewable energy applications beyond PSCs. The success of COFs in improving PSCS suggests that they could be applied to other energy technologies, such as fuel cells and batteries. Future research is expected to focus on optimizing the integration of COFs into PSCs, exploring new COF designs, and extending their use to other renewable energy technologies.

The broader societal impact of this research is significant. Renewable energy sources such as solar power are crucial in the fight against climate change, and improving the performance of PSCs can accelerate the global transition away from fossil fuels. By making solar energy more efficient, durable, and cost-effective, this research could contribute to a greener and more sustainable future. Overall, this research on COFs for PSCs represents an important step forward in the development of more efficient and sustainable energy solutions. By addressing key issues related to solar cell stability and performance, the findings of this study have the potential to shape the future of solar energy and contribute to broader efforts to mitigate climate change.

Acknowledgements

This dissertation would not have been possible without the generous funding from the Singapore National Research Foundation through the Competitive Research Program and the Ministry of Education Singapore.

I am deeply grateful to my main supervisor, Prof. Nripan Mathews, for his unwavering guidance, support, patience, and encouragement. Prof. Mathews has been instrumental in helping me acquire the skills necessary to pursue my Ph.D. During this time, he has provided insightful ideas to address the challenges I encountered in my research. Additionally, he connected me with knowledgeable mentors who have significantly contributed to the improvement and direction of my work.

I would also like to extend my heartfelt thanks to my co-supervisor, Dr. Sumod A. Pullarkat, for his invaluable assistance in procuring the necessary equipment and chemicals. Dr. Sumod has been pivotal in helping me tackle various issues, such as material purification and data characterization. His challenging questions have taught me to think critically and find scientifically accurate solutions.

Additionally, I would like to express my sincere gratitude to my thesis advisory committee members, Prof. Dalton and Prof. Bates, for their invaluable feedback and guidance throughout my research journey. Their expertise and constructive criticism have been crucial in refining my work and ensuring its academic rigor.

This thesis greatly benefited from the input of Dr. Ayan A. Zhumekenov, Dr. Anil Kanwat, Dr. Teddy Salim, Dr. Tay Yeow Boon, Dr. Benny Febriansyah, Darrell Jun Jie Tay and Aakash Sharma, who patiently reviewed many drafts and improved the quality of my work. Also, I want to thank my colleagues and seniors in RTP, MSE and SPMS have created a warm, supportive, and cooperative laboratory atmosphere.

Table of Contents

Chapter 4 Synthesis and Characterization of Semiconducting Functionalized sp^2 Carbon-Conjugated Covalent Organic Frameworks (sp^2c-COF)..............................69

Chapter 5 Functionalized sp^2 Carbon-Conjugated Covalent Organic Frameworks for Interfacial Modulation of Inverted Perovskite Solar Cells..................................89

Table Captions

Figure Captions

Figure 1.1 Tuning the electronic properties of semiconducting COFs through varying electroactive organic building block and functionalities.

Figure 1.2 Schematic representation of defects at the NiO_x/perovskite interface.

Figure 1.3 Schematic representation of the interfacial dual-passivation approach using sp^2c-COF.

Figure 2.1 Generational progress in solar cell technologies, with perovskite emerging as the third generation, achieving efficiencies close to those of traditional silicon-based cells.

Figure 2.2 Major milestones in the development of PCE of PSCs from 2009 to 2025.

Figure 2.3 (a) Schematic representation of the architecture of a typical PSC. (b) Diagram illustrating the structure of the MHP semiconductor family, generally expressed by the chemical formula ABX_3. Adapted with permission from Saliba *et al.*[1].

Figure 2.4 Schematic illustration of the perovskite device architectures; mesoporous and planar (n-i-p and p-i-n).

Figure 2.5 (a) Schematic illustration of the interaction of the π-conjugated Lewis base IDIC and Pb^{2+}. (b) Molecular structure of IDIC featuring carbonyl and cyano end groups. Adapted with permission from Huang *et al.*[2].

Figure 2.6 Illustration of design principles of different topologies in COFs[3]. *No permission is required for thesis purposes.*

Figure 2.7 Common condensation reactions forming various types of linkages in COFs [3]. *No permission is required for thesis purposes.*

Figure 2.8 Diagrammatic illustration of the properties and benefits associated with different synthetic approaches for COFs [3]. *No permission is required for thesis purposes.*

Figure 2.9 White light-emitting diodes based on COF (c) reference LED turned off and (d) on, and the same LED coated with COF (e) off and (f) on[4]. *No permission is required for thesis purposes.*

Figure 4.1 Schematic illustration of TFPPy synthesis.

Figure 4.2 (a) FTIR spectrum of TFPPy monomer using the KBr pellet method. (b) ^{1}H-NMR spectrum of TFPPy monomer.

Figure 4.3 (a, b) DFT geometry optimization of TFPPy monomer using the B3LYP/6-311G(d,p) basis set. (a) Three-dimensional view, and (b) Theoretical electronic frontier states LUMO and HOMO. (C, gray; O, red; H, white). (c, d) Electronic absorption and emission properties of TFPPy monomer (c) UV-Vis spectra, (inserted Tauc's plot) and (d) PL spectra.

Figure 4.4 (a) The reaction scheme for the synthesis of sp^{2}c-COF, connected via C=C bonding, through the condensation of TFPPy knot and PDAN linker.

Figure 4.5 Structure confirmation of sp^{2}c-COF using FTIR and solid-state NMR. (a) FTIR spectrum of sp^{2}c-COF compared to that of TFPPy and PDAN monomers. (b) Solid-state ^{13}C CP-MAS NMR spectrum of sp^{2}c-COF compared to that of TFPPy monomer.

Figure 4.6 Schematics representation of the two stacking models (b) Experimental XRD

Figure 5.1 (a) Photographic image of the deposition process using in-situ solvothermal method. (b) FE-SEM image of the resultant film featuring presence of bulk domains.

Figure 5.2 (a) Schematic diagram of the synthetic procedures of liquid-liquid interfacial method. (b) FE-SEM images of the surface morphology of formed film.

Figure 5.3 (a-b) Top-view and side-view FE-SEM images of pristine and sp^2c-COF-coated NiO_x films, respectively. (c) FE-SEM images of sp^2c-COF powder. (d) Contact angle of water, DMF and DMSO on NiO_x and NiO_x/sp^2c-COF.

Figure 5.4 (a) Schematics of the sp^2c-COF-modified PSCs with the inverted p-i-n device architecture. (b) band alignments diagram. (c) *J–V* curves for the reverse and forward scans of the control and the sp^2c-COF-modified PSCs. (d) The PCE enhancement levels achieved in different reported surface modifiers for NiO_x-based p-i-n devices.

Figure 5.5 (a) J-V curves for the control and the sp^2c-COF-modified PSCs devices. (b) The EQE curves and the corresponding integrated J_{sc} values calculated from the IPCE spectrum. The statistical distribution of devices paramaters: (c) PCE, (d) V_{oc}, (e) J_{sc}, and (f) FF.

Figure 5.6 (a) Light intensity dependence of V_{oc} measurements and (b) Ideality factor calculation using the natural logarithm of the intensity.

Figure 5.7 Statistical distribution of devices hysteresis.

Figure 5.8 Statistical distribution of devices' (a) series resistance and (b) shunt resistance.

Figure 5.9 (a,c) Top-view and (d,e) cross-sectional FE-SEM images of the pristine (control) and the sp^2c-COF-modified perovskite thin films, respectively.

Figure 6.7 The statistical distribution photovoltaics parameters; PCE, V_{oc}, J_{sc}, and FF for the control and sp^{2}c-COF doped devices at various concentrations.

Figure 6.8 Schematic representation of the synthetic route and the FTIR spectra of (a,b) COF-5 and (c,d) TFP-DBD COF.

Figure 6.9 Photographic image of the pyrene-based COFs (sp^{2}c-COF, ILCOF-1 and SH-COF) and model COFs (COF-5 and TFP-DBD COF) as powder and suspended in DMF.

Figure 6.10 The statistical distribution photovoltaics parameters; PCE, V_{oc}, J_{sc}, and FF for the control and pyrene-based COFs, and model COFs doped devices.

Figure 6.11 The XRD pattern of the pristine, IL-COF-1 and SH-COF modified perovskite films.

Figure 6.12 **(a)** PL spectra and (**c-e**) TRPL spectra and (**f**) UV-vis spectra of unmodified perovskite film and perovskite treated with ILCOF-1 and SH-COF.

Figure 6.13 XPS of (a) Pb 4f and (b) I 3d for pristine, ILCOF-1 and SH-COF modified perovskite, respectively.

Figure 6.14 Schematic representation of the post-modification reaction of ILCOF-1 to yield COF-921.

Figure 6.15 Photographic images of the post-modification reaction of ILCOF-1 to yield COF-921.

Figure 6.16 FTIR spectra of ILCOF-1 before and after modification (COF-921).

Figure 6.17 Solid-state ^{13}C NMR of ILCOF-1 and COF-921.

Abbreviations

PSCs	Perovskite Solar Cells
PCE	Power Conversion Efficiency
COFs	Covalent Organic Frameworks
NiO_x	Nickel Oxide
HTL	Hole Transport Layer
ETL	Electron Transport Layer
HTM	Hole Transport Material
ETM	Electron Transport Material
V_{oc}	Open-circuit voltage
FF	Fill Factor
J_{sc}	Short-Circuit Current Density
sp^2c-COFs	sp^2 Carbon-Conjugated COFs
HOMO	Highest Occupied Molecular Orbital
LUMO	Lowest Unoccupied Molecular Orbital
MHP	Metal Halide Perovskites
DSSCs	Dye-Sensitized Solar Cells
LEDs	Light-Emitting Diodes
SAMs	Self-Assembled Monolayers
PL	Photoluminescence
CVD	Chemical Vapor Deposition
PVD	Physical Vapor Deposition
LbL	Layer-by-Layer
PXRD	Powder X-ray Diffraction
FTIR	Fourier Transforms Infrared
NMR	Nuclear Magnetic Resonance
FE-SEM	Field Emission Scanning Electron Microscopy
TGA	Thermogravimetric analysis
BET	Brunauer-Emmett-Teller Method
UPS	Ultraviolet Photoelectron Spectroscopy

XPS	X-ray Photoelectron Spectroscopy
DFT	Density Functional Theory
VBM	Valence Band Maximum
CBM	Conduction Band Minimum
CV	Cyclic Voltammetry
TFPPy	1,3,6,8-tetrakis(p-formylphenyl)pyrene
ITO	Indium Tin Oxide
FTO	Fluorine Tin Oxide

Chapter 1

Introduction

Perovskite solar cells (PSCs) have gained significant attention due to their high power conversion efficiencies (PCEs) and low production costs. However, their long-term stability remains a critical challenge, primarily due to defects in the perovskite layer and at the interfaces between functional layers. These defects hinder charge extraction, causing non-radiative recombination and reducing device performance. Addressing these issues is essential for improving the efficiency and durability of PSCs. This chapter examines the potential of covalent organic frameworks (COFs) to overcome these challenges, particularly through defect passivation. It introduces the design principles and hypotheses behind the use of COFs, focusing on sp^2 *carbon-conjugated COFs as interfacial passivation agents and pyrene-based COFs as bulk dopants. By improving charge transport and stabilizing interfaces, this work aims to enhance PSC performance. The chapter also outlines the objectives and scope of the thesis, presents a brief overview of the dissertation structure, and highlights key findings, underscoring the importance of COFs in advancing PSC technology.*

1.1 Background and Motivation

Perovskite solar cells (PSCs) have made significant strides in the field of photovoltaics due to their exceptional optoelectronic properties, ease of fabrication, and low production costs. Since their debut in 2012,[5,6] PSCs have achieved power conversion efficiencies (PCEs) that now rival traditional silicon-based solar cells, with single-junction PSCs reaching 27% efficiency and tandem devices surpassing 30%.[7–10] This impressive performance, combined with the relatively simple and inexpensive fabrication processes, positions PSCs as a promising technology for addressing the growing global demand for renewable energy. Despite these advancements, the commercialization of PSCs remains hindered by several critical challenges, particularly in terms of long-term stability and scalability. One of the primary obstacles to achieving commercially viable PSCs is the presence of defects within the perovskite absorber layer and at the interfaces between different functional layers. These defects can lead to non-radiative recombination, which diminishes device efficiency and accelerates degradation under operational conditions. Furthermore, trap states within the perovskite material and at the interfaces exacerbate charge carrier losses, leading to further declines in performance.[11–18] In addition to addressing these defects, the scalability of PSC manufacturing processes must be improved to enable the large-scale production of high-efficiency devices. Current deposition methods for thin films often struggle to maintain uniformity and crystallinity over large areas, resulting in performance variations that limit the practical application of PSCs. Therefore, innovative strategies that address both the defect passivation and scalability challenges are essential for advancing PSC technology toward commercial deployment.[19–21]

Covalent Organic Frameworks (COFs) have emerged as a promising class of materials that can address these challenges due to their highly tunable structures, high surface areas, and crystalline porous networks. COFs offer unique opportunities for defect passivation in both the bulk perovskite material and at the interfaces between the perovskite and transport layers. Additionally, COFs can be processed using scalable solution-based techniques, making them well-suited for integration into large-area PSC devices.[22] Furthermore, COFs provide an opportunity to directly tune their electronic properties, allowing precise control over the bandgap and charge transport characteristics of the material (**Figure 1.1**).[23–26] This tunability is particularly important for optimizing the performance of COFs as defect passivation agents in PSCs, where matching the energy levels of the COF to the perovskite and transport layers can enhance charge extraction and reduce recombination.[27,28]

This thesis investigates the application of semiconducting COFs in PSCs, focusing on their role in passivating defects, improving charge extraction, and enabling scalable fabrication processes. The research explores how COFs can be designed, synthesized, and post-synthetically modified to enhance the efficiency and stability of PSCs, contributing to the development of commercially viable perovskite solar technologies.

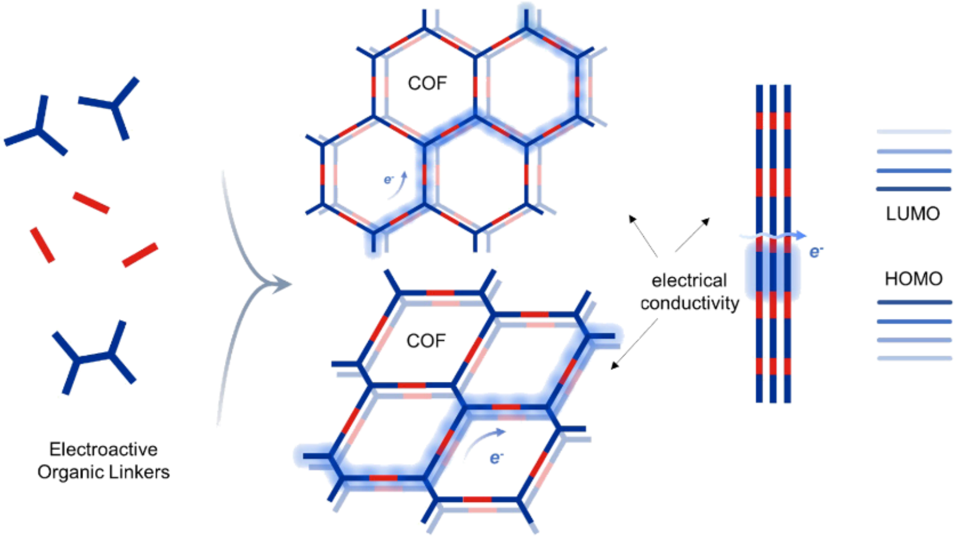

Figure 1.1 Tuning the electronic properties of semiconducting COFs through varying electroactive organic building block and functionalities.

1.2 Problem Statement

Metal halide perovskites represent one of the most exciting developments in photovoltaics, offering the potential for efficient, low-cost solar cells that can be produced using solution processing techniques. However, the commercialization of PSCs is hindered by several significant challenges:

Interfacial Defects: The interfaces between the perovskite absorber layer and the adjacent transport layers are critical for efficient charge extraction. However, these interfaces often contain defects, such as undercoordinated ions and vacancies, which result in charge accumulation and non-radiative recombination. These defects reduce the overall PCE and contribute to the degradation of the perovskite material. This is particularly evident in PSCs using nickel oxide (NiO_x) as the hole transport layer (HTL), where defects such as Ni^{3+} and Pb^{2+} ions at the interface create recombination centers that limit device performance. [29,30] Typically, Ni^{3+} cations in NiO_x layers function as Brønsted proton-acceptors and Lewis electron-acceptors, resulting in the deprotonation of cationic amines and oxidation of iodide species. This process creates PbI_2-rich barriers that impede hole extraction at the perovskite/NiO_x interface. Such imperfections contribute to carrier accumulation and inefficient charge transport at interfaces, resulting in non-radiative recombination, hysteresis, and significant limitations in open-circuit voltage (V_{oc}) and fill factor (FF), as well as intrinsic degradation of perovskite materials (**Figure 1.2**).[30–32]

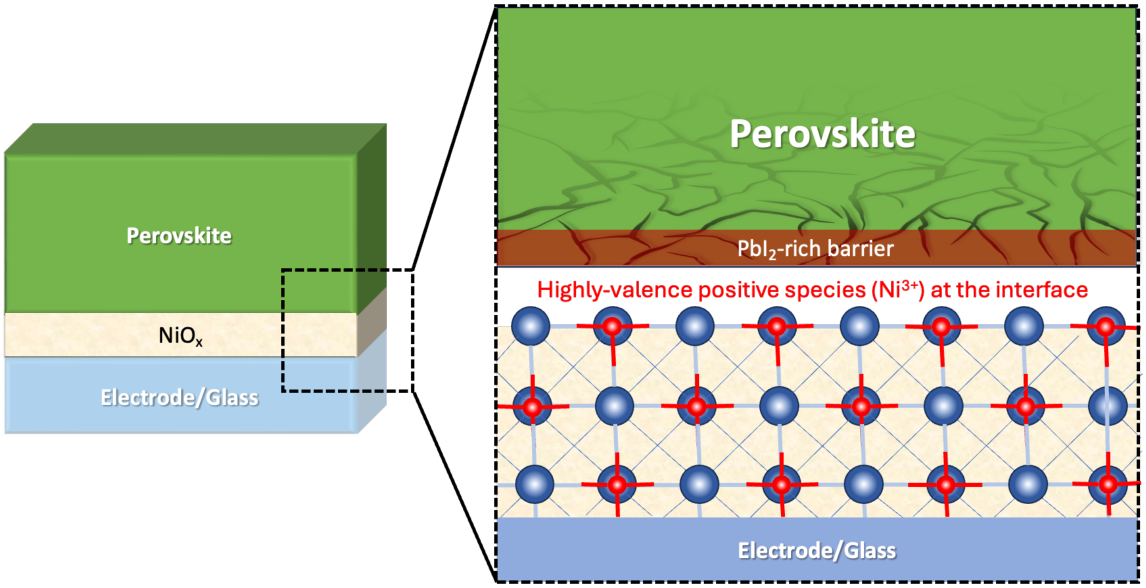

Figure 1.2 Schematic representation of defects at the NiO_x/perovskite interface.

Trap States in the Bulk Perovskite Material: Bulk defects, commonly referred to as trap states, are inherent to the perovskite material due to its fabrication methods and composition. These trap states, including vacancies and undercoordinated Pb^{2+}, serve as non-radiative recombination centers, reducing charge carrier mobility and increasing hysteresis in device performance. Effective strategies for trap state passivation are required to mitigate these losses and improve the operational stability of PSCs.[33–35]

The objective of this thesis is to explore the use of semiconducting COFs as a solution to these challenges. COFs possess unique properties that make them well-suited for both defect passivation and scalable fabrication, offering a promising approach to improving the efficiency and stability of PSCs while enabling their large-scale production.

1.3 Design Principles and Hypotheses

The design principles guiding this research are based on the unique properties of COFs, which allow for the targeted passivation of defects and the improvement of charge transport in PSCs. The hypotheses presented in this thesis are structured around the dual role of COFs as both interfacial passivation agents and bulk dopants in PSCs, as well as the direct tuning of their electronic properties through post-synthetic modification.

1. Design Principle 1: Dual-Passivation at the NiO_x/Perovskite Interface Using COFs

The first design principle focuses on addressing interfacial defects at the NiO_x/perovskite junction, which are a significant source of non-radiative recombination and performance losses in PSCs. NiO_x, a widely used HTL in PSCs, introduces defects such as Ni^{3+} cations that react with the perovskite layer to form recombination centers, leading to reduced charge extraction efficiency. The hypothesis is that sp^2 carbon-conjugated COFs (sp^2c-COFs), with electron-donating functional groups such as cyano (-C≡N), can act as Lewis bases to passivate both Ni^{3+} at the NiO_x surface and undercoordinated Pb^{2+} in the perovskite layer (**Figure 1.3**). This dual-passivation strategy is expected to reduce the density of recombination centers at the interface, facilitate more efficient charge extraction, and improve the overall PCE of the PSCs. In addition to passivating defects, the porous and crystalline structure of sp^2c-COFs is designed to act as a scaffold for controlling perovskite crystallization, leading to larger grain sizes and fewer grain boundaries. This structural control is expected to further reduce trap states and improve charge carrier mobility, ultimately enhancing device performance.

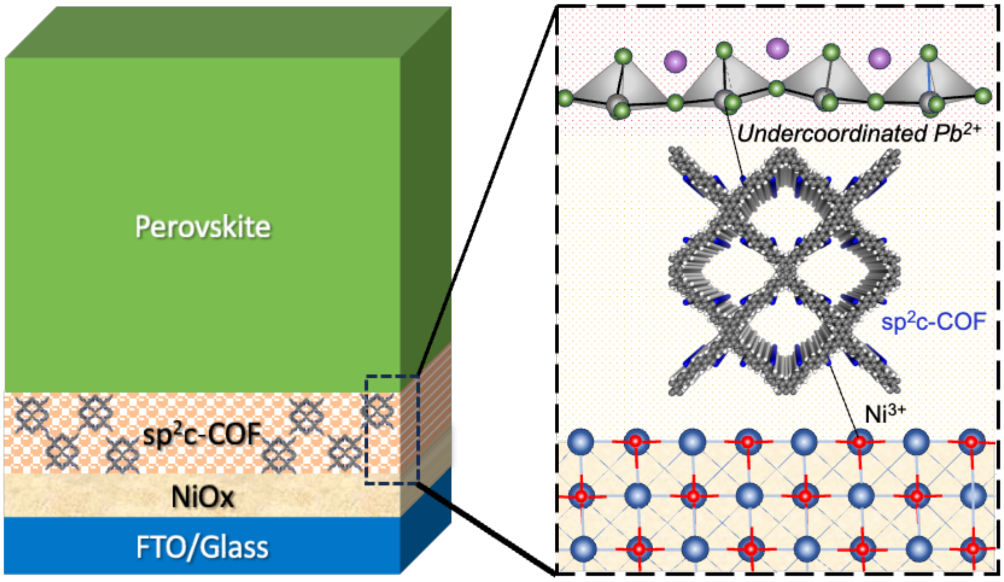

Figure 1.3 Schematic representation of the interfacial dual-passivation approach using sp^2c-COF.

2. Design Principle 2: Bulk Trap State Passivation Using Pyrene-Based COFs

The second design principle addresses trap states in the bulk perovskite material, which are a major source of non-radiative recombination and efficiency losses. Pyrene-based COFs, such as ILCOF-1 and SH-COF, are hypothesized to serve as bulk dopants that can coordinate with undercoordinated Pb^{2+} ions in the perovskite layer, thereby passivating trap states and improving charge transport. The incorporation of these COFs into the bulk perovskite material is expected to enhance crystallinity, reduce the density of trap states, and improve charge carrier mobility. The hypothesis is that this approach will lead to significant improvements in the PCE of PSCs. Furthermore, the tunability of COFs allows for the optimization of their electronic properties, such as bandgap and charge transport pathways, making them highly adaptable to different perovskite compositions and device architectures. This versatility is crucial for maximizing the effectiveness of COFs as defect passivation agents and for integrating them into large-area PSCs produced through scalable fabrication methods.

3. Design Principle 3: Post-Synthetic Modification for Bandgap Tuning

One of the most promising aspects of COFs is their tunability through post-synthetic modification, which allows for the precise control of their electronic properties, particularly the bandgap. Unlike COFs synthesized a priori, where the electronic structure is predetermined by the choice of building blocks, post-synthetic modification offers greater flexibility in fine-tuning the material's properties without altering the underlying framework. This approach enables the strategic introduction of donor-acceptor moieties or modification of linker units within the COF structure, allowing for incremental adjustments to the bandgap to match the energy levels of the perovskite layer and transport materials. Such adaptability is particularly advantageous for optimizing the integration of COFs into PSCs, as it facilitates the precise alignment of the COF's highest occupied molecular orbital (HOMO) and lowest unoccupied molecular orbital (LUMO) with the perovskite band edges. This electronic tuning is crucial for enhancing charge extraction, reducing recombination losses, and improving overall device performance.

Hypotheses

Hypothesis 1: Functionalized sp^2 carbon-conjugated COFs can be designed to passivate defects at the NiO_x/perovskite interface, reducing non-radiative recombination and improving charge extraction in PSCs. This dual-passivation strategy is expected to enhance both the efficiency and stability of the devices.

Hypothesis 2: Pyrene-based COFs can be used as bulk dopants in the perovskite layer to passivate trap states, improve crystallinity, and enhance charge carrier mobility. This approach is anticipated to lead to higher PCE in PSCs. The bandgap of COFs can be tuned through post-synthetic modification, allowing for the optimization of their electronic properties for enhanced charge extraction and reduced recombination in PSCs.

1.4 Objectives and Scope

The primary objectives of this thesis are:

1. **To design and synthesize COFs** with tailored functional groups that enable them to act as defect passivation agents at the NiO_x/perovskite interface and within the bulk perovskite material.
2. **To incorporate COFs into PSC architectures** as both interfacial passivation layers and bulk dopants, with the goal of improving charge extraction, reducing recombination losses, and enhancing device efficiency.
3. **To develop scalable solution-processing techniques** for COF thin films deposition that can be applied to PSCs without compromising film quality or device performance.
4. **To optimize the bandgap of COFs** through post-synthetic modification, aligning their electronic properties with the perovskite and transport layers to enhance charge extraction and device performance.
5. **To evaluate the performance of COF-enhanced PSCs** through a comprehensive set of characterization techniques, including electrical, optical, and morphological analyses, to determine the impact of COF integration on the devices performance.

The scope of this research encompasses the design, synthesis, and characterization of semiconducting COFs, the integration of these materials into both p-i-n (CsFA-based) and n-i-p ($FAPbI_3$-based) PSCs, and the evaluation of their impact on device performance. This thesis explores both the fundamental material properties of COFs and their practical application in improving the efficiency of PSCs.

1.5 Dissertation Overview

This dissertation is structured into seven chapters that comprehensively cover the background, methodology, experimental results, and conclusions of the research. Each chapter is summarized below:

Chapter 1: Introduction – Introduces the key challenges in PSC technology, outlines the research hypotheses, and presents the objectives and scope of the study.

Chapter 2: Literature Review – Provides a detailed review of the current state of research in PSCs, focusing on defect passivation strategies, the role of interfacial engineering, and the potential of COFs in optoelectronic devices.

Chapter 3: Materials and Methods – Describes the materials used, the synthesis of COFs, and the fabrication of PSC devices. This chapter also outlines the characterization techniques used to evaluate the properties and performance of the materials and devices.

Chapter 4: Synthesis and Characterization of sp^2c-COFs – Presents the synthesis and characterization of semiconducting sp^2 carbon-conjugated COFs, including elemental analysis, thermal stability, nitrogen adsorption, and crystallinity supported by modelling and simulation. The chapter discusses the optoelectronic and electrical properties of sp^2c-COF and its potential for defect passivation.

Chapter 5: Integration of sp^2c-COFs into PSCs – Explores the incorporation of sp^2c-COFs as interfacial layers in PSCs, evaluating their impact on device performance. The chapter examines the characteristics of sp^2c-COF thin films, the fabrication and performance of MA-free CsFA-based PSCs, and the impact of sp^2c-COF on the PCE. It highlights the dual passivation effect of sp^2c-COF on NiO_x and Pb^{2+} defects, using techniques like XPS and FTIR, and concludes with a summary of the findings and their implications.

Chapter 6: Pyrene-based COFs as bulk dopant in PSCs – Focuses on using pyrene-based conjugated COFs as additives in PSCs. It covers the synthesis of ILCOF-1 and SH-COF and the fabrication of $FAPbI_3$ solar cells. The chapter evaluates the effects of COF doping on optical properties, crystallinity, and carrier dynamics, and examines COF interactions with Pb^{2+} ions. It also explores a strategy for direct bandgap tuning of COFs through post-synthetic modifications. The chapter concludes with a summary of findings and the benefits of using pyrene-based COFs in PSCs.

Chapter 7: Conclusions and Future Directions – Summarizes the key findings of the research, evaluates the hypotheses, and discusses potential future research directions in the application of COFs in photovoltaics and other optoelectronic devices.

1.6 Findings and Outcomes/Originality

This research makes several novel contributions to the field of PSCs, including:

1. Introduction of sp^2 Carbon-Conjugated COFs as interfacial passivation layers, demonstrating their ability to reduce defects, enhance charge extraction, and improve the stability of PSCs.
2. Demonstration of Pyrene-Based COFs as bulk dopants for trap state passivation, leading to improved perovskite crystallinity, enhanced charge carrier mobility, and higher PCE.
3. Development of Scalable Solution-Processing Techniques for COF thin films, providing a pathway for the large-scale fabrication of high-efficiency PSCs.
4. Insight into the mechanisms of COF-Perovskite Interactions, offering a deeper understanding of how COFs can be used to address the key challenges of defect passivation and scalability in PSCs.
5. Demonstration of tuning of the COFs bandgap through direct post-synthetic strategy, by converting imine linkage to thiazole.

Chapter 2

Literature Review

This chapter provides an overview of the advancements in PSCs, with a particular focus on their evolving architectures, material properties, and the persistent challenges that limit their efficiency and stability. It examines critical components such as electron and hole transport layers (ETLs and HTLs), interfacial defects, and material degradation, all of which are crucial in the development of high-performance solar cells. Special attention is given to the role of defects at the interfaces, such as trap states and surface vacancies, which are known to significantly impact the efficiency of PSCs by causing non-radiative recombination and limiting charge transport. The chapter also introduces COFs as a promising material for addressing these challenges. COFs offer unique opportunities for enhancing PSC performance by enabling better defect passivation, improving interfacial engineering, and providing long-term stability to the devices. In the context of this thesis, this chapter lays the theoretical foundation and identifies the key challenges that guide the experimental investigations. By discussing the potential of COFs for improving PSCs, the chapter sets the stage for the research efforts aimed at advancing the design and implementation of more efficient and durable solar cell technologies.

2.1 Perovskite Solar Cells (PSCs)

In the past few decades, the demand of sustainable clean energy has increasingly risen. Solar cell technology has gained the most interest since the sun is a continuous source of energy that exceeds 10,000 times the current consumption demand. Despite the rapid advances in photovoltaic (PV) devices, the currently used solar cells still suffer from low efficiency, high cost and scalability issues. Metal halide perovskites (MHP) have emerged as third-generation solar cells owing to their excellent optical and electrical properties (**Figure 2.1**).[36,37] Recently, The progress in PSCs have shown extraordinary achievements reaching a high PCE of 27.0% for devices-based on a single junction,[10,38] 30.1% for a perovskite-based tandem architecture, and 34.6% for tandem devices based on a perovskite/silicon architecture.[10,39] Moreover, the estimated fabrication cost of PSCs is half the of the silicon-based solar cells.[40] These attractive advances over the last few years have encouraged the transformation of PSCs from laboratory to commercial market.[41–45]

2.1.1 Development of PSCs

PSCs have undergone rapid development since their inception, evolving from a niche photovoltaic technology to one of the most promising alternatives to conventional silicon solar cells. The history of PSCs began in 2009, when Miyasaka *et al.* first reported the use of methylammonium lead halide ($CH_3NH_3PbX_3$) perovskites as light absorbers in dye-sensitized solar cells (DSSCs), achieving an efficiency of around 3.8%.[46] Although these early devices exhibited rapid degradation due to the instability of the perovskite in liquid electrolytes, the initial results demonstrated the high potential of perovskite materials for solar energy applications. These early perovskite DSSCs used mesoporous titanium dioxide (TiO_2) scaffolds to transport electrons, but the material's vulnerability to moisture posed significant challenges.[47] A major breakthrough occurred in 2012, when Snaith *et al.* and Park *et al.* independently replaced the liquid electrolyte with solid-state hole transport materials (HTMs), such as spiro-OMeTAD, leading to the first solid-state PSCs.[47–49] This transition to solid-state architecture eliminated the issue of electrolyte degradation and allowed researchers to explore a variety of perovskite compositions and device architectures. By 2014, PCEs had surged past 15%, thanks to improvements in perovskite film morphology, compositional engineering, and interfacial layer optimization (**Figure 2.2**).[50] The development of mixed-halide perovskites, such as $CH_3NH_3PbI_{3-x}Br_x$, enabled better control over the material's bandgap and improved stability under environmental stressors such as moisture and heat.[51]

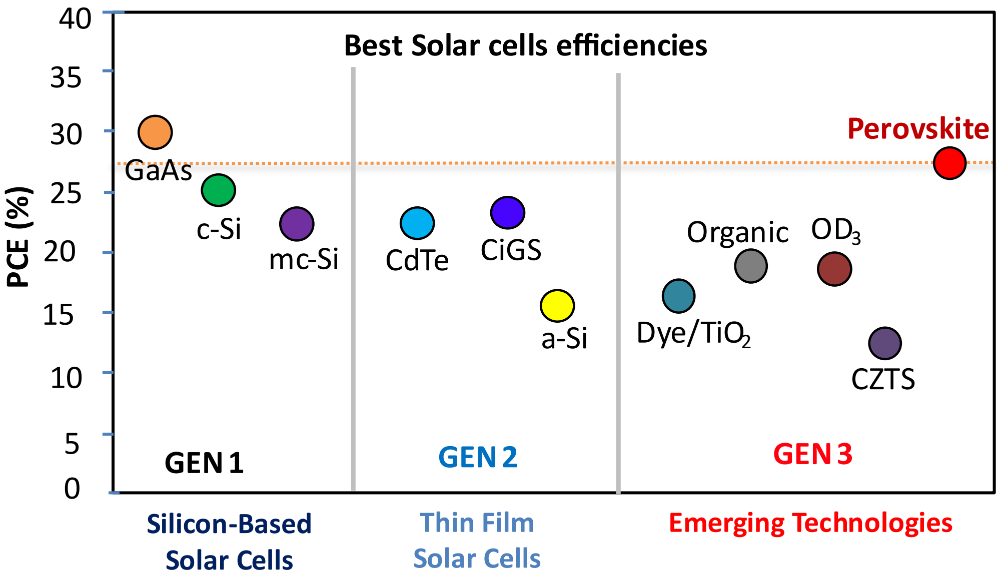

Figure 2.1 Generational progress in solar cell technologies, with perovskite emerging as the third generation, achieving efficiencies close to those of traditional silicon-based cells.

Since then, PSCs have experienced rapid advancements in efficiency and stability. Researchers have shifted their focus to addressing long-standing issues with material stability, environmental degradation, and lead toxicity. A significant innovation was the introduction of formamidinium lead iodide ($FAPbI_3$) and mixed-cation perovskites, which offered enhanced thermal stability and a broader absorption range in the visible spectrum.[52] Formamidinium-based perovskites have proven to be more stable than their methylammonium counterparts, and further doping with cesium (Cs^+) and rubidium (Rb^+) has led to improved structural stability and higher PCEs.[51,53] By 2017, the PCE of PSCs had exceeded 22%, placing them in direct competition with established silicon solar cells.[54]

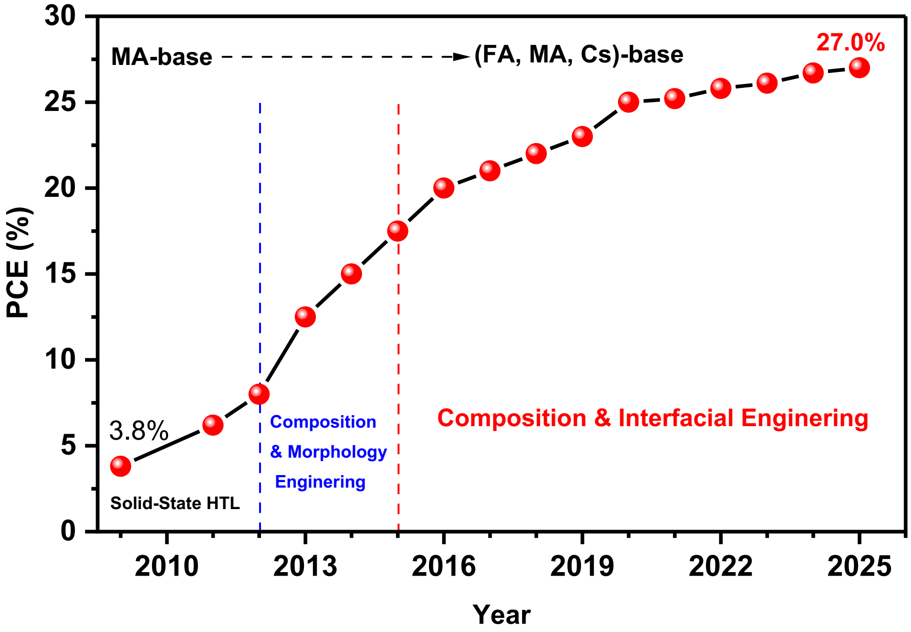

Figure 2.2 Major milestones in the development of PCE of PSCs from 2009 to 2025.

Recent Developments: 2023-2024: The most recent advancements in PSCs, particularly between 2023 and 2024, have largely focused on improving both the efficiency and long-term stability of these devices. These efforts have involved innovative approaches to material design, device architecture, and fabrication techniques, as well as new strategies for addressing the environmental impact of lead-based perovskites. One notable area of progress is in the development of passivation techniques, which have been crucial for mitigating the negative effects of defects at the perovskite grain boundaries and interfaces. These defects typically act as non-radiative recombination centers, reducing the efficiency of the solar cell. In 2024, a novel surface passivation strategy was reported involving the immobilization of formamidinium cations at the perovskite surface, significantly reducing defect density and improving both efficiency and stability.[55] This approach extended the operational lifetime of PSCs under continuous illumination, addressing a key hurdle for the commercialization of this technology. In parallel, improvements ETLs and HTLs have also played a critical role in advancing PSC technology. For instance, recent studies have introduced graphene-based HTLs, which exhibit superior thermal stability and reduced parasitic absorption compared to traditional organic HTLs like spiro-OMeTAD.[56]

Additionally, research on inverted planar PSC architectures has demonstrated PCEs exceeding 25%, benefiting from improved charge extraction and reduced recombination losses at the perovskite/transport layer interfaces.[54,57] These developments underscore the importance of optimizing the interfacial layers to minimize energy losses and extend device longevity.

Another significant trend in recent PSC research has been the push toward lead-free perovskite materials.[58] Although lead-based perovskites continue to dominate in terms of efficiency, concerns about lead's toxicity have driven the search for alternative materials.[59–61] Tin-based perovskites (e.g., $CH_3NH_3SnI_3$) have emerged as the most promising candidates, but their tendency to oxidize in ambient conditions has limited their practical application.[62] Recent advances in stabilizing tin-based perovskites using surface passivation and additive engineering have shown promising results, with devices reaching efficiencies of over 10% and improved environmental stability.[62,63] Despite these gains, further research is needed to fully realize the potential of lead-free PSCs. The rise of tandem solar cells has also marked a significant milestone in perovskite solar cell research. Tandem cells, which combine perovskites with other photovoltaic technologies such as silicon, have demonstrated record-breaking efficiencies. In 2024, perovskite-silicon tandem cells reached PCEs of 34.6%, benefiting from the complementary absorption properties of the two materials.[64,65] Tandem solar cells are expected to play a pivotal role in the future of PSCs, offering a pathway to surpass the theoretical efficiency limits of single-junction cells and enabling more cost-effective, high-efficiency solar modules.

Moreover, the commercialization prospects of PSCs have been bolstered by recent progress in scalable fabrication methods. Techniques such as blade coating, slot-die coating, and inkjet printing have enabled the production of large-area perovskite solar modules with minimal efficiency loss compared to small-scale lab devices.[66] Researchers have also developed advanced encapsulation techniques to protect PSCs from environmental degradation, further enhancing their durability and bringing them closer to commercial deployment.[67,68]

2.1.2 Physical and Optical Properties of Perovskites

The unique material properties of perovskites have made them the centrepiece of recent solar cell technology advancements. The versatility of its crystal structure allows for easy compositional tuning, which in turn modulates key properties such as bandgap, charge carrier mobility, and stability.

Crystal Structure and Electronic Properties: Perovskites exhibit a characteristic three-dimensional (3D) cubic or tetragonal structure. Generally, perovskites are compounds with the chemical composition of ABX_3, where A is a monovalent cation (such as methylammonium (MA^+), formamidinium (FA^+) or Cs^+), B is divalent metal cation (such as Pb^+ or Sn^+), and X is monovalent anion (such as I^-, Br^- or Cl^-).[36,37] This structure features a metal cation at the center of the octahedral framework, with the halide anions occupying the vertices and the organic cation in the cuboctahedral void (**Figure 2.3**). This arrangement allows for exceptional charge-carrier mobility, a key parameter for high-efficiency solar cells. For example, methylammonium lead iodide ($CH_3NH_3PbI_3$), one of the most studied perovskites, exhibits balanced electron and hole mobilities, ensuring efficient charge transport and minimal recombination losses.[69] The charge-carrier diffusion lengths in these materials can exceed 1 μm, which is significantly longer than in many other photovoltaic materials.[51,69] The electronic properties of perovskites are heavily influenced by their band structure, which can be tailored by modifying the composition of the 'A', 'B', and 'X' sites. The bandgap of perovskites is typically direct, ranging from 1.5 to 2.3 eV, depending on the halide composition. For example, replacing iodide with bromide increases the bandgap from 1.55 eV to 2.3 eV, making it possible to fine-tune the absorption properties for various applications, including tandem solar cells. The tunability of the bandgap also enables the use of perovskites in multi-junction solar cells, where different bandgaps are required to absorb different wavelengths of the solar spectrum efficiently.[70,71]

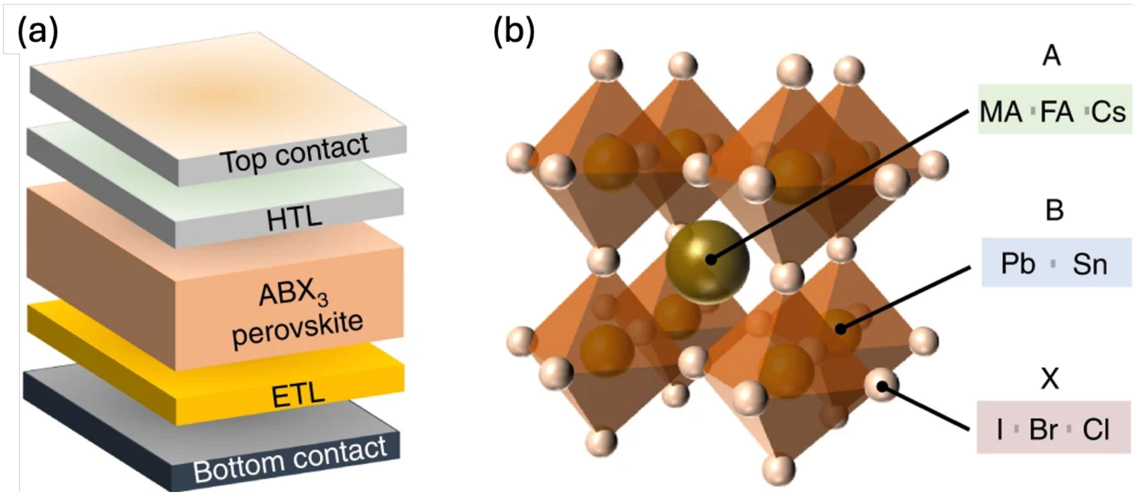

Figure 2.3 (a) Schematic representation of the architecture of a typical PSC. (b) Diagram illustrating the structure of the MHP semiconductor family, generally expressed by the chemical formula ABX_3. Adapted with permission from Saliba *et al.*[1].

Optical Properties: Perovskites exhibit strong light absorption across the visible spectrum, making them highly attractive for photovoltaic applications. For example, methylammonium lead iodide ($MAPbI_3$) exhibits an absorption coefficient exceeding 10^5 cm^{-1}, enabling it to absorb over 90% of incident light within a thickness of just a few hundred nanometres.[72] This high absorption coefficient allows for the creation of thin-film solar cells, reducing material usage and enabling flexible devices. The optical properties of perovskites are further enhanced by their ability to form high-quality films with minimal defects. Advances in fabrication techniques, such as solvent engineering, thermal annealing, and additive doping, have greatly improved film crystallinity and reduced surface roughness, which are critical for achieving high device performance.[73,74] Additionally, researchers have developed methods for tuning the photoluminescence and electroluminescence properties of perovskites, making them suitable not only for solar cells but also for applications in light-emitting diodes (LEDs) and photodetectors.[75,76]

Defects and Recombination Losses: Defects within perovskite films, such as vacancies, interstitials, and grain boundaries, have a significant impact on their photovoltaic performance. These defects often act as non-radiative recombination centers, reducing the efficiency of solar cells by allowing charge carriers to recombine before they can be extracted. For instance, iodine vacancies are particularly detrimental, as they lead to the formation of deep traps that facilitate recombination.[77,78] To address this issue, researchers have employed various passivation strategies, including the use of organic molecules and fullerene derivatives, to passivate these defects and improve the overall stability and performance of PSCs.[79,80] Recent studies have demonstrated that passivating grain boundaries and surface defects can significantly reduce non-radiative recombination and enhance both the open-circuit voltage and fill factor of PSCs. For example, the introduction of 2D perovskite layers at the grain boundaries of 3D perovskite films has been shown to dramatically improve the stability of the material under operational conditions by preventing moisture and oxygen ingress.[81–83] These passivating layers also help mitigate ion migration, a key issue in perovskite stability, which can lead to hysteresis in the current-voltage characteristics of the solar cells.

Material Stability: Material stability remains one of the most critical challenges for PSCs. Early perovskites, such as methylammonium lead iodide, were highly sensitive to moisture, oxygen, and heat, which led to rapid degradation of the material and a significant drop in device performance.[84] Recent advances in material engineering have led to the development of more stable perovskite compositions, such as FA-based and Cs-doped perovskites, which exhibit enhanced thermal and moisture stability.[85,86] In particular, formamidinium lead iodide ($FAPbI_3$) has emerged as one of the most promising materials for stable, high-efficiency PSCs due to its superior thermal stability compared to methylammonium-based perovskites.[87] Moreover, researchers have developed several innovative encapsulation techniques that protect PSCs from environmental degradation. For example, the use of hybrid organic-inorganic encapsulation layers and flexible polymer coatings has significantly improved the long-term operational stability of PSCs, enabling them to maintain high efficiencies under real-world conditions.[67,68] The issue of long-term stability has also prompted extensive research into the degradation mechanisms of perovskites under operational conditions. Studies have shown that exposure to light, oxygen, and moisture can cause the decomposition of perovskite materials into lead iodide (PbI_2) and other byproducts, leading to a decrease in efficiency over time. To combat this, researchers have employed a range of strategies, including the use of protective barrier layers, passivation of grain boundaries, and the incorporation of more robust inorganic cations into the perovskite structure.[88]

Emerging Trends in Material Engineering: The field of perovskite material engineering continues to evolve rapidly, with several new trends emerging in recent years. One notable development is the use of low-dimensional (2D and quasi-2D) perovskites, which have shown great promise in enhancing the stability of PSCs while maintaining high efficiency. These materials consist of alternating organic and inorganic layers that act as barriers to moisture and oxygen, preventing degradation and extending the operational lifetime of the solar cells.[89,90] Another exciting trend is the exploration of lead-free perovskites, driven by environmental and health concerns associated with lead's toxicity.[58,91] Tin-based perovskites (e.g., $CH_3NH_3SnI_3$) have garnered significant attention as potential alternatives, although they still suffer from lower efficiencies and stability compared to lead-based perovskites.[62,63] Recent advancements in passivation techniques and material synthesis have helped improve the performance of tin-based PSCs, but further research is needed to fully realize their potential.[92,93] In summary, the unique material properties of perovskites, including their tunable bandgap, high absorption coefficient, and remarkable charge-carrier mobility, have made them a focal point in the development of next-generation solar cells. Despite challenges related to stability and ion migration, ongoing research in material engineering and device architecture continues to push the boundaries of what is possible with PSCs.

2.1.3 Device Architectures in PSCs

The architecture of PSCs has been a critical focus of research since the inception of the technology, significantly influencing the PCE and stability of the devices. Broadly, the most common device architectures are categorized into two main types: mesoscopic and planar structures. Within these categories, different arrangements, such as n-i-p (normal) and p-i-n (inverted) configurations, have been developed, each offering distinct advantages in terms of performance, processing, and long-term stability. Understanding the role of different layers and how they contribute to device function is essential to advancing PSC technology.

Mesoscopic Architecture: The mesoscopic architecture was among the earliest designs for PSCs, inspired by DSSCs. This structure typically incorporates a mesoporous scaffold, such as TiO_2, infiltrated with a perovskite absorber layer. In this configuration, the mesoporous TiO_2 layer acts as an ETL while the perovskite serves as both the light absorber and the hole transport medium.[94] Early developments of mesoscopic PSCs achieved remarkable efficiency improvements due to the high surface area provided by the mesoporous structure, which facilitated efficient charge separation and transport.[95,96] The traditional mesoscopic structure consists of a conductive substrate (usually fluorine-doped tin oxide, FTO), a compact TiO_2 layer, followed by the mesoporous TiO_2 scaffold infiltrated with perovskite, and HTL such as spiro-OMeTAD. A metal contact, typically gold, is used as the back electrode (**Figure 2.4**). The high electron mobility of TiO_2 combined with the efficient perovskite light absorber resulted in initial PCEs exceeding 17% in early iterations of this architecture.[96] One of the challenges with the mesoscopic architecture is its sensitivity to UV light, which can cause degradation in the TiO_2 layer, leading to device instability.[97] To address this, researchers have explored alternative metal oxides like zinc oxide (ZnO) and tin oxide (SnO_2), which offer greater stability and comparable electron transport properties.[98] Despite these advances, the mesoscopic structure has been gradually phased out in favor of planar architectures, which offer simpler fabrication processes and improved scalability.

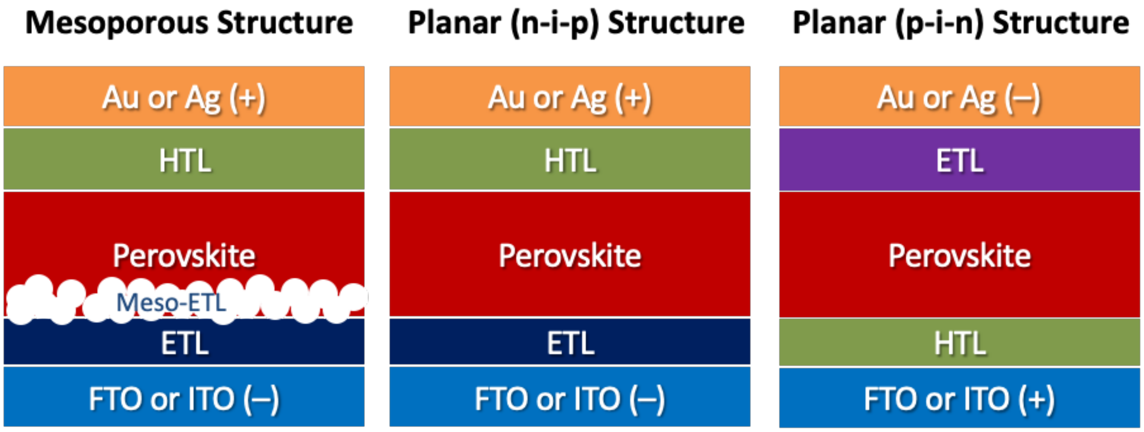

Figure 2.4 Schematic illustration of the perovskite device architectures; mesoporous and planar (n-i-p and p-i-n).

Planar Architecture: The planar structure emerged as a prominent alternative to the mesoscopic architecture, offering a simplified device design and enhanced flexibility in material choice. Planar PSCs do not utilize a mesoporous scaffold; instead, they consist of a thin, flat perovskite layer positioned between ETL and HTL.[99] This structure can be fabricated using solution-processing techniques, such as spin coating, or more scalable methods like blade coating and inkjet printing. There are two primary configurations within planar PSCs: the n-i-p and the p-i-n structure **(Figure 2.4)**. In the n-i-p configuration, the ETL is deposited directly on the conductive substrate, followed by the perovskite layer, the HTL, and the back metal contact (typically gold or silver).[36] Common ETL materials in this configuration include TiO_2, SnO_2, and ZnO, while spiro-OMeTAD remains a popular HTL choice.[100] The n-i-p configuration typically offers higher PCEs due to the efficient charge extraction by the ETL and HTL layers. However, the reliance on organic HTLs like spiro-OMeTAD has posed challenges in terms of stability, as these materials are prone to degradation under prolonged exposure to light and heat. In contrast, the p-i-n configuration places the HTL directly on the substrate, followed by the perovskite layer, the ETL, and the back metal contact. This inverted structure was initially developed to mitigate some of the stability issues associated with the n-i-p configuration. In the p-i-n architecture, alternative HTL materials, such as NiO_x and poly(triarylamine) (PTAA), have been explored to improve stability. In particular, NiO_x has gained attention due to its robustness and compatibility with flexible substrates. Similarly, fullerene derivatives (e.g., PCBM) and ZnO are frequently used as ETLs in this configuration due to their high electron mobility and stability under illumination.[101]

Electron and Hole Transport Layers: The choice of ETL and HTL plays an important role in affecting the performance and stability of PSCs. These layers facilitate the collection and transport of electrons and holes to the respective electrodes while minimizing recombination losses. In addition, the quality of the interfaces between the transport layers and the perovskite layer can significantly impact the device's efficiency and long-term stability.[102] TiO_2 has been the most widely used ETL in mesoscopic PSCs, owing to its excellent electron mobility and ability to form a stable interface with the perovskite layer. However, TiO_2 is known to suffer from photocatalytic activity under UV illumination, which can degrade the perovskite layer over time.[103] To address this issue, SnO_2 has emerged as a promising alternative ETL material due to its superior electron mobility, wider bandgap, and resistance to UV-induced degradation.[103] ZnO is another candidate, but it has been found to react with the perovskite layer at elevated temperatures, leading to the formation of undesired byproducts that reduce device efficiency.[104] On the HTL side, spiro-OMeTAD has been the gold standard for achieving high PCEs in both mesoscopic and planar n-i-p PSCs. However, its relatively high cost and instability under operating conditions have driven the search for alternative HTLs. NiO_x has emerged as a stable and cost-effective alternative, particularly in inverted (p-i-n) PSCs, where it has demonstrated good compatibility with various perovskite compositions and excellent thermal stability.[105–107] PTAA and poly(3-hexylthiophene) (P3HT) have also been investigated for use as HTLs due to their processability and ability to form good interfaces with perovskites.[100] Recent advancements have also explored the use of 2D materials, such as graphene and transition metal dichalcogenides (e.g., MoS_2), as transport layers. These materials offer high charge-carrier mobility and flexibility, making them suitable for next-generation PSCs, including flexible and wearable solar cells.[56]

2.1.4 Stability and Interface Challenges in PSCs

Despite the impressive progress made in PSC device architectures, several challenges remain. Stability continues to be a major concern, particularly for organic HTLs like spiro-OMeTAD, which degrade over time under operating conditions. The ongoing search for more stable, cost-effective transport layers is crucial for the commercialization of PSC technology. Moreover, the scalability of PSC fabrication remains an issue, as many high-efficiency devices are produced using small-area lab-scale techniques that are difficult to scale up to industrial production. Another devices instabilities originate from the perovskite layer itself, including the degradation of the perovskite in humidity, grain boundaries recombination and UV-induced degradation. While others caused by the interfacial defects that occur on the interfaces between perovskite and charge transport layers. For example, NiO_x interfacial defects that cause photodegradation of perovskite and the halide vacancies trap states and under-coordinated Pb^{2+} that that lead to charge recombination:

Perovskite-NiO_x Interface Problem: A variety of HTMs in p–i–n perovskite architecture were employed, including poly (3,4-ethylenedioxythiophene):poly(styrenesulfonate) (PEDOT:PSS)[108], PTAA[109] , and NiO_x[110]. NiO_x is considered the most a promising HTL candidate with the superior characteristics of wide-bandgap, excellent optical transparency, high stability, and low cost. Compared to conventional PSCs that require high-temperature sintering of TiO_2 (up to 500°C), inverted PSCs incorporating NiO_x as the HTL can be fabricated under milder processing conditions, making them more compatible with flexible and low-temperature device fabrication.

Various synthesis methods have been developed to optimize NiO_x thin films, each offering distinct advantages in terms of film quality, scalability, and cost-effectiveness. The sol-gel method is widely used due to its simplicity, involving the dissolution of nickel precursors in organic solvents, followed by spin-coating and high-temperature annealing to achieve the desired film morphology and crystallinity.[111] Sputtering, a physical vapor deposition (PVD) technique, provides uniform and high-quality films but requires vacuum conditions.[112] Spray pyrolysis facilitates large-area deposition by spraying nickel precursor solutions onto a heated substrate, promoting thermal decomposition.[113] More advanced techniques such as atomic layer deposition (ALD) enable precise thickness control and superior film uniformity through sequential exposure to nickel and oxygen precursors.[114] Additionally, thermal evaporation can be employed to deposit high-purity NiO_x films under vacuum.[115] Despite these advantages, NiO_x suffers from intrinsic defects that can lead to charge recombination and carrier loss in PSCs, potentially limiting device performance. Therefore, optimizing NiO_x synthesis and surface engineering is crucial to mitigating defect-induced losses and enhancing the efficiency and stability of perovskite solar cells.

Moreover, semiconducting NiO_x exhibit redox and photocatalytic reactivity, which can significantly impact the stability of PSCs. One critical issue is the interaction between high-valence Ni^{3+} in NiO_x and iodide (I^-) in perovskites, leading to undesired interfacial degradation. Ni^{3+} sites in NiO_x can act as Brønsted proton acceptors and Lewis electron acceptors, facilitating the deprotonation of the cationic amines and oxidation of iodide species. The oxidation process results in the formation of $PbI_{2-x}Br_x$–rich interfacial barriers, hindering efficient hole extraction and increasing charge recombination losses.[116] Additionally, the presence of oxygen vacancies, Ni interstitials, and nonstoichiometric nickel species contributes to defect states within the NiO_x layer, promoting deep trap states and impeding charge transport. These defects collectively reduce the PCE, accelerate the degradation of PSCs, and shorten their operational lifetime. Addressing these challenges requires defect passivation strategies such as surface modifications, doping, and interface engineering to suppress nonradiative recombination and improve device stability.

Research Efforts: Many research efforts have been dedicated to solving this problem. For example, Chen *et. al.* reported *in situ* passivation strategy through soaking of NiO_x-based HTL in hydroiodic acid (HI) during roll-to-roll printing method. In which, Ni^{3+} compound on the film surface was reduced to nickel iodide (NiI_2) via HI redox reaction.[117] He *et. al.* modified the surface of the NiO_x film using potassium chloride (KCl) to optimize the ordering of the perovskite crystals at the interface, therefore minimizing interface defects and limiting charge recombination.[118] McGehee *et. al.* reported a strategy to overcome the redox reaction through providing additional A-site cations in perovskite to compensate the formation of $PbI_{2-x}Br_x$ at the perovskite-NiO_x interface.[116] Self-assembled monolayers (SAMs) is another reported technique has been investigated.[119] Self-assembled donor-acceptor dye molecules was introduced to supress the interfacial reaction between NiO_x and perovskite, leads to PCE and lifetime improvements.[120]

Halide vacancies trap states, under-coordinated Pb^{2+} and charge recombination: The halide vacancies trap states are one of the major factors that limits the advancement of the device performance. Trapping of the charge carriers occur to due to the defects on the surface or on the grain boundaries which induce carriers' loss, limiting the carrier's lifetime and causes hysteresis in the I-V curves. The vacancies of halides may be the source of the defects on the bulk and surface. The decomposition of halide ions leads to under-coordinated Pb atoms or clusters, which form a carrier recombination centres. The carrier recombination causes reduction of current density and fill factor leading to increase of the efficiency. Therefore, it is necessary to develop new techniques to passivate the surface defects of under-coordinated Pb atoms. The most successful techniques is to treat perovskite film with electron-rich Lewis base that can coordinate with under-coordinated Pb atoms by donating a lone pair of electrons.

Research efforts: A Lewis base is an electron-rich molecule with lone pairs of electrons available for donation to cationic species.[121] In perovskites, Lewis bases can interact with undercoordinated Pb^{2+} ions, helping to passivate defects.[122] Typically, electron-rich moieties are organic molecules containing donor sites like nitrogen (N), oxygen (O), or sulfur (S). N-donor groups, often found in structures such as pyridine, cyano, or primary amino groups, feature nitrogen atoms with lone electron pairs available for bonding. For example, the addition of pyridine in an antisolvent leads to improvement of the film quality through slowing the film formation, enhance the surface defects passivation, and increases PCE from 16.9 to 19%.[123] Long-chain polymers that contain pyridine can bond with under-coordinated Pb^{2+} and fill the A-vacancies.[124,125] An additive based on amino Lewis base improved the stability of PSCs, maintaining 95% of the initial PCE upon exposure to ambient temperature and humidity.[126] N-containing Lewis bases such as theophylline and theobromine, and small molecules such as urea and caffeine have been proven to slow the perovskite film degradation through defect passivation leading to high efficiency and stability.[127,128]

O-based polymers such as poly (methyl methacrylate) PMMA have improved heterogeneous nucleation via adduct formation with PbI_2 which leads to Gibbs free energy minimization and the formation of smooth perovskite films.[129] Other polymers functionalized with C=O groups were reported to effectively passivate the perovskite defects, resulting to stability enhancement.[130–132] It is well known that sulfur (S) binds more strongly to lead (Pb) than oxygen (O), which can be attributed to Hard and Soft Acid–Base (HSAB) theory. As a soft Lewis base, sulfur exhibits a stronger affinity for the soft Lewis acid lead compared to oxygen, which is a harder base. Additionally, the greater polarizability of sulfur-donor bases allows them to engage in more effective orbital interactions with lead, thereby enhancing the binding strength relative to oxygen-donor bases.[133] Numerous studies on sulfur-based organic compounds, such as thiourea, thiophene, and related derivatives, demonstrate their ability to interact with under-coordinated Pb^{2+} ions, forming Lewis acid-base adducts.[134–136] A copolymer of perylene diimide and thiophene was employed as a multifunctional interfacial layer between the perovskite and $PC_{61}BM$, effectively passivating the under-coordinated Pb on the perovskite layer.[137]

The introduction of n-type organic semiconductors with π-conjugated Lewis bases can effectively passivate halide vacancies at perovskite interfaces by forming Lewis acid-base adducts with under-coordinated Pb ions at the interfaces and grain boundaries (**Figure 2.5**). This approach led to notable improvements in inverted PSCs through the addition of a π-conjugated Lewis base. For example, IDIC, a well-known non-fullerene acceptor widely used in high-efficiency organic solar cells, was employed as an interfacial layer between the perovskite and $PC_{61}BM$.[2] The π-conjugated Lewis base, with its carbonyl (C=O) and cyano (C≡N) groups, effectively passivated under-coordinated Pb ions in $MAPbI_3$, combining trap-passivation with charge-extraction capabilities.[2]

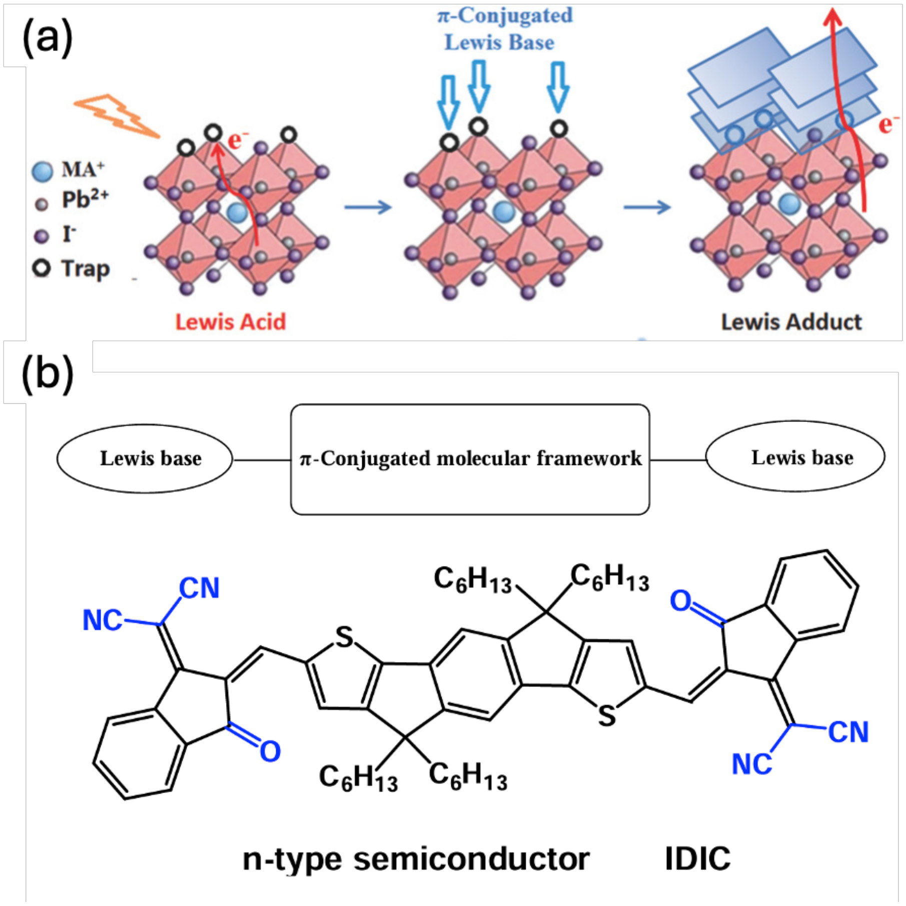

Figure 2.5 (a) Schematic illustration of the interaction of the π-conjugated Lewis base IDIC and Pb^{2+}. (b) Molecular structure of IDIC featuring carbonyl and cyano end groups. Adapted with permission from Huang *et al.*[2].

2.2 Covalent Organic Frameworks (COFs)

2.2.1 Definition and Structure of COFs

COFs are a class of crystalline, porous materials entirely composed of light elements connected by covalent bonds, forming highly ordered, extended networks. Introduced by Yaghi *et al.* in 2005,[138] COFs are known for their modularity, which allows for the precise design of their chemical and structural properties to meet specific functional requirements. Unlike other porous materials such as zeolites and metal-organic frameworks (MOFs), COFs are purely organic in nature, composed of carbon (C), boron (B), nitrogen (N), hydrogen (H) and oxygen (O) atoms that form reticulated networks.[139] This all-organic composition gives COFs exceptional tunability in terms of their chemical functionality, pore size, and topological architecture.[3,140] The unique characteristics of COFs arise from the selection of organic building blocks that connect via covalent bonds through reversible condensation reactions. These reactions typically involve the formation of imine, boroxine, or boronate ester linkages, which allow for the creation of highly stable and crystalline frameworks.[141] The reversibility of these reactions plays a crucial role in error correction during synthesis, leading to highly ordered frameworks with well-defined, periodic pore structures. COFs can exist in either 2D or 3D forms. 2D COFs consist of covalently bonded layers of atoms that are stacked in a parallel fashion, creating one-dimensional channels perpendicular to the planes. These materials exhibit large surface areas, uniform pore sizes, and high porosity, making them ideal for applications that require efficient mass transfer, such as catalysis and gas separation.[142] In contrast, 3D COFs feature covalent bonding in all three spatial directions, resulting in robust networks with interconnected pores.[143] These materials offer superior mechanical strength and thermal stability, which are beneficial for applications such as gas storage and energy storage devices. One of the key advantages of COFs is their customizable nature, which allows researchers to engineer their structures at the molecular level.[144] By selecting different building blocks, the size, shape, and functionality of the pores can be finely tuned, enabling the development of materials tailored for specific tasks, such as selective gas adsorption, chemical sensing, or catalytic activity.[141] This tunability is what sets COFs apart from other porous materials, as it allows for the precise control of their structural and functional properties.

2.2.2 Types of COFs

COFs are categorized into two main types based on their structural organization: 2D COFs and 3D COFs as shown in **Figure 2.6**.

2D COFs: 2D COFs are constructed from planar sheets of covalently bonded atoms. These sheets stack atop one another through weak van der Waals forces or π-π interactions, creating ordered, one-dimensional channels that run perpendicular to the layers. The arrangement of the layers in 2D COFs can vary, from eclipsed stacking, where the layers are perfectly aligned, to staggered stacking, which can introduce additional porosity and affect the material's properties.[140,141] The high surface area and uniform pore structure of 2D COFs make them ideal candidates for applications such as gas separation, molecular sieving, and catalysis. COF-5, for example, was one of the first 2D COFs synthesized and is known for its hexagonal pore structure, formed through the condensation of boronic acids and catechols.[145,146] 2D COFs are also being explored for their potential in electronic applications due to their high charge mobility and ability to transport electrons efficiently through the stacked layers.

3D COFs: In contrast to 2D COFs, 3D COFs extend their covalent bonding in all three dimensions, forming complex, interconnected networks. These frameworks are typically more rigid and stable than their 2D counterparts, with well-defined pore architectures that enhance their mechanical and thermal stability.[142] The interconnected nature of the pores in 3D COFs allows for improved mass transport and makes them particularly suited for applications that involve the storage and separation of gases, as well as for use in catalysis and energy storage devices. A notable example of a 3D COF is COF-300, which is synthesized through imine condensation, resulting in a cubic structure with high porosity and exceptional stability.[3]

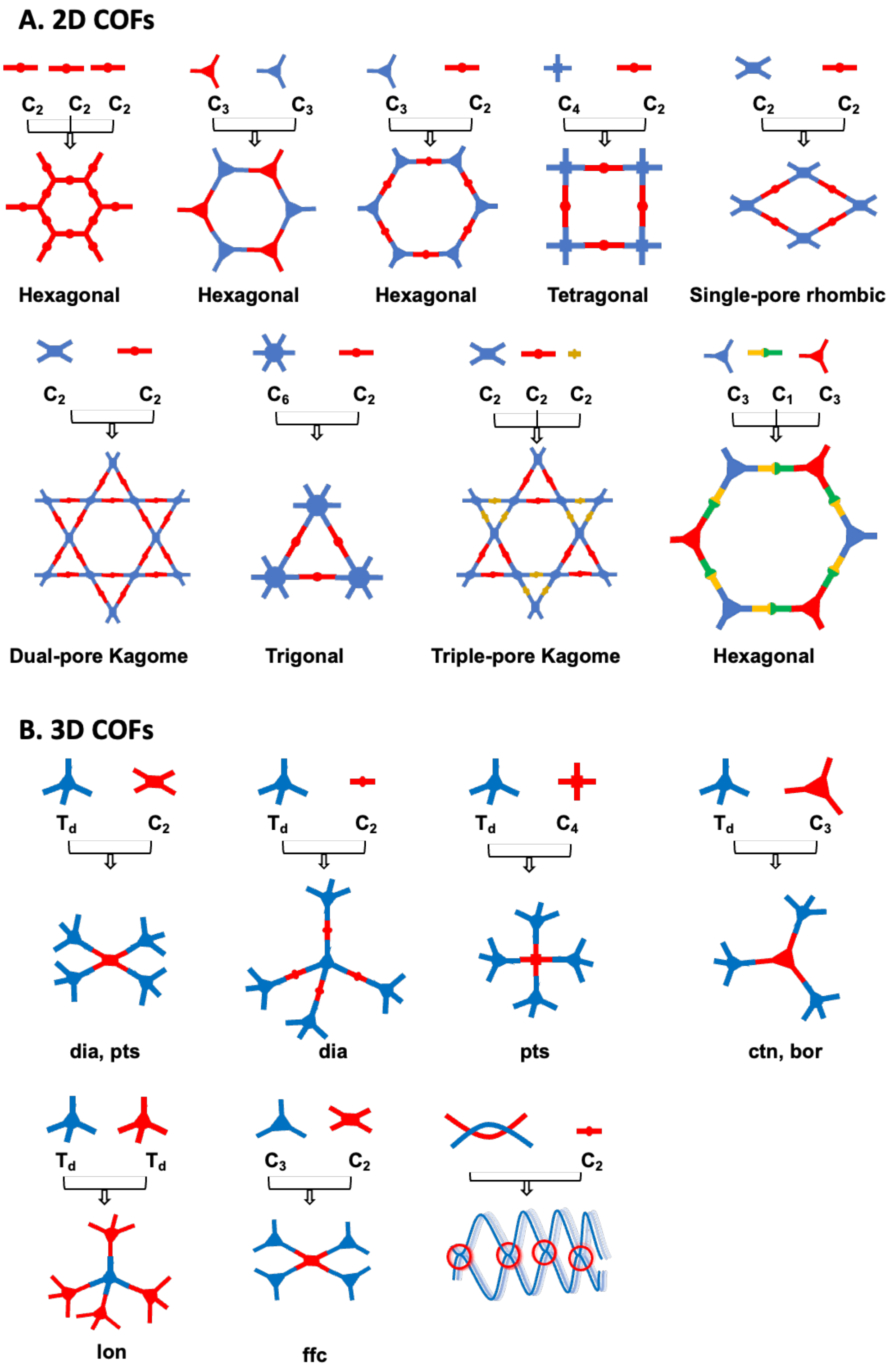

Figure 2.6 Illustration of design principles of different topologies in COFs [3]. *No permission is required for thesis purposes.*

2.2.3 Design Principles of COFs

The design of COFs is rooted in reticular chemistry, a field that focuses on constructing extended, crystalline networks from well-defined organic building blocks linked by strong covalent bonds.[147] This synthetic strategy allows for precise control over the structure, functionality, and porosity of the resulting material, enabling the design of COFs with specific properties tailored to various applications such as gas storage, catalysis, and photovoltaics. The main design principles that govern the construction of COFs are:

Selection of Building Blocks: The choice of organic building blocks is a critical step in the design of COFs. These building blocks are often small molecules with multiple reactive sites, such as boronic acids, aldehydes, amines, or nitriles. These molecules act as nodes or connectors within the COF framework, and their geometry determines the final topology of the COF structure. For example: Trigonal planar building blocks lead to 2D hexagonal or honeycomb-like structures.[3,148] Tetrahedral or octahedral building blocks can result in 3D networks with more complex architectures. The building blocks' chemical composition and geometry influence not only the topology but also the pore size, pore shape, and chemical functionality of the COF. This versatility in design makes COFs highly adaptable for a wide range of applications, from molecular sieves to catalysts.

Linkers and Nodes: The linkers in COFs are organic units that connect the building blocks, creating an extended network. These linkers determine the dimensionality and connectivity of the framework. For example, Linear linkers typically result in 1D channels in 2D COFs.[149] While, trigonal or tetrahedral linkers create 3D networks with interconnected pores.[150] The nodes are the points where linkers converge and can be functionalized to add specific chemical functionalities to the framework. These nodes are often functionalized with various chemical groups to impart catalytic activity, selectivity, or adsorptive properties.[151] The careful selection of both linkers and nodes allows researchers to control the surface area, pore structure, and chemical reactivity of the COF, which is essential for its application in catalysis, gas adsorption, and beyond.

Linkage types: One of the defining features of COFs is the type of covalent linkages used to form the extended framework. These linkages determine the stability, rigidity, and chemical resistance of the COF. **Figure 2.7** shows an examples of common linkage types include:

- **Boronate Ester Linkages**: Formed from boronic acids and catechols, boronate esters are among the earliest linkages used in COFs. These linkages typically result in highly porous structures but may exhibit lower chemical stability under acidic conditions.[152]
- **Imine Linkages**: Derived from the reaction between aldehydes and amines, imine-linked COFs are known for their excellent thermal stability and chemical robustness.[153] Imine linkages also allow for post-synthetic modification, where functional groups can be introduced without compromising the framework's integrity.[154]
- **β-Ketoenamine Linkages**: This type of linkage, formed through the reaction of aromatic amines and diketones, offers even greater stability, particularly under acidic and basic conditions. β-Ketoenamine-linked COFs are highly suited for applications where chemical durability is crucial.[155,156]
- **Hydrazone Linkages**: These linkages are formed through the condensation of hydrazides with aldehydes and provide a balance between porosity and chemical stability.[157] Hydrazone-linked COFs are being increasingly explored for their potential in catalysis and energy storage applications.[158]
- **C=C Linkages (sp^2 Carbon-Conjugated COFs):** These linkages, characterized by C=C bonds between carbon atoms, are particularly notable for their high electrical conductivity and extended π-conjugation, which facilitates efficient charge transfer.[159,160] This makes C=C-linked COFs particularly attractive for applications in photovoltaics and optoelectronics.[160–162] Their rigid framework, formed through robust covalent bonds, contributes to their excellent chemical stability and thermal resistance.

The choice of linkage type in COFs has profound implications for both the stability and functionality of the material. As such, careful consideration must be given to this aspect during the design phase, as different linkages offer distinct advantages depending on the intended application. For instance, imine-linked COFs are particularly advantageous for photovoltaic applications due to their thermal stability, chemical robustness, and ease of functionalization, making them suitable for integrating into PSCs where stability and fine-tuning of electronic properties are critical.[120,153,163] In contrast, β-ketoenamine-linked COFs, with their resilience in harsh chemical environments, are better suited for catalytic applications, where chemical durability and stability under extreme conditions are essential. Similarly, C=C-linked COFs (sp^2 carbon-conjugated frameworks) hold great promise for applications in optoelectronics and energy storage, due to their extended π-conjugation and enhanced charge transfer capabilities.[160–162] These linkages provide the necessary mechanical stability and electronic properties for efficient charge transport, making them ideal for high-performance photovoltaic devices. Ultimately, the selection of linkage type is a key factor that determines the performance, durability, and applicability of COFs, and it must be tailored to align with the specific requirements of the target application, whether it be in solar energy conversion, catalysis, or other advanced material technologies.

Functionalization: Functionalization of COFs involves the incorporation of specific chemical groups into the framework, either during synthesis or through post-synthetic modification.[141] Functionalization allows COFs to be tailored for specific applications, such as catalysis, gas separation, or photovoltaics. For example, COFs can be functionalized with:

- Metal complexes to enhance catalytic activity.[164]
- Hydrophobic or hydrophilic groups to improve their performance in separation processes.[165]
- Lewis base groups for defect passivation in PSCs.[166]

Post-synthetic modification, in particular, provides additional flexibility by allowing the introduction of new functionalities after the COF has been synthesized.[167] This approach enables fine-tuning of the COF's properties without altering its underlying structure, making it possible to optimize the material for specific applications. For instance, the bandgap of COFs can be precisely tuned via post-synthetic modification, allowing for better alignment of electronic properties with the active materials in PSCs. In summary, the design of COFs is guided by the careful selection of building blocks, linkers, and nodes, the choice of appropriate linkage types for desired stability and functionality, and the ability to functionalize the framework for specific applications. These principles allow for the creation of tailored materials with diverse properties and make COFs highly versatile for a wide range of advanced applications in materials science and energy conversion technologies.

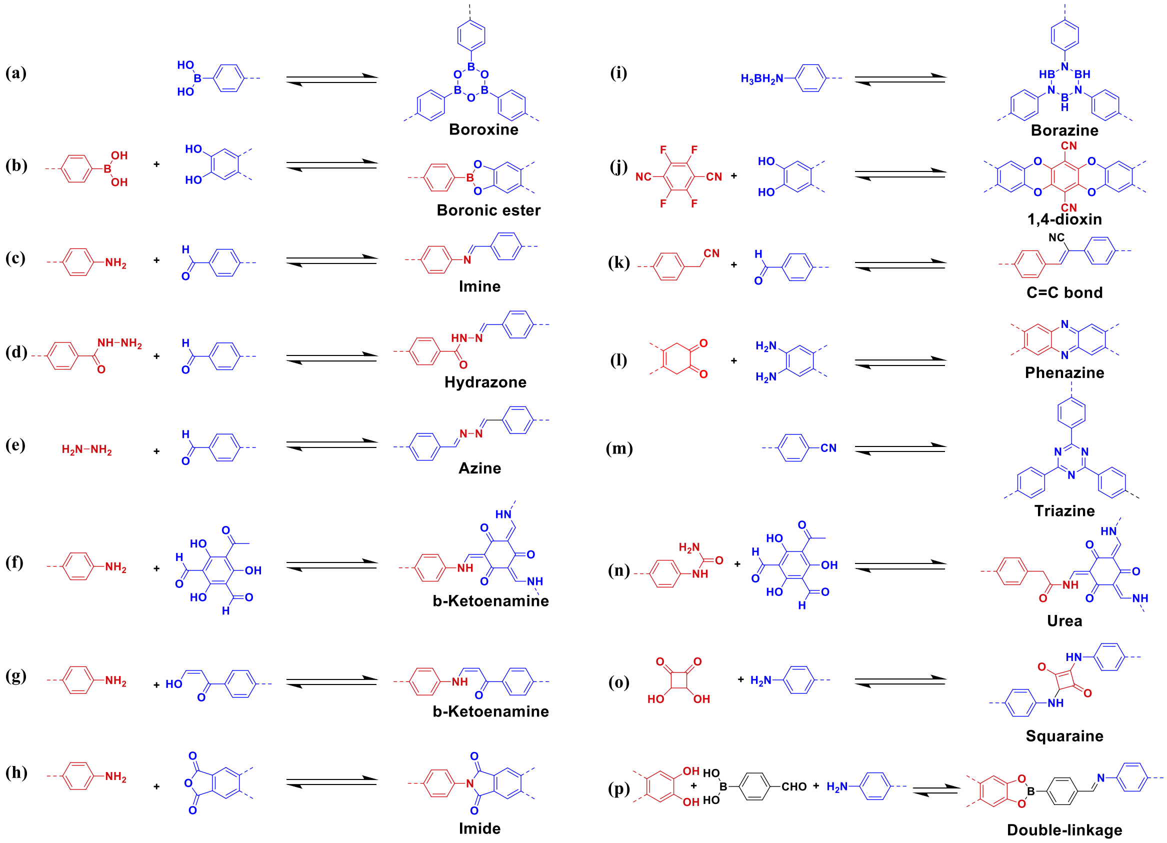

Figure 2.7 Common condensation reactions forming various types of linkages in COFs[3]. *No permission is required for thesis purposes.*

2.2.4 Synthesis Methods of COF Powder

The synthesis of COFs relies on the use of reversible condensation reactions that allow for the formation of highly ordered, crystalline materials. These reactions involve the formation of covalent bonds between organic building blocks, resulting in the creation of extended networks with well-defined pore structures. Several methods have been developed to synthesize COFs, each with its own advantages (**Figure 2.8**).

Solvothermal Synthesis: Solvothermal synthesis is one of the most common methods used to produce COFs. In this process, the monomers are dissolved in a solvent and heated in a sealed vessel (typically an autoclave) at high temperatures (~ 90-120 ^{o}C) and pressures. These conditions facilitate the condensation reactions that form the covalent bonds, leading to the formation of highly crystalline COFs with well-defined pore structures and high surface areas.[148] Solvothermal synthesis is widely used due to its ability to produce COFs with high degrees of crystallinity, but the reaction conditions must be carefully controlled to ensure the desired structural and functional properties are achieved.

Mechanochemical Synthesis: Mechanochemical synthesis involves the use of mechanical force to drive the condensation reactions between the monomers, typically through grinding or ball milling. This method is advantageous in that it is solvents-free, making it a more environmentally friendly and cost-effective approach to COF synthesis.[168] Mechanochemical synthesis has been shown to produce highly crystalline COFs with good yields, and it is particularly useful for synthesizing frameworks that are difficult to obtain using traditional solvothermal method.

Ionothermal Synthesis: Ionothermal synthesis is a variation of solvothermal synthesis that uses ionic liquids as the solvent and reaction medium. Ionic liquids offer several advantages, including high thermal stability, low vapor pressure, and the ability to dissolve a wide range of organic molecules.[169,170] This method is particularly useful for synthesizing COFs with unique topologies or for introducing functional groups into the framework during synthesis. The use of ionic liquids also allows for the synthesis of COFs at lower temperatures, which can be beneficial for preserving the structural integrity of sensitive building blocks.[168]

Microwave-Assisted Synthesis: This method uses microwave irradiation to rapidly heat the reaction mixture, significantly reducing the time required to produce crystalline COFs. Microwave-assisted synthesis has been shown to produce COFs with high degrees of crystallinity in a matter of minutes, making it an attractive option for large-scale production.[171] Additionally, this method allows for the synthesis of COFs with complex architectures and high porosity, making it suitable for a wide range of applications.

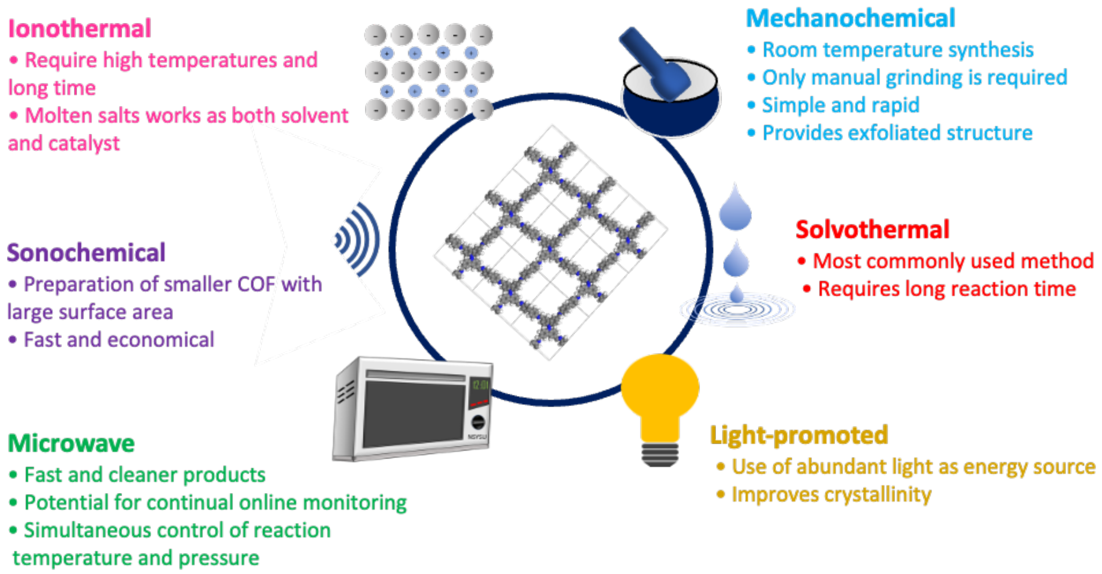

Figure 2.8 Diagrammatic illustration of the properties and benefits associated with different synthetic approaches for COFs[3]. *No permission is required for thesis purposes.*

2.2.5 Synthesis Methods of COF Thin Films

The fabrication of COF thin films is a growing area of research due to the potential applications of these films in a variety of fields, including optoelectronics, energy storage, sensors, membranes, and catalysis.[144,172–174] Unlike the bulk powders of COFs, thin films provide the advantage of integrating COFs directly into devices while maintaining control over thickness, morphology, and orientation on the substrate.[173–175] Developing efficient methods for fabricating high-quality, defect-free, and uniform COF thin films is essential for realizing their potential in practical applications. Several synthesis strategies have been developed to deposit COF thin films onto substrates with precise control over their structural properties. These strategies include solvothermal deposition, interfacial polymerization, layer-by-layer assembly, and vapor-phase deposition. Each method offers distinct advantages and challenges, and the choice of method is often determined by the intended application of the COF thin film.

Solvothermal Deposition: Solvothermal deposition is one of the most common methods used to synthesize COF thin films. In this process, a solution of COF precursors (monomers) is prepared, and a solid substrate is immersed in the solution, typically inside an autoclave or a sealed reaction vessel. The system is then heated to elevated temperatures (usually between 80 °C and 150 °C) under autogenous pressure, allowing the monomers to polymerize directly on the surface of the substrate. This technique is particularly effective for producing crystalline COF films with high degrees of order and uniform thickness.[172,175] During solvothermal deposition, several parameters can be tuned to control the thickness and crystallinity of the film, including the concentration of the monomers, the reaction temperature, the choice of solvent, and the duration of the reaction. For example, using a more concentrated solution or increasing the reaction time typically leads to thicker films. Conversely, lower concentrations or shorter reaction times result in thinner films. One of the main advantages of this method is that it allows for the formation of highly ordered, crystalline COF films with well-defined pore structures. However, the solvothermal method also has limitations. It often requires relatively high temperatures and long reaction times, which can be a challenge when working with temperature-sensitive substrates. Furthermore, controlling the orientation and alignment of the COF thin films can be difficult, particularly for applications that require specific pore alignment or anisotropic properties. Solvothermal deposition is widely used in the synthesis of COF thin films for catalysis and gas separation membranes due to the highly porous and crystalline nature of the resulting films. It is also employed in the fabrication of COF-based sensors and optoelectronic devices where film crystallinity is critical for performance.[176,177]

Interfacial Polymerization: Interfacial polymerization is another widely used technique for synthesizing COF thin films. In this method, two immiscible phases (typically an aqueous phase and an organic phase) containing complementary monomers are brought into contact at a liquid-liquid interface. Polymerization occurs at the interface, leading to the formation of a thin film of COF material.[178] One of the key advantages of interfacial polymerization is that it allows for the fabrication of ultrathin COF films with precisely controlled thicknesses, often in the range of a few nanometers to a few micrometers.[179,180] This method also enables the production of large-area COF films with uniform thickness, making it ideal for applications in membrane technology and gas separation.[180,181] Furthermore, the mild reaction conditions (typically room temperature or slightly elevated temperatures) make this method compatible with a wide range of substrates, including polymers, metals, and ceramics. Interfacial polymerization can also be extended to air-liquid and liquid-solid interfaces, where the COF thin film forms at the boundary between the liquid phase and air or between a liquid phase and a solid substrate.[182–184] The thin films produced by this method are often highly uniform and defect-free, making them suitable for applications that require high precision, such as optical devices and sensors. COF films synthesized via interfacial polymerization are widely used in gas separation membranes, optical coatings, and sensor devices. The ability to produce ultrathin, highly uniform films makes this method ideal for applications that require high sensitivity and selectivity.[185]

Layer-by-Layer (LBL) Assembly: LbL assembly is a versatile and highly controllable method for constructing COF thin films with precise controlling of layer thickness and composition. This technique involves the sequential deposition of monomers onto a substrate, followed by polymerization to form the COF structure. Typically, the monomers are alternately deposited from solution, and after each deposition step, a polymerization reaction is carried out to form a single layer of the COF film.[186] One of the advantages of the LbL assembly approach is its ability to precisely control the film thickness by adjusting the number of deposition cycles. Additionally, this method allows for the incorporation of different monomers or functional groups into each layer, enabling the fabrication of multilayered COF films with tailored chemical and physical properties.[187] The LbL method also offers excellent control over the orientation and alignment of the COF layers, which is crucial for applications that require anisotropic properties or specific pore alignments. Although LbL assembly is highly controllable, it can be time-consuming, especially for thicker films, as each layer must be deposited and polymerized sequentially. The method also requires careful optimization of the deposition and polymerization conditions to ensure uniformity and minimize defects.[188] LbL assembly is particularly useful in applications that require highly controlled film thickness and composition, such as in sensors, batteries, and supercapacitors. The ability to introduce functional layers with different properties also makes this method ideal for applications in catalysis and energy storage.[189]

Vapor-Phase Deposition: Vapor-phase deposition is an advanced technique that involves the vaporization of COF monomers followed by their condensation and polymerization on a solid substrate. This method can be divided into two main approaches: chemical vapor deposition (CVD) and physical vapor deposition (PVD). In CVD, volatile precursors are introduced into a reaction chamber, where they react and deposit as a solid film on the substrate surface.[190] CVD is particularly effective for the growth of highly uniform and conformal thin films with excellent control over film thickness and crystallinity. This method is ideal for depositing COF thin films on substrates with complex geometries, such as nanostructured surfaces or porous materials.[191,192] In contrast, PVD involves the physical vaporization of the monomers followed by their condensation onto a substrate. Unlike CVD, no chemical reaction occurs during deposition, making PVD a simpler technique for depositing thin films of materials that are sensitive to chemical reactions. Vapor-phase deposition methods are advantageous for producing COF thin films with high uniformity and defect-free surfaces. Additionally, these methods offer excellent control over film thickness and morphology, making them ideal for applications in electronic and optoelectronic devices. However, vapor-phase deposition typically requires specialized equipment and high vacuum conditions, which can limit its scalability for large-area film production.[193] COF thin films produced by vapor-phase deposition are used in optoelectronics, microelectronics, and membrane technology.[194,195] The high uniformity and conformality of the films make them suitable for use in nanoscale devices and sensors.

Challenges and Future Directions: While significant progress has been achieved in the synthesis of COF thin films, several challenges remain. One of the main challenges is achieving defect-free, highly crystalline films with controlled thickness and orientation, especially for large-area substrates. Many of the current methods, such as solvothermal deposition and LbL assembly, are time-consuming and difficult to scale up for industrial applications. Additionally, controlling the alignment of the COF pores and layers remains a critical issue for applications that require anisotropic properties, such as in catalysis and separation membranes. Future research will likely focus on developing more efficient, scalable synthesis methods that allow for greater control over the structure and properties of COF thin films. Techniques such as continuous flow synthesis and roll-to-roll processing may offer solutions for scaling up the production of COF films, while advances in vapor-phase deposition techniques could enable the fabrication of highly uniform films with complex geometries.[196] Additionally, the incorporation of functional materials, such as nanoparticles or metal complexes, into COF thin films could open up new possibilities for applications in catalysis, energy storage, and sensing.

2.2.6 Applications of COFs in Material Science

COFs, with their tunable structure, large surface area, and high chemical stability, have found applications across various domains of material science. Their versatility in design allows them to function in a wide range of fields, from gas storage and catalysis to energy storage and optoelectronics. Some of the most promising applications of COFs include:

Catalysis: COFs have gained significant attention as highly effective materials for use in catalysis due to their large surface areas, uniform pore structures, and the ability to incorporate active catalytic sites directly into their frameworks.[197,198] These characteristics make COFs highly suitable as catalysts or catalyst supports in various chemical reactions, offering advantages such as enhanced selectivity, stability, and reusability. One of the key attributes of COFs is their tunability.[199] The covalent linkage of functional groups—such as amines, thiols, or carboxylic acids—within a well-organized porous structure allows for the design of highly selective catalytic systems.[200–202] For instance, COFs functionalized with metal complexes, organic catalysts, or chromophores can facilitate a wide range of chemical transformations, including hydrogenation, oxidation, and carbon dioxide reduction.[203,204] Their ordered structure ensures efficient mass transport through the pores, which enhances reaction kinetics and allows reactants and products to diffuse easily throughout the framework. In addition to traditional catalytic applications, imine-linked COFs, for example, have been shown to function as photocatalysts by incorporating light-responsive units such as transition metals or chromophores into the framework.[203] These COFs can mediate redox reactions under light irradiation, opening up possibilities for solar-driven catalysis and environmental remediation. Another notable advantage of COFs in catalysis is their exceptional stability. The strong covalent bonds within the framework endow these materials with high thermal and chemical resilience, allowing them to perform effectively in harsh reaction conditions, such as high temperatures or aggressive solvents.[197,205] Additionally, the high surface area of COFs allows for the exposure of more active sites, which improves catalytic efficiency.

Gas Storage and Separation: The porous nature and high surface area of COFs make them ideal candidates for gas storage and separation applications. COFs have been shown to selectively adsorb gases such as hydrogen, methane, and carbon dioxide, making them valuable for use in energy storage and carbon capture technologies.[206,207] The tunable pore size and functionality of COFs allow for the selective capture of specific gases, enhancing their performance in gas separation processes.

Energy-Related Applications: Batteries and Supercapacitors: COFs have gained prominence in energy storage systems such as batteries and supercapacitors due to their high surface area, tunable pore structures, and the ability to incorporate redox-active species within the framework. The ordered structure of COFs allows for efficient ion transport and storage, which is critical for achieving high energy densities in supercapacitors.[208,209] Additionally, COFs can be functionalized with redox-active groups such as quinones or transition metal complexes, enabling them to store and release charge during cycling in battery systems.[210] Recent studies have demonstrated the use of COFs as cathode materials in lithium-ion batteries, where their chemical stability and structural rigidity contribute to enhanced cycling performance and capacity retention.[211]

Optoelectronic Devices: COFs have emerged as promising materials for optoelectronic devices, including solar cells and light-emitting diodes (LEDs), owing to their highly tunable structural and electronic properties. COFs stand out due to their inherent modularity, allowing for precise control over their bandgap, charge mobility, and surface chemistry, which are crucial properties for efficient optoelectronic performance. The ability to incorporate π-conjugated systems into the COF backbone enhances the transport of charges (electrons and holes), which is essential for achieving high efficiency in devices that rely on charge separation, such as solar cells and LEDs.

COFs in Solar Cells: One of the most significant applications of COFs in optoelectronics is in solar energy conversion, particularly in organic and PSCs. COFs have shown great promise as light-harvesting materials due to their tunable bandgaps and the ability to integrate donor-acceptor (D-A) systems.[120,163,212] In these systems, the donor unit provides electrons, while the acceptor unit withdraws them, facilitating efficient charge separation under illumination.[27] This mechanism is vital for converting light into electrical energy, as it prevents the recombination of electron-hole pairs, which can otherwise limit the efficiency of the photovoltaic device. One of the unique advantages of COFs over traditional materials in solar cells is their highly ordered pore structures, which can be designed to optimize light absorption and charge transport. By controlling the size and arrangement of these pores, researchers can enhance the light-harvesting efficiency of COFs, improving the overall PCE of the solar cell.[28,213] The incorporation of COFs into the active layer or as interfacial layers in solar cells has led to significant improvements in PCE and long-term stability by reducing charge recombination and passivating defects within the perovskite film.[120,214–217] Furthermore, COFs offer thermal and chemical stability, which is critical for the longevity of photovoltaic devices. Organic materials traditionally used in solar cells often suffer from degradation due to exposure to environmental stressors such as light, heat, and moisture. The robust covalent bonding within COFs provides resistance against these factors, making them excellent candidates for enhancing the stability of next-generation solar cells.[218] Their stability can also contribute to the development of tandem solar cells, where multiple layers of light-absorbing materials are stacked to capture different wavelengths of light, thereby maximizing energy conversion.

COFs in Light-Emitting Diodes (LEDs): In addition to solar cells, COFs are also gaining attention for their applications in LEDs. The ability to tune the electronic properties of COFs through the selection of building blocks and functional groups makes them ideal for use in LEDs, where the emission of light depends on the electronic transitions within the material.[219] The incorporation of π-conjugated systems into COFs enhances their charge transport properties and enables the precise control of their electronic band structure, which is critical for achieving efficient electroluminescence.[220] COFs can be designed to emit light in specific regions of the spectrum, including the visible, ultraviolet (UV), and near-infrared (NIR) ranges, by tailoring the nature of the organic linkers and the connectivity within the framework. This tunability opens up possibilities for developing multicolor and white LEDs, which are highly sought after for applications in displays, lighting, and optoelectronic devices (**Figure 2.9**).[4,221] Another advantage of COFs in LED applications is their high thermal stability, which prevents the degradation of the material under the high operational temperatures typically experienced in LEDs. This property is particularly important for enhancing the lifetime of the device and maintaining its efficiency over extended periods of use.[219] Additionally, COFs exhibit good mechanical stability, which allows them to be integrated into flexible LED devices that require materials capable of withstanding mechanical stresses without losing their optoelectronic properties.[22] In more advanced applications, COFs can be utilized in organic light-emitting transistors (OLETs), which combine the functionalities of transistors and LEDs in a single device. These devices can be used for display technologies and sensors, benefiting from the high charge mobility and the tunable emission properties of COFs.[22,222] Moreover, the design flexibility of COFs allows for the incorporation of dopants or other functional molecules into the framework, further enhancing the luminescent efficiency and color purity of the emitted light.

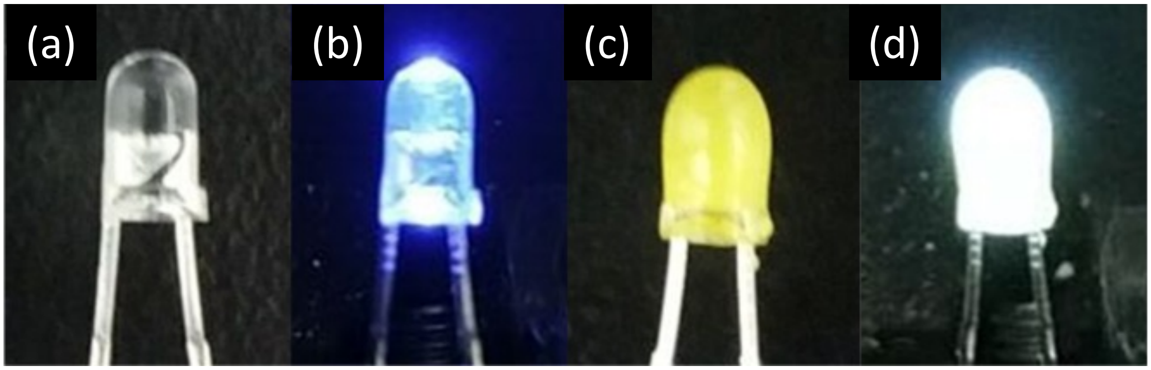

Figure 2.9 White light-emitting diodes based on COF (c) reference LED turned off and (d) on, and the same LED coated with COF (e) off and (f) on [4]. *No permission is required for thesis purposes.*

Challenges and Future Outlook: Despite the promising potential of COFs in optoelectronic devices, several challenges remain. Achieving high crystallinity and defect-free films is critical for maximizing the performance of COF-based solar cells and LEDs, but this often requires careful control over the synthesis and deposition processes. Additionally, controlling the alignment and orientation of COF thin films is particularly challenging, yet essential for ensuring optimal charge transport and light emission in devices. Further research is needed to explore new strategies for improving the scalability of COF-based materials for industrial applications. One promising avenue is the development of vapor-phase deposition and solution-processing techniques, which could enable the production of large-area COF films with high uniformity and crystallinity.[190,196] Moreover, integrating COFs with other advanced materials, such as quantum dots or perovskites, could further enhance their performance in hybrid optoelectronic devices. Looking ahead, the development of next-generation photovoltaic and LED technologies will likely benefit from the continued exploration of COFs, particularly in terms of enhancing device efficiency, stability, and flexibility. The unique properties of COFs, combined with their tunability and structural versatility, position them as promising materials for revolutionizing the field of optoelectronics.

2.2.7 Potentials of Integrating COFs in PSCs

The rapid rise of PSCs in the realm of next-generation photovoltaics has spurred the exploration of various materials aimed at enhancing their efficiency, stability, and scalability. Among these materials, COFs have emerged as promising candidates due to their tunable structures, excellent charge transport properties, and chemical versatility. These unique characteristics of COFs offer significant potential for overcoming several key challenges faced by PSCs, particularly in areas such as charge transport, interfacial engineering, and defect passivation.

Improving Charge Transport: One of the most critical factors influencing the efficiency of PSCs is the ability to transport photogenerated charges (electrons and holes) efficiently to their respective electrodes without significant recombination losses.[223] COFs, with their highly ordered and porous structures, provide an ideal framework for enhancing charge transport in PSCs. Several studies have demonstrated the potential of COFs in improving charge carrier mobility through different structural and compositional modifications. For instance, Jiang *et al.* reported the synthesis of a π-conjugated COF with enhanced charge mobility, attributing the improvement to the extended π-electron delocalization within the framework, which facilitated better charge carrier transport.[224] Similarly, another study by Dey *et al.* explored donor-acceptor (D-A) type COFs, where electron-donating (D) and electron-accepting (A) moieties were alternately arranged, creating an internal electric field that promoted charge separation and reduced recombination losses.[225] These findings suggest that engineering COFs with tailored electronic structures can significantly enhance their function as charge transport materials.

Furthermore, COFs have been investigated as ETLs and HTLs in PSC architectures. For example, a recent work by Wang *et al.* demonstrated that incorporating a benzothiadiazole-based COF as an ETL led to an increase in PCE due to improved electron mobility and reduced interface defects.[226] Likewise, a porphyrin-based COF studied by Li *et al.* exhibited high hole mobility when used as an HTL, contributing to better hole extraction and stability in PSCs.[227] These studies illustrate the potential of COFs in optimizing charge transport pathways and highlight their role in minimizing recombination losses, thereby leading to enhanced device performance. By integrating these literature precedents, it becomes evident that COFs offer a versatile platform for improving charge transport in PSCs. The ability to fine-tune their electronic properties through molecular design enables better control over charge separation, transport, and collection, which are crucial for achieving higher current densities and PCEs in perovskite solar cells.

Interface Engineering and Defect Passivation: Interfacial defects in PSCs often lead to non-radiative recombination, which can significantly reduce the efficiency and operational stability of the device. COFs, with their customizable pore structures and surface chemistry, offer a promising solution for addressing these interfacial challenges.[215] The ability to functionalize COF surfaces with various chemical groups allows for the passivation of surface defects in the perovskite layer, thereby minimizing charge traps and enhancing the stability of the PSC.[215] By serving as interfacial layers between the perovskite absorber and the transport layers, COFs can also improve the energy-level alignment, facilitating more efficient charge transfer across the device. For example, COFs with tailored functional groups can chemically interact with the perovskite material, passivating under-coordinated lead (Pb^{2+}) ions or halide vacancies at the interface, leading to reduced non-radiative recombination and enhanced device stability.[166,218] Incorporating COFs into PSCs can also help mitigate issues related to hysteresis, a common problem in PSCs where the device's performance varies depending on the direction of the voltage scan. The well-defined and consistent porosity of COFs can help stabilize ion migration within the perovskite material, thus reducing hysteresis and improving the reproducibility of the solar cell's performance.[223]

Enhancing Device Stability: One of the primary challenges facing the commercialization of PSCs is their inherent instability under environmental conditions such as heat, moisture, and light exposure. COFs, known for their high thermal and chemical stability, offer an opportunity to improve the long-term stability of PSCs.[214,217,218,228,229] The robust covalent bonding within COFs provides resistance to moisture ingress and thermal degradation, making them suitable for use in environments where conventional organic materials would degrade. By integrating COFs as protective interfacial layers, it is possible to shield the perovskite layer from external environmental factors, thus prolonging the operational lifetime of PSCs. In addition to improving stability, the incorporation of COFs can also enhance the mechanical robustness of flexible PSCs, which is essential for the development of lightweight, portable solar devices.

COFs in Tandem and Multi-Junction Solar Cells: Tandem and multi-junction solar cells, which combine multiple light-absorbing layers with complementary bandgaps, offer the potential to exceed the PCE limits of single-junction PSCs. COFs, with their tunable bandgaps and ability to be synthesized with a wide range of functional groups, are attractive candidates for use in such architectures. By optimizing the optical and electronic properties of COFs, they can be integrated as interlayer materials that facilitate efficient charge transfer between the different sub-cells in a tandem structure.[230] For instance, by incorporating COFs with a bandgap tuned to the near-infrared region, it is possible to enhance the light-harvesting capabilities of the tandem solar cell, thereby increasing its overall efficiency.[231] Additionally, the excellent charge transport properties of COFs help ensure that charge carriers generated in the different sub-cells are efficiently collected, minimizing recombination losses and boosting the device's performance.

Solution-Processed COF Thin Films for Scalable PSC Fabrication: A significant advantage of COFs in PSC applications is their solution-processability, which facilitates the deposition of thin films over large areas using scalable techniques such as spin-coating, doctor-blading, and inkjet printing.[232–234] This is crucial for the commercialization of PSCs, where large-scale, uniform, and high-quality thin films are required for the mass production of solar modules. Solution-processed COF thin films offer the potential to be seamlessly integrated into existing fabrication processes for PSCs. These thin films can be deposited at low temperatures, making them compatible with flexible substrates and roll-to-roll manufacturing processes.[196] The ability to fabricate COF thin films through scalable solution-processing methods directly addresses one of the key bottlenecks in the commercialization of PSC technology, enabling the production of high-efficiency solar cells at lower costs and with greater ease of manufacturing. The integration of COFs into

PSCs represents a significant advancement in photovoltaic technology, offering potential improvements in charge transport, defect passivation, and long-term stability.[27,28,166,213–218,223,228,229,235,236] However, several challenges remain unresolved, particularly regarding the scalable synthesis of COF thin films, the precise mechanisms by which COFs enhance PSC performance, and the optimization of COF structures for perovskite-based devices. These challenges form the basis of the research questions explored in this thesis, as well as the critical research gaps that are addressed through the development of novel solution-processing methods and tailored COF designs.

2.3 Questions to Answer Based on Literature

Based on the existing body of research in the field of PSCs and the emerging use of COFs, several key questions remain unresolved. These questions highlight critical gaps in current knowledge, particularly concerning defect passivation, interfacial engineering, and the scalability of solution-processed COF thin films. The following are the primary questions that your research addresses:

- How can COFs be engineered to effectively passivate trap states within the perovskite layer?

  Trap states within the perovskite layer are one of the primary causes of non-radiative recombination, which limits the PCE of PSCs. Various approaches have been attempted to address these defects, but the use of COFs as passivation agents remains underexplored. What specific design strategies can be used to develop COFs that interact with and passivate defect sites within the perovskite material, thus improving charge carrier mobility and reducing recombination losses?

- What role can COFs play in mitigating NiO_x defects at the interface with the perovskite layer?

  NiO_x is widely used as a hole transport material in PSCs, but surface defects such as oxygen vacancies and under-coordinated nickel ions lead to increased charge recombination. What potential does the incorporation of COF-based interfacial layers hold in passivating these defects, improving energy level alignment, and enhancing the overall efficiency of NiO_x-based PSCs?

- How do COFs influence charge transport and recombination dynamics in PSCs, particularly when used as interfacial passivation layers?
  The ability of COFs to facilitate charge transport and reduce recombination losses is crucial for improving PSC efficiency. However, the exact mechanisms through which COFs influence charge dynamics at the interfaces between the perovskite and transport layers are not yet fully understood. How do COFs impact the separation of charge carriers and the reduction of recombination at the interface, and what are the best design approaches for maximizing their effectiveness in this role?

- Can solution-processed COF thin films be scaled for large-area PSC production without sacrificing film quality and device performance?
  Scalability is a key challenge in the commercialization of PSCs. While solution-processed methods offer a promising route for COF thin film deposition, there are concerns regarding uniformity, crystallinity, and the integration of these films over large areas. What techniques and optimizations can be employed to ensure that solution-processed COF thin films retain their high performance when scaled for large-area applications?

- How do COFs contribute to the long-term stability of PSCs, particularly in mitigating environmental degradation?
  While COFs are known for their thermal and chemical stability, their role in enhancing the operational stability of PSCs under real-world conditions remains underexplored. How can COFs be used to protect the perovskite layer from environmental factors such as moisture, light, and heat, and what are the potential mechanisms by which COFs improve the long-term durability of PSCs?

- What design principles can be applied to tailor COF structures for both bulk and interfacial defect passivation in PSCs?

The versatility of COFs allows for their customization at both the bulk and interfacial levels. What specific functional groups, linkers, and structural configurations are most effective in passivating defects throughout the perovskite layer and at critical interfaces, and how can these design principles be optimized to improve overall device performance?

2.4 Summary, Research Gap and Thesis Contributions

COFs have emerged as promising materials for enhancing the performance and stability of PSCs. Although COFs have shown potential in areas such as charge transport, interfacial engineering, and scalability of thin films, there remain several critical research gaps that hinder their widespread application in PSCs. In particular, the challenges posed by NiO_x defects and trap states in perovskite materials have yet to be fully addressed, and the role of COFs in mitigating these issues remains largely unexplored.

Research Gaps Identified:

- **Mitigating NiO_x Defects in PSCs:** NiO_x is a widely HTL in PSCs due to its excellent transparency, suitable energy levels, and chemical stability. However, NiO_x can introduce surface defects at the interface with the perovskite layer, including trap states such as under-coordinated nickel ions and surface oxygen vacancies. These defects can lead to non-radiative recombination, which limits the overall PCE and stability of PSCs. While various approaches have been explored to passivate these defects, the potential for using COFs as passivation layers remains underexplored. COFs offer a tunable platform for designing interfacial layers that can mitigate NiO_x defects, passivate surface trap states, and improve the overall energy alignment between the perovskite absorber and the NiO_x HTM. By engineering COFs with functional groups that specifically interact with NiO_x surfaces, it may be possible to suppress recombination losses and improve charge extraction, leading to enhanced performance and stability in PSCs.

- **Passivation of Trap States in PSCs Using COFs:** Trap states within the perovskite layer, such as grain boundary defects and under-coordinated ions (e.g., Pb^{2+}), are major sources of non-radiative recombination in PSCs. These defects hinder charge carrier mobility and reduce the efficiency of the PSCs. Although several passivation strategies have been proposed, including the use of molecular additives and surface treatments, COFs offer a unique and promising alternative for trap state passivation. The highly ordered and porous structure of COFs can be tailored to interact with specific defect sites within the perovskite layer, effectively passivating trap states and reducing recombination. COFs can be functionalized with various chemical groups, such as amines, carboxylates, or thiols, which can chemically bind to defect sites and neutralize them. This passivation reduces the number of charge traps and improves overall charge extraction, leading to higher PCEs. Despite their potential, the application of COFs for trap state passivation remains underdeveloped, marking a significant gap in the current research landscape.
- **Role of COFs in Reducing Non-Radiative Recombination:** Non-radiative recombination at trap states is one of the primary loss mechanisms in PSCs, reducing their efficiency and operational stability. COFs, with their tunable chemistry and high surface area, have the potential to suppress non-radiative recombination by passivating both bulk and surface trap states within the perovskite layer. However, little research has been done to explore the specific interactions between COFs and trap states, particularly how COFs can enhance charge transport and reduce recombination in solution-processed PSCs. This research aims to address this gap by developing tailored COF structures that can be integrated into PSCs to passivate trap states and enhance the performance of the solar cells. By targeting both bulk and interfacial defects, your work could lead to significant improvements in device efficiency and longevity.

- **Incorporating COFs as Interfacial Passivation Layers:** Trap states are also prevalent at the interfaces between the perovskite layer and adjacent transport layers, such as NiO_x, which serve as ETL or HTL. These interfacial defects exacerbate charge recombination, limiting the performance of PSCs. COFs could be employed as interfacial passivation layers to address this issue by passivating surface defects at these interfaces and improving energy level alignment between the perovskite layer and the transport materials. COFs have the potential to stabilize interfaces, reduce charge accumulation, and enhance charge extraction in PSCs. By carefully designing COFs with appropriate functional groups, it is possible to create buffer layers that suppress recombination and improve charge transfer across the interface, leading to more efficient PSCs with better operational stability. However, this approach remains largely unexplored, providing a significant opportunity for this research to contribute to this emerging field.

- **Exploring COF-Enhanced NiO_x-Based PSCs:** Despite the known issues with NiO_x surface defects, COFs have not yet been widely explored in NiO_x-based PSCs. The potential for COFs to act as both passivation layers and interface stabilizers in these systems represents a promising area for future exploration. By addressing the defects inherent in NiO_x while also improving charge transport and energy alignment, COFs could significantly boost the performance and stability of NiO_x-based PSCs. This research seeks to explore this underdeveloped area by designing COFs that can effectively passivate NiO_x defects and improve charge extraction. This novel application of COFs could provide a pathway for higher efficiency, long-lasting PSCs suitable for large-scale solar energy deployment.

- **Challenges in Scaling Solution-Processed COF Thin Films:** While COFs offer great potential for enhancing PSC performance, particularly in passivating trap states and stabilizing interfaces, the scalability of solution-processed COF thin films remains a challenge. Current methods for COF film deposition, including spin-coating and solution-casting, must be optimized to ensure uniformity, crystallinity, and compatibility with large-area solar cell production. This research addresses this gap by developing a scalable, solution-processed method for COF thin films that can be integrated into PSC architectures. This method enables the deposition of COF layers over large areas, facilitating the transition from small-scale laboratory devices to commercially viable PSC modules.

Thesis Contributions

This PhD thesis contributes to closing these research gaps by:

- Investigating the role of COFs in passivating trap states within the perovskite layer, leading to reduced recombination and enhanced charge transport.
- Developing solution-processed COF thin films that can be scaled up for large-area PSC production, addressing key challenges in the commercialization of high-efficiency PSCs.
- Exploring the application of COFs as interfacial passivation layers, particularly for mitigating NiO_x defects and improving energy level alignment in NiO_x-based PSCs.
- Addressing the unexplored potential of COFs in both bulk and interfacial passivation within PSCs, opening up new pathways for the design of more efficient, stable, and scalable photovoltaic devices.

By addressing these gaps, this research advances the fundamental understanding of COFs in PSCs and contributes to the development of next-generation photovoltaic technologies with improved efficiency and stability. This work represents a significant step toward the commercialization of COF-enhanced PSCs for large-scale solar energy applications.

Chapter 3

Experimental Methodology

This chapter provides a comprehensive overview of the synthetic methods, characterization tools, modelling and simulation approaches, and statistical analysis techniques employed in the research. The chapter begins with detailed protocols for the synthesis of COFs, focusing on optimizing their structure and properties for application PSCs. It also outlines the various tools and techniques used to characterize these materials, ensuring their suitability for device integration. Additionally, the chapter delves into the modelling and simulation methods used to understand the behavior of COFs at the molecular level. Finally, the statistical analysis methods applied to evaluate the performance and reproducibility of the experimental data are discussed, providing a solid framework for the interpretation of devices results. This chapter serves as a crucial foundation for the experimental work and theoretical studies presented in next chapters.

3.1 Rationale for Selection of Materials/Methods/Simulations

The selection of materials, fabrication techniques, and simulations in this research was carefully designed to address key performance bottlenecks in PSCs. These choices were informed by both fundamental material properties and their potential to enhance defect passivation, charge transport, and stability, ensuring high efficiency and long-term operational viability.

Selection of materials: The materials used in this study were selected based on their ability to optimize charge carrier dynamics and suppress non-radiative recombination, which are critical for improving PSC performance.

Covalent Organic Frameworks (COFs): were chosen due to their high crystallinity, tunable electronic properties, and well-defined porous structures, which make them highly suitable for defect passivation. Specifically, sp^2 carbon-conjugated COFs were integrated at the interface to mitigate defect states at the perovskite/hole transport layer boundary, thereby reducing interfacial recombination losses. Additionally, pyrene-based COFs were selected for bulk doping, enhancing charge transport through extended π-conjugation while simultaneously passivating deep-level defects within the perovskite matrix.

Perovskite Compositions: The selection of cesium and formamidinium-based perovskites (CsFA and $FAPbI_3$) was driven by their superior thermal stability compared to methylammonium-based alternatives. Cs incorporation stabilizes the black-phase $FAPbI_3$, preventing undesirable phase transitions that degrade device performance. NiO_x was selected due to its chemical stability, suitable band alignment, and compatibility with scalable deposition techniques. Despite its favorable attributes, NiO_x suffers from interfacial defects that limit hole extraction efficiency. This presented an opportunity to assess the defect-passivating efficacy of COFs at the NiO_x/perovskite interface, validating their role in improving charge extraction and device stability.

Selection of methods: To ensure high-quality material synthesis and device fabrication, the following techniques were employed:

COF Synthesis: A solution-based solvothermal method was chosen due to its ability to produce highly crystalline COFs under controlled reaction conditions. This approach allows for precise tuning of framework porosity and functionalization, ensuring optimal electronic properties for PSC integration. Soxhlet extraction was employed for purification, effectively removing unreacted monomers and residual solvents that could compromise electronic performance.

Perovskite Film Deposition: The spin-coating method combined with antisolvent dripping was selected to ensure uniform, high-quality thin-film formation. This technique facilitates controlled nucleation and grain growth, resulting in smooth, defect-free perovskite layers that minimize charge trapping and recombination.

Device Architecture Optimization: Interface engineering techniques were applied to integrate COFs at critical junctions, demonstrating their impact on charge transport and defect suppression. By comparing COF-treated and untreated devices, this study systematically quantified the benefits of COF-based passivation strategies.

Selection of simulations: To complement the experimental work, computational modelling and simulations were chosen to to validate experimental findings and provide deeper insights into material interactions at the molecular level. Force Field simulations were employed to predict the stacking orientation of COF layers and their impact on charge transport pathways. By simulating different stacking configurations, this approach provided insight into how COFs influence carrier mobility and recombination dynamics

Characterizations techniques: A comprehensive suite of advanced characterization techniques was employed to systematically evaluate the structural, optical, electronic, and photovoltaic properties of the materials and devices in this study. These techniques were carefully selected to ensure a thorough understanding of the interactions between COFs and perovskites, the effectiveness of defect passivation strategies, and their impact on overall device performance.

To confirm the chemical composition and structural integrity of the synthesized COFs, Nuclear Magnetic Resonance (NMR) spectroscopy was utilized, providing detailed insights into the molecular framework and connectivity of organic linkers. This was complemented by Fourier Transform Infrared (FTIR) spectroscopy, which was instrumental in identifying functional groups and verifying the successful formation of key chemical bonds within the COF network. Additionally, UV-Vis spectroscopy was employed to analyze the optical absorption properties of the COFs and their interaction with the perovskite layer, ensuring that their integration did not introduce undesired absorption losses or energy misalignment.

To evaluate the morphology, crystallinity, and elemental composition of the thin films, high-resolution microscopy and surface analysis techniques were used. Field Emission Scanning Electron Microscopy (FE-SEM) provided critical insight into the surface topology, grain size distribution, and overall uniformity of the perovskite and COF-passivated layers, which are key factors in ensuring efficient charge transport. Meanwhile, X-ray Photoelectron Spectroscopy (XPS) was employed to probe the elemental composition and chemical states at the interface, helping to confirm the interaction between COFs and the perovskite absorber, as well as their role in passivating defects and suppressing interfacial recombination.

Beyond structural and morphological assessments, a detailed investigation into the optoelectronic properties of the materials was conducted. Photoluminescence (PL) spectroscopy was used to examine the emission characteristics of the perovskite layer, allowing for an assessment of non-radiative recombination losses. The effectiveness of COFs in passivating trap states and enhancing charge carrier lifetime was further quantified using Time-Resolved Photoluminescence (TRPL) measurements, which provided insights into charge carrier dynamics and recombination kinetics at the COF-perovskite interface.

Finally, the photovoltaic performance of the fabricated PSCs was evaluated through current-voltage (J-V) characterization, which provided critical performance metrics, including power conversion efficiency (PCE), fill factor (FF), open-circuit voltage (V_{oc}), and short-circuit current density (J_{sc}). These parameters were used to assess the extent to which COF integration contributed to performance enhancements, particularly in terms of improved charge extraction and reduced non-radiative losses. By systematically correlating these characterization results, this study established a robust framework for understanding the role of COFs in advancing the efficiency and stability of perovskite solar cells.

3.2 Chemicals and Reagents

COFs Synthesis Reagents: 1,3,6,8-tetrabromopyrene 97%, 4-formylphenylboronic acid 95%, tetrakis(triphenylphosphine)-palladium(0) 99%. 1,4-dioxane 99.8%, 1-4-dioxane 99.8%, mesitylene 98%, acetic acid 37%, NaOH, 1,2-dichlorobenzene and 1-butanol were purchased from (Sigma-Aldrich). 1,4-benzenediboronic acid (BDBA) 98 % (TCI), 2,5-diamino-1,4-benzenedithiol dihydrochloride (DBD) 97%, 1,3,5-triformylphloroglucinol (TFP) 98% were purchased from (TCI). 1,4-phenylenediacetonitrile 97% and iodine crystals were purchased from (Alfa Aesar). Potassium carbonate (AR grade, Qrec), and 2,3,6,7,10,11-hexahydroxytriphenylene (HHTP) 95% (Acros Organics),

Perovskite Solar Cell Devices Reagents: The pre-etched fluorine-doped and indium-doped tin oxide-coated (FTO and ITO) glass substrates were purchased from AGC chemicals. Nickel (II) nitrate hexahydrate, ethylene diamine, caesium iodide (CsI), buckminsterfullerene (C_{60}), bathocuproine (BCP), DMF, DMSO, tert-butyl pyridine (tBP) and lithium bis(trifluoromethanesulfonyl)imide (LiTFSI) were obtained from Sigma Aldrich. Methylammonium bromide (MABr), methylammonium chloride (MACl) and formamidinium iodide (FAI) were purchased from GreatCellSolar. Lead (II) iodide (PbI_2) and lead (II) bromide ($PbBr_2$) were purchased from Tokyo Chemical Industries (TCI) and Spiro-OMeTAD was obtained from LumTech.

3.3 Synthetic Procedures of COFs

3.3.1 Synthesis of 1,3,6,8-tetrakis(p-formylphenyl)pyrene (TFPPy)

In 100 ml flask, a mixture of 1,3,6,8-tetrabromopyrene (0.50 g, 0.965 mmol), 4-formylphenylboronic acid (0.87 g, 5.79 mmol), tetrakis(triphenylphosphine)-palladium(0) (0.06 g, 0.05 mmol), and K_2CO_3 (1.05 g, 7.5 mmol) were dissolved in anhydrous 1,4-dioxane (15 mL). The mixture was condensed at 90 °C under inert gas for three days. The resultant yellow viscous liquid was poured into ice-cooled concentrated HCl. The mixture was filtered and rinsed with diluted HCl (2M) after stirring. The product was washed and extracted three times in chloroform, and the solvents was removed in a rotary evaporator. The resultant powder was repeatedly washed using MeOH to afford a bright yellow powder of TFPPy (72% yield).

3.3.2 Synthesis of sp^2c-COF

In a 50-mL Schlenk flask, a mixture of TFPPy (150.0 mg, 0.24 mmol) and 1,4-Phenylenediacetonitrile (PDAN) (75.8 mg, 0.48 mmol) were dissolved in a combination of mesitylene/1,4-dioxane (10 mL, 1/5 by vol.). The flask was sonicated for 2 minutes to get a homogenous solution. Aqueous NaOH solution (1.0 mL, 4 M) was injected to the mixture, and the tube was tightly sealed. The mixture was degassed through ultravacuum in three steps “freeze-pump-thaw” cycles in liquid nitrogen. After reaching room temperature, the sealed tube was stirred and left at 120 °C for 72 h. The mixture was left to cool at room temperature, and then the powder was filtered and washed with H_2O and THF many times. A Soxhlet extraction in THF was performed on the resultant powder for two days to remove the trapped unreacted monomers. Finally, the product was dried in an oven under vacuum at 120 °C overnight to obtain an orange crystalline powder (85% yield).

3.3.3 Synthesis of ILCOF-1

ILCOF-1 was synthesized following the method described by El-Kaderi,[237] with modification to the solvent used in the reaction. A 50-mL Schlenk flask was charged with TFPPy (200.0 mg, 0.32 mmol, 1 equiv), p-phenylenediamine (70 mg, 0.64 mmol, 2 equiv) in a mixture of 1,2-Dichlorobenzene/1-butanol (10 mL, 1/1 by vol.), the mixture was sonicated for 2 minutes to get a homogenous solution. aqueous acetic acid (1.0 mL, 6 M) was added to the mixture, and the tube was sealed. The mixture was degassed through ultravacuum in three "freeze-pump-thaw" cycles in liquid nitrogen. After reaching room temperature, the sealed tube was stirred and heated at 120 °C for 4 days. After cooling down, the powder was collected by filtration. Then, the yield was washed with a acetone, water, methanol and dioxan. Followed by a Soxhlet extraction in acetone for 1 day to remove the trapped unreacted monomers. The resultant powder was then activated under vacuum overnight and then activated by heating at 120 °C for 2 h (83% yield).

3.3.4 Synthesis of SH-COF

The same synthetic method of ILCOF-1 was followed in SH-COF, in which p-phenylenediamine was replaced with 2,5-Diamino-1,4-benzenedithiol dihydrochloride (DBD) using the same molar ratio (87% yield).

3.3.5 Synthesis of COF-5

The synthesis method for COF-5 was adapted from previous studies. [138,146] A solution was prepared by mixing 1,4-benzenediboronic acid (BDBA; 185 mg, 1.116 mmol) and 2,3,6,7,10,11-hexahydroxytriphenylene (HHTP; 241.5 mg, 0.745 mmol) in a 3:2 molar ratio in a 1:1 volume mixture of mesitylene and 1,4-dioxane (20 mL). The mixture was sonicated for 2 minutes to ensure homogeneity. It was then degassed using three freeze-pump-thaw cycles in liquid nitrogen. The sealed vial was brought to room temperature and heated to 100 °C in an oven for three days. After cooling to room temperature, the mixture was filtered, washed with acetone, and dried under vacuum (88% yield).

3.3.6 Synthesis of TFP-DBD COF

TFP-DBD was synthesized through Schiff-base reactions coupled with irreversible enol-to-keto tautomerization, following the literature in [238]. To begin, 84 mg of 1,3,5-Triformylphloroglucinol (TFP) and 142.8 mg of 2,5-Diamino-1,4-benzenedithiol dihydrochloride (DBD) were dissolved separately in two 10 mL glass tubes containing 4 mL of a THF and 1-butanol mixture (2:1.5, v). Both solutions were sonicated and then combined in a 20 mL sealed Schlenk tube and sonicated for an additional minute. Next, 0.2 mL of 6 M acetic acid was added slowly, and the mixture was degassed with liquid nitrogen. The sealed tube was heated at 88 °C for two days. The resulting product was filtered and thoroughly washed with DMF and THF to remove any unreacted monomers. The powder was then activated by immersing it in methanol for 6 hours, with the solvent being replaced three times to ensure the removal of any residual precursors or solvents from the COF pores. Finally, the red powder was dried under vacuum at 88 °C overnight (92% yield).

3.3.7 Synthesis of COF-921

COF-921 was syntheses according to the procedures reported by Yaghi.[154] To a 50-mL Schlenk flask, 2,5-diaminobenzene-1,4-dithiol dihydrochloride (257.0 mg, 1.05 mmol, 4 equiv) was added. Next, 5.0 mL of a DMF/water (3/1 by vol.) solution was poured into the vial. ILCOF-1 (100 mg, 0.26 mmol, 1 equiv) was then added, followed by another 5.0 mL of the same DMF/ water solvent mixture to ensure the COF falls completely of the flask walls. The vial was sealed and heated at 85 °C under oxygen gas for 2 days. After allowing it to cool, the solid was filtered out. The solid was sequentially washed with acetone, methanol, THF, water, methanol again, and acetone. The resulting powder was soaked in DMF over 1 day, replacing the solvent five times. Following this, the powder was washed with acetone using Soxhlet extraction for 1 day, dried under vacuum overnight, and finally activated at 120 °C for 1 hour (98% yield).

3.4 Perovskite Solar Cell Devices Fabrication

3.4.1 CsFA-based Perovskite Solar Modules

ITO-covered glass substrate was sonicated in detergent, acetone, ethanol, and isopropanol and dried using nitrogen flow. The dry substrate was exposed to UV-Ozone treatment under 254 nm UV irradiation with a continuous O_3 flow for 30 min to enhance its hydrophilicity. NiO_x solution was prepared by dissolving equal moles of $Ni(NO_3).6H_2O$ and ethylene diamine in ethylene glycol solvent at 0.3 M concentration. The solution was heated on a hotplate at 60 °C for 2 h. A thin layer of freshly prepared NiO_x was spin-coated at 6000 rpm for 60 s, followed by annealing at 325 °C for 60 min. A solution of sp^2c-COF was prepared by dispersing 0.5 mg of sp^2c-COF powder in 1 ml of DMF and sonicated for 24 h to yield a homogenous suspension. Then 50 μL of sp^2c-COF suspension was spin-coated on top of the NiO_x film at 4000 rpm for 30 seconds. The perovskite precursors were deposited using an antisolvent method with a two-step spin-coating. Typically, 50 μL of perovskite precursors was dropped at the center of the substrate; then the spin coater was run at 1000 rpm for 10 s and then 6000 rpm for 30 s; 150 μL of chlorobenzene was added as an antisolvent at the 22nd s of the high-speed step. The substrates were subsequently placed on a hotplate for annealing at 100 °C for 60 min. Then, PEAI (1.5 mg/mL in chlorobenzene) was spin-coated at 5000 rpm for 30 s. The ETL was deposited by thermally evaporating a thin layer of C60 followed by another thin layer of BCP. Finally, a 100-nm layer of pure silver was thermally evaporated using four-cell masks. The devices were stored in a dry box for further measurements.

3.4.2 $FAPbI_3$-based Perovskite Solar Modules

The pre-etched fluorine-doped tin oxide-coated glass substrates were washed sequentially with decon soap, DI water, and isopropanol (IPA) for 15 min. each under sonication. FTO substrates were then dried and treated with UV-ozone for 15 min. A thin blocking layer of planar TiO_2 is then spray-pyrolyzed onto the substrates at 450 °C followed by a layer of rougher mesoporous TiO_2 spin-coated on top of c-TiO_2 at 3000 rpm for 30 sec. The mesoporous TiO_2 solution is made by taking 1 part of TiO_2 paste and diluted by 9 parts of absolute ethanol. The electron transport layer-coated substrates were then treated with UV-ozone for 15 min. before being transferred to a nitrogen-filled glovebox for the deposition of subsequent layers. The perovskite solution was prepare by dissolving 1.35M FAI , 1.35M PbI_2, and 35 mol.% of MACl in 4:1 DMF:DMSO mixed solvent. The solution was then spin-coated on the meso-TiO_2 substrate at 6000 rpm for 50 sec. Approximately 200 µL of chlorobenzene was dropped on the substrate 10 sec. after the start of the spin to induce rapid crystallization. Films were then annealed at 150 °C for 10 min. Afterward, a surface passivation layer of n-octylammonium iodide (OAI) in isopropanol was statically spin-coated at 6000 RPM for 30 sec. followed by spin coating of hole-transporting layer. For HTL, a solution of Spiro-OMeTAD (72.3 mg/mL) in chlorobenzene was doped with tert-butyl pyridine (tBP) (28.5 µL) and lithium bis(trifluoromethanesulfonyl)imide (LiTFSI) (17.5 µL of a 520 mg/mL stock solution in acetonitrile). Subsequently, metal electrodes were thermally evaporated (~100 nm) on top of the device. During electrode deposition, a shadow mask was used with an electrode area of 0.2 cm^2. Devices were then measured under 1 sun intensity according to measurement standards. All the films for characterization purposes were made on washed FTO substrates with no ETL and HTL deposition.

3.5 Instrumentation and Characterization

Nuclear magnetic resonance (NMR) spectra: ^1H NMR spectra were recorded using Bruker Avance 400 spectrometer with $CDCl_3$ solvent and tetramethylsilane (TMS) as the external standard. Chemical shift values are provided in (ppm). Solid-state NMR spectra were recorded using a Bruker Avance III HD 400 MHz instrument equipped with a 4 mm MAS probe with a MAS frequency of 12 kHz. Cross-polarized-MAS (CP/MAS) was used to collect ^{13}C NMR spectral data at 150 MHz. The ^{13}C [^1H] CPMAS high-power proton decoupling was utilized during data collection with a MAS frequency of 14 kHz, with a contact pulse time of 5 ms.

Fourier transforms infrared (FTIR) spectra: FTIR spectra were recorded using a

PerkinElmer Frontier spectrophotometer. The samples were prepared using the bulk KBr plate method; the data were recorded after 64 scans at a resolution of 8 cm^{-1}.

Thermogravimetric analysis (TGA): TGA was evaluated using a TA Q-500 facility under the continuous purge of nitrogen gas at a rate of 60 mL min^{-1}. The sample was loaded into the Pt cell, sealed, and heated over the temperature range from 40 to 800 ° with a increasing temperature at rate of 20 °C min^{-1}.

Powder X-ray diffraction (PXRD): PXRD was analysed using a Siemens D5000 diffractometer through monochromatic Cu/Kα radiation (wavelength = 0.1542 nm); the powder sample was placed on XRD sample holder, then measured at incident angles (2θ) from 1 to 30° with an 0.02° increment steps.

Field Emission Scanning Electron Microscopy (FE-SEM): FE-SEM pictures were taken with a Jeol 7600F at 5kV with a working distance of 8mm.

Nitrogen Sorption Measurements: N_2 sorption measurements were carried out at 77K using a “Micromeritics ASAP 2020 Surface Area and Porosity analyser”. The sample was dried under a vacuum at 120 °C overnight before the measurements. The specific surface area was calculated using “Brunauer-Emmett-Teller (BET) method” using the instrument's software. The pore size distribution and the surface volume were deducted using “the non-local density functional theory model”.

Elemental analysis: Elemental contents was calculated using an Elementar Vario EL III Elemental Analyzer.

Cyclic voltammetry: CV measurements were performed by a metrohm autolab electrochemical analyser in a three-electrode electrochemical cell with a scan rate of 0.2 V s^{-1}. The sample was dispersed in DMF, stirred for 6 h before being drop cast on carbon glass, and dried under vacuum to form a thin film for measurements. Tetrabutylammonium hexafluorophosphate (0.1 M) in acetonitrile was used as a supporting electrolyte for the carbon glass working electrode. A platinum wire was utilized as an auxiliary electrode. The experiments were carried out against Ag/Ag+ couple (0.01 mol L^{-1}) as a reference electrode.

Solid state UV-Vis Spectroscopy: UV-vis spectra of bulk sp^2c-COF powder were recorded using a Shimadzu UV-2600 UV-VIS Spectrophotometer in diffuse reflectance mode; barium sulfate ($BaSO_4$) was used as the reflectance reference. Relative absorbance was deducted from the reflectance spectra through Kubelka−Munk transformation using the **equation 3.1**:

$$\frac{\alpha}{S} = \frac{(1-R)^2}{2R} \tag{3-1}$$

Equation 3.1: Relative absorbance deduction from the reflectance spectra through Kubelka−Munk transformation, R is the reflectance, α is the “absorption coefficient,” and S is the “scattering coefficient.”

Photoluminescence Spectroscopy (PL): The PL spectra were collected using a WITec alpha 300RAS confocal Raman microscope. For PL measurements, “blue line of a linearly polarized CW solid laser (457 nm)” was chosen, and the excitation power was optimized below 0.8 µW to avoid possible photodegradation.

Time-resolved photoluminescence (TRPL): TRPL measurements were carried out using an ultrafast laser system. The 800 nm laser output, produced by a regenerative amplifier (Coherent LibraTM, 1kHz, 50fs) and driven by a Ti-sapphire oscillator (Coherent VitesseTM, 80MHz, 100fs), was transformed to 500 nm via an optical parametric amplifier (Coherent OPerA SoloTM). The photoluminescence generated by the 500 nm excitation was collected using a back-scattering setup. The collected light was channeled through an optical fiber into a monochromator (Princeton Instrument Acton SP2750) and captured by a CCD camera (Princeton Instrument PIXIS: 100).

Ultraviolet photoelectron spectroscopy (UPS): UPS was performed on Kratos AXIS supra with helium I source, measured from −3.78 to 21.22 eV with a 0.025 eV step size and 65.15 ms dwell time.

X-ray photoelectron spectroscopy (XPS): XPS was investigated using Kratos AXIS supra with aluminum X-ray monochromatic, region scan was performed with a step size of 0.1 eV with a 221.40 ms dwell time.

Conductivity measurements: Electric conductivity was measured using a two-probe setup. Powder samples were grounded and pressed into disk-shaped plates (diameter = 1.35 cm, thickness = 0.1 cm) using a hydraulic press. Two gold electrodes were evaporated on the pallets with a rectangular shape with a length of 150 µm and a width of 4000 µm. The voltage was applied in a range of (-1 to 1 V), and the corresponding generated current was recorded using Keithley 4200 source meter. The conductivity (s) was calculated using the **equation 3.2**:

$$R = \frac{V}{I}$$

$$r = R\frac{A}{l}$$

$$\sigma = \frac{1}{\rho} \tag{3.2}$$

Equation 3.2: Conductivity calculation, R is resistance, V is voltage; I is current, r is resistivity, and A and l are the cross-section and length of the electrode, respectively

Perovskite solar cell characterization: The current-voltage (*I–V*) measurements of unencapsulated devices were carried out using a Keithley 2612B source meter under ambient conditions (70% RH ± 10%) and 25 °C. Devices with an active area of 0.20 cm^2 were tested using mask aperture area of 0.086 cm^2. The 1.5 AM sunlight simulator with an incident light power of 100 $mW \cdot cm^{-2}$ was calibrated using a Newport 91150V NREL-certified reference cell. LabView software was used to sweep voltages from −0.1 to +1.1 V for a forward scan and vice versa for a reverse scan at a rate of 0.4 $V\ s^{-1}$. The current density (*J-V*) curve was plotted from (*I-V*) data by dividing the current (I) by mask aperture area. The power conversion efficiency (PCE) = open-circuit voltage (V_{oc}) × short-circuit current density (J_{sc}) × fill factor (FF).

3.6 Statistical Analysis

The device with the highest PCE was designated as the champion. The performance parameters of 28 devices were analyzed and visually represented using a box plot, which includes individual data points and a normal distribution curve on the right side (Figure 3). The whiskers of the box plot extend to the most extreme data points within 1.5 times the interquartile range (IQR) from the first and third quartiles, capturing potential outliers. The central box spans from the 25th percentile (Q1) to the 75th percentile (Q3), encapsulating the interquartile range where the middle 50% of the data lies. A horizontal line within the box indicates the median value of the dataset, providing a measure of central tendency. The inclusion of individual data points allows for a granular view of the distribution, while the normal distribution curve offers a comparative perspective on the data's conformity to a normal distribution.

3.7 Modeling and simulation

Molecular modeling and classical force field (FF) simulation were performed using the BIOVIA Materials Studio suite. The space group of the sp^2c-COF system was determined as C2/m. The Forcite module was employed through energy minimization to optimize the atomic coordinates and the unit cells. The cell was optimized using volume relaxation in which the unit cell structure was kept constant. A universal force field was applied to obtain the interatomic forces. Furthermore, the Ewald method was utilized to assign the van der Waals atomic forces and the electrostatic contribution in the layered structure. Optimization convergence was achieved through three stages; the initial and intermediate optimization was performed through a quasi-Newton algorithm with a mild convergence. Finally, Energy and force convergence was attained after 500 iterations using a conjugate gradient algorithm by setting a threshold of $1\text{x}10^{-3}$ kcal mol^{-1} and $5\text{x}10^{-3}$ kcal mol^{-1} for energy and force convergence, respectively.

Chapter 4*

Synthesis and Characterization of Semiconducting Functionalized sp^2 Carbon-Conjugated Covalent Organic Frameworks (sp^{2}c-COF)

This chapter describes the synthesis and characterization of sp^{2}c-COF through Knoevenagel polycondensation. Characterization confirmed successful synthesis, with X-ray Powder Diffraction (XRD) revealing an AA stacking pattern. The sp^{2}c-COF exhibited high thermal stability, withstanding temperatures up to 510°C, and demonstrated microporosity with a BET surface area of 700 m²/g and a pore size of 1.89 nm. Optical studies showed absorption in the UVA and UVB regions and fluorescence at 572 nm. Ultraviolet photoelectron spectroscopy (UPS) and cyclic voltammetry (CV) identified sp^{2}c-COF as an n-type semiconductor with HOMO and LUMO levels at -5.77 eV and -3.87 eV, respectively. Increased conductivity was observed upon iodine doping, indicating sp^{2}c-COF's potential for enhancing charge transport in PSCs.

---

* This section is substantially published as H. R. Abuzeid, D. J. J. Tay, B. Febriansyah, A. Kanwat, T. Salim, A. A. Zhumekenov, S. A. Pullarkat, and N. Mathews. Functionalized sp^2 Carbon-Conjugated Covalent Organic Frameworks for Interfacial Modulation of Inverted Perovskite Solar Cells. *Small Methods*, 2025, 9, 2400666. DOI: 10.1002/smtd.202400666. Reproduced with permission. Copyright © 2025, John Wiley and Sons.

4.1 Introduction

Covalent organic frameworks (COFs) are an emerging class of porous and crystalline functional organic materials, synthesized through reversible condensation of organic linkers, stitching them together by robust covalent bonds and extending into two- or three-dimensional (2D or 3D) networks.[3,138] Intrinsically, COFs possess high surface areas, exceptional chemical stability, as well as tuneable and pre-designable functional structures, which makes them suitable for diverse range of applications including gas separation, catalysis, sensing, supercapacitors, and optoelectronics.[141,166,213,215,235,239,240]

Within the realm of emerging COF linkages, sp^2 carbon-conjugated COFs (sp^{2}c-COFs) have attracted considerable attention since their introduction in 2016, driven by the unparalleled characteristics of continuous π-conjugation, high crystallinity, enduring porosity, distinctive optoelectronic properties, and exceptional chemical stability. The inherent sp^2 C=C linkages in these COFs serve to concurrently improve both the chemical stability and the in-plane π-electron delocalization of COFs. These addresses certain limitations observed in existing COF systems.[160] The first sp^2 carbon-conjugated COF was introduced in 2016 through the process of base-catalyzed Knoevenagel condensation.[241] In the next two years, Jiang et. al. introduced a new family of pyrene-based sp^2 COFs with a remarkable ferromagnetic phase transition and a substantial increase in conductivity, representing an unprecedented phenomenon.[162,242] Following these seminal reports, there has been remarkable progress in the development of sp^{2}c-COFs with a rapidly growing number of publications each year.[160] However, application of sp^2 carbon conjugated COF in photovoltaics devices remain unexplored.

This chapter discuss the synthesis and extensive structural characterization of the pyrene-based sp^{2}c-COF featuring a 2D structure with extended π-conjugation system and π-π interactions between the sheets, as well as containing electron-donating cyano (-CN) groups. It also demonstrates key optoelectronic and electrical properties of the material, including a narrow bandgap of 1.97 eV and enhanced electrical conductivity. By taking advantage of these structural and semiconducting features of sp^{2}c-COF, which can help facilitate charge transport and passivate defects, it is introduced as a promising material for interfacial modulation of in perovskite solar cells.

4.2 Synthesis and Structural Confirmation of TFPPy

The monomer, 1,3,6,8-tetrakis(4-formylphenyl)pyrene (TFPPy), was synthesized following the reported Suzuki-Miyaura cross-coupling reaction of 1,3,6,8-tetrabromopyrene and 4-formylephenylboronic acid (**Figure 4.1**).[243] The TFPPy structure was confirmed by both Fourier-transform infrared (FTIR) and proton nuclear magnetic resonance (^{1}H-NMR) spectroscopies. Specifically, the FTIR spectrum featured absorption bands at 2817 and 2725 cm^{-1}, attributed to the C-H stretching of the aldehyde group, and strong signals at 1700 cm^{-1} and 1601 cm^{-1}, assigned to C=O of the aldehyde group and the C=C bond of the aromatic rings, respectively (**Figure 4.2a**). Meanwhile, ^{1}H-NMR showed a resonance signal at 10.18 ppm originating from the proton of the aldehyde group, and signals at 8.18 ppm **(**s, 4H), 8.09 ppm (d, *J* = 6 Hz, 8H), 8.05 ppm (s, 2H) and 7.85 ppm (d, *J* = 6 Hz, 8H) from the protons of the aromatic rings (**Figure 4.2b**).

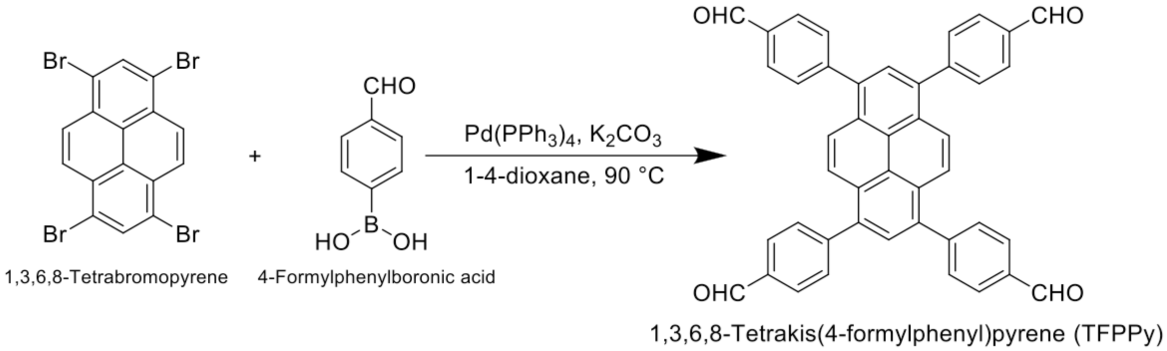

Figure 4.1 Schematic illustration of TFPPy synthesis.

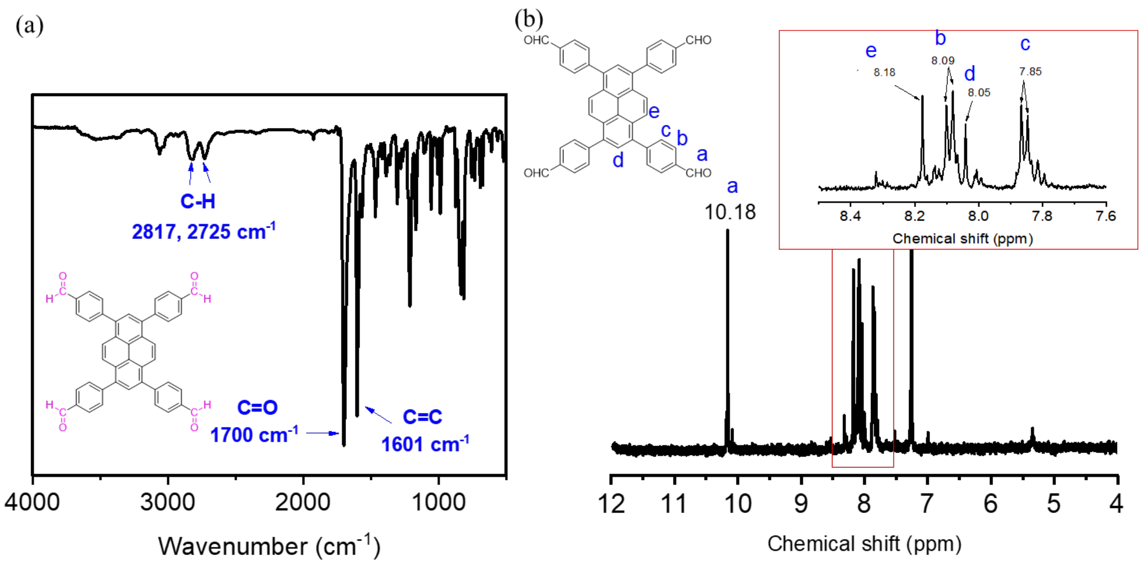

Figure 4.2 (**a**) FTIR spectrum of TFPPy monomer using the KBr pellet method. (**b**) ^{1}H-NMR spectrum of TFPPy monomer.

4.2.1 Computational study: Density functional theory (DFT) calculations

Density functional theory (DFT) calculations of TFPPy monomer structure were performed with a Gaussian package using the B3LYP/6-311G(d,p) basis. The results showed that the TFPPy monomer adopts a nonplanar conformation, with the side-chain (Ar-CHO) moiety bending out of the plane. This distortion is facilitated by the flexible σ-bond connecting it to the fused benzene rings, allowing the structure to minimize repulsive interactions between the aromatic hydrogen atoms and the pyrene core. The dihedral angle between the two intersecting planes is measured to be 52.5°. An optimized structure from various angles is shown in **Figure 4.3a**. The calculation of the electronic frontier orbitals of TFPPy revealed HOMO and LUMO levels at -5.81 eV and -2.54 eV suggesting a fundamental wide bandgap of 3.27 eV. Moreover, the frontier orbitals are delocalized in TFPPy as shown in (**Figure 4.3b**).

4.2.2 Optical Properties of TFPPy

The absorption spectrum of TFPPy was measured in the solid-state and over the 300-800 nm absorption range. The spectrum showed that TFPPy absorbs in a lower range of Visible light below 500 nm and covers the UV spectrum UVA (320-400 nm) and UVB (280-320 nm) (**Figure 4.3c**). The optical bandgap of TFPPy was calculated from the onset absorption spectra using Tauc's plot, revealing an indirect bandgap of 2.2 eV. To elucidate the emission characteristics of TFPPy, it was dissolved in chloroform and measured upon excitation at a wavelength of 350 nm. It was clear that TFPPy emits a strong blue light, with an emission peak at 457 nm. **Figure 4.3d** shows the luminescence spectra and an image of the blue emission.

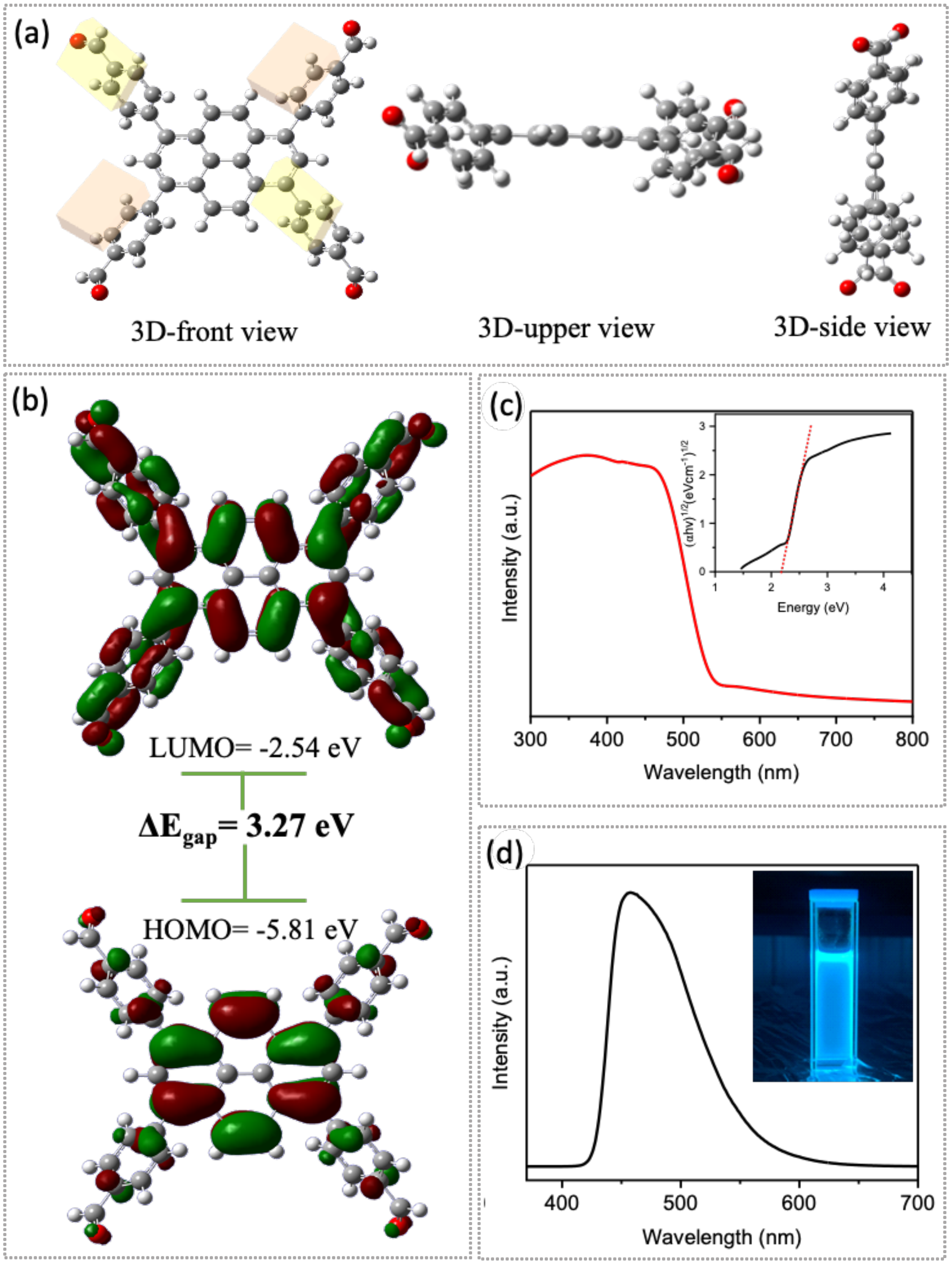

Figure 4.3 (**a, b**) DFT geometry optimization of TFPPy monomer using the B3LYP/6-311G(d,p) basis set. (a) Three-dimensional view, and (**b**) Theoretical electronic frontier states LUMO and HOMO. (C, gray; O, red; H, white). **(c, d)** Electronic absorption and emission properties of TFPPy monomer (**c**) UV-Vis spectra, (inserted Tauc's plot) and (**d**) PL spectra.

4.3 Synthesis and Characterization of sp^{2}c-COF

The TFPPy monomer was then reacted with 1,4-phenylenediacetonitrile (PDAN) linker under solvothermal conditions via C=C Knoevenagel polycondensation to result in the target sp^{2}c-COF featuring the pyrene unit (**Figure 4.4**).[242] The successful synthesis of the sp^{2}c-COF was confirmed using different characterization techniques. The FTIR spectroscopy showed the disappearance of the signal from the C-H of the aldehyde group of TFPPy (at 2720 cm^{-1}) and the appearance of absorption band at 2220 cm^{-1} in sp^{2}c-COF, assigned to the -C≡N stretch that originated from PDAN linker, indicating the successful polycondensation reaction between TFPPy and PDAN monomers (**Figure 4.5a**). Solid-state ^{13}C-NMR revealed a signal from the cyano-group at 108 ppm (**Figure 4.5b**). The elemental analysis verified the C, H, and N content in the synthesized sp^{2}c-COF. The experimental weight percentages were found to be around 88.89%, 4.31%, and 6.80%, respectively, closely matching the calculated values of 89.49%, 3.99%, and 6.52%.

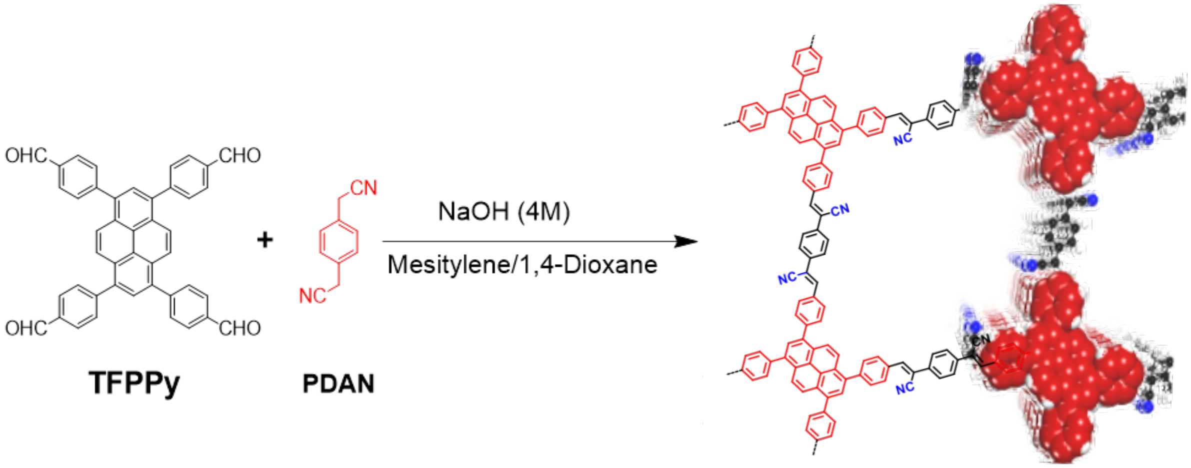

Figure 4.4 (a) The reaction scheme for the synthesis of sp^{2}c-COF, connected via C=C bonding, through the condensation of TFPPy knot and PDAN linker.

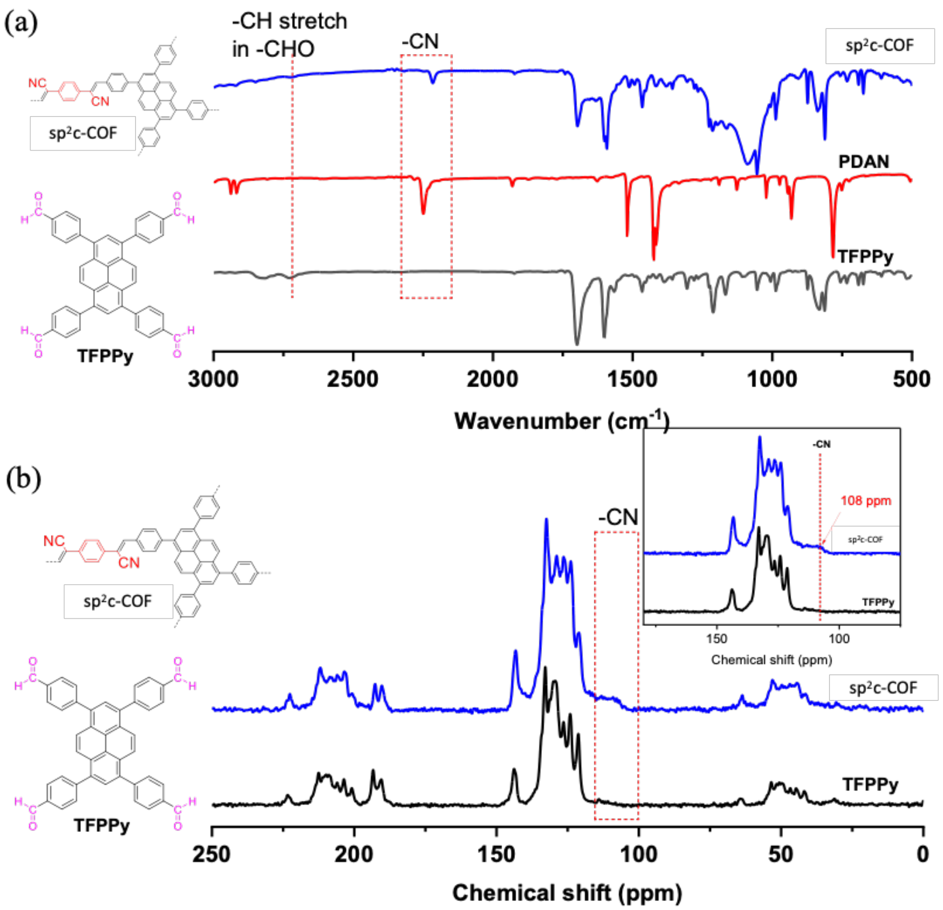

Figure 4.5 Structure confirmation of sp^{2}c-COF using FTIR and solid-state NMR. (a) FTIR spectrum of sp^{2}c-COF compared to that of TFPPy and PDAN monomers. (b) Solid-state ^{13}C CP-MAS NMR spectrum of sp^{2}c-COF compared to that of TFPPy monomer.

4.4 Crystallinity Analysis Supported by Modelling and Simulation

X-ray Powder Diffraction (XRD) of sp^{2}c-COF showed its crystalline nature with two strong peaks at 3.5 and 8.0° assigned to (110) and (220) diffraction planes, and signals at 5.4 and 12.6° attributed to (200) and (420) planes, respectively. The broad peak at around 24.4° was assigned to (001) plane resulting from the π-π-stacking of the extended tetragonal sp^{2}c-COF layers with the interlayer distance of about 3.6 Å (**Figure 4.6b**). Typically, the layers in 2D COFs are stacked vertically in either eclipsed (AA) or staggered (AB) patterns. In the AA eclipsed stacking model, the layers sit on top of each other forming columns with 1D open channels. Whereas, in the AB staggered stacking model, the layers are offset by half a unit cell (**Figure 4.6a**). To understand the stacking pattern in sp^{2}c-COF, molecular modelling and classical force field (FF) simulation for sp^{2}c-COF were performed. Density functional–based tight binding (DFTB) calculations were utilized to optimize the structure of the 2D single layer and the two possible stacking models: eclipsed (AA) and staggered (AB), for which the simulated XRD pattern were generated (**Figure 4.6c,d**).

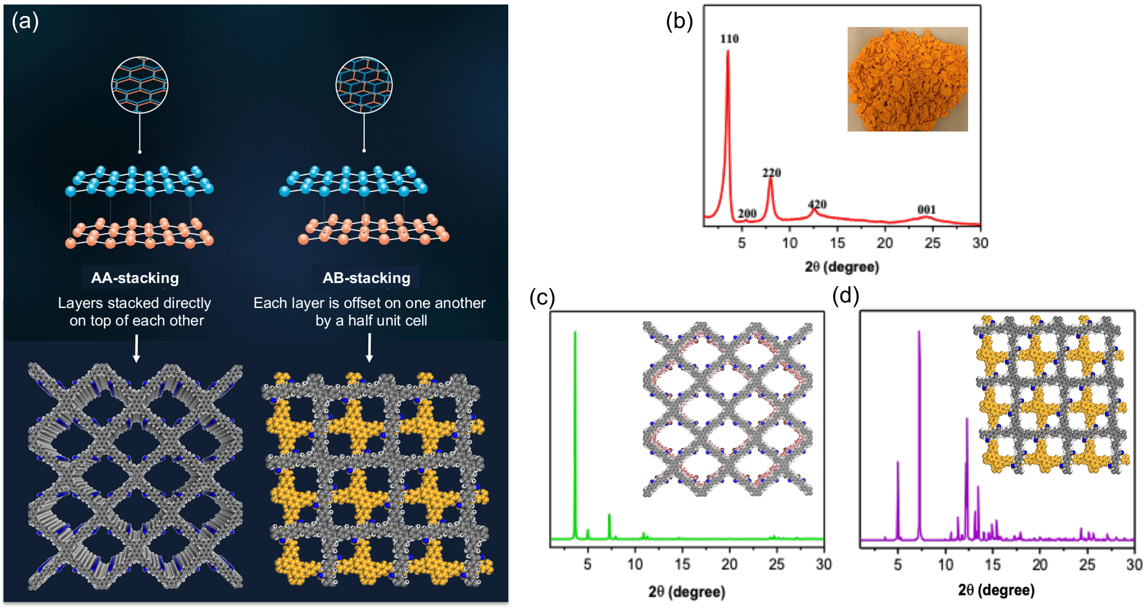

Figure 4.6 Schematics representation of the two stacking models (b) Experimental XRD pattern of sp^{2}c-COF powder, simulated XRD patterns for (c) AA-stacking and (d) AB-stacking models.

Retrieval refinement was performed on the XRD patterns of the two models compared with the experimental XRD using a C2/m space group and lattice parameters of a = 34.46 Å, b = 35.50 Å, and c = 3.72 Å. The XRD pattern of the simulated structure reproduced the experimental results with neglectable differences. By comparing the experimental and simulated XRD of the two possible stacking patterns, it was found that sp^{2}c-COF preferentially forms in the AA stacking pattern as shown in **Figure 4.7a,b**, suggesting that sp^{2}c-COF layers arranged in AA stacking are the most thermodynamically favourable configuration. The AA stacking model suggests that sp^{2}c-COF may have two pathways for charge transfer: (i) in-plane, i.e. along the single sp^{2}c-COF sheet via π-conjugation, and (ii) out-of-plane, i.e. between the individual sp^{2}c-COF sheets via columnar π-π stacking (**Figure 4.7c,d**).

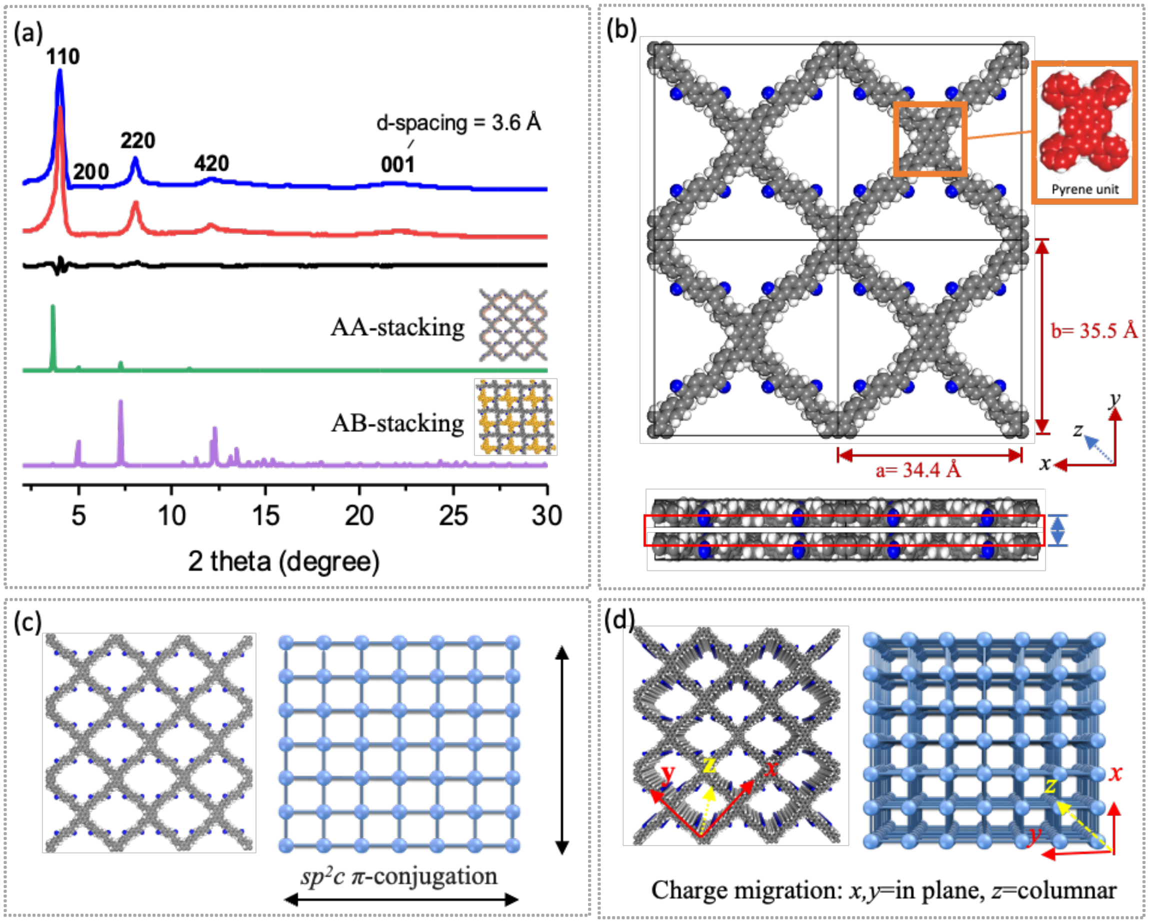

Figure 4.7 (a) Experimental XRD pattern (red curve), Rietveld-refined XRD pattern (blue curve), the difference (black curve) between them, simulated XRD patterns for AA- (green) and AB- (purple) stacking models. (b) Top- and side-view representations of sp^{2}c-COF sheets (2×2×2) extended in two dimensions (2D), displaying the AA-stacking model. The schematics of two charge transfer pathways within sp^{2}c-COF: (c) along single sp^{2}c-COF sheet via π-conjugation, and (d) between the individual sp^{2}c-COF sheets via columnar π-π stacking.

4.5 Chemical and Thermal Stability

The chemical and thermal stability of sp^2c-COF is a crucial criterion for determining their suitability for application in PSCs. The sp^2c-COF product was found to be chemically stable and insoluble in water, as well as common organic solvents used in perovskite preparation such as, DMF and DMSO. Furthermore, it also displayed excellent thermal stability. Thermogravimetric analysis (TGA) was used as an analytical technique to measure a material's thermal stability and the proportion of its volatile components by recording the change in the sample's weight when heated at a constant rate. The excellent thermal stability of sp^2c-COF was confirmed using TGA by heating the sample from 100 to 800° at a rate of 20° C min^{-1} under a nitrogen atmosphere. The thermal decomposition temperature in which 5% and 10% weight loss occurs is referred to as ($T_{d5\%}$ and $T_{d10\%}$), respectively, and the amount of residue after heating at 800 °C (Char yield) was used as the standard to measure the thermal stability. TGA showed that sp^2c-COF is stable up to 450-500 °C with only 10% loss ($T_{d10\%}$) at 510 °C and char yield residue of 61.6% after heating at 800 °C. The high thermal stability of sp^2c-COF is attributed to its structural rigidity owing to covalently-bonded carbon-carbon network (**Figure 4.8**). Furthermore, the reported data showed that the weight loss that occurred below 450 °C is attributed to a loss in crystallinity, followed by a drop in weight at 450 °C due to thermal degradation and releasing of volatile by-products.[244] These properties underline the potential of sp^2c-COF as an interfacial layer for perovskite deposition.

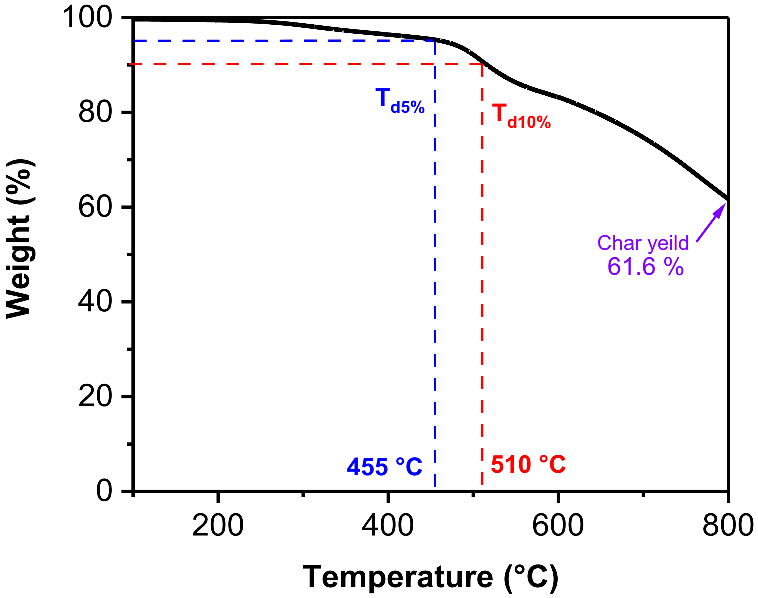

Figure 4.8 TGA of sp^{2}c-COF under N_2 atmosphere, heated from 100 to 800 °C at a rate of 20 °C min^{-1}. $T_{d5\%}$ and $T_{d10\%}$ are the thermal decomposition temperatures of sp^{2}c-COF at 5 and 10% losses, respectively.

4.6 Porosity and Pore Size

The porosity of sp^{2}c-COF was elucidated by nitrogen adsorption, and desorption isotherm at 77 K. The sp^{2}c-COF showed reversible nitrogen sorption Isotherm and a sharp rise in nitrogen uptake at a relatively low-pressure region (P/P_o = 0.1) forming a type I isotherm that indicates the microporosity properties of sp^{2}c-COF channels. Moreover, sp^{2}c-COF showed a high "Brunauer-Emmett-Teller (BET) surface area" of 700 cm^{-2} g^{-1}. In addition, the pore size distribution calculated using "non-local density functional theory (NLDFT)" showed uniform 1.89 nm pores (**Figure 4.9**).

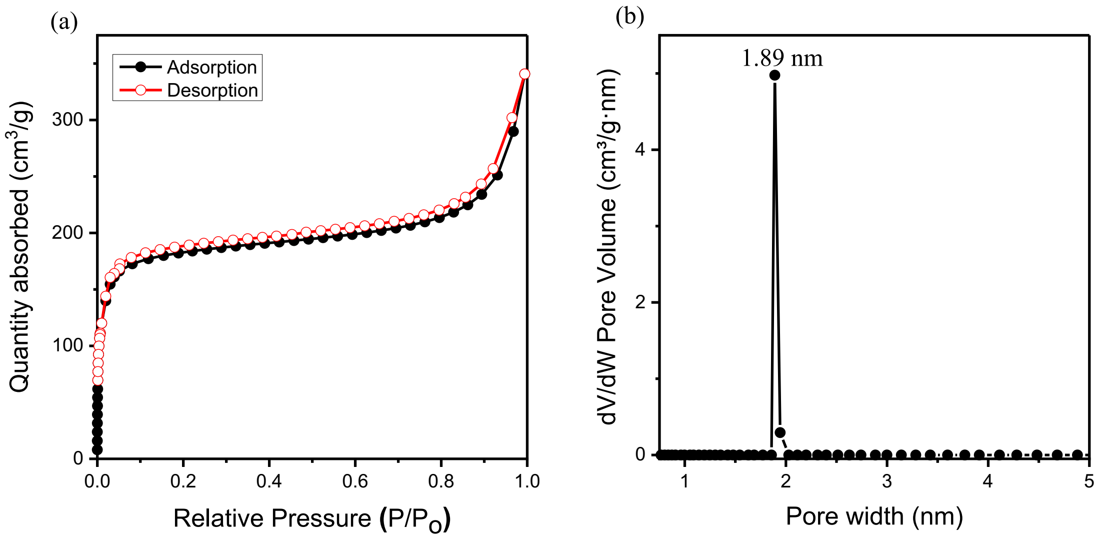

Figure 4.9 (a) Nitrogen Adsorption-desorption isotherms measured at 77 K and (b) Pore size distribution profile calculated using NLDFT.

4.7 Optical characteristics

To understand the optical properties of sp^{2}c-COF, UV-Vis spectrum was measured, which revealed an absorption band in the UVA and UVB regions with the maximum at 373 nm and the edge at ~550 nm (**Figure 4.10a**). The optical bandgap (E_g^{opt}) estimated from the Tauc plot for an indirect semiconductor was found to be around 1.97 eV (**Figure 4.10b**). Notably, this is smaller than the optical bandgap of TFPPy monomer (2.20 eV) (**Figure 4.3c**), suggesting the delocalization of electron density due to the extended π-conjugation of 2D sp^{2}c-COF layers. Meanwhile, the fluorescence emission spectrum of the thin film sample upon a 490-nm excitation revealed a broad signal centered at 572 nm (2.17 eV) with the full-width at half maximum (FWHM) value of 121 nm (**Figure 4.10a**). This signal is red-shifted by 115 nm with respect to the signal from the TFPPy monomer (457 nm, see **Figure 4.3b**). In sp^{2}c-COF, the pyrene knot is a typical chromophore that stacked into a column forming excimers. In sp^{2}c-COF, the pyrene knot serves as a typical chromophore that stacks into a column, forming excimers. Excimer emission from pyrene is a well-documented phenomenon and is frequently cited in photophysics textbooks as a classic example of excimer emission.[245] For example, pyrene-based COF (PPy-COF) linked via boroxine linkage emits blue luminescence, redshifted by 63 nm from the monomer pyrene, due to the pyrene unit's emission without π-conjugation along the COF backbone.[246] Thus, the 115 nm redshift in sp^{2}c-COF emission signal can be attributed to the extended π-conjugation of sp^{2}c-COF framework as well as excimer formation.[159,162]

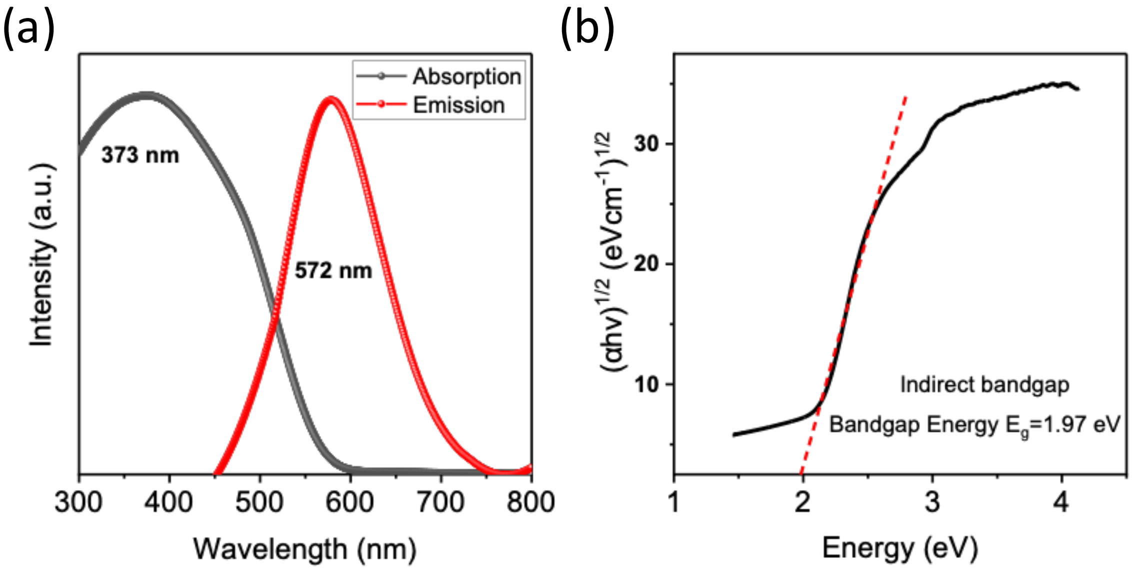

Figure 4.10 (a) Solid state electronic absorption and emission bands of sp^{2}c-COF and (b) Tauc's plot showing the optical bandgap of 1.97 eV for sp^{2}c-COF.

The chemical stability of sp^{2}c-COF in solvents is crucial factor for its integration into PSCs, as it must withstand exposure to various organic solvents such as (dimethylformamide) and DMSO (dimethyl sulfoxide) during solution processing. To assess its stability under these conditions, fluorescence spectra of sp^{2}c-COF were measured in different solvents after excitation at 490 nm, as shown in **Figure 4.11**. The results demonstrate that despite changes in solvent environment, sp^{2}c-COF maintains its structural integrity and exhibits strong luminescence. In THF, it shows an intense orange emission at 577 nm, a minor 5 nm red-shift from the solid state thin film. In more polar solvents like acetone and DMF, the emission shifted to 588 nm (16 nm red-shift), while in DMSO and acetonitrile, a slight increase to 590 nm (18 nm red-shift) was observed. The largest red-shift (20 nm) occurred in methanol, which is the most polar solvent tested. These systematic red-shifts are attributed to the solvent relaxation effect, where polar solvents stabilize the excited-state dipole moment, leading to a bathochromic shift (**Table 4.1**).[247] Crucially, the emission remains strong and well-defined across all tested solvents, indicating that the sp^{2}c-COF framework does not degrade or undergo structural changes in these environments. This stability is particularly important for its role in perovskite devices, where exposure to solvents during fabrication could otherwise lead to material degradation or performance losses.

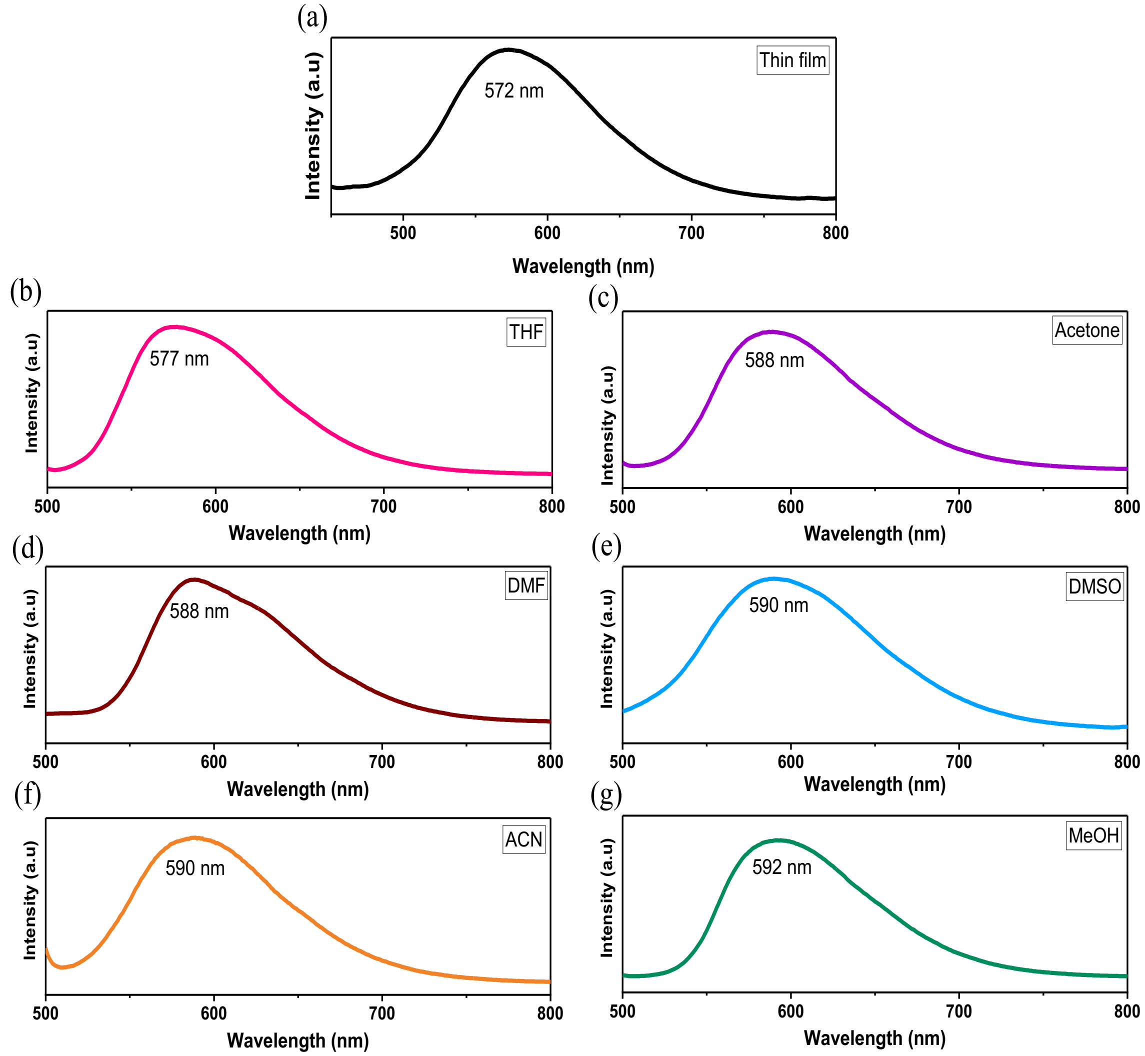

Figure 4.11 Fluorescence spectra of sp^{2}c-COF excited at 490 nm: (a) thin film form; dispersed in various organic solvents: (b) THF, (c) acetone, (d) DMF, (e) DMSO, (f) acetonitrile, and (e) methanol.

Table 4.1 Luminescence peaks of sp^{2}c-COF dispersed in various solvents.

	THF	Acetone	DMF	DMSO	ACN	MeOH
Emission band Wavelength (nm)	577	588	588	590	590	592
Relative polarity	0.207	0.355	0.386	0.444	0.46	0.765

4.8 Electrical and Optoelectronic Characteristics

4.8.1 Fermi level, Valence, and Conductance Bands

The positions of energy band levels of sp^{2}c-COF are important to consider when utilized sp^{2}c-COF as an interfacial layer for PSCs. The ultraviolet photoelectron spectroscopy (UPS) measurements provided insights into the electronic band structure of sp^{2}c-COF. The work function was calculated by subtracting the excitation photon energy (HeI, 21.22 eV) from the high-binding energy cut-off (18.22 eV), resulting in a Fermi level of -3.0 eV relative to vacuum. The low-energy tail of the UPS spectrum was utilized to identify the valence band minimum (E_{VBM}) at 1.70 eV below the Fermi level, leading to a E_{VBM} of –4.70 eV versus vacuum (**Figure 4.12a**). With an optical bandgap of 1.97 eV, the valence band minimum (E_{VBM}) position is estimated to be at -2.73 eV relative to vacuum. This indicate that sp^{2}c-COF Fermin level lies closer to the conductance band revealing an n-type semiconductor. Moreover, these energy bands positions of sp^{2}c-COF found to be close to the perovskite band edge positions, which is an essential aspect for efficient charge transfer (refer to energy-level diagram in **Figure 4.12c**).

4.8.2 Electrochemical Bandgap

Furthermore, cyclic voltammetry (CV) measurements of sp^{2}c-COF were carried to investigate electrochemical bandgap (E_g^{elec}) (**Figure 4.12b**). After the first cycle, the oxidation and reduction potentials stabilized at -0.93 eV and 0.97 eV, respectively. The HOMO and LUMO levels were calculated using the onset values of oxidation and reduction potentials to be -5.77 eV and -3.87 eV, respectively, showing E_g^{elec} of 1.90 eV. These data are consistent with the optical bandgaps and UPS results.

4.8.3 Electrical Conductivity

To further explore its potential as an interfacial layer in PSCs, the electrical conductivity of sp^{2}c-COF pellets was examined using a two-probe electrode method, both in its pristine form and when doped with iodine vapor. Pristine sp^{2}c-COF exhibited relatively low conductivity of 1.09×10^{-14} S cm^{-1}. Interestingly, iodine-doped sp^{2}c-COF showed a ten orders of magnitude higher conductivity of 2.21×10^{-4} S cm^{-1} (**Figure 4.12d and Table 4.2**). This can be attributed to the increased charge-carrier concentration.[248] It also suggests that sp^{2}c-COF can potentially demonstrate superior charge transport upon interaction with the perovskite layer which is abundant of iodine species.

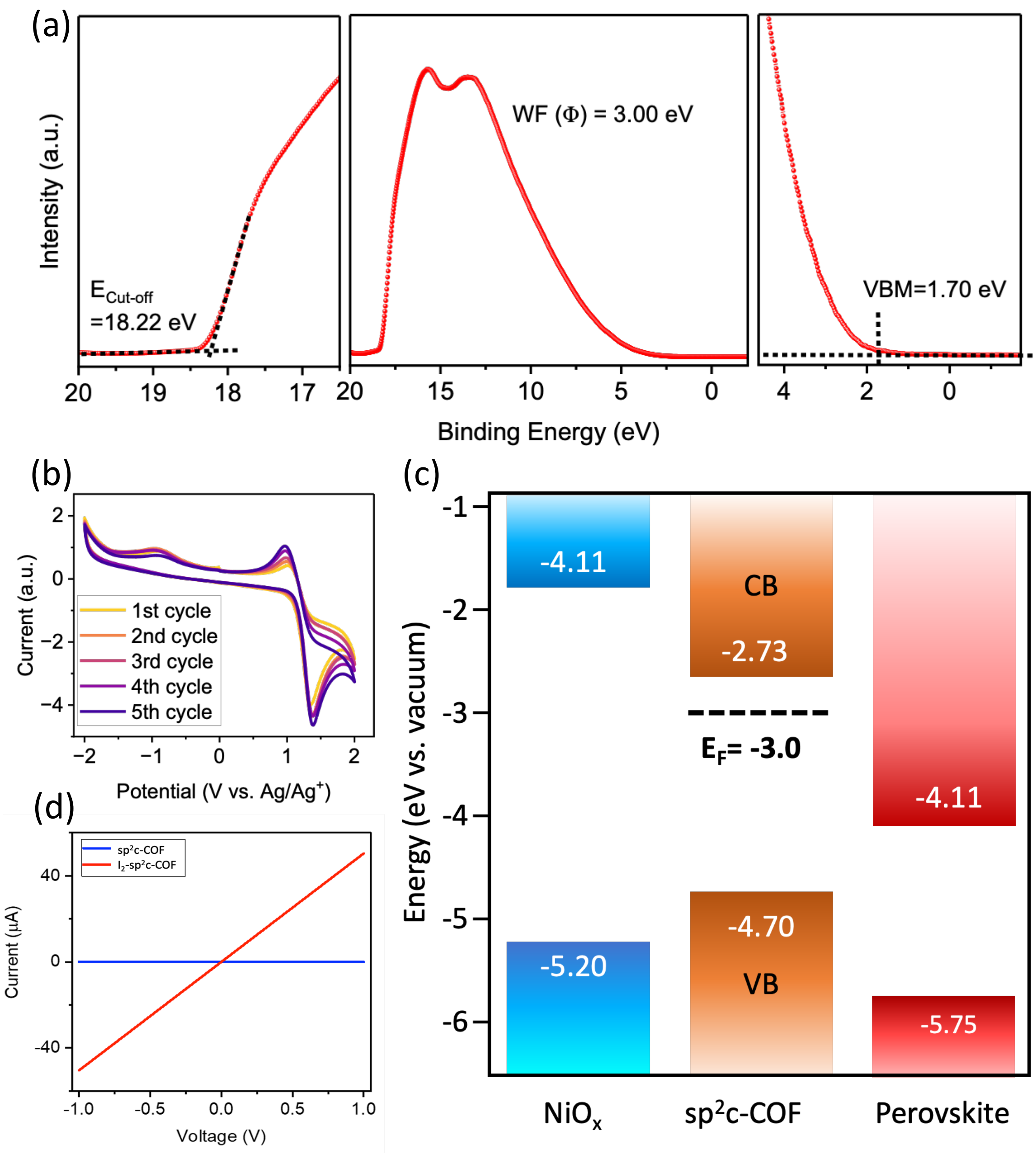

Figure 4.12 (a) UPS spectra of sp^{2}c-COF (b) Cyclic voltammetry plot of sp^{2}c-COF. (c) Energy-level diagram of NiO$_x$/sp^{2}c-COF/perovskite, where the VBM of sp^{2}c-COF was determined by UPS measurement. (d) *I*–*V* curves of pristine sp^{2}c-COF (blue) and I_2-sp^{2}c-COF after 48 h of iodine doping (red).

Table 4.2 A comparison of the electrical conductivities of the sp^{2}c-COF and other analogous COFs at ambient temperature before and after doping.

Name	Doping method	Dopant	Method (pellet)	Electrical conductivity (S cm^{-1})		Ref.
				Before doping	After doping	
sp^{2}c-COF	Chemical	Iodine	2-Probe	1.09×10^{-14}	2.21×10^{-4}	This work
TTF-COF	Chemical	Iodine	2-Probe	N/A	2.1×10^{-7}	[249]
TTF-ph-COF	Chemical	Iodine	2-Probe	N/A	$\sim10^{-5}$	[224]
TTF-Py-COF	Chemical	Iodine	2-Probe	N/A	$\sim10^{-6}$	
POR-COF	N/A	Iodine	2-Probe	4.6×10^{-11}	1.5×10^{-7}	[250]
sp^{2}c-COF	Chemical	Iodine	2-Probe	6.1×10^{-16}	7.1×10^{-4}	[159]
TTF-COF	Chemical	Iodine	2-Probe (film)	1.2×10^{-6}	2.8×10^{-3}	[251]
	Chemical	Iodine			1.0×10^{-5}	
	Chemical	TCNQ			N/A	
TP-COF	N/A	Iodine	2-Probe	N/A	N/A	[252]
ZnPc-pz-I$_2$	No bond	Iodine	2-Probe	N/A	2.1×10^{-7}	[248]
CuPc-pz-I$_2$	No bond	Iodine	2-Probe	N/A	1.8×10^{-6}	[248]
PPy-COF	N/A	Iodine	2-Probe	N/A	N/A	[246]
FL-COF-1	Chemical	Iodine	4-Probe	N/A	1×10^{-4}	[253]
T-COF 4	N/A	TCNQ	N/A	N/A	N/A	[254]
COF-DC-8	N/A	Iodine	4-Probe	2.5×10^{-5}	N/A	[255]
TONG-COF	Chemical	Iodine	4-Probe	5.0×10^{-12}	2.0×10^{-3}	[256]
			2-Probe	1.6×10^{-5}	1.5×10^{-3}	

4.9 Conclusions

In conclusion, this chapter successfully demonstrates the synthesis and structural confirmation of TFPPy and its integration into sp^{2}c-COF. The synthesis of TFPPy via Suzuki-Miyaura cross-coupling was validated through FTIR and ^{1}H-NMR spectroscopy, revealing characteristic aldehyde and aromatic proton signals. Density functional theory (DFT) calculations provided insights into the non-planar structure and significant dihedral angle of TFPPy, along with a wide bandgap of 3.27 eV. The optical properties of TFPPy, including UV-Vis absorption and luminescence, highlighted its strong blue light emission at 457 nm. The subsequent formation of sp^{2}c-COF through Knoevenagel polycondensation with 1,4-phenylenediacetonitrile (PDAN) was confirmed by FTIR, solid-state ^{13}C-NMR, and elemental analysis. XRD analysis revealed the crystalline nature and AA stacking pattern of sp^{2}c-COF, supported by molecular modeling and simulation. The sp^{2}c-COF exhibited excellent chemical and thermal stability, withstanding temperatures up to 510 °C while maintaining structural integrity. Nitrogen adsorption-desorption isotherms indicated a high BET surface area of 700 cm^2/g and uniform pore size distribution of 1.89 nm, confirming its microporosity. Optical studies showed absorption in the UVA and UVB regions, with a red-shifted fluorescence emission at 572 nm. UPS and CV measurements confirmed the n-type semiconductor nature of sp^{2}c-COF, with HOMO and LUMO levels at –5.77 eV and –3.87 eV, respectively. Electrical conductivity studies demonstrated a significant increase in conductivity upon iodine doping, underscoring the potential of sp^{2}c-COF for enhanced charge transport in PSCs.

Chapter 5*

Functionalized sp^2 Carbon-Conjugated Covalent Organic Frameworks for Interfacial Modulation of Inverted Perovskite Solar Cells

This study investigates, for the first time, the utilization of a pyrene-based sp^2 carbon-conjugated covalent organic framework (sp^{2}c-COF) as an interfacial layer in inverted PSCs. Functionalized with cyano (–CN) Lewis base groups, the sp^{2}c-COF exhibits a dual effect, simultaneously passivating both the NiO_x and the perovskite layers. Detailed characterization results highlight the role of sp^{2}c-COF in reducing the Ni^{3+} defect density in NiO_x films and forming Lewis acid-base adducts with undercoordinated Pb^{2+} on the perovskite surfaces, thereby inhibiting interfacial redox reactions and suppressing non-radiative recombination. Moreover, sp^{2}c-COF leads to improved crystallinity of perovskite films. Benefiting from the synergistic effects, sp^{2}c-COF-modified devices delivered a champion efficiency of 17.64%. These findings underscore the potential of sp^{2}c-COF as a functional interface material for PSCs, offering enhanced efficiency and stability, as well as advancing application of COFs in photovoltaic technologies.

---

* This section is substantially published as H. R. Abuzeid, D. J. J. Tay, B. Febriansyah, A. Kanwat, T. Salim, A. A. Zhumekenov, S. A. Pullarkat, and N. Mathews. Functionalized sp^2 Carbon-Conjugated Covalent Organic Frameworks for Interfacial Modulation of Inverted Perovskite Solar Cells. *Small Methods*, 2025, 9, 2400666. DOI: 10.1002/smtd.202400666. Reproduced with permission. Copyright © 2025, John Wiley and Sons.

5.1 Introduction

Metal halide perovskites (MHPs) have recently emerged as the next-generation solution-processable semiconductors suitable for a wide range of optoelectronic applications including solar cells, light-emitting diodes (LEDs), and photodetectors. [91,257–259] Since their first introduction in 2012,[5,6] solid-state perovskite solar cells (PSCs) have already achieved remarkable success with the current power conversion efficiencies (PCEs) for single-junction devices reaching 27.0%.[7–10] Meanwhile, all-perovskite and perovskite-silicon tandem solar cells have also achieved impressive 30.1% and 34.6% PCEs, respectively.[10,65] However, despite these advances, PSCs still face significant challenges with respect to their environmental and operational stability. Specifically, perovskite materials are intrinsically prone to degradation under various environmental conditions such as humidity and heat. Additionally, interfacial defects between different layers of their devices can also lead to a reduced lifespan.[11–18] Thus, addressing these issues is critical toward more durable and efficient PSCs.

Recently, PSCs with an inverted p-i-n structure have demonstrated excellent stability and efficiency reaching 26% which is closely match that of n-i-p PSCs (27%), thus, marking a pivotal development in photovoltaic research.[260] Inorganic nickel oxide (NiO_x) is one of the most affordable, thermally and chemically stable, yet effective hole-transporting materials (HTMs) used in p-i-n PSCs.[261–263] Inverted PSCs with NiO_x have also shown great potential for flexible and tandem solar cell applications.[264,265] However, the relative efficiencies of NiO_x-based inverted PSCs are typically low, primarily due to the interfacial defects at the NiO_x and perovskite heterointerfaces. These imperfections generally involve unfavorable trap states in the buried interface (undercoordinated Pb^{2+}) and NiO_x surface defects (Ni^{3+}) that can result in undesirable interfacial chemical reactions.[29,30] This contributes to carrier accumulation and inefficient charge transport at interfaces, resulting in non-radiative recombination, hysteresis, and severe limitation of the open-circuit voltage (V_{oc}) and fill factor (FF) as well as intrinsic degradation of perovskite materials.[30–32] Therefore, interface engineering presents a crucial strategy for achieving high efficiency in NiO_x-based inverted perovskite photovoltaics.

Over the past decade, various strategies have been employed to passivate the surface defects and enhance the PSCs efficiency and stability such as precursors optimizations,[266,267] and device interfacial modulation.[31,32] Among various strategies, a straightforward yet effective approach involves integrating small organic molecules and/or self-assembled monolayers (SAMs) containing Lewis acid/base groups that effectively passivate defects through acid-base interactions.[268–270] Recently, covalent organic frameworks (COFs) have emerged as functional additives in PSCs, offering several advantages over small molecules and SAMs.[166,214,218] COFs, formed through reversible condensation of organic linkers into two- or three-dimensional (2D or 3D) networks, provide continuous structural order with more efficient charge transfer pathways and reduced recombination losses compared to the discrete structures of small molecules and SAMs.[3,138,218] Their modular nature allows precise tuning of electronic properties and surface functionality.[214,216,239,240] Among emerging COF systems, sp^2 carbon-conjugated COFs (sp^2c-COFs) have attracted considerable attention due to their extended C=C π-conjugation, which facilitates efficient in-plane charge transport.[160] Jiang *et al.* introduced sp^2c-COFs based on electroactive pyrene units, featuring low bandgaps and exceptionally high electrical conductivity, making them ideal for interfacial modulation in inverted PSCs.[162,242] Furthermore, sp^2c-COFs are insoluble in common solvents, which ensures they remain intact and maintain their integrity and functionality as interfacial layers during perovskite layer deposition. Additionally, their porous structure aids in controlling perovskite crystallization, resulting in higher crystallinity, larger grain sizes, and a more uniform perovskite layer, thereby enhancing PSC efficiency and stability.[214,235]

In this study, the sp^2c-COF was introduced as an interfacial layer between NiO_x and perovskite in inverted-structure PSCs to tackle the heterointerface defects. Synthesis and extensive structural characterization were performed for the pyrene-based sp^2c-COF featuring a 2D structure with extended π-conjugation system and π-π interactions between the sheets, as well as containing electron-donating cyano (-CN) groups. The key optoelectronic and electrical properties of the material were demonstrated, including a narrow bandgap of 1.97 eV and enhanced electrical conductivity. By taking advantage of these structural and semiconducting features of sp^2c-COF, which can help facilitate charge transport and passivate defects,[246] CsFA-based ($Cs_{0.08}FA_{0.92}PbI_3$, where FA is formamidinium or $CH(NH_2)_2^+$) inverted p-i-n PSCs was fabricated, with a thin sp^2c-COF interlayer introduced between the perovskite and the NiO_x layers. It was demonstrated that the sp^2c-COF not only improves the perovskite crystallinity but also reduces the non-radiative recombination and interfacial reactions, resulting in an 11.6% increase in PCEs from 15.81% to 17.64%. it is believed that this strategy for interface engineering can be a significant step towards integrating electroactive COFs in PSCs to further boost the photovoltaic performance.

5.2 Sp^2c-COF Thin Film Fabrications and Characterizations

To integrate sp^2c-COF as an interfacial layer between NiO_x and perovskite, a smooth thin film of sp^2c-COF must be deposited on the NiO_x surface. However, the insolubility of sp^2c-COFs in common organic solvents presents a challenge for achieving a controlled smooth layer. Several methods have been developed for depositing COF thin films. For example, interfacial synthesis involves the polymerization of monomers at the interface of two immiscible solvents, allowing for the formation of thin COF films. Chemical vapor deposition (CVD) is a scalable method where gaseous reactants form a thin COF layer on a substrate, known for producing high-quality, crystalline COF films. Layer-by-layer assembly involves the sequential deposition of monomer layers, which react to form COFs, allowing precise control over film thickness and composition. Solvothermal synthesis involves synthesizing COFs in a solvent at high temperatures and pressures, with the resulting COF powders processed into films, though achieving smooth layers can be challenging. Electrochemical synthesis uses an electric field to drive the polymerization of COF monomers on an electrode surface, enabling the formation of thin films. Spin-coating involves depositing a solution of COF precursors on a substrate, which is then spun at high speed to create a uniform thin film.

In this section, several methods have been investigated to deposit a smooth sp^2c-COF thin layer. Each method has its own advantages and challenges, and the choice of method depends on factors such as the desired film quality, scalability, reproducibility, ease of processing, and time efficiency, and the interfacial layer requirements.

5.2.1 Solvothermal Method

In this method, clean indium tin oxide (ITO) substrates are placed both vertically and horizontally in the autoclave. A mixture of TFPPy and PDAN in dioxane, and KOH were added to an autoclave and heated in an oven at 120 for 2 days to directly fabricate thin films on the surface. Afterward, the substrates are collected and washed. The formed layers are visible to the naked eye but are non-homogeneous, with the layers on the vertical substrates appearing thicker on the side closer to the autoclave bottom (**Figure 5.1a**). The non-uniformity of the film thickness is likely due to gravitational effects and uneven distribution of reactants within the autoclave. The thicker layers observed on the vertical substrates near the bottom suggest that the monomers and catalyst may settle during the reaction, leading to an uneven deposition. This issue is compounded by the limited control over the reaction environment within the autoclave, making it difficult to achieve consistent results across multiple substrates.

Moreover, the presence of bulk domains, as revealed by field-emission scanning electron microscopy (FE-SEM) in **Figure 5.1b**, suggests that the reaction conditions favor the formation of larger, aggregated structures rather than a smooth, continuous film. This could be due to factors such as the concentration of reactants, reaction time, and temperature, all of which need to be carefully optimized to improve film quality. Given these challenges, alternative methods such as interfacial synthesis or spin-coating might be more suitable for producing high-quality, reproducible sp^{2}c-COF thin films. These methods offer better control over film thickness and uniformity, as well as scalability, making them more appropriate for PSCs application.

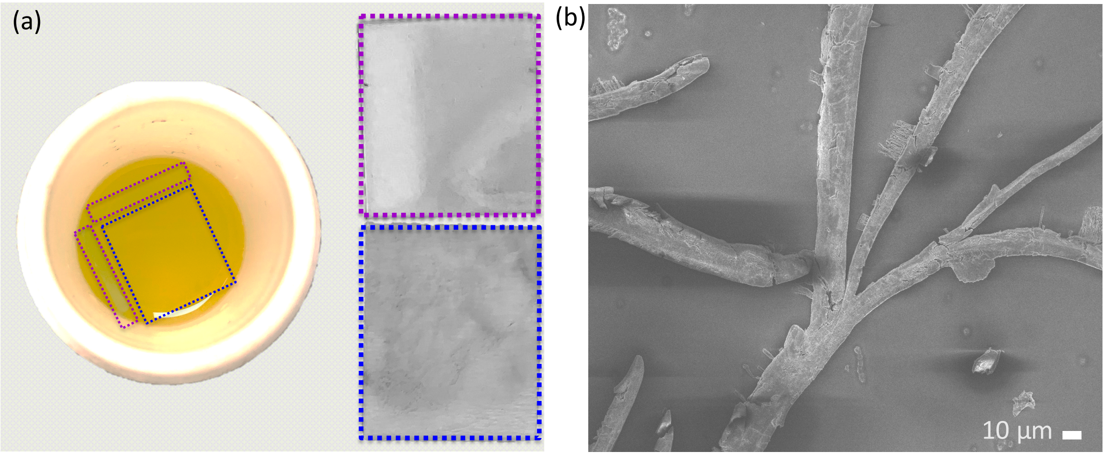

Figure 5.1 (a) Photographic image of the deposition process using in-situ solvothermal method. (b) FE-SEM image of the resultant film featuring presence of bulk domains.

5.2.2 Free-standing Thin Film Using Liquid-Liquid Interfacial Method

The synthesis of self-standing thin films of COFs can be achieved through a liquid-liquid interface method, where a condensation reaction occurs at the boundary between two immiscible liquids.[144,174,271] In this process (shown in **Figure 5.2a**), TFPPy (0.5 M) and PDAN (1.0 M) monomers were sonicated in dichloromethane (DCM) to create a nonaqueous solution, which is then transferred to a beaker. An aqueous solution of the catalyst (4 M KOH) was carefully added along the beaker wall, forming two distinct liquid layers. After several hours, a thin film begins to form at the interface. After 72 h, the aqueous layer was meticulously removed using a glass pipette. The self-standing thin film, now at the sp^2c-COF layer, was then lifted onto a clean ITO substrate by slowly dipping the substrate into the solution with the ITO side facing the thin film. The substrate was subsequently washed with water, methanol and DCM, and then oaked in DCM for 10 hours. SEM characterization of the resulting sp^2c-COF film reveals a homogeneous surface, free of pinholes or bulk powder (**Figure 5.2b**).

Despite the success of this method, several challenges have been identified. The thin film layer exhibits low mechanical stability, making it prone to collapse during the removal of the aqueous layer. This can be an issue especially during handling and transfer processes, which may lead to defects or damage, necessitating extremely careful handling during the lifting procedure. Additionally, the method requires a significant amount of solvents to produce the thin film, raising environmental concerns due to the large solvent usage. The scalability of this method is also limited by the surface area of the thin film, posing challenges for large-scale production. Furthermore, achieving consistent quality and thickness of the thin films can be challenging, as slight variations in the process can lead to significant differences in the film properties. Finally, fine-tuning the reaction conditions, such as the concentration of monomers and catalysts, temperature, and reaction time, is crucial for optimizing the quality of the thin films.

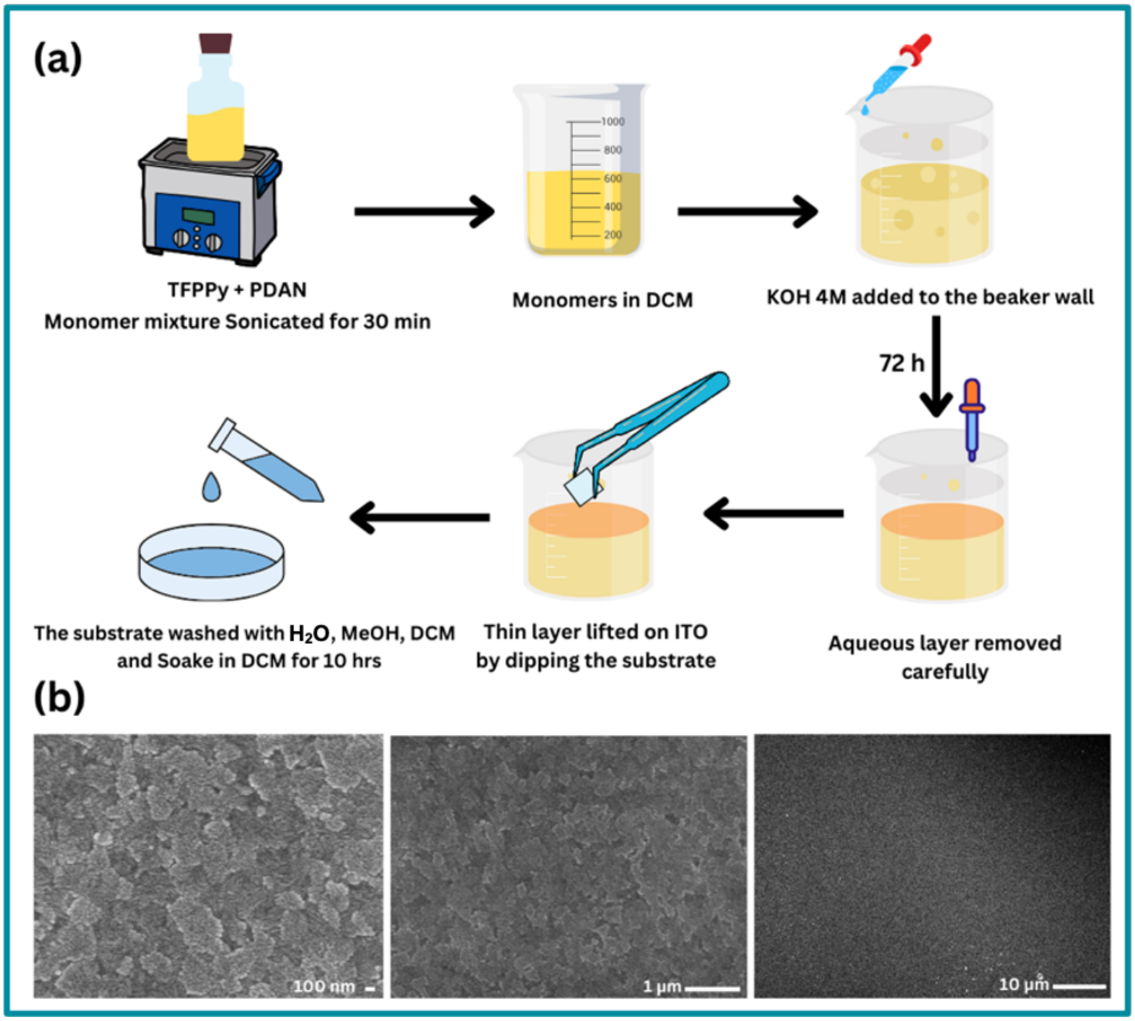

Figure 5.2 (a) Schematic diagram of the synthetic procedures of liquid-liquid interfacial method. (b) FE-SEM images of the surface morphology of formed film.

5.2.3 Spin-Coating Method

Spin-coating is a simple, effective and widely used method in fabricating PSCs. It can produce highly uniform thin films with controlled thickness, which is crucial for the performance of these cells. Additionally, spin-coating allows for reproducible film quality, essential for consistent device performance. While traditionally used for small-scale applications, advancements in spin-coating techniques are making it more scalable for larger-area applications. These advantages make spin-coating a preferred method in the development of PSCs, contributing to their rapid advancement and increasing efficiency.

To prepare a thin film of sp^2c-COF by spin-coating, the pre-synthesized bulk powder was sonicated in DMF (0.5 mg m^{-1}) for 24 hours to form a homogenous suspension. This suspension was spin-coated on top of NiO_x layer (**Figure 5.3a**). The morphologies of powder and thin-film samples of sp^2c-COF were examined using FE-SEM. As seen from **Figure 5.3c**, the powder sample adopts a belt morphology. Whereas the thin film of sp^2c-COF showed a uniform array of nanograins covering the whole NiO_x surface, with no bulk particle aggregates or pinholes **Figure 5.3b**. This change in morphology is due to the exfoliation of COFs induced by ultrasonication. The cross-section SEM image of the sp^2c-COF layer on top of NiO_x revealed a thickness of ~20 nm **(Figure 5.3a,b**).

Spin-coating offers several advantages over both the liquid-liquid interfacial and solvothermal methods for creating COF thin films. It produces highly uniform films with precise thickness control, which is crucial for consistent film properties. The process is simple, quick, and cost-effective, requiring less solvent and materials. Spin-coating also provides high reproducibility and can be easily scaled up for larger substrates, making it suitable for industrial applications. Overall, spin-coating stands out for its uniformity, simplicity, reproducibility, cost-effectiveness, and scalability.

Wettability: On the other hand, the wettability of sp^2c-COF layer is an important requirement for achieving uniform and pinhole-free deposition of perovskite films. Therefore, the wettability of both pristine and sp^2c-COF-coated NiO_x films were investigated by various polar solvents such as water, DMF, and DMSO. As can be seen from **Figure 5.3d**, in all three cases, the contact angle increased upon coating NiO_x with the sp^{2}c-COF layer. Interestingly, the increment was the largest for water, indicating the hydrophobic nature of sp^{2}c-COF. However, the sp^{2}c-COF surface showed acceptable wettability by both DMF and DMSO solvents. These observations suggest that sp^{2}c-COF layer can be beneficial for both spin-coating the perovskite layer and protecting it from water molecules.

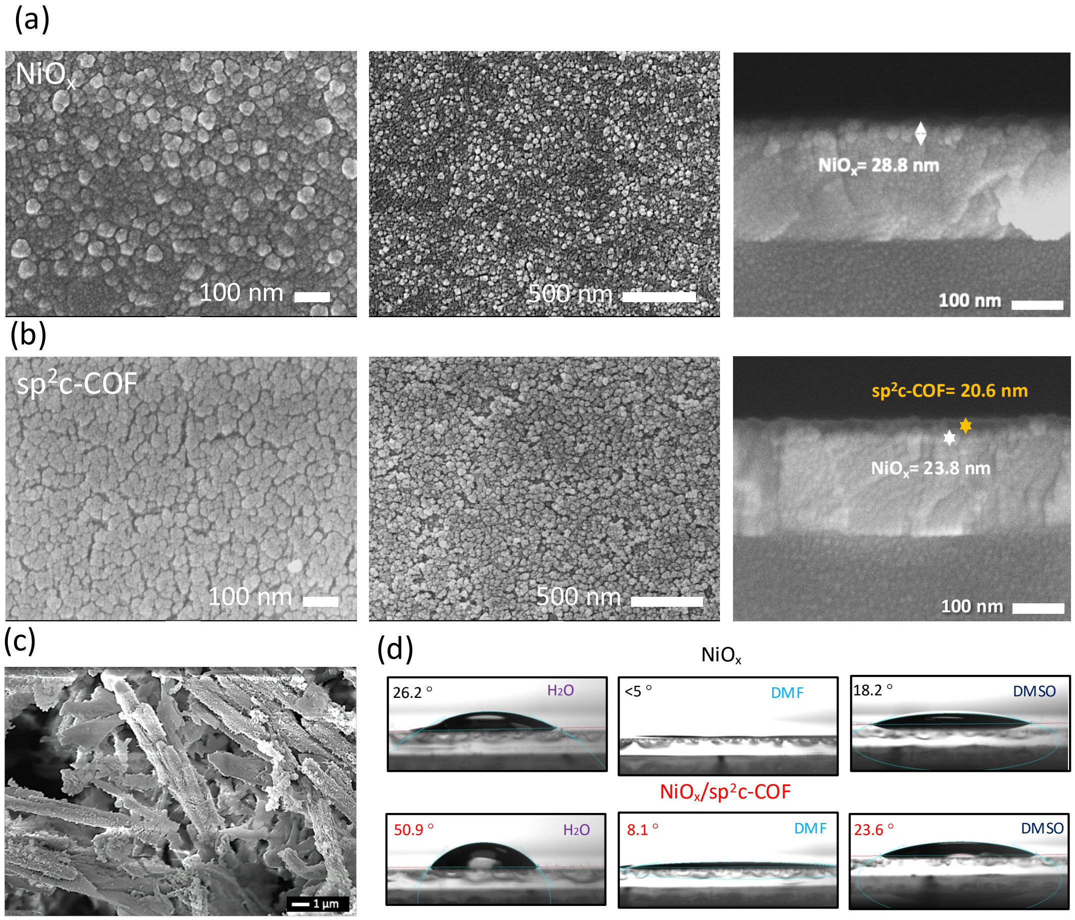

Figure 5.3 (a-b) Top-view and side-view FE-SEM images of pristine and sp^{2}c-COF-coated NiO$_x$ films, respectively. (c) FE-SEM images of sp^{2}c-COF powder. (d) Contact angle of water, DMF and DMSO on NiO$_x$ and NiO$_x$/sp^{2}c-COF.

5.3 Devices Fabrication and Characterizations

In this study, CsFA-based perovskite ($Cs_{0.08}FA_{0.92}PbI_3$, where FA is formamidinium or $CH(NH_2)_2^+$) was chosen in the fabrication of PSCs devices. CsFA-based perovskites offer several advantages over traditional methylammonium ($CH_3NH_3^+$)-based compositions, including higher thermal and operational stabilities. PSCs were fabricated with the following device architecture for the control samples: FTO/NiO_x/perovskite ($Cs_{0.08}FA_{0.92}PbI_3$)/PEAI/C_{60}/BCP/Ag (**Figure 5.4a**). The NiO_x HTL, the CsFA-perovskite absorber and PEAI passivation layers were successively deposited on top of a FTO substrate using a spin-coating method. This was followed by thermal evaporation of the fullerene (C_{60}) ETL, bathocuproine (BCP) buffer layer, and 100 nm-thin silver (Ag) electrodes. It is worth mentioning that the BCP buffer layer is generally introduced to prevent the charge accumulation.[272]

Meanwhile, to demonstrate the effect of sp^2c-COF on the PSCs performance, a very thin layer of sp^2c-COF was spin-coated between the NiO_x HTL and the perovskite layer in the modified devices. Both the control and the sp^2c-COF-modified devices were then tested under 1.5 AM simulated sunlight to measure their current density–voltage (*J–V*) characteristics (**Figure 5.4c** and **5.5a**), see **Table 5.1** for further details)**.** The champion devices for the control achieved PCE value 15.81%, this value has notably increased in the sp^2c-COF-modified to 17.64%, representing an approximate 11.6% enhancement. This improvement is substantial when compared to other reported NiO_x modifiers (**Figure 5.4d**) and **Table 5.2**). The PCE increase was mainly due to the enhancement of the fill factor (FF) from 67.97% to 75.24% and the short-circuit current density (J_{sc}) from 21.90 to 22.13 mA cm^{-2}, respectively.

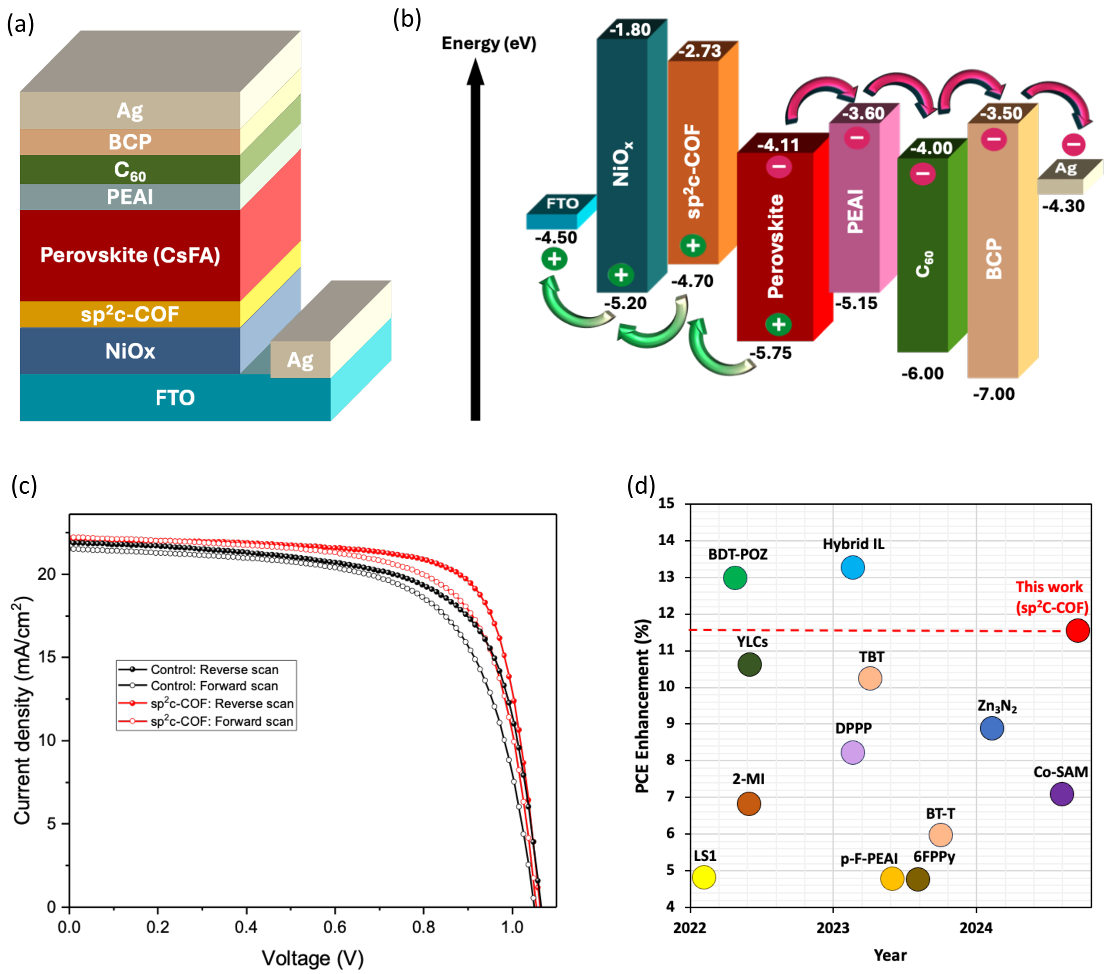

Figure 5.4 (a) Schematics of the sp^{2}c-COF-modified PSCs with the inverted p-i-n device architecture. (b) band alignments diagram. (c) *J–V* curves for the reverse and forward scans of the control and the sp^{2}c-COF-modified PSCs. (d) The PCE enhancement levels achieved in different reported surface modifiers for NiO_x-based p-i-n devices.

Table 5.1 Photovoltaic parameters of control and sp^{2}c-COF modified devices.

Value	Devices	V_{oc} (V)	J_{sc} (mA/cm^2)	FF (%)	PCE (%)
Campion device	Control	1.06	21.29	67.97	15.82
	sp^{2}c-COF	1.06	22.13	75.24	17.65
Median value	Control	1.05	20.11	67.90	14.16
	sp^{2}c-COF	1.06	20.27	73.92	15.97
Maximum value	Control	1.07	21.90	70.15	15.82
	sp^{2}c-COF	1.07	22.16	75.90	17.65

Table 5.2 The summarized PCE enhancements in reported interfacial layers between NiO$_x$ and perovskite relative to the control.

Materials	Device architecture	Year	PCE enhancement (%)	Reference
LS1	ITO/NiO$_x$ /perovskite/PCBM/BCP/Ag	2022.01	4.9	*ACS Appl. Mater. Interfaces* **2022**, *14, 6794−6800*
BDT-POZ	ITO/NiO$_x$ /perovskite/PCBM/BCP/Ag	2022.04	13.0	*J. Energy Chem.* **2022**, *67, 797–804*
2-MI	ITO/NiO$_x$ /perovskite/PCBM/BCP/Ag	2022.05	7.9	*J. Energy Chem.* **2022**, *68, 35–41*
YLCs	ITO/NiO$_x$ /perovskite/PCBM/BCP/Ag	2022.05	10.7	*ACS Appl. Mater. Interfaces* **2022**, *14, 26135−26147*
DPPP	FTO/NiO$_x$/Me-4PACz/perovskite/PEAI/C$_{60}$/SnO$_2$/Ag	2023.02	8.4	*Science* **2023**, *379, 690–694*
Hybrid IL	ITO/NiO$_x$/perovskite/C$_{60}$/BCP/Ag	2023.02	13.4	*Adv. Mater.* **2023**, *35, 2212258*
TBT	ITO/NiO$_x$ /perovskite/PCBM/BCP/Ag	2023.03	10.3	*Sol. RRL* **2023**, *7, 2300018*
p-F-PEAI	ITO/NiO$_x$/perovskite/Spiro-OMeTAD/Cu	2023.05	4.8	*Small Methods* **2024**, *8, 2300241.*
6FPPy	ITO/NiO$_x$/perovskite/PCBM/BCP/Ag	2023.06	4.8	*Nano Energy.* **2023**, *111, 108363*
BT-T	ITO/NiO$_x$ /perovskite/ PCBM/BCP/Ag	2023.08	6.0	*Adv. Mater.* **2024**, *36, 2303869*
Zn$_3$N$_2$	ITO/NiO$_x$/perovskite/PCBM/ZnO NPs/Ag	2024.01	9.0	*Small* **2024**, *20, 2311362*
Co-SAM	ITO/NiO$_x$/perovskite/PEABr/PCBM/ BCP/ag	2024.01	7.1	*Adv. Mater.* **2024**, *36, 2311970*
sp^{2}c-COF	**ITO/NiO$_x$ /perovskite/ PEAI/C$_{60}$/BCP/Ag**	**2024.08**	**11.6**	**This work**

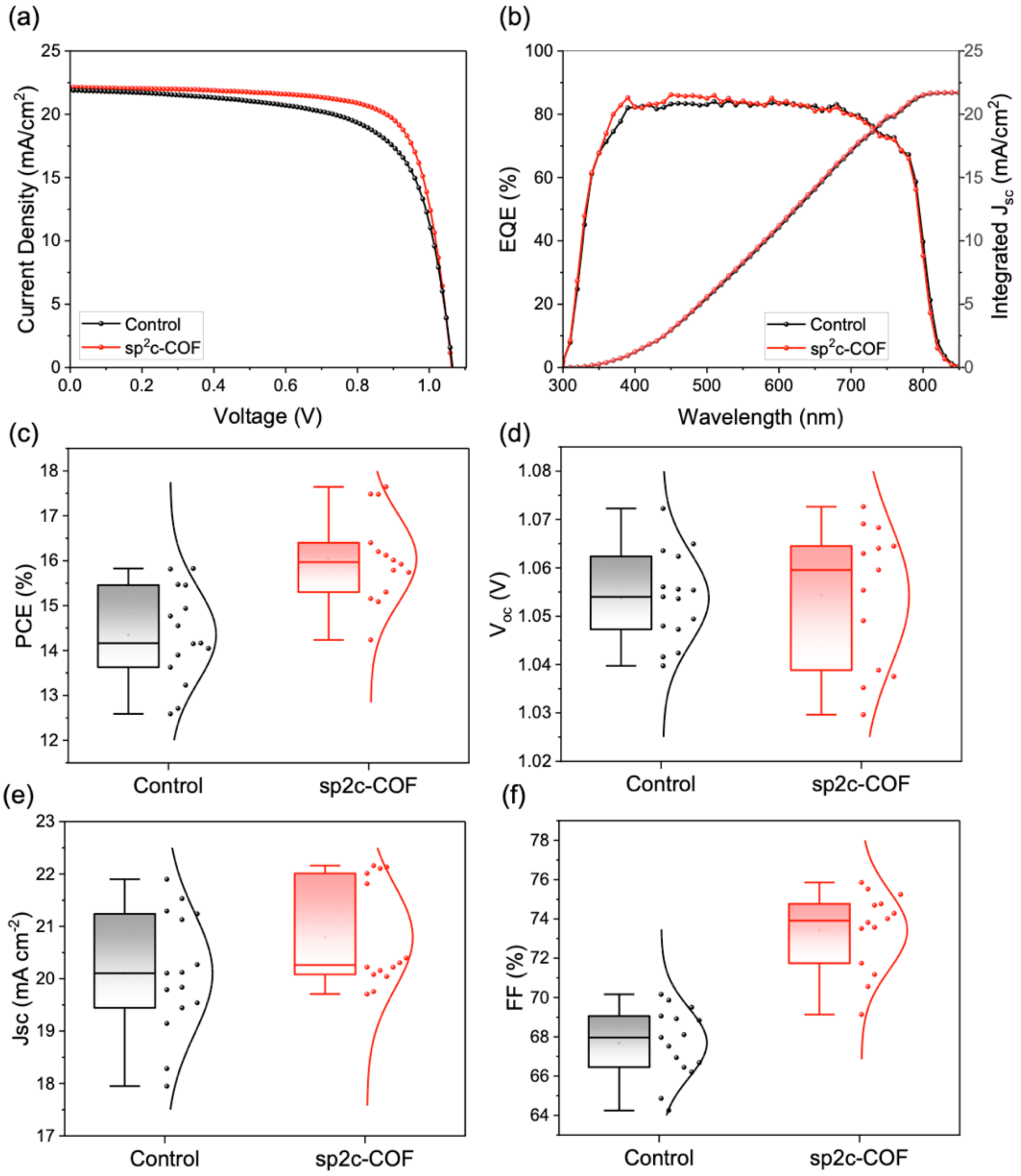

Figure 5.5 (a) J-V curves for the control and the sp^{2}c-COF-modified PSCs devices. (b) The EQE curves and the corresponding integrated J_{sc} values calculated from the IPCE spectrum. The statistical distribution of devices paramaters: (c) PCE, (d) V_{oc}, (e) J_{sc}, and (f) FF.

The statistics of 28 devices (**Figures 5.5c-f**) showed an improvement of the median PCE from 14.16% to 15.97%, respectively. The median J_{sc} values also increased from 20.11 to 20.27 mA/cm^2 with the introduction of the sp^{2}c-COF interlayer. Meanwhile, the integrated J_{sc} values derived from the external quantum efficiencies (EQEs) were found to be 21.69 and 21.74 mA cm^{-2} for the control and the sp^{2}c-COF-modified devices, respectively, closely reproducing the J_{sc} values from the $J-V$ curves (**Figure 5.5b**). Bandgap energy the control and the sp^{2}c-COF-modified devices calculated the EQE spectrum were determined to be 1.56 eV.

Furthermore, the median V_{oc} value also slightly increases with the sp^{2}c-COF introduction. However, the effect of the sp^{2}c-COF introduction on V_{oc} becomes more noticeable under low light intensities. The V_{oc} values under different light intensities from 0.1 to 0.6 suns were used to obtain the ideality factors for the corresponding devices (**Figure 5.6**). This revealed that the sp^{2}c-COF-modified devices show a lower ideality factor (1.967 kT/q) than the control ones (2.218 kT/q), while the sp^{2}c-COF-modified devices demonstrated a lower hysteresis than the control ones (**Figure 5.7**), suggesting the effective passivation of defects at the interfaces by the sp^{2}c-COF. Similarly, the median FF value noticeably increased from 67.90% to 73.92% upon the sp^{2}c-COF introduction. It is believed that these improvements can be attributed to the reduction in non-radiative recombination due to the lower trap density in the sp^{2}c-COF-modified devices.[34] On the other hand, the series resistance decreases from 57.17 to 47.47 ohms and the shunt resistance increases from ~11 to ~16 k-ohms with sp^{2}c-COF introduction (**Figure 5.8**). This highlights the effect of sp^{2}c-COF interlayer in enhancing the electrical conduction and the quality of NiO_x layer.

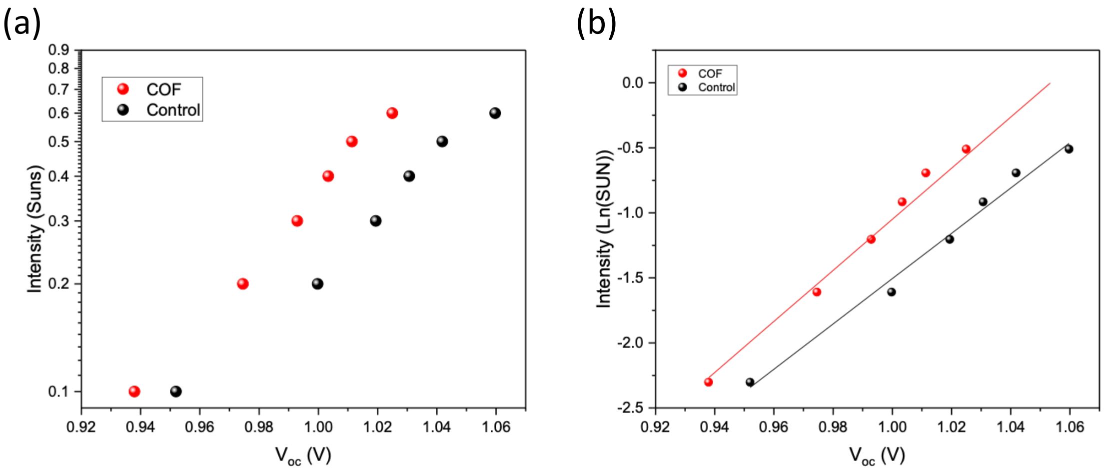

Figure 5.6 (a) Light intensity dependence of V_{oc} measurements and (b) Ideality factor calculation using the natural logarithm of the intensity.

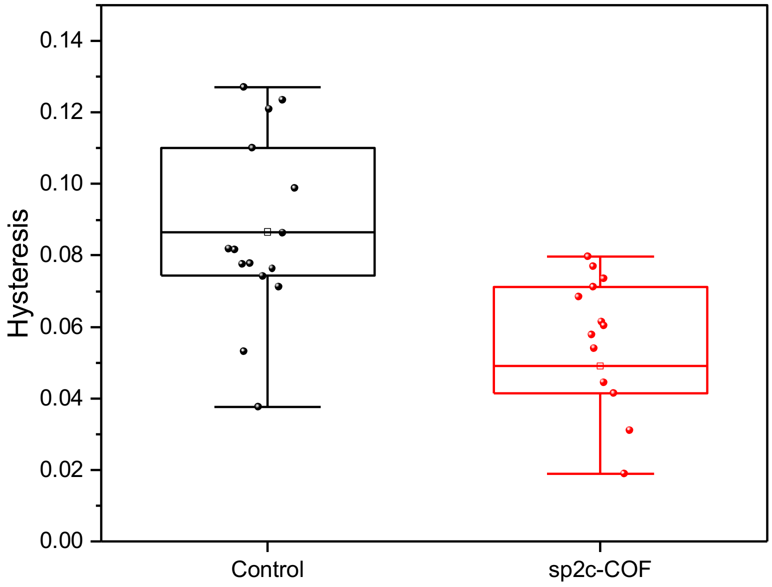

Figure 5.7 Statistical distribution of devices hysteresis.

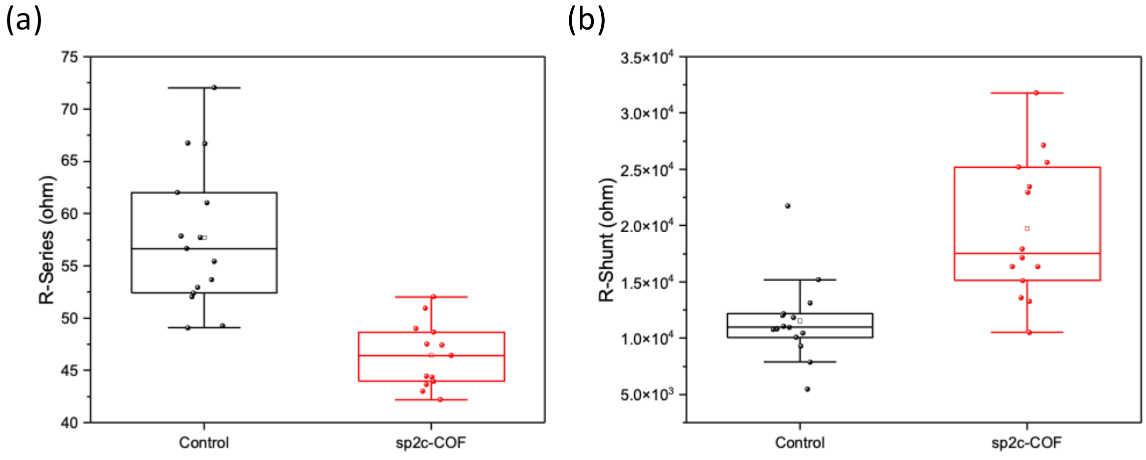

Figure 5.8 Statistical distribution of devices' (a) series resistance and (b) shunt resistance.

5.4 Role of sp^{2}c-COF in CsFA-Perovskite Film

5.4.1 Morphology and Crystallinity

To discern the difference in the photovoltaic performance of the control and the sp^{2}c-COF-modified devices, the effect of sp^{2}c-COF on the morphology and crystallinity of perovskite films were investigated. **Figure 5.9a,b** shows the top-view FE-SEM images of the pristine (control) and sp^{2}c-COF-modified perovskite films. As can be seen, no pinholes were observed in both samples, while the sp^{2}c-COF-modified films showed larger crystal domains as compared to the pristine samples. This can be attributed to the hydrophobic porous nature of sp^{2}c-COF, which effectively promotes slower perovskite crystallization resulting in larger grain sizes and reduced trap density.[235] Furthermore, the cross-section images of the control and sp^{2}c-COF-modified perovskite films showed significant difference between the two samples (**Figure 5.9c,d)**. Specifically, in the pristine sample, it was observed an increased number of grain boundaries that are parallel to the substrate. Such grain structures may impede the charge transfer across the perovskite film, as well as act as sites for perovskite degradation. [273–275] That larger grains in the sp^{2}c-COF-modified samples provide a reduced number of non-radiative recombination centers, which likely results in their higher PCE values.[276]

The improved crystallinity of the perovskite film upon the introduction of the sp^{2}c-COF layer was also confirmed by XRD analysis (**Figure 5.9e,f**). Both the control and the sp^{2}c-COF-modified films showed similar XRD peaks positions corresponding to the main perovskite phase. However, the intensity of the XRD pattern of (100), (111), (200) and (211) diffraction peaks has increased in the sp^{2}c-COF-modified. Localized XRD (100) pattern at 13.94° showed a 32% increase in intensity, with FWHM value of sp^{2}c-COF-modified film (0.265°) relatively smaller than that in the pristine sample (0.355°), this data suggesting the enhancement of crystallinity upon introduction of sp^{2}c-COF. Furthermore, the sp^{2}c-COF-modified films also showed a lower content of unreacted PbI_2 in the film observed by its smaller signal at 12.62°. This reduction can be attributed to the inhibition of interfacial redox reactions between Ni^{3+} and perovskite, as well as the passivation of undercoordinated Pb^{2+}.

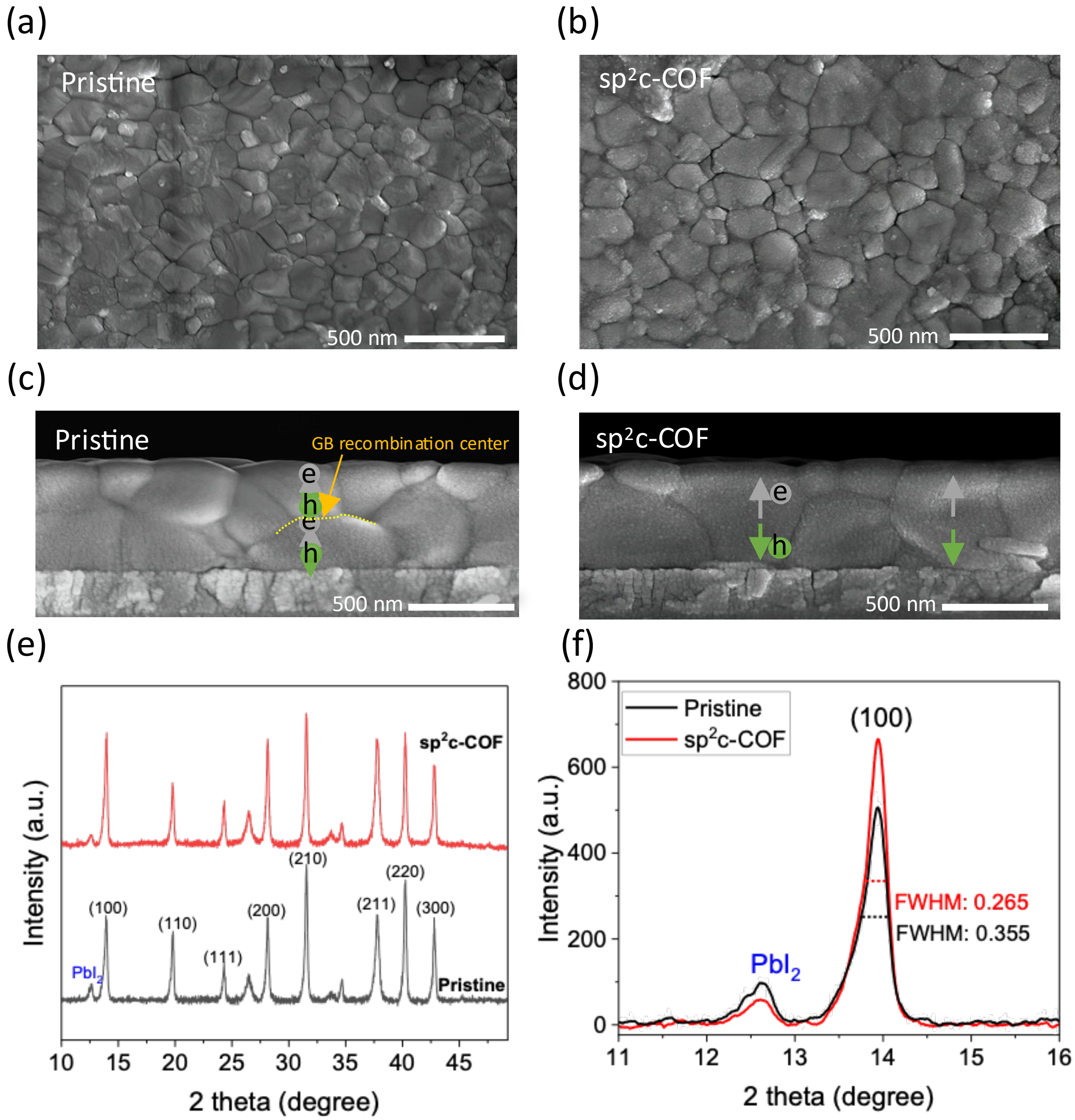

Figure 5.9 (a,c) Top-view and (d,e) cross-sectional FE-SEM images of the pristine (control) and the sp^{2}c-COF-modified perovskite thin films, respectively. Scale bars: 500 nm. (e,f) XRD patterns the pristine and the sp^{2}c-COF-modified perovskite thin films.

5.4.2 Charge Transport and Carriers Dynamics

To understand the effect of sp^{2}c-COF on the carrier dynamics, the steady-state PL of the pristine and modified perovskite films were measured. Notably, the PL signal intensity reduces upon introduction of the sp^{2}c-COF interlayer between the NiO$_x$ and the perovskite layers, which suggests that sp^{2}c-COF can efficiently passivate the interface allowing charge transfer from the perovskite to NiO$_x$ layer (**Figure 5.10a**). To gain further insights, the time-resolved PL (TRPL) spectra of both samples were measured (**Figure 5.10b** and **Table 5.3**). TPRL results showed that sp^{2}c-COF-modified perovskite films exhibit longer carrier lifetime (5.27 ns) compared to the control ones (4.81 ns), indicating a reduction in trap density. Furthermore, the pristine and sp^{2}c-COF-modified samples showed similar steady-state UV-vis absorption profiles (**Figure 5.10c**), except for the slight increment in the absorption near the UV region for the modified samples, which is likely due to the ability of sp^{2}c-COF to act as an UV absorber.

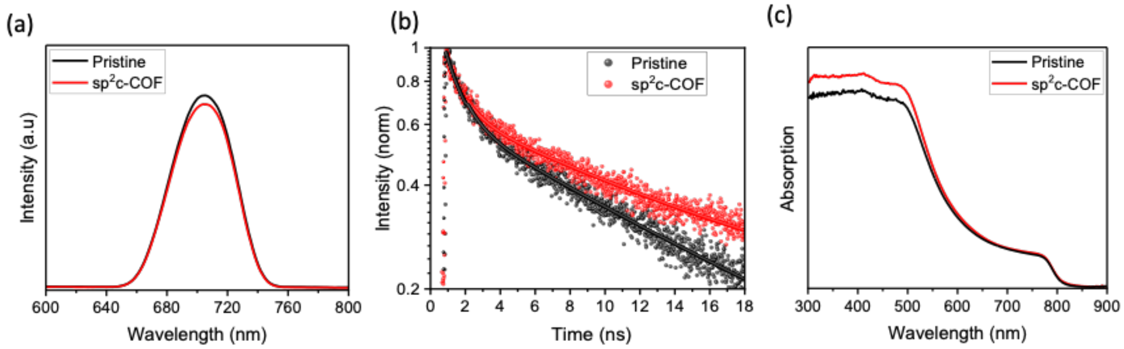

Figure 5.10 (a) Photoluminescence, TRPL and (c) absorption spectra of the pristine and the sp^{2}c-COF-modified perovskite thin films.

Table 5.3 Fitting parameters of the decay amplitude and decay time calculated from TRPL spectra.

	τ_{avg} (ns)	τ_1 (ns)	τ_2 (ns)	A1	A2
Control	4.81	1.00	13.84	0.20	0.29
sp^{2}c-COF-modified	5.27	1.05	14.50	0.26	5.27

5.4.3 NiO$_x$ Defects Passivation

To study the interaction between sp^{2}c-COF and NiO$_x$, X-ray photoelectron spectroscopy (XPS) was utilized to reveal the Ni^{3+}/Ni^{2+} ratio on the surface of as-deposited NiO$_x$ films (As-Dep NiO$_x$) both with and without the sp^{2}c-COF interlayer. The Ni 2p$_{3/2}$ signal typically consists of two peaks at 854 eV and 856 eV, generally assigned to Ni^{2+} and Ni^{3+}, respectively, and a peak around 861 eV belonging to a satellite signal.[29,30] The Ni^{3+}/Ni^{2+} ratio, estimated from the integrated area of each peak, was found to be 3.9 and 3.4 for the pristine and the sp^{2}c-COF-coated NiO$_x$ films, respectively (**Figure 5.11a,c**). This demonstrates that the introduction of the sp^{2}c-COF interlayer can help lower the Ni^{3+} defect density in NiO$_x$ films and, thus, reduce their redox reaction with the perovskite layer. Interestingly, it was observed that the Ni^{3+}/Ni^{2+} ratio on the surface of pristine NiO$_x$ films treated with UV-Ozone for 5 min (UVO NiO$_x$) can reach the values as high as 6.6 (**Figure 5.11b**).[29] Meanwhile, this ratio in the sp^{2}c-COF-coated UVO NiO$_x$ films drops to 1.6 (**Figure 5.11d**). This observation highlights the importance of using the sp^{2}c-COF interlayers for the long-term stability of PSCs under device operation conditions which typically involves their exposure to UV from the sunlight.

5.4.3 Perovskite Trap Defects Passivation

To gain insight into underlying interactions between the sp^{2}c-COF and the perovskite layers, depth profiling XPS was used to examine the binding energy (BE) peaks of Pb and I species at sp^{2}c-COF/perovskite interface. The XPS results revealed a distinct shift of approximately 0.20 eV towards higher BE positions in the Pb 4f spectra when treated with the sp^{2}c-COF (**Figure 5.11e**). This shift indicates an interplay between the cyano-group of the sp^{2}c-COF and the Pb^{2+} ions of the perovskite via Lewis acid-base interaction. Notably, a similar shift in BE was observed in I 3d signal, suggesting the decrease in the electron-withdrawing capability of Pb atoms (**Figure 5.11f**).[166] On the other hand, FTIR spectrum of the sp^{2}c-COF blended with PbI$_2$ powder also showed a notable decrease in the characteristic vibration intensity of the cyano-group at ~2215 cm^{-1}, confirming the XPS results (**Figure 5.12**). This interaction between sp^{2}c-COF and the perovskite is believed to plays a crucial role in passivating the trap states at interfaces which can help improve the performance of PSCs.

In summary, The XPS analysis revealed significant insights into the role of the sp^{2}c-COF interlayer in enhancing the stability and performance of PSCs. The reduction in the Ni^{3+}/Ni^{2+} ratio on the surface of NiO_x films coated with sp^{2}c-COF suggests a mitigation of redox reactions with the perovskite layer, thereby contributing to improved device stability. Additionally, the observed shift in the Pb 4f and I 3d signals at the sp^{2}c-COF/perovskite interface indicates an interaction between sp^{2}c-COF and the perovskite. This interaction plays a crucial role in passivating trap states at interfaces, thereby enhancing device performance. Overall, these findings highlight the importance of sp^{2}c-COF as an interfacial layer in PSCs, offering both stability and performance enhancements crucial for their practical application in solar energy harvesting.

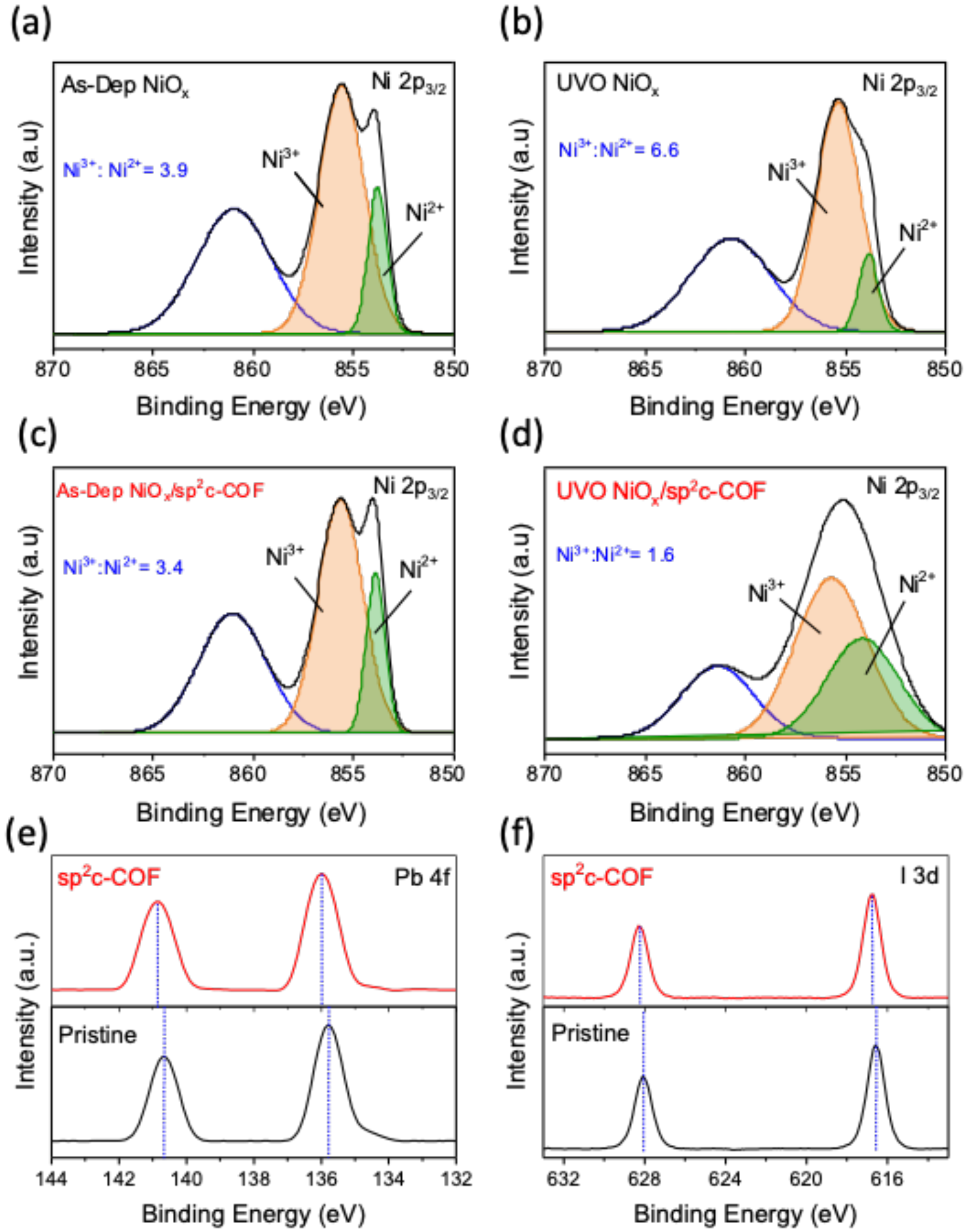

Figure 5.11 XPS of Ni 2p$_{3/2}$ in the pristine (a) as-deposited NiO$_x$ and (b) UV-Ozone-treated NiO$_x$ films. XPS of Ni 2p$_{3/2}$ in the sp^{2}c-COF-coated (a) as-deposited NiO$_x$ and (b) UV-Ozone-treated NiO$_x$ films. XPS of (e) Pb 4f and (f) I 3d for pristine and sp^{2}c-COF modified perovskite, respectively.

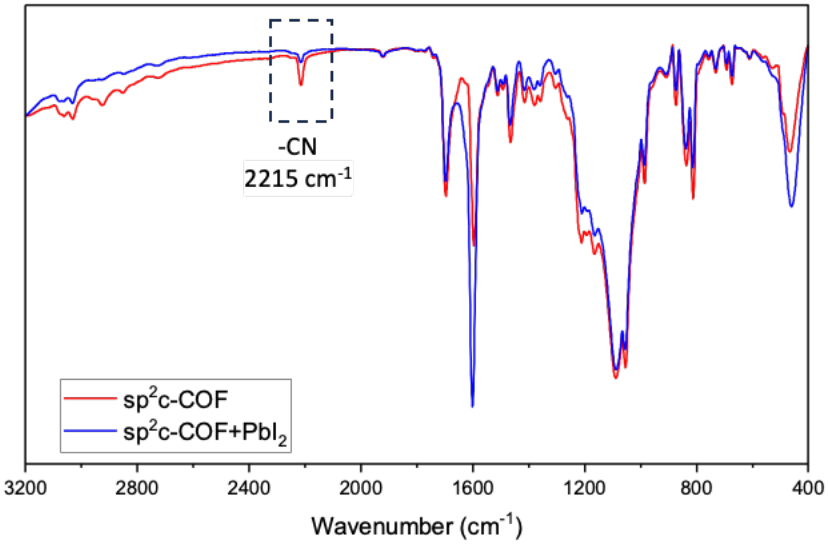

Figure 5.12 FTIR spectra of sp^{2}c-COF and a mixture of sp^{2}c-COF with PbI$_2$.

5.5 CONCLUSIONS

This study presents a comprehensive investigation into the utilization of sp^{2}c-COF as an interfacial layer in CsFA-based inverted PSCs. The introduction of sp^{2}c-COF between the NiO$_x$ HTL and the perovskite layer resulted in notable enhancements in device performance. Through a series of characterizations and device testing, valuable insights were gained into the mechanisms underlying these improvements. Firstly, structural analysis confirmed the successful synthesis and stability of sp^{2}c-COF, essential for its application in PSCs. Meanwhile, the optical and electronic properties of sp^{2}c-COF demonstrated its potential as an effective interfacial layer. Specifically, the sp^{2}c-COF displayed a low bandgap and HOMO-LUMO levels close to the perovskite band edge positions. Device fabrication and characterization highlighted the significant enhancement in PSC performance upon incorporating sp^{2}c-COF. It was found that the introduction of sp^{2}c-COF improves the perovskite crystallinity and reduces the non-radiative recombination. This results in an over 10% increase of both FF and PCE of CsFA-based inverted PSCs, with the champion device achieving a PCE of 17.64%. Additionally, sp^2c-COF-modified devices demonstrated reduced hysteresis and improved electrical conductivity, further contributing to enhanced performance and stability. Moreover, functionalized with cyano (-CN) Lewis base groups, the sp^2C-COF has shown a dual effect, passivating both the NiO_x and the perovskite layers and inhibiting the interfacial redox reactions between the two layers. In conclusion, this study introduced sp^2c-COF as a promising interfacial layer for inverted PSCs, achieving significant improvement in device performance. Through a combination of structural, optical, electronic, and device characterizations, the mechanisms underlying these improvements was elucidated. The synergistic effects of sp^2c-COF on the perovskite film, including better crystallinity, reduced trap density, and improved charge transport, contribute to the overall enhancement of the PCE. These findings pave the way for the exploration and integration of COFs as new functional materials for next-generation PSCs with better efficiency and stability.

Chapter 6

Investigation of Pyrene-based Covalent Organic Frameworks as a dopant in Perovskite Solar Cells

This chapter explores the development and application of pyrene-based COF as novel dopants for enhancing the performance of PSCs. Through the successful synthesis and integration of ILCOF-1 and SH-COF into the perovskite matrix, the study demonstrates significant improvements in crystallinity, optoelectronic properties, and overall device efficiency. The precise energy band alignment of these COFs with the perovskite layer enables efficient charge transfer, reducing recombination losses and enhancing PCE in n-i-p device architectures. The research highlights the importance of molecular design in COF-based doping strategies, as pyrene units within the COF structure facilitate continuous conjugation, which proves critical for achieving higher efficiencies compared to non-pyrene COFs. PL and TRPL studies further confirm the enhanced charge transfer dynamics, particularly in SH-COF-doped samples. Additionally, post-synthetic modification of ILCOF-1 to COF-921 reduces the optical bandgap, enhancing light absorption and further optimizing electronic properties for solar energy applications. XPS depth profiling suggests Lewis acid-base interactions between COFs and the perovskite layer, contributing to trap state passivation and improved charge carrier mobility. Overall, the findings presented in this chapter underscore the potential of pyrene-based COFs to significantly advance the efficiency and stability of PSCs, providing a pathway for future exploration in COF design and solar cell optimization.

6.1 Introduction

PSCs have emerged as a highly promising technology in the field of photovoltaics due to their remarkable PCE, ease of fabrication, and low material costs. The rapid progress in PSCs, with efficiencies exceeding 26%, has positioned them as strong contenders to traditional silicon-based solar cells, which have dominated the market for decades.[10,277] The key to this impressive performance lies in the unique properties of perovskite materials, particularly their high absorption coefficients, long carrier diffusion lengths, and tunable bandgaps.[64,278,279] However, despite these advantages, several challenges remain, particularly regarding the long-term stability and further enhancement of device efficiency. Among the strategies to address these issues, bulk doping additives have gained significant attention.[280–282] Bulk doping, the intentional introduction of specific dopants into the perovskite layer, plays a critical role in tailoring the electrical and optical properties of perovskite materials. Doping can influence the charge carrier dynamics, defect density, and crystallinity of the perovskite films, which are crucial factors that determine the overall performance of PSCs.[282,283] The choice of dopants and their concentrations are pivotal in modulating these properties, thereby affecting the efficiency and stability of the solar cells.

One of the major goals of bulk doping is to reduce the defect density within the perovskite crystal structure. Defects, such as vacancies, interstitials, and grain boundaries, can act as non-radiative recombination centers, severely limiting the device efficiency.[284] By incorporating suitable dopants, it is possible to passivate these defects, leading to improved charge carrier lifetimes and reduced recombination losses.[285] For instance, the introduction of alkali metals such as lithium (Li), sodium (Na), potassium (K), rubidium (Rb), and cesium (Cs) into the perovskite matrix has been shown to effectively improve the morphology of perovskite films, suppress ion migration, reduce non-radiative recombination, and passivate bulk and interface defects and thereby increase the PCE of PSCs.[286–289]

One of the most prominent objectives of bulk doping is bandgap engineering, which is crucial for optimizing light absorption and energy conversion. By doping with elements that introduce shallow energy levels within the bandgap, it is possible to enhance the V_{oc} of the solar cells, which directly correlates with the device efficiency.[290–292] For example, the incorporation of halide ions such as Cl^- and Br^- into the perovskite structure has been reported to widen the bandgap of the perovskite material, leading to higher V_{oc} and improved PCE in PSCs.[293–295] Additionally, metal cations like lead (Pb) and tin (Sn) can be partially substituted with other metals to fine-tune the bandgap and improve the light absorption properties of the perovskite layer.[296,297] In conclusion, bulk doping additives play a crucial role in advancing the performance and stability of PSCs. By carefully selecting and optimizing dopants, researchers can address critical issues related to defect passivation and bandgap engineering.

In this chapter, a preliminary investigation into the doping of perovskite using pyrene-based COFs, specifically ILCOF-1 and SH-COF, is presented. Both COFs are characterized by highly conjugated structures linked via imine groups (-C=N), which contribute to their electronic properties. SH-COF, in particular, is functionalized with an electron-donating thiol (-SH) group, introducing an intramolecular donor-acceptor push-pull effect. This effect is anticipated to reduce the bandgap and facilitate charge transfer within the material. Additionally, the Lewis base characteristics of the SH group are expected to enable the formation of Lewis acid-base adducts with Pb^{2+} trap defects, potentially passivating these defects in the perovskite layer. Through a comprehensive analysis of the structural, optical, and electronic properties, the suitability of both COFs for integration with $FAPbI_3$ perovskite will be assessed. Furthermore, the performance of the resulting devices will be evaluated, with a particular focus on the role of these COFs in enhancing the power conversion efficiency (PCE) of the solar cells.

6.2 Synthesis of Pyrene-based COFs (ILCOF-1 and SH-COF)

Two imine-linked COFs, ILCOF-1 and SH-COF, which are based on a pyrene core were synthesized using solvothermal method. As shown in **Figure 6.1**, For ILCOF-1, the condensation reaction is between TFPPy and p-phenylenediamine (PDA), while for SH-COF, it is between TFPPy and 2,5-diaminobenzene-1,4-dithiol dihydrochloride (DBD). The reaction is carried out in a solvent mixture of n-butanol and dichlorobenzene (1:1 v/v), with aqueous acetic acid acting as a catalyst. This mixture is heated to 120 °C and maintained at this temperature for three days. The obtained powder has a yield of 83% for ILCOF-1 and 87% for SH-COF, respectively. After the reaction, the resultant powders are subjected to a purification process. This involves filtering the powders and washing them sequentially with acetone, methanol, and dioxane. To further purify the COFs and remove any trapped guest molecules, such as solvents and unreacted monomers, Soxhlet extraction was employed. This continuous washing technique ensures that the pores of the COFs are free from any impurities. Finally, the purified COFs are activated by applying a vacuum at room temperature for 12 hours. This step ensures that any remaining volatile substances are removed, leaving behind a clean and active material ready for further characterization and application.

6.2.1 Structure Confirmation

The strutcure of ILCOF-1 was confirmed using FTIR spectra, showing noticeable reduction of the –CHO stretching band at ~1699 cm^{-1} from TFFPy monomer and the appearance of the characteristic C=N bond stretching vibration bands at around 1621 cm^{-1} (**Figure 6.2a**) The solid-state NMR results provide insightful details about the chemical environment within the COFs (**Figure 6.2b**). The chemical shift observed around 150 ppm in ILCOF-1 and SH-COF is attributed to the carbon atoms in imine groups (–C=N), indicating the presence of these groups within the structure. Similarly, the shift near 170 ppm corresponds to carbon atoms functionalized with thiol groups (C-SH) in SH-COF. Additionally, the peaks detected between 115 and 145 ppm are associated with the aromatic structures of the COFs, reflecting the characteristic resonance of aromatic carbons due to their delocalized π-electrons. Importantly, the absence of signals at approximately 185 ppm, which would correspond to the carbonyl (CHO) groups on TFPPy subunits from the starting monomers, confirms the successful and quantitative formation of the COF structures. This absence indicates that the starting monomers have been fully converted into the desired framework, ensuring the structural integrity and successful synthesis of the COFs.

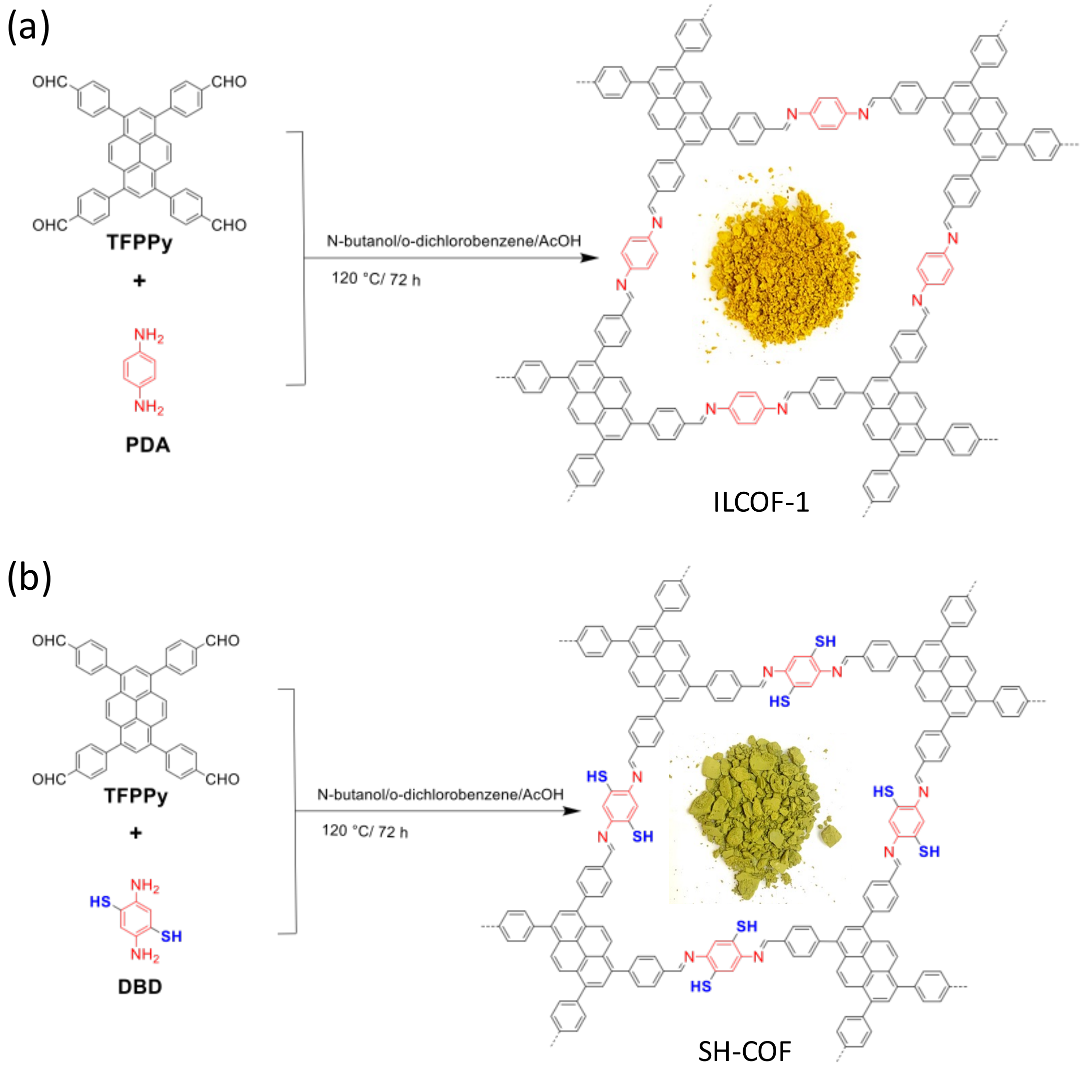

Figure 6.1 Schematic representation for the condensation reaction of ILCOF-1 and SH-COF.

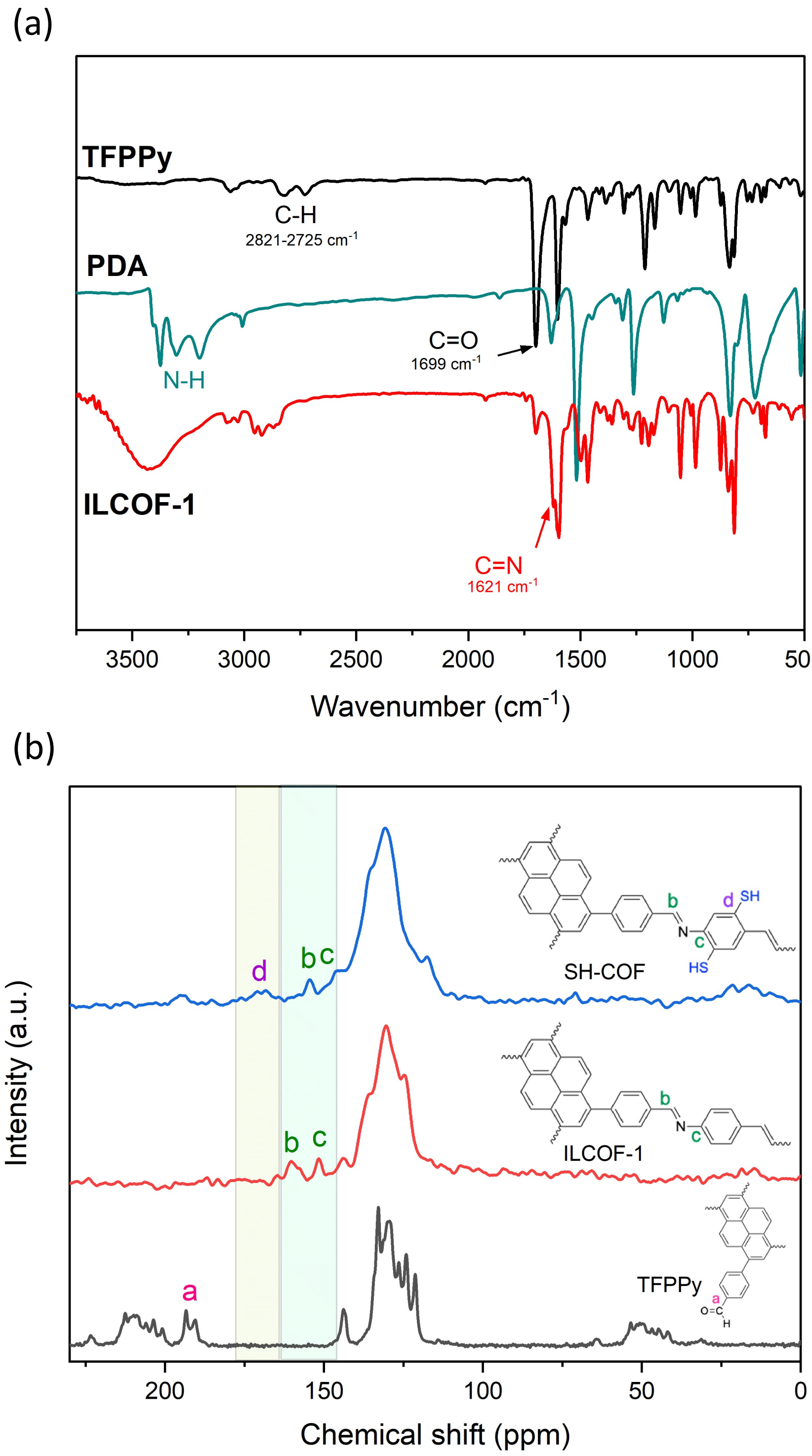

Figure 6.2 (a) FTIR spectra of ILCOF-1 and (b) Solid state NMR spectra of ILCOF-1 and SH-COF.

6.2.2 Optical Characteristics and Bandgap Analysis

To elucidate the optical properties of IL-COF and SH-COF, UV-Vis spectroscopy measurements were conducted. Maximum absorption bands were observed in the UVA and UVB regions (325-450 nm) for both COFs. Notably, stronger absorption in the visible light range (500-800 nm) was exhibited by SH-COF compared to ILCOF-1. This difference is visually evident in the sample colors: ILCOF-1, which is imine-based, appears yellow, while the thiol-functionalized SH-COF is green (**Figure 6.3a,b**). The optical bandgaps (E_g^{opt}) for ILCOF-1 and SH-COF were estimated using Tauc's plot, yielding values of approximately 2.06 eV and 1.93 eV, respectively. These values indicate a semiconducting nature of both COFs (**Figure 6.3c,d**). Notably, these E_g^{opt} values are smaller than the core building block TFPPy (2.20 eV), values for both COFs are lower than that of the core building block TFPPy (2.20 eV), suggesting enhanced electron delocalization due to the extended π-conjugation within the 2D COF layers.

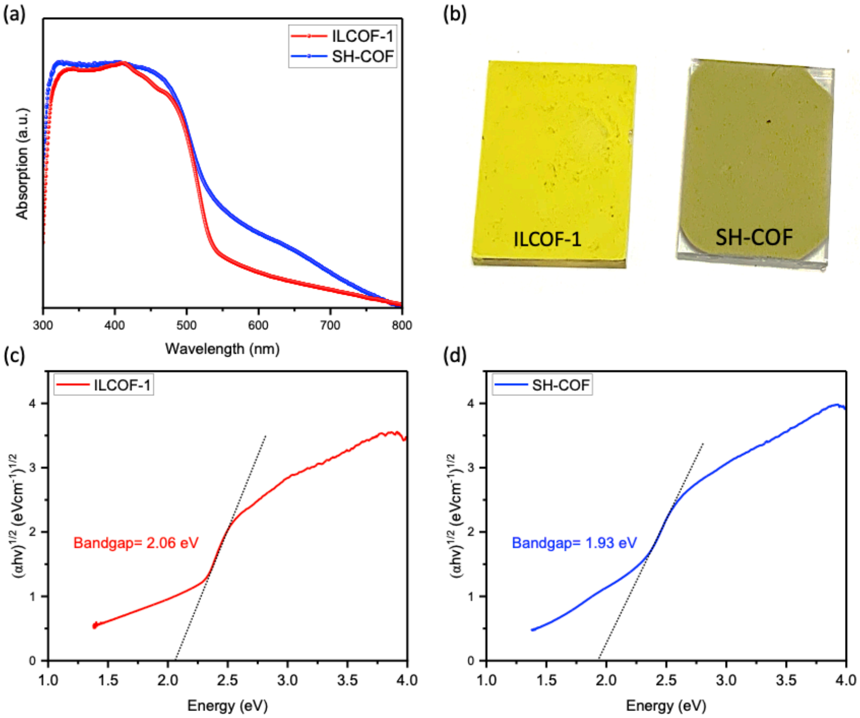

Figure 6.3 (a) UV-Vis spectra (b) photographic image and (c,d) Tauc's plots of ILCOF-1 and SH-COF.

6.2.3 Energy Band Levels

To further determine the exact positions of energy band levels of ILCOF-1 and SH-COF, UPS measurements were performed. The work function was calculated by subtracting the excitation photon energy (HeI, 21.22 eV) from the high-binding energy cut-off of ILCOF-1 (18.99 eV) and SH-COF (18.73 eV), resulting in a Fermi level of -2.23 eV and -2.49 eV, respectively, relative to vacuum. The low-energy tail of the UPS spectrum was utilized to identify the valence band maximum (E_{VBM}) for ILCOF-1 and SH-COF at 1.20 eV and 1.87 eV below the Fermi level, leading to a E_{VBM} of –3.43 eV and -4.36, respectively, versus vacuum (**Figure 6.4a, Table 6.1**). With an optical bandgap of 2.06 eV (ILCOF-1) and 1.93 eV (SH-COF), the conductance band minimum (E_{CBM}) positions were estimated to be at -3.43 eV (ILCOF-1) and -4.36 (SH-COF) relative to vacuum. This indicate that for both COFs the Fermi level lies closer to the conductance band revealing an n-type semiconductor. Moreover, these energy bands positions were found to be close to the $FAPbI_3$ perovskite band edge positions (VBM=-5.4 eV, CBM=-3.9 eV), which is an essential aspect for efficient charge transfer.[298] (refer to energy-level diagram in **Figure 6.4b**).

In an n-i-p device structure, doping perovskite with ILCOF and SH-COF can significantly enhance charge transport properties. The conduction band minimum (CBM) of both ILCOF (-1.73 eV) and SH-COF (-2.43 eV) are higher than that of perovskite (-3.9 eV), facilitating efficient electron transport from the perovskite to the COFs. Similarly, the valence band maximum (VBM) of ILCOF (-3.43 eV) and SH-COF (-4.36 eV) are higher than that of perovskite (-5.4 eV), promoting hole transport from the COFs to the perovskite. Additionally, the Fermi levels of ILCOF (-2.23 eV) and SH-COF (-2.49 eV) are closer to their respective CBMs, indicating their potential as effective electron transport layers (ETLs). This alignment of energy levels ensures that both ILCOF and SH-COF can enhance charge separation and transport, improving the overall performance of PSCs.

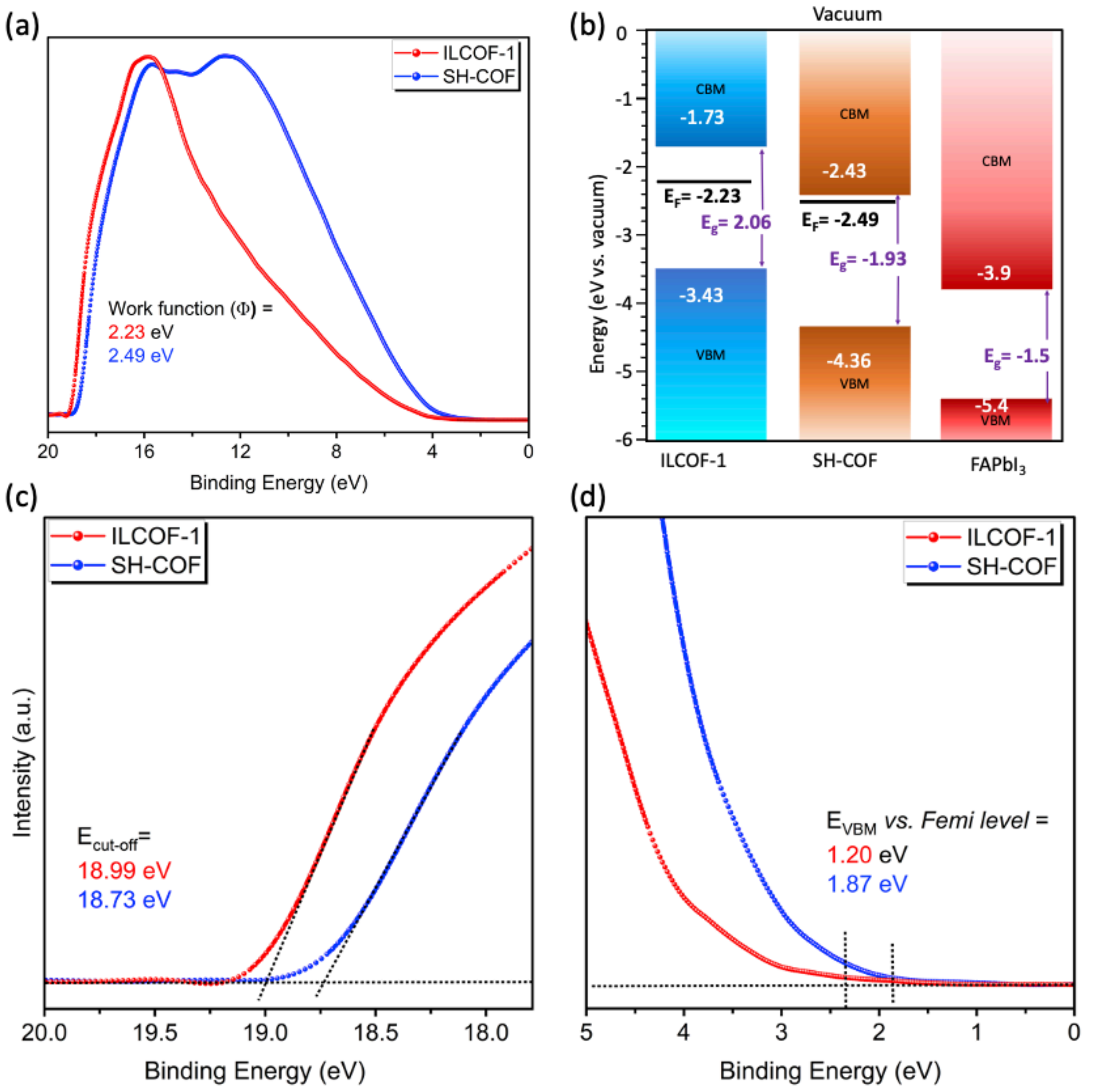

Figure 6.4 (a,c,d) UPS spectra (b) Energy band alignments of ILCOF-1 and SH-COF with $FAPbI_3$.

Table 6.1 Optoelectronic parameters of ILCOF-1 and SH-COF.

COFs	VBM vs E_F	$E_{cut\text{-}off}$	Work function	VBM	Optical bandgap	CBM
IL-COF-1	1.20	18.99	-2.23	-3.43	2.06	-1.37
SH-COF	1.87	18.73	-2.49	-4.36	1.93	-2.43

6.3 $FAPbI_3$-based (n-i-p) Devices Fabrication

To fabricate highly efficient perovskite solar cell (PSC), the conventional architectures (n-i-p), FTO/c-TiO_2/m-TiO_2/$FAPbI_3$/OIA/Li-Spiro-OMeTAD/Au was utilized. The compact (c-) and mesoporous (m-) TiO_2 electron transporting materials (ETMs) were subsequently deposited on the ITO surface using spin-coating and spray-pyrolyzed method, respectively. $FAPbI_3$ perovskite was spin-coated on the mesoporous TiO_2 with a mixed solvent solution. Chlorobenzene was dropped on the substrate to induce rapid crystallization, followed by annealing. A surface passivation layer of OAI in IPA was spin-coated, followed by the HTL. The HTL composed of 2,2″,7,7″-tetrakis[N,N-di(4-methoxyphenyl)amino]-9,9′-spirobifluorene (spiro-OMeTAD) doped with lithium bis(trifluoromethanesulfonyl)imide (LiTFSI). A 100 nm of metal electrodes (Au) were thermally evaporated on top of the device using a shadow mask (**Figure 6.5**). Devices were measured under standard conditions. Films for characterization were made on washed FTO substrates without ETL and HTL deposition.

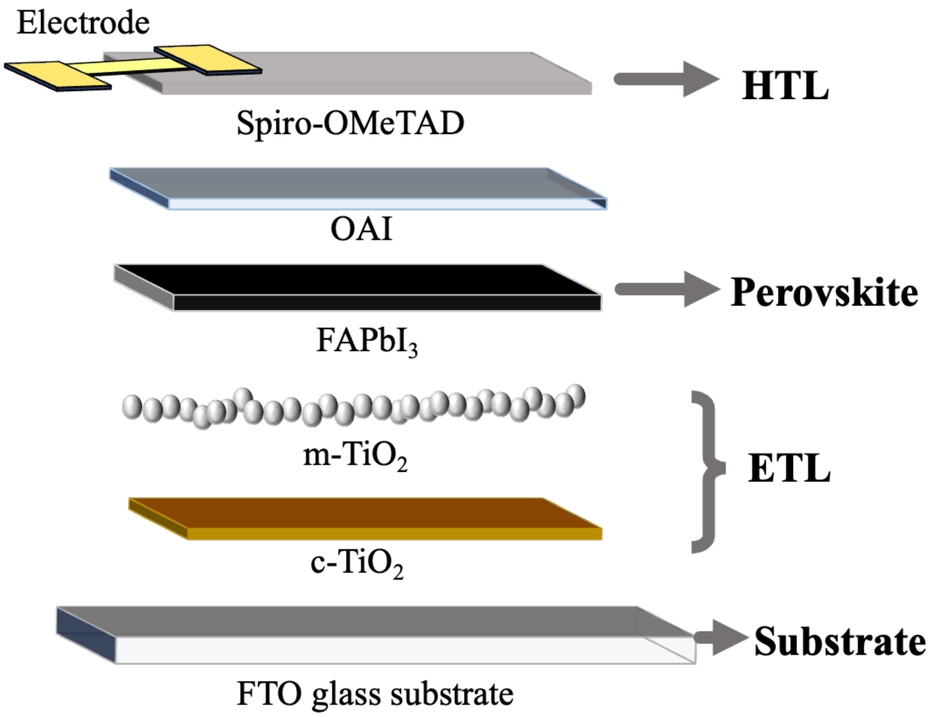

Figure 6.5 $FAPbI_3$-based n-i-p perovskite solar cell device architecture.

6.4 Bulk doping of $FAbI_3$ perovskite using sp^2c-COF

For the modified devices, a stock solution of sp^2c-COF in DMF at a concentration of 0.5 mg/mL was prepared. This solution was then sonicated for 24 hours to ensure complete dissolution and uniform dispersion of the sp^2c-COF. From this stock solution, the perovskite solution was prepared by adding varying amounts of sp^2c-COF stock solution. Specifically, amounts of 2, 4, 6, and 8 µL of the sp^2c-COF stock solution was added to 1 mL of the perovskite solution. Each mixture was stirred for two hours to ensure thorough mixing and incorporation of the sp^2c-COF into the perovskite matrix. Following this, the modified perovskite solutions were spin-coated onto the substrates to form the active layers of the devices, followed by annealing in an inert atmosphere inside a glovebox (**Figure 6.6a**). Both the control and the sp^2c-COF-modified devices were then tested under 1.5 AM simulated sunlight to measure their current density–voltage (*J–V*) characteristics.

Devices Performance: The performance of PSCs doped with sp^2c-COF at various concentrations was systematically analyzed, with results summarized in **Table 6.2 and Figure 6.6b,c**. Control devices without sp^2c-COF doping exhibited a V_{oc} of 1.08 V, J_{sc} of 23.88 mA cm^{-2}, a fill factor (FF) of 70.72%, and a power conversion efficiency (PCE) of 18.33%. Across different concentrations, the V_{oc} remained stable at 1.07-1.08 V. Doping with 2 µL of sp^2c-COF reduced the J_{sc} to 21.86 mA cm^{-2}, but significantly increased the FF to 79.0%, resulting in a slightly higher PCE of 18.49%. Increasing the sp^2c-COF concentration to 4 µL slightly improved the J_{sc} to 22.43 mA cm^{-2} and further increased the FF to 80.14%, enhancing the PCE to 19.36%. At 6 µL of sp^2c-COF, the J_{sc} slightly increased to 22.44 mA cm^{-2} and the FF improved to 80.48%, achieving the highest PCE of 19.43%. However, at the highest concentration of 8 µL, the J_{sc} slightly increased to 22.48 mA cm^{-2}, but the FF dropped to 76.89%, resulting in a reduced PCE of 18.53%. These results indicate that the optimal concentration of sp^2c-COF for enhancing PSC performance is 6 µL, where the highest PCE of 19.43% was achieved. The observed trends suggest that while sp^2c-COF doping can significantly enhance the FF and overall efficiency of PSCs, there is a threshold beyond which further increases in concentration may lead to diminishing returns or even adverse effects on device performance.

The increase in FF with sp^2c-COF doping can be attributed to enhanced charge transport properties, reduced series resistance, and better interface quality between the perovskite layer and the charge transport layers. These factors collectively facilitate smoother charge transfer and reduce recombination losses. On the other hand, the decrease in J_{sc} with sp^2c-COF doping can be explained by several factors. Firstly, sp^2c-COF might alter the optical properties of the perovskite layer, absorbing some of the incident light and reducing the generation of electron-hole pairs. Secondly, higher concentrations of sp^2c-COF might introduce additional recombination centers or defects, trapping charge carriers and reducing the number of free carriers available for current generation. Lastly, the addition of sp^2c-COF could cause changes in the morphology of the perovskite layer, potentially hindering the efficient generation and collection of charge carriers. Balancing these effects is crucial, and the optimal concentration of 6 μL of sp^2c-COF appears to maximize the positive impacts on FF while minimizing the negative effects on J_{sc}, resulting in the highest PCE.

The statics of the devices of 47 devices of the control and sp^2c-COF modified devices has showed an increased in the median PCE upon increasing the concentrations of sp^2c-COF, reaching 17.3% and 17.6% after doping of 4 μL and 6 μl compared to median of 15.3% for the control devices (**Figure 6.7** and **Table 6.2**). Similar trend has been observed in V_{oc}. However, the fill factor of the control (68.5%) has systematically increased from upon increasing the concentrations reaching a peak of 74.8 % at 4 μL and 6 μL.

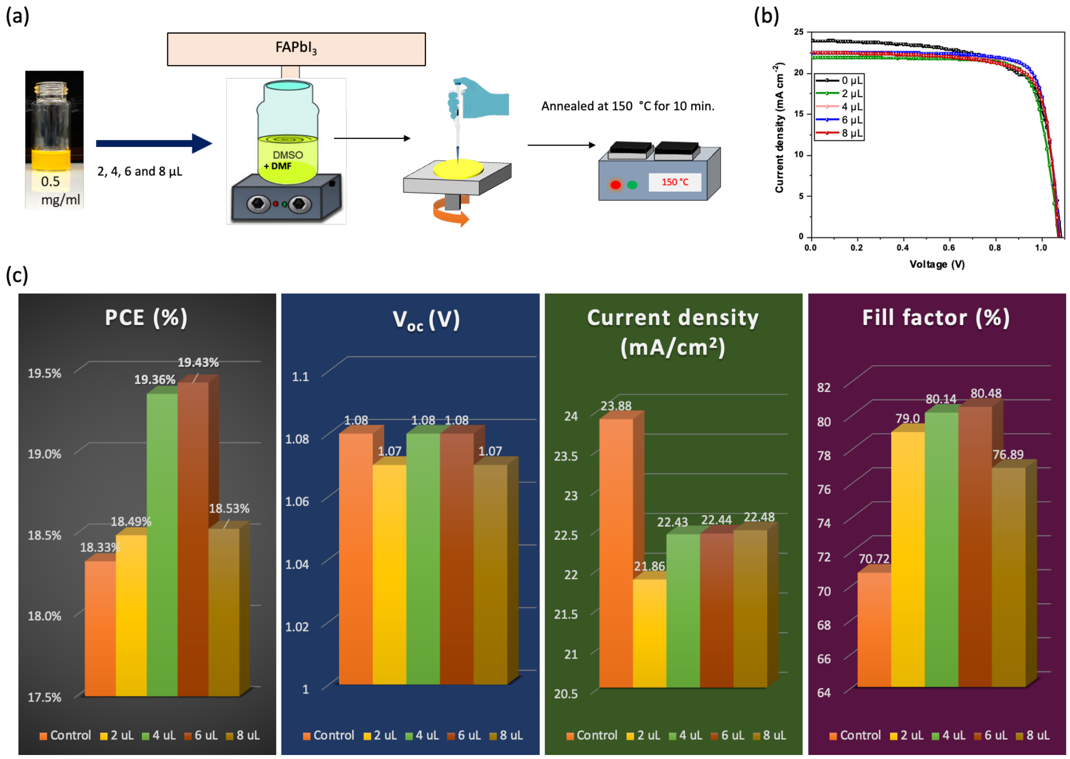

Figure 6.6 (a) Schematic representation of the bulk doping procedures of sp^{2}c-COF in FAPbI$_3$ perovskite. (b) I-V curve and (c) photovoltaics parameters for control devices and sp^{2}c-COF doped devices at various concentrations.

Table 6.2 Devices performance parameters of the control and sp^{2}c-COF modified devices at various concentrations.

Devices	Value	V_{oc} (V)	J_{sc} (mA cm^{-1})	Fill Factor (%)	PCE (%)
Control	Champion	1.08	23.88	70.72	18.33
	Median	1.05	23.12	67.94	15.35
sp^{2}c-COF (2 μL)	Champion	1.07	21.86	79.0	18.49
	Median	1.03	21.30	69.76	14.94
sp^{2}c-COF (4 μL)	Champion	1.08	22.43	80.14	19.36
	Median	1.04	21.54	74.59	17.18
sp^{2}c-COF (6 μL)	Champion	1.08	22.44	80.48	19.43
	Median	1.06	21.41	74.53	17.58
sp^{2}c-COF (8 μL)	Champion	1.07	22.48	76.89	18.53
	Median	1.05	21.36	73.07	16.31

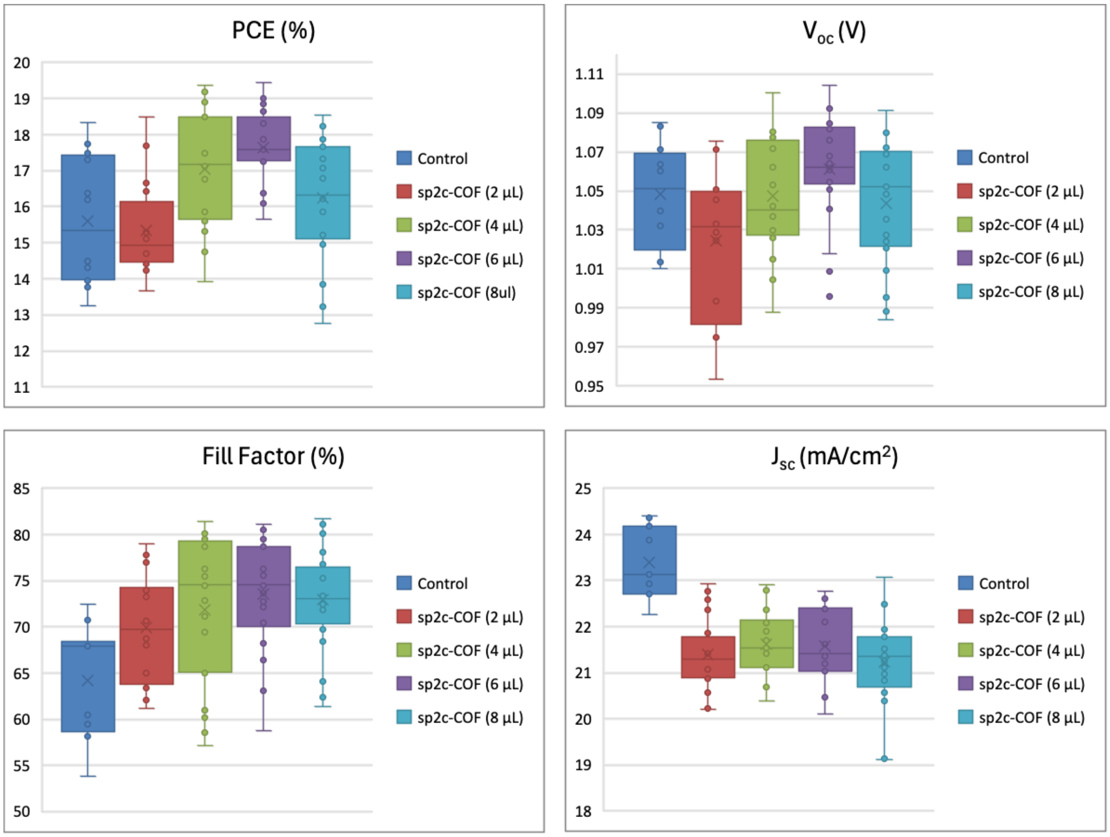

Figure 6.7 The statistical distribution photovolatics paramaters; PCE, V_{oc}, J_{sc}, and FF for the control and sp^{2}c-COF doped devices at various concentrations.

6.5 Bulk doping of FAbI$_3$ Perovskite using Pyrene-based COFs

To compare the effect of pyrene-based COFs on PSCs, two other COFs were selected as model systems that do not incorporate pyrene. The first model COF, COF-5, was based on the HHTP unit, which is structurally similar to TFPPy but lacks continuous conjugation. This structural difference could influence its electronic properties and interaction with the perovskite layer. The absence of continuous conjugation in COF-5 might result in different charge transport characteristics compared to pyrene-based COFs. The second model COF, TFP-DBD, was chosen as an analogue to SH-COF without the pyrene unit. This selection allows the isolation of the effect of the pyrene moiety on the overall performance of the COF in the solar cell. By comparing TFP-DBD with SH-COF, the impact of the presence or absence of pyrene on the optical and electronic properties of the COF and its interaction with the perovskite layer can be better understood.

Both COFs were synthesized following the detailed procedures (**Figure 6.8a,c** and refer to synthetic methods in **Chapter 3**). The successful synthesis of these COFs was confirmed using FTIR spectroscopy, as shown in **Figure 6.8b,d**. The FTIR spectra provided clear evidence of the expected functional groups, confirming the formation of the desired COF structures. COF-5 showed a characteristic peak at 1346 cm^{-1} assigned to B-O bonds formation, TFP-DBD COF showed broad peak centred at 1580 cm-^{1} and with an edge at 1612 cm^{-1} is assigned to the C=C and C=N bonds, respectively. By comparing these model COFs with the pyrene-based COFs (**Figure 6.9**), the specific contributions of the pyrene units to the performance of PSCs are aimed to be elucidated, thereby advancing the understanding of how different COF structures can be optimized for improved device performance.

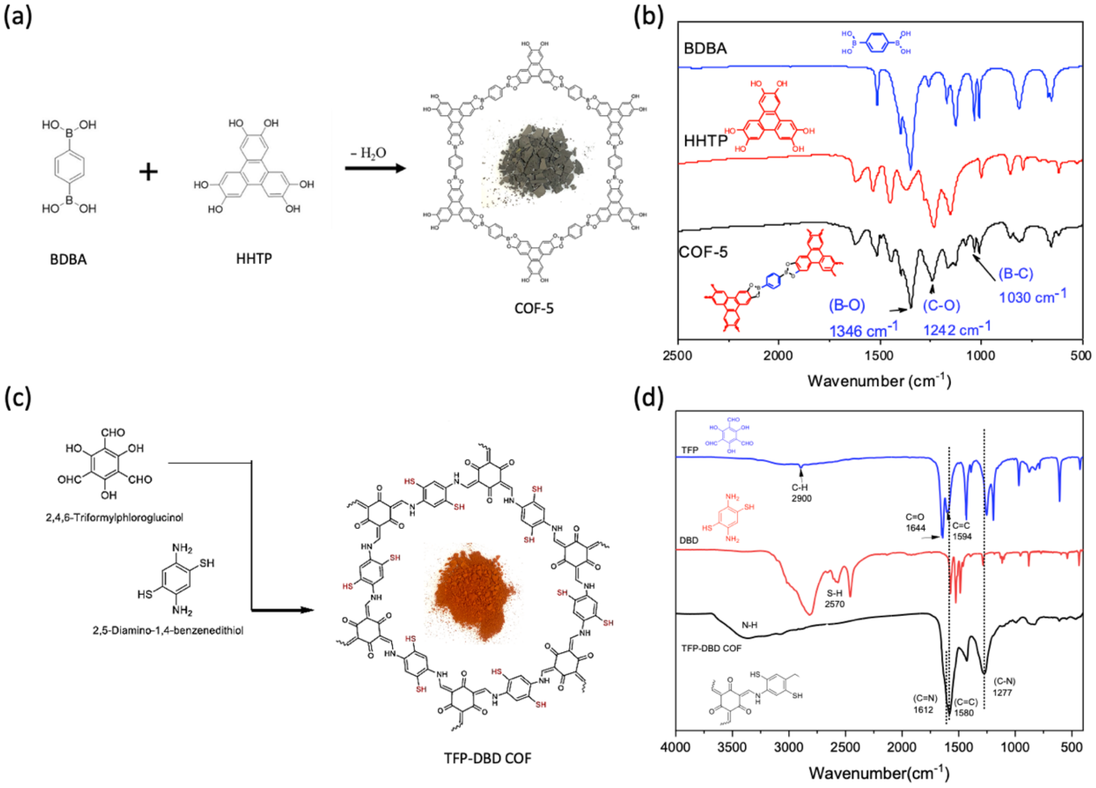

Figure 6.8 Schematic representation of the synthetic route and the FTIR spectra of (a,b) COF-5 and (c,d) TFP-DBD COF.

Figure 6.9 Photographic image of the pyrene-based COFs (sp^{2}c-COF, ILCOF-1 and SH-COF) and model COFs (COF-5 and TFP-DBD COF) as powder and suspended in DMF.

Devices Performance: The performance metrics of the champion PSCs devices, both undoped (control) and doped with various COFs, are summarized in the **Table 6.3**. The parameters evaluated include V_{oc}, J_{sc}, FF, and PCE. The control sample, without any COF doping, exhibited a V_{oc} of 1.08 V, a J_{sc} of 23.88 mA/cm^2, a FF of 70.72%, and a PCE of 18.33%. These values serve as the baseline for comparison with the doped devices. The ILCOF-1 doped sample showed a slight decrease in V_{oc} to 1.04 V and J_{sc} to 22.87 mA/cm^2. However, the FF significantly improved to 81.56%, resulting in an increased PCE of 19.48%. This indicates that ILCOF-1 doping enhances the overall efficiency of the solar cell despite the minor reductions in V_{oc} and J_{sc}. Similarly, the SH-COF doped sample exhibited a V_{oc} of 1.05 V and a J_{sc} of 22.63 mA cm^{-2}. The FF was the highest among all samples at 81.90%, leading to a PCE of 19.49%. The high FF suggests that SH-COF doping effectively improves the charge transport and reduces recombination losses.

In contrast, the COF-5 doped sample had the lowest Voc at 0.95 V but maintained a relatively high Jsc of 23.45 mA/cm^2. The FF was 74.80%, resulting in a PCE of 16.60%.

The lower Voc and FF indicate that COF-5 doping may introduce defects or increase recombination, negatively impacting the overall efficiency. The limited charge transport in COF-5 can be attributed to its lack of conjugation and poor stability. Previous studies have shown that COF-5 possesses an indirect bandgap of 3.6 eV and a direct bandgap of 3.9 eV, as determined by DFT calculations.[299] These values are close to the insulator bandgap (> 4 eV), significantly restricting its charge transport capabilities.[300] Similarly, the TPT-DBD COF doped sample showed a V_{oc} of 1.04 V and a J_{sc} of 22.95 mA/cm². However, the FF was the lowest among all samples at 66.45%, leading to the lowest PCE of 15.83%. The reduced FF suggests that TPT-DBD COF doping may adversely affect the charge transport properties. In conclusion, doping PSCs with ILCOF-1 and SH-COF significantly improves their power conversion efficiency, primarily due to the enhanced fill factor. In contrast, COF-5 and TPT-DBD COF doping result in lower efficiencies, likely due to increased recombination losses and defects. These findings highlight the potential of pyrene-based COFs to enhance the performance of PSCs and guide future research in optimizing COF materials for solar cell applications.

Table 6.3 Devices performance parameters of the champion devices of ILCOF-1, SH-COF, COF-5 and TPT-DBD COF.

Devices	V_{oc} (V)	J_{sc} (mA cm^{-1})	Fill Factor (%)	PCE (%)
Control	1.08	23.88	70.72	18.33
ILCOF-1	1.04	22.87	81.56	19.48
SH-COF	1.05	22.63	81.90	19.49
COF-5	0.95	23.45	74.80	16.60
TPT-DBD COF	1.04	22.95	66.45	15.83

The statistical analysis of 50 devices of the control and devices modified with different COFs, including ILCOF-1, SH-COF, COF-5, and TPT-DBD COF is shown in **Figure 6.10** and **Table 6.4.** For the control devices, the median values demonstrate solid performance with a V_{oc} of 1.04 V, a J_{sc} of 23.03 mA cm^{-2}, an FF of 64.21%, and a PCE of 14.49%. The ILCOF-1-modified devices show only minimal changes from the control devices, with a slight reduction in J_{sc} to 22.37 mA cm^{-2}. However, the fill factor improves to 68.68%, resulting in a median PCE that remains nearly unchanged at 14.41%. This suggests that the ILCOF-1 modification has a modest impact on median performance. In contrast, SH-COF-modified devices exhibit substantial improvements in performance. While the V_{oc} and J_{sc} are slightly reduced compared to the control devices, the fill factor increases significantly to 77.04%, resulting in a higher PCE of 15.84%. This indicates that SH-COF consistently enhances device performance, particularly through better charge transport.

On the other hand, the COF-5 modification caused a substantial decrease in performance, with the median V_{oc} dropping to 0.88 V and the FF falling to 50.69%. Consequently, the PCE declines to 9.72%, making COF-5 the least effective modification among the group. Finally, the TPT-DBD COF modification results in moderate changes, with a V_{oc} of 0.93 V, a J_{sc} of 22.50 mA cm^{-2}, and a fill factor of 59.56%. These values lead to a PCE of 12.18%, indicating that TPT-DBD COF has a noticeable but less impactful effect on device performance compared to SH-COF. In summary, the median values indicate that SH-COF is the most effective in enhancing device performance, while COF-5 has a detrimental impact. ILCOF-1 and TPT-DBD COF show moderate effects, with slight variations in performance compared to the control devices.

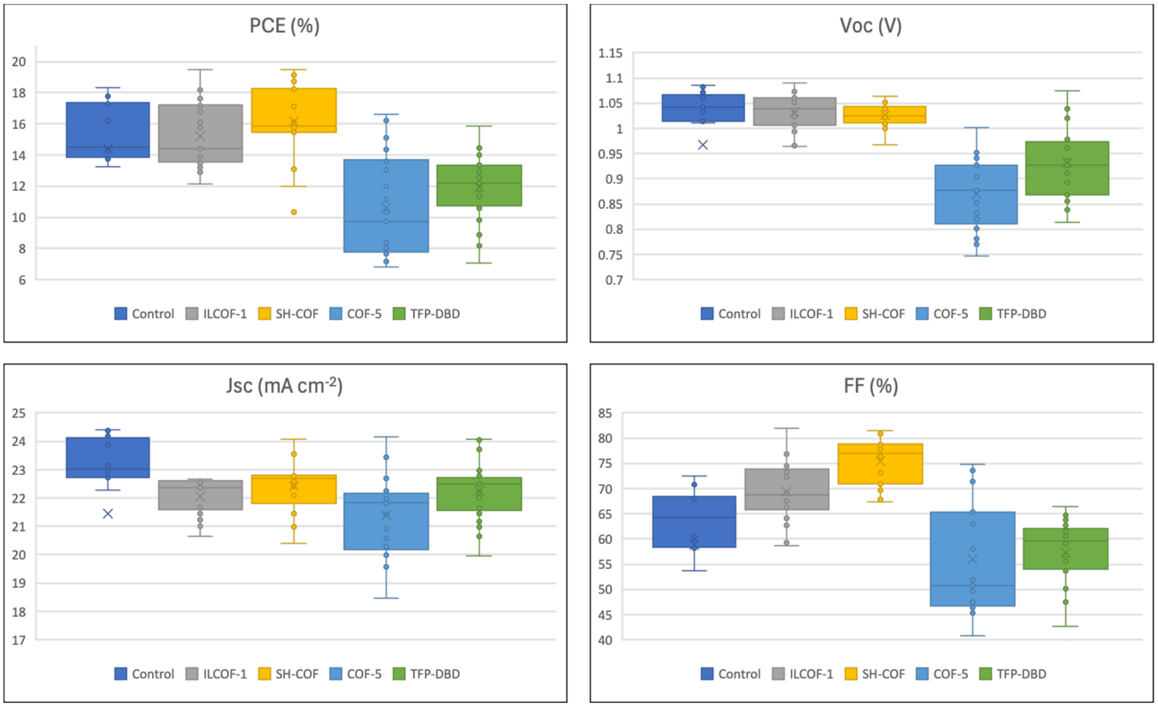

Figure 6.10 The statistical distribution photovoltaics parameters; PCE, V_{oc}, J_{sc}, and FF for the control and pyrene-based COFs, and model COFs doped devices.

Table 6.4 The median values for performance parameters for control devices and devices modified with ILCOF-1, SH-COF, COF-5, and TPT-DBD COF.

Devices	**V_{oc} (V)**	**J_{sc} (mA cm^{-1})**	**Fill Factor (%)**	**PCE (%)**
Control	1.04	23.03	64.21	14.49
ILCOF-1	1.04	22.37	68.68	14.41
SH-COF	1.03	22.70	77.04	15.84
COF-5	0.88	21.84	50.69	9.72
TPT-DBD COF	0.93	22.50	59.56	12.18

6.6 Role of Pyrene-Based COFs (ILCOF-1 and SH-COF) on Perovskite Films

6.6.1 Crystallinity

The improved crystallinity of the perovskite film upon the introduction of bulk doping using pyrene-based COFs was thoroughly investigated using XRD analysis (**Figure 6.11**). The pristine and the ILCOF-1 and SH-COF modified perovskite films exhibited similar XRD peak positions that corresponded to the primary perovskite phase, indicating that the fundamental crystalline structure remained unchanged. Specifically, the intensity of the localized (100) diffraction peak at 13.94° was not significantly altered by the incorporation of SH-COF, thereby preserving the crystalline integrity of the perovskite. In contrast, the ILCOF-1 modified perovskite films demonstrated a notable increase in the intensity of the (100) peak, suggesting an enhancement in crystallinity due to the introduction of ILCOF-1. Additionally, the analysis revealed that both the control and modified films showed no significant presence of unreacted PbI_2, as indicated by the absence of a prominent signal at 12.62°. This observation confirms that the doping process did not lead to incomplete reactions or residual lead iodide in the films.

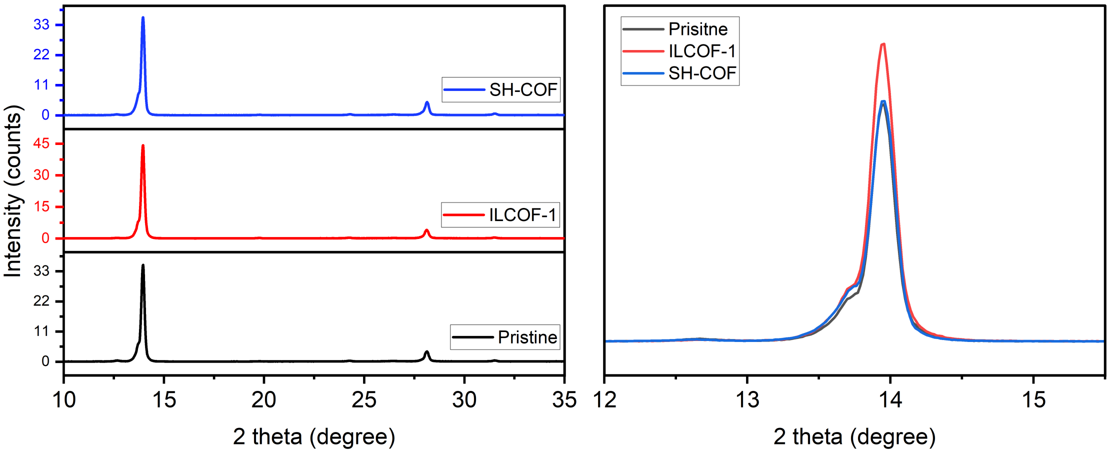

Figure 6.11 The XRD pattern of the pristine, IL-COF-1 and SH-COF modified perovskite films.

6.6.2 Charge Transport and Carrier Dynamics

To elucidate the effects of pyrene-based COFs (ILCOF-1 and SH-COF) on carrier dynamics, PL and TRPL measurements were performed to investigate the charge transfer dynamics between the perovskite and COFs. Upon doping perovskite with pyrene-based COFs (ILCOF-1 and SH-COF), a noticeable PL quenching effect was recorded, revealing an enhanced charge transfer process from perovskite to COFs. The quenching effect was notably stronger in perovskite doped with SH-COF, suggesting a more efficient charge transfer (**Figure 6.12a**). These findings imply that both COFs can passivate trap defects in perovskite and provide pathways for charge transfer.

To validate this hypothesis, TRPL measurements were conducted by monitoring the peak emission at 795 nm. Using bi-exponential decay function to fit the data, reveals two distinct carrier lifetimes (**Figure 6.12b-e**). This analysis indicates that PL decay in perovskite occurs via two relaxation pathways: fast and slow decay processes.[301–303] The fast decay component (τ_1) is characterized by a rapid drop in intensity shortly after excitation, typically associated with non-radiative recombination processes such as surface or trap-assisted recombination. The slow decay component (τ_2) follows the fast decay and represents a more gradual decrease in intensity, usually associated with radiative recombination where charge carriers recombine to emit photons (**Table 6.5**).

The control sample exhibited the longest average decay time (9.87 ns), indicating slower overall recombination. The fast decay component (0.162 ns) was relatively short, while the slow decay component (28.461 ns) was quite long, suggesting a significant contribution from radiative recombination. The ILCOF-1 modified sample showed a shorter average decay time (8.46 ns), indicating faster recombination compared to the control. The fast decay component (0.190 ns) was slightly longer than the control, and the slow decay component (21.174 ns) was shorter, suggesting reduced non-radiative recombination and faster radiative recombination. The SH-COF modified sample had the shortest average decay time (7.42 ns), indicating the fastest recombination. The fast decay component (0.213 ns) was the longest among the three samples, and the slow decay component (20.050

ns) was also shorter than the control, indicating efficient charge transfer and reduced non-radiative recombination. Overall, the data suggest that both ILCOF-1 and SH-COF modifications enhance charge transfer efficiency, leading to faster radiative recombination times and slower non-radiative recombination compared to the pristine perovskite sample. Furthermore, the pristine and COFs-modified samples showed similar steady-state UV-vis absorption profiles (**Figure 6.12f**), except for the slight increment in the absorption near the UV region for the modified samples, which is likely due to the ability of sp^{2}c-COF to act as an UV absorber.

Table 6.5 Fitting parameters of the decay amplitude and decay time calculated from TRPL spectra.

	τ_{avg} (ns)	τ_1 (ns)	τ_2 (ns)	A1	A2
Control	9.87	0.162	28.461	0.442	0.231
ILCOF-1	8.46	0.190	21.174	0.346	0.225
SH-COF	7.42	0.213	20.050	0.373	0.213

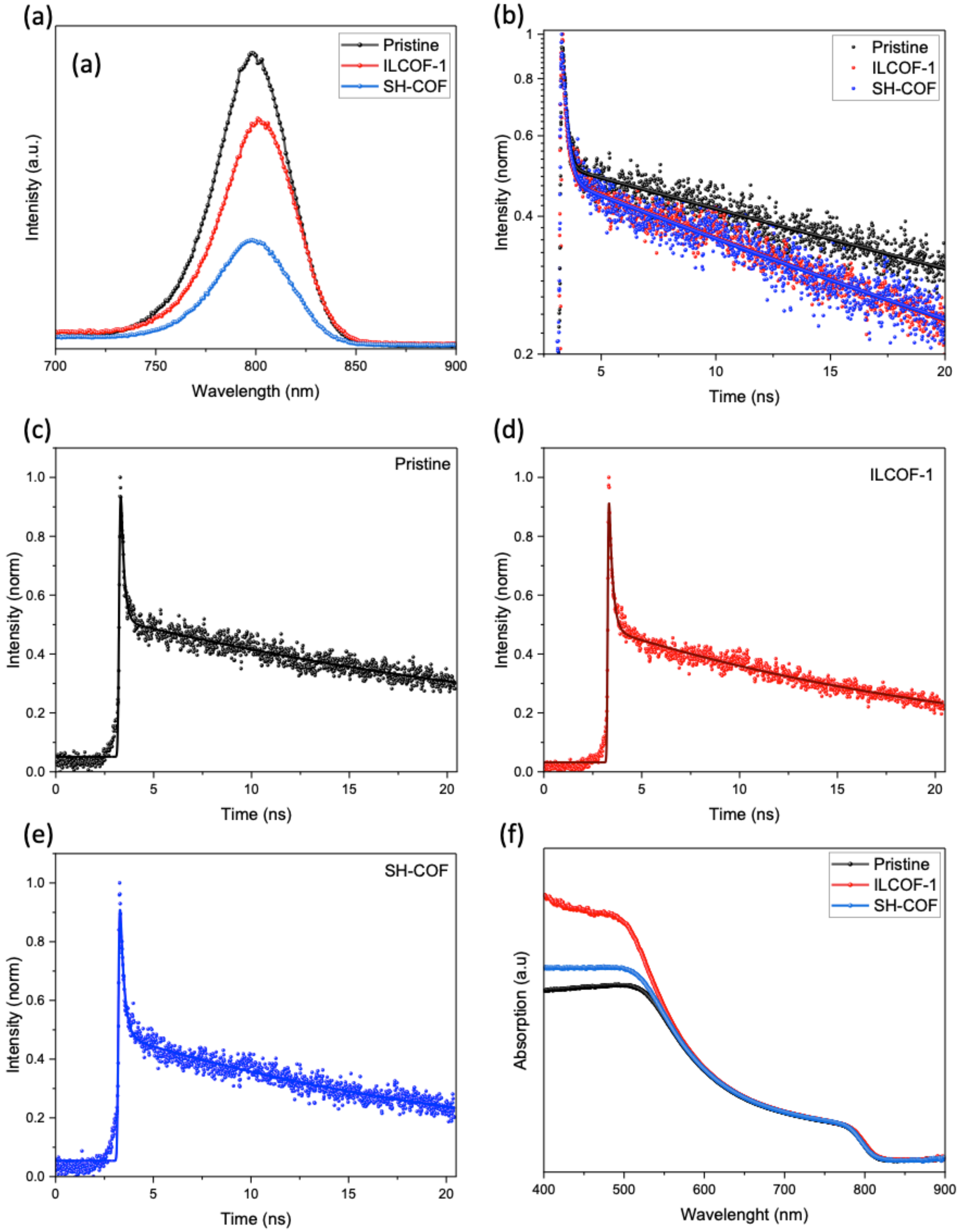

Figure 6.12 **(a)** PL spectra and (**c-e**) TRPL spectra and (**f**) UV-vis spectra of unmodified perovskite film and perovskite treated with ILCOF-1 and SH-COF.

6.6.3 Interaction of Pyrene-COFs with Pb^{2+} on Perovskite

To gain insight into underlying interactions between the ILCOF-1 and SH-COF and the perovskite layers, depth profiling XPS were used to examine the binding energy (BE) peaks of Pb and I species in perovskite layer. The XPS results revealed a distinct shift of approximately 0.10 eV and 0.20 eV towards higher BE positions in the Pb 4f spectra when treated with the ILCOF-1 and SH-COF, respectively (**Figure 6.13a**). This shift indicates an interplay between the electron donating imine (=N-) and thiol (-SH) groups in the respective COFs and the Pb^{2+} ions of the perovskite via Lewis acid-base interaction. Notably, a similar shift in BE was observed in corresponding I 3d signal, suggesting the decrease in the electron-withdrawing capability of Pb atoms (**Figure 6.13b**).[166] This interaction between Pyrene-COFs (ILCOF and SH-COF) and the perovskite plays a crucial role in passivating the trap states in perovskite which can help improve the performance of PSCs.

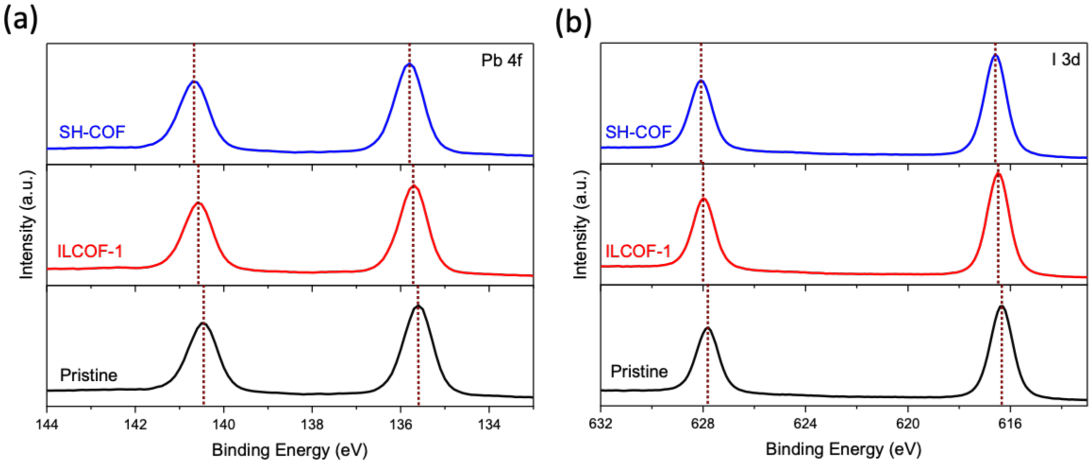

Figure 6.13 XPS of (a) Pb 4f and (b) I 3d for pristine, ILCOF-1 and SH-COF modified perovskite, respectively.

6.7 Direct Bandgap Tuning of Pyrene-COFs as a candidate for PSCs

The rational design behind bandgap tuning in ILCOF-1 through post-synthetic modification to convert it into COF-921 leverages the introduction of new electronic environments via linker substitution and oxidative cyclization. ILCOF-1, which contains imine linkages, has a relatively large bandgap (2.06 eV) due to the limited electron delocalization and the nature of the imine bond. By replacing the imine linkages with thiazole linkages during the conversion to COF-921, electron-rich azole groups are introduced into the framework. These thiazole groups have higher degrees of π-electron delocalization compared to the imine bonds, which leads to a reduction in the bandgap. This design strategy takes advantage of the electron-donating properties of the thiazole groups, effectively narrowing the bandgap and enhancing the electronic conductivity of the material. Additionally, the post-synthetic approach allows for precise control over the framework's crystallinity and structure, preserving its porous nature while optimizing its electronic properties for potential applications in optoelectronics and semiconductors. Thus, this rational modification offers a methodical way to fine-tune the bandgap of the material by tailoring the electronic characteristics of the linkers while maintaining structural integrity and stability.

6.7.1 Post-synthetic Approach

The post-synthetic method for converting ILCOF-1 to COF-921 involves a two-step process: linker substitution and oxidative cyclization. The imine-linked ILCOF-1is first treated with a functionalized linker, specifically 2,5-diaminobenzene-1,4-dithiol dihydrochloride, to replace the original imine linkages. The presence of water during this process enhances the rate of imine hydrolysis and improves the linker exchange efficiency. After the substitution, the framework undergoes oxidative cyclization under an oxygen atmosphere, transforming the imine bonds into benzothiazole (for COF-921) linkages (**Figure 6.14**).[154]

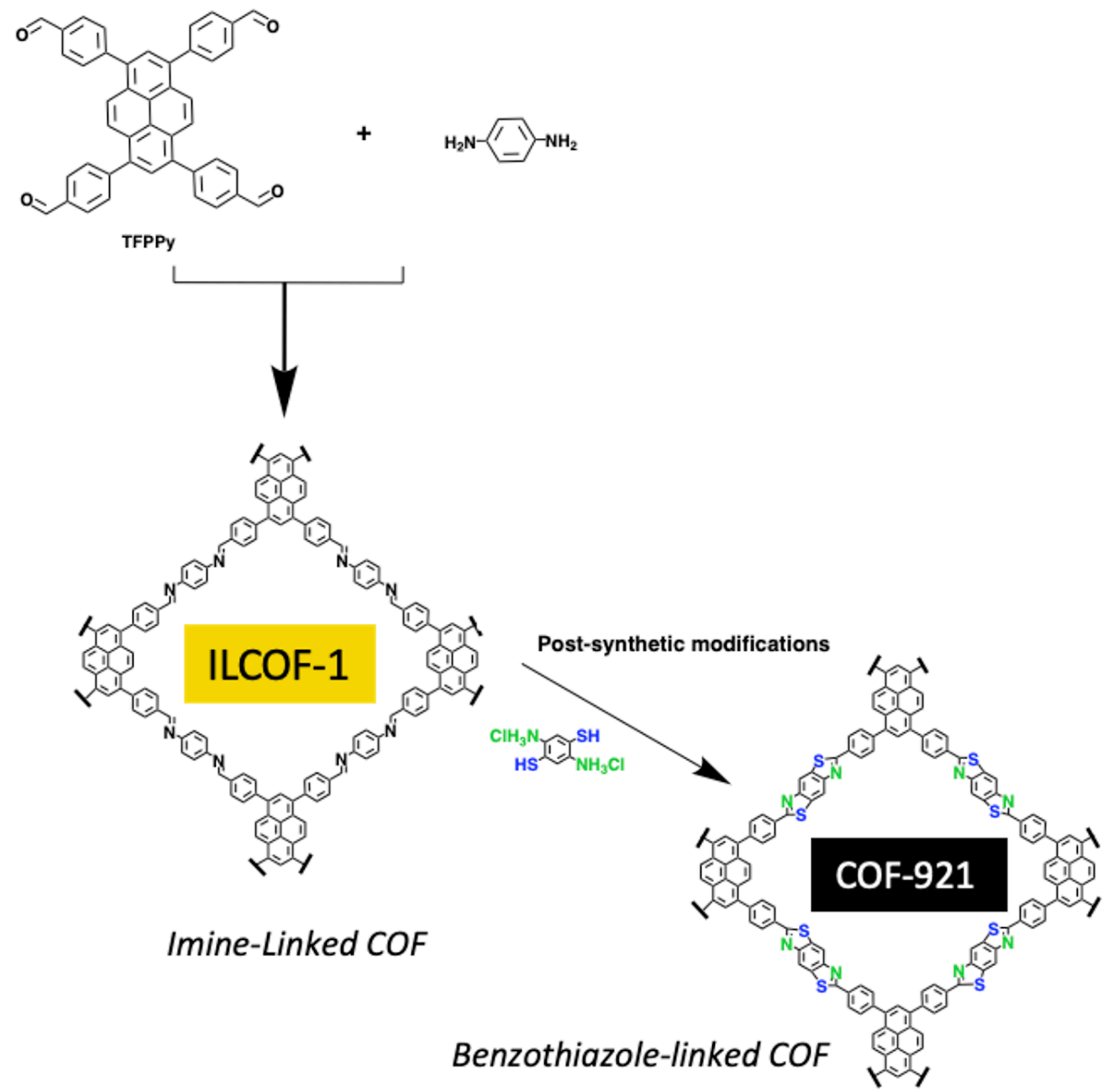

Figure 6.14 Schematic representation of the post-modification reaction of ILCOF-1 to yield COF-921.

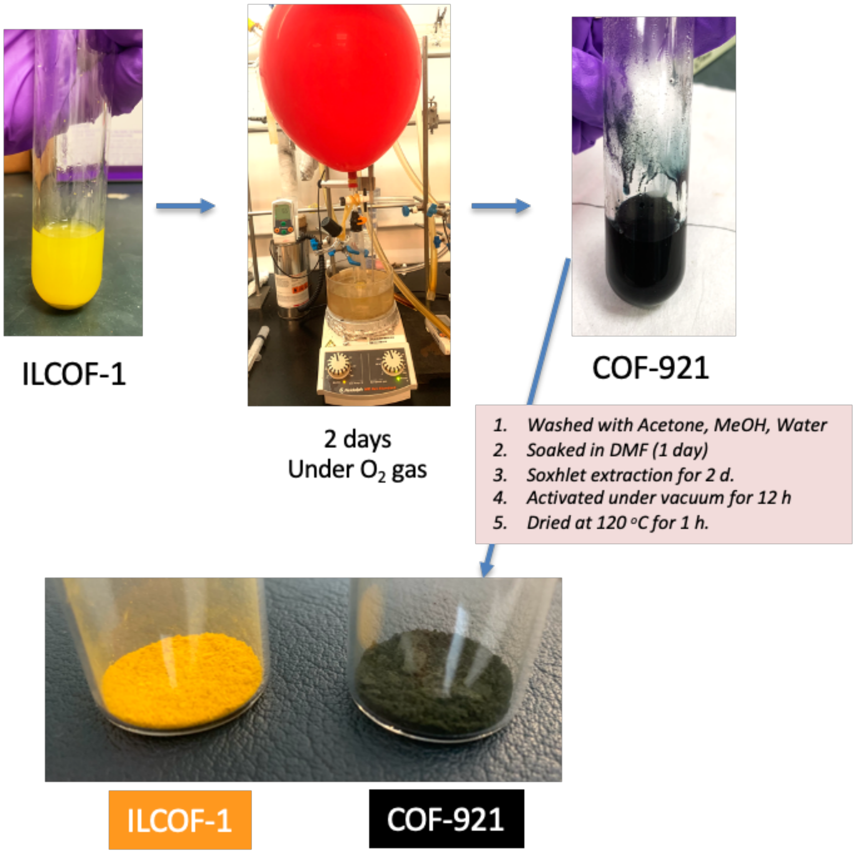

Figure 6.15 Photographic images of the post-modification reaction of ILCOF-1 to yield COF-921.

The conversion of ILCOF-1 to COF-921 was observed in changing the colour of ILCOF-1 from yellow to greenish black (COF-921) as shown in **Figure 6.15**. Moreover, the conversion was proven through NMR and FTIR spectroscopy by observing changes in the chemical environment associated with the linkages. FTIR showed attenuation of the characteristic imine stretch absorption band at 1605 cm^{-1}. This attenuation is consistent with the imine linkages having been replaced by thiazole linkages (**Figure 6.16**). The solid-state ^{13}C NMR spectra of ILCOF-1 showed prominent peak is observed at 160 ppm, which corresponds to the carbon atom in the imine linkage. After the conversion, this peak is significantly attenuated in COF-921, indicating the loss of the imine bond. For COF-921, a new resonance appears at 167 ppm, which is attributed to the carbon of the benzothiazole ring (**Figure 6.17**).

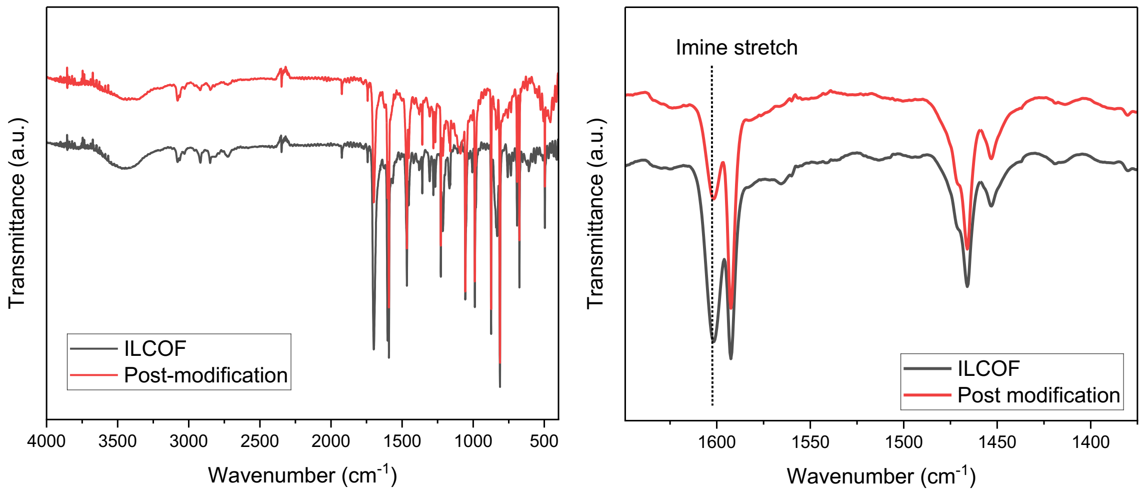

Figure 6.16 FTIR spectra of ILCOF-1 before and after modification (COF-921).

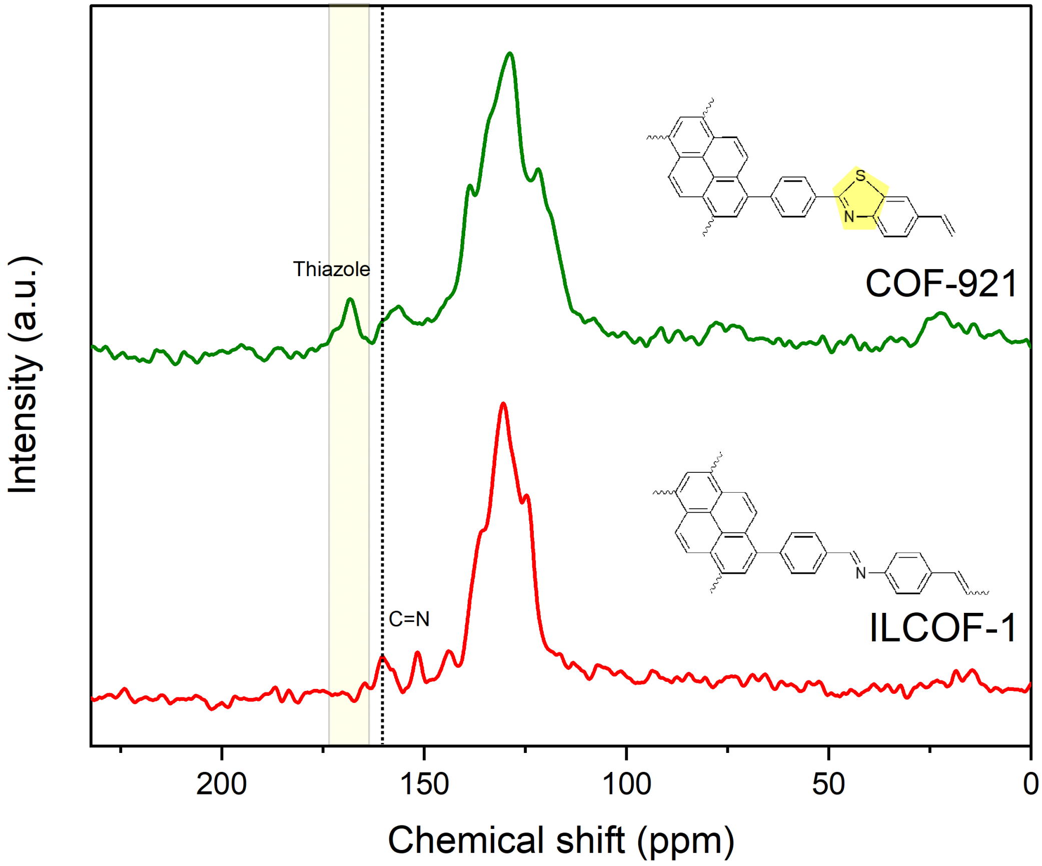

Figure 6.17 Solid-state ^{13}C NMR of ILCOF-1 and COF-921.

6.7.2 Change of the Optical Bandgap

The UV-Vis spectrum (plot a) demonstrates that COF-921 exhibits enhanced absorption in the visible light region, particularly between 800 and 530 nm, compared to ILCOF-1. This increased absorption aligns with the color change observed in COF-921. The absorption edge of COF-921 is positioned around 500 nm, which is at a shorter wavelength than ILCOF-1 and SH-COF, both of which have absorption edges near 550 nm (**Figure 6.18a**). The bandgap determined from a Tauc plot (plot b) reveals that COF-921 has an optical bandgap of 1.71 eV, which is significantly narrower than the bandgaps of ILCOF-1 (2.06 eV) and SH-COF (1.93 eV) (**Figure 6.18b**). This narrowing of the bandgap indicates that the post-synthetic conversion from imine to thiazole linkages in COF-921 has effectively lowered the bandgap, improving light absorption and electronic properties.

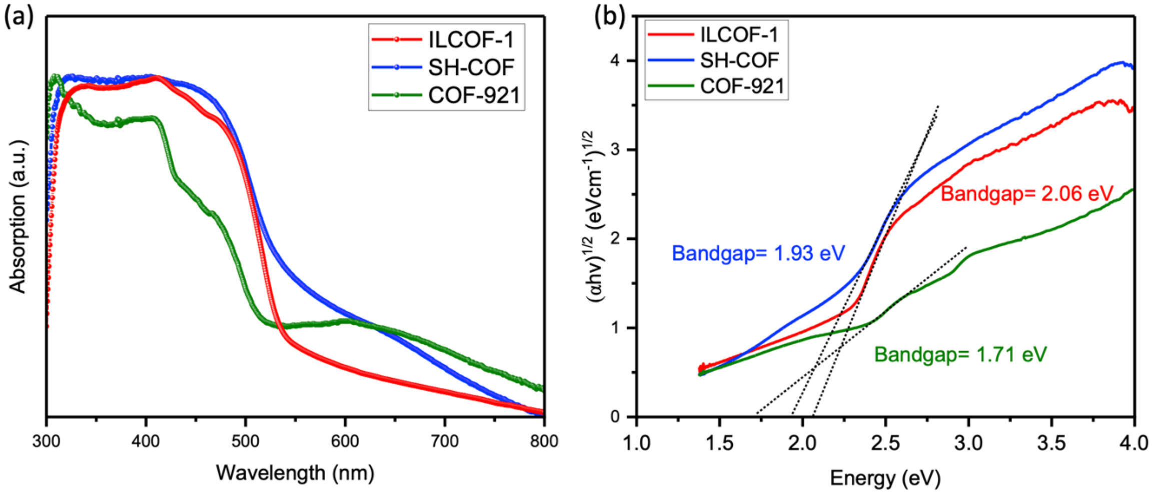

Figure 6.18 (a) UV-Vis spectra and (b) Tauc plot for ILCOF-1, SH-COF and COF-921.

6.7.3 Band Edges positions

In addition to the optical properties, UPS data suggest that COF-921 exhibits significant shifts in electronic properties compared to ILCOF-1. While the valence band maximum (VBM) relative to the Fermi level remains the same at 1.20 eV, the work function of COF-921 slightly shifts to -2.12 eV, reflecting a reduction in electron affinity. The conduction band minimum (CBM) also shifts from -1.37 eV in ILCOF-1 to -1.61 eV in COF-921, implying better alignment for electron conduction. These changes are indicative of greater electron delocalization due to the introduction of thiazole linkages, resulting in improved electronic properties and potentially better conductivity. Comparatively, SH-COF shows even more significant band edge shifts, further narrowing the bandgap and deepening the VBM and CBM positions, indicating enhanced electronic characteristics across the series. These insights into the electronic and optical properties reveal how post-synthetic modification via imine-to-thiazole conversion in COFs can effectively tune the bandgap and band edge positions (**Figure 6.19, 6.20** and **Table 6.6**), making materials like COF-921 and SH-COF more efficient for applications that require precise electronic and optical control, such as in photovoltaics or optoelectronics.

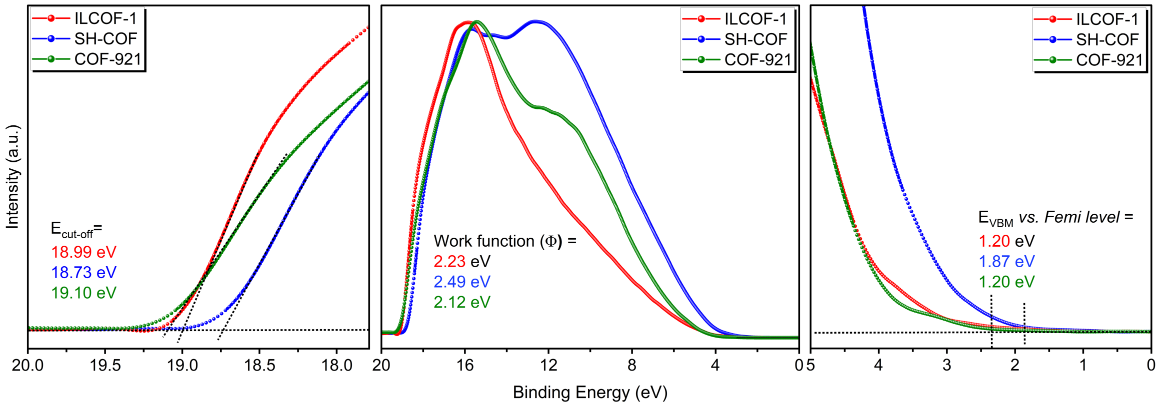

Figure 6.19 UPS spectra of ILCOF-1, SH-COF and COF-921.

Table 6.6 Comparison of valence band maximum (VBM) relative to Fermi level (EF), $E_{cut\text{-}off}$, work function, VBM, Optical Bandgap, and conduction band minimum (CBM) for IL-COF-1, SH-COF, and COF-921.

COFs	VBM vs E_F	$E_{cut\text{-}off}$	Work function	VBM	Optical bandgap	CBM
IL-COF-1	1.20	18.99	-2.23	-3.43	2.06	-1.37
SH-COF	1.87	18.73	-2.49	-4.36	1.93	-2.43
COF-921	1.20	19.10	-2.12	-3.32	1.71	-1.61

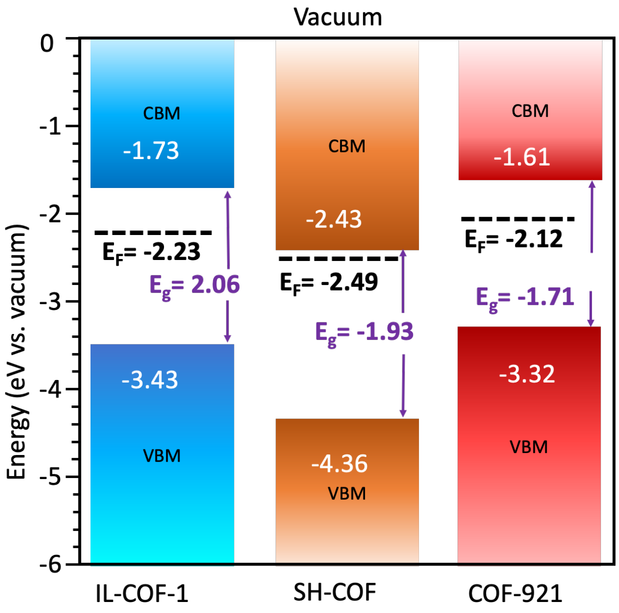

Figure 6.20 Comparison of the Band edges energy of the ILCOF-1, SH-COF and COF-921.

6.8 Conclusion

The research presented in this chapter provides a comprehensive investigation into the role of pyrene-based COFs in enhancing the performance of PSCs. Through systematic exploration of the introduction of ILCOF-1 and SH-COF into the perovskite matrix, significant improvements in crystallinity, optoelectronic properties, and overall device efficiency were observed. The successful synthesis of these COFs, confirmed through techniques such as FTIR, solid-state NMR, and XPS, highlights the importance of maintaining the structural integrity and functional groups of COFs in ensuring effective interaction with perovskite films.

A critical insight gained from this study is the impact of COF doping on the energy band alignment within PSCs. The precise tuning of the conduction and valence band edges of ILCOF-1 and SH-COF to align with those of the perovskite layer enables more efficient charge transfer and reduced recombination losses. This alignment proves particularly advantageous in n-i-p device architectures, where COFs serve as electron transport layers, promoting smoother charge transport between the perovskite layer and electrodes.

The chapter also underscores the significance of the pyrene moiety within the COF structure. Comparisons between pyrene-based COFs and non-pyrene-based counterparts, such as COF-5 and TFP-DBD, reveal that the extended conjugation offered by pyrene units is key to achieving high power conversion efficiencies (PCEs). In contrast, non-pyrene COFs, despite structural similarities, fail to achieve comparable performance, underscoring the critical role of molecular design in COF-based doping strategies. TRPL)studies further demonstrate that the incorporation of ILCOF-1 and SH-COF leads to significant PL quenching, indicating efficient charge transfer from the perovskite to the COFs. Faster recombination times observed in TRPL measurements support the enhanced charge transfer dynamics, particularly in SH-COF-doped samples, which exhibit superior charge transport efficiency. XPS depth profiling provides additional insights into the interaction mechanisms between the COFs and the perovskite layer. Shifts in the binding energy of Pb 4f and I 3d spectra suggest Lewis acid-base interactions between Pb^{2+} ions in the perovskite and functional groups in the COFs. This interaction likely contributes to trap state passivation, which enhances charge carrier mobility and reduces recombination losses within the PSCs.

Moreover, the conversion of ILCOF-1 to COF-921 represents a significant advancement in post-synthetic modification of COFs, as it successfully transforms imine linkages into thiazole linkages. This modification leads to a reduction in the optical bandgap from 2.06 eV in ILCOF-1 to 1.71 eV in COF-921, reflecting enhanced π-conjugation and electronic delocalization. These changes result in improved light absorption, optimized energy levels, and greater efficiency in charge transfer. The lower bandgap and refined electronic properties make COF-921 a superior candidate for integration into PSCs, particularly in applications that benefit from reduced recombination and enhanced light harvesting capabilities. In summary, this chapter demonstrates the tremendous potential of pyrene-based COFs as dopants in PSCs. Through their ability to enhance crystallinity, optimize energy band alignment, and promote efficient charge transfer, these COFs pave the way for the development of high-efficiency, stable PSCs. The findings highlight the critical importance of molecular design and post-synthetic modification in unlocking the full potential of COFs in solar energy applications. Future research should continue to explore the fine-tuning of COF structures to further optimize their interaction with perovskite materials, potentially leading to even higher efficiencies and greater long-term stability in PSC devices.

Chapter 7

Conclusions and Recommendations

Chapter 7 provides a comprehensive analysis of the findings from this thesis, which explores the incorporation of covalent organic frameworks (COFs) into perovskite solar cells (PSCs) as a strategy to enhance both efficiency and stability. Two primary hypotheses are evaluated: the use of sp^2 *carbon-conjugated COFs (*sp^2*c-COFs) as interfacial passivation layers and the use of pyrene-based COFs (such as ILCOF-1 and SH-COF) as bulk dopants to reduce trap states within the perovskite film. The results confirm that* sp^2*c-COFs effectively dual-passivate surface defects at the* NiO_x*/perovskite interface, resulting in improved charge extraction, reduced non-radiative recombination, and an increase in power conversion efficiency (PCE) from 15.82% to 17.64%. Additionally, bulk doping with pyrene-based COFs improved the crystallinity of perovskite films, reduced trap densities, and achieved a PCE of ~19.5% for both COFs (ILCOF-1 and SH-COF). The chapter concludes by evaluating the successful proof of both hypotheses, discussing their implications for PSC development, and offering practical recommendations for future research. These include exploring new COF materials, optimizing integration techniques, and extending the application of COFs beyond photovoltaics.*

7.1 Introduction

The continuous pursuit of enhanced PCE and operational stability in PSCs has placed particular emphasis on addressing the degradation mechanisms that limit their commercial viability. As PSCs approach the efficiency benchmarks of traditional silicon-based solar cells, the main obstacle preventing widespread deployment remains their long-term stability and sensitivity to environmental conditions. These weaknesses stem from the intrinsic material properties of perovskites, such as their susceptibility to moisture and oxygen, as well as the accumulation of defects at the interfaces within the device, particularly between the perovskite absorber and transport layers. In this context, this thesis explored innovative solutions for mitigating interfacial defects and reducing trap states by incorporating covalent organic frameworks (COFs) into PSCs architectures. The work aimed to prove or disprove two hypotheses regarding the potential benefits of using sp^2 carbon-conjugated COFs (sp^2c-COFs) and pyrene-based COFs as functional additives within PSCs. The objective of Chapter 7 is to provide a comprehensive summary of the key findings, evaluate the hypotheses, analyse the extent to which the research targets were met, and offer practical recommendations for future research.

7.2 Summary of Findings

This thesis presented several significant contributions to the understanding of how COFs can be used to improve the performance of PSCs. By exploring the dual-passivation strategy using sp^2c-COFs and the bulk doping of perovskites with pyrene-based COFs, this research demonstrated measurable improvements in PCE and quality of perovskite materials. The findings also underscore the potential of COFs as a versatile material platform for photovoltaic applications.

7.2.1 Interfacial Defects and Their Mitigation

One of the primary challenges in PSCs is the presence of interfacial defects, particularly at the heterointerfaces between the perovskite active layer and the charge transport layers.

These defects, including trap states at the buried interfaces, lead to non-radiative recombination, reduced charge carrier lifetimes, and overall lower device efficiencies. For example, the NiO_x/perovskite interface is particularly susceptible to the formation of defects, which are known to result from undercoordinated lead (Pb^{2+}) atoms and Ni^{3+} cations on the surface of the NiO_x layer. This thesis confirmed that the use of sp^2c-COFs as interfacial passivation layers could significantly reduce the density of these interfacial defects. The sp^2c-COF layer acted as a dual-passivator, interacting chemically with both Ni^{3+} species in the NiO_x layer and undercoordinated Pb^{2+} sites in the perovskite. This dual-passivation mechanism helped to mitigate non-radiative recombination at the interfaces, leading to improved charge extraction and higher V_{oc} and FF. Devices incorporating sp^2c-COF showed a clear improvement in their overall PCE compared to control devices, rising from an average of 15.82% in untreated devices to 17.65% in sp^2c-COF-treated devices.

7.2.2 Trap State Reduction and Bulk Doping

Trap states, both within the bulk of the perovskite film and at the surface, play a crucial role in limiting the performance of PSCs. These trap states, often resulting from lead halide vacancies or grain boundary defects, act as recombination centers that lower the efficiency of charge carrier transport through the device. To address this, the thesis explored the use of pyrene-based COFs, such as ILCOF-1 and SH-COF, as bulk dopants to reduce trap state densities and improve the crystallinity of the perovskite films. The incorporation of these COFs into the perovskite matrix was found to have a profound effect on the quality of the perovskite films. Specifically, the use of SH-COF, with its thiol functional groups, was highly effective in coordinating with undercoordinated lead (Pb^{2+}) atoms, thereby reducing the density of trap states. This led to an improvement in the crystallinity of the films, as a result, the PCE of SH-COF-doped devices reached 19.49%, compared to 18.33% in control devices. Furthermore, the introduction of ILCOF-1 as a bulk dopant resulted in improved crystallinity and charge transfer dynamics, further contributing to the enhancement of device performance.

7.3 Hypotheses Evaluation

The central hypotheses of this thesis were twofold:

Hypothesis 1: sp^2 carbon-conjugated COFs (sp^2c-COFs) can serve as effective interfacial passivation layers in PSCs, leading to improved efficiency and stability by dual-passivating surface defects at the NiO_x/perovskite interface.

Hypothesis 2: Pyrene-based COFs, such as ILCOF-1 and SH-COF, can act as bulk dopants in PSCs, improving film crystallinity, reducing trap state densities, and thereby enhancing efficiency.

Both hypotheses were tested through extensive experimentation and were ultimately proven to be valid based on the results obtained. The results of this thesis confirmed that the incorporation of COFs significantly improves the performance of PSCs. Below is an in-depth evaluation of the two hypotheses, including a discussion on their extent of proof and validation through experimentation.

Hypothesis 1: Dual-Passivation using sp^2c-COFs

This hypothesis posited that introducing sp^2c-COF into the PSC architecture as interfacial layers would result in the passivation of surface defects at the NiO_x/perovskite interface. These interfacial defects, which include undercoordinated Pb^{2+} sites and Ni^{3+} surface defects, contribute significantly to the degradation of device performance through non-radiative recombination and inefficient charge transport. The thesis demonstrated that sp^2c-COFs can chemically interact with these defects, acting as Lewis bases that form stable complexes with the defective sites. The electron-donating -CN groups on the sp^2c-COFs were found to reduce Ni^{3+} active species into more stable Ni^{2+} ions. Similarly, the coordination of sp^2c-COF molecules with Pb^{2+} defects at the perovskite surface mitigated the formation of PbI_2-rich barriers, which are known to impede hole extraction. The success of this dual-passivation strategy was proven by a series of experiments, where sp^2c-COF-treated devices showed significant reductions in non-radiative recombination, as indicated by improved photoluminescence (PL) quenching measurements and enhanced ideality factor. The effects of sp^2c-COF on the perovskite also evident in the crystallinity and morphology of the perovskite films. XRD and SEM analyses revealed that sp^2c-COF-modified films exhibited larger grain sizes and fewer grain boundaries compared to pristine films. This reduction in grain boundaries, which are often sources of trap states, contributed to a higher degree of crystallinity and better phase purity in the perovskite films.

Additionally, sp^2c-COF-modified devices exhibited substantial improvements in the fill factor (FF), which rose from an average of 67.97% in untreated devices to 75.24% in treated devices. These improvements translated into higher PCE, with COF-treated devices reaching a champion devices efficiency of 17.65%, compared to 15.82% for untreated devices. In conclusion, the first hypothesis was fully validated by the experimental results. The dual-passivation of interfacial defects using sp^2c-COFs proved to be an effective approach for enhancing the PCE of PSCs. This approach could potentially be applied to other types of photovoltaics where interfacial defects limit device performance.

Hypothesis 2: Pyrene-Based COFs as Bulk Dopants

The second hypothesis suggested that pyrene-based COFs, such as ILCOF-1 and SH-COF, could serve as effective bulk dopants in perovskite films, reducing trap state densities and improving film crystallinity, ultimately leading to enhanced PCE. In this thesis, pyrene-based COFs were incorporated into the bulk of the perovskite layer as dopants. The specific chemical structures of ILCOF-1 and SH-COF allowed them to interact with undercoordinated Pb^{2+} atoms. SH-COF, in particular, exhibited strong coordination with Pb^{2+} defects through, effectively reducing the density of trap states in the perovskite bulk. TRPL measurements showed that the carrier lifetimes in SH-COF-treated films were significantly extended compared to control films, indicating reduced recombination losses.

The incorporation of ILCOF-1 and SH-COF led to significant improvements in the PCE of the devices up to 19.48% and 19.49%, respectively compared to the control devices

(18.33%). The ability to tune the electronic properties of these COFs through chemical modification further enhances their potential as versatile additives in photovoltaic applications.

7.4 Practical Recommendations for Future Research

This thesis has demonstrated the significant potential of COF-modified PSCs in improving stability and efficiency, but several key challenges remain that must be addressed to transition this technology toward practical applications. Future research should directly tackle these challenges to optimize COF integration and ensure scalability for commercial viability.

Optimizing COF Materials for Enhanced Passivation and Charge Transport: While this thesis has demonstrated the effectiveness of COFs as both interfacial passivators and bulk dopants, further optimization of their chemical structure and functionalization could unlock even greater performance gains in PSCs. Future research should focus on engineering COFs with tailored electronic properties, ensuring better energy level alignment with perovskites and charge transport layers. One potential direction is the design of COFs with extended π-conjugation, which could facilitate more efficient charge delocalization and transport. Additionally, functionalizing COFs with electron-rich groups such as amine, thiophene, or phosphine could strengthen their interaction with perovskites, enhancing defect passivation at both grain boundaries and interfaces. Investigating alternative COF linkers and topologies, such as 3D frameworks, may further improve charge transfer and mitigate recombination losses. Another promising avenue is post-synthetic modification, which allows fine-tuning of COF properties after synthesis. By introducing specific functional groups, post-synthetic modification can optimize hydrophobicity, ion migration suppression, and charge transfer efficiency, making COFs even more effective in stabilizing perovskite layers. Research into how post-synthetic modification influences bandgap tuning and carrier mobility could lead to the development of COFs specifically designed for hole or electron transport layers, potentially reducing reliance on conventional NiO_x or SnO_2 transport layers. By refining COF design through chemical modifications and energy level engineering, future studies can further enhance their role in perovskite photovoltaics, improving both efficiency and long-term device performance.

Long-Term Operational Stability and Environmental Effects: Although this study demonstrated the potential of COF-passivated PSCs under controlled conditions, their real-world stability remains an open question. Future work should focus on assessing the performance of COF-modified PSCs under real-world operational conditions. This includes exposure to fluctuating temperatures, oxygen, humidity, and light intensities that more closely mimic the environments in which solar panels are typically deployed. Moving beyond the standard 85°C/85% relative humidity tests, real-world stability tests should include extended outdoor testing in different climates. This would provide more accurate data on how COF-modified PSCs degrade over time under actual operating conditions. Such studies could reveal new degradation pathways or interactions between the COFs and environmental factors that were not apparent in controlled laboratory settings. In conjunction with stability testing, research should investigate how COFs can be integrated with advanced encapsulation strategies to further protect PSCs from environmental degradation. Encapsulation layers incorporating COFs could provide an additional barrier against moisture and oxygen, while also enhancing mechanical robustness and reducing thermal stress.

Scalable and Uniform COF Integration Techniques: A critical limitation encountered in this work was the challenge of achieving uniform COF deposition across large-area PSC modules. While COFs showed excellent passivation effects at the lab scale, scaling up these benefits requires improved processing techniques. Future research should focus on developing scalable COF deposition methods, such as layer-by-layer assembly, molecular layer deposition (MLD), or vapor-phase deposition, to achieve uniform coverage with precise thickness control. Additionally, optimizing solution-phase COF synthesis to ensure high crystallinity and defect-free frameworks at larger scales will be essential. Techniques such as *in situ* polymerization or templated synthesis could help minimize structural inconsistencies and ensure reproducibility in industrial-scale fabrication.

Economic Viability and Sustainable Production: For COF-modified PSCs to move toward commercialization, future studies must evaluate the cost-effectiveness of COF integration. The high cost of COF synthesis remains a challenge, and research should focus on reducing synthesis costs through low-energy reaction routes, scalable solvent-free methods, and utilization of inexpensive precursors. Additionally, exploring recycling strategies for COF-modified perovskite layers could contribute to sustainability efforts. Investigating COF reusability after device degradation and developing circular economy models for their recovery could significantly enhance the long-term feasibility of this technology.

Expanding COF Applications Beyond PSCs: Given the versatility of COFs demonstrated in this thesis, future research should explore their potential applications beyond PSCs. The unique properties of COFs, such as their high surface area, tunable electronic properties, and chemical stability, make them attractive candidates for a wide range of optoelectronic and energy-related applications. For example, COFs could be applied in organic or hybrid light-emitting diodes as charge transport layers or emission layers. Their ability to stabilize defect-prone materials and their tunable bandgaps could make them valuable components in high-efficiency, stable LEDs. Moreover, COFs' porosity and ability to selectively interact with specific chemical species make them promising materials for chemical sensors and photodetectors. Future work could investigate COFs' roles in detecting environmental pollutants, gas sensors, or photodetection in ultraviolet or infrared ranges. As COFs have already shown promise in energy storage applications, such as supercapacitors and lithium-ion batteries. Further research into their electrochemical properties and how they can be tuned for specific storage applications could expand their utility in energy storage devices.

7.5 Conclusions

The research presented in this thesis demonstrates that COFs represent a promising material platform for improving the PCE and stability of PSCs. Through the utilization of sp^2c-COFs as interfacial passivation layers and pyrene-based COFs (such as ILCOF-1 and

SH-COF) as bulk dopants, this work has shown measurable improvements in the PCE of PSCs. The incorporation of COFs led to significant reductions in interfacial and bulk defects, which are major contributors to non-radiative recombination and device degradation. The dual-passivation strategy employed by sp^2c-COFs successfully mitigated defect formation at the NiO_x/perovskite interface, resulting in enhanced charge extraction and improved device stability. Similarly, bulk doping with pyrene-based COFs led to improved crystallinity, larger grain sizes, and reduced trap state densities in the perovskite films, contributing to higher PCEs and longer operational lifetimes. This thesis has also highlighted several areas for future research, including the exploration of new COF materials and functional groups, real-world stability testing, optimization of COF integration techniques, and potential applications beyond PSCs. Addressing these areas will be critical for further advancing the field and unlocking the full potential of COF-modified PSCs for commercial applications. In conclusion, this research represents a significant step forward in the development of COF-based materials for next-generation photovoltaics. The ability of COFs to address both interfacial and bulk defects, coupled with their tunable properties and chemical stability, makes them highly attractive candidates for improving the performance, stability, and commercial viability of PSCs and other optoelectronic devices.

REFERENCES

[1] Y. Zhou, L. M. Herz, A. K. Y. Jen, M. Saliba. *Nat. Energy* **2022**, 7, 794.

[2] Y. Lin, L. Shen, J. Dai, Y. Deng, Y. Wu, Y. Bai, X. Zheng, J. Wang, Y. Fang, H. Wei, W. Ma, X. Cheng Zeng, X. Zhan, J. Huang. *Adv. Mater.* **2017**, 29, 1604545.

[3] H. R. Abuzeid, A. F. M. EL-Mahdy, S. W. Kuo. *Giant* **2021**, 6, 100054.

[4] H. Ding, J. Li, G. Xie, G. Lin, R. Chen, Z. Peng, C. Yang, B. Wang, J. Sun, C. Wang. *Nat. Commun.* **2018**, 9, 1.

[5] M. M. Lee, J. Teuscher, T. Miyasaka, T. N. Murakami, H. J. Snaith. *Science* **2012**, 338, 643.

[6] H. S. Kim, C. R. Lee, J. H. Im, K. B. Lee, T. Moehl, A. Marchioro, S. J. Moon, R. Humphry-Baker, J. H. Yum, J. E. Moser, M. Grätzel, N. G. Park. *Sci. Rep.* **2012**, 2, 1.

[7] N. J. Jeon, J. H. Noh, Y. C. Kim, W. S. Yang, S. Ryu, S. Il Seok. *Nat. Mater.* **2014**, 13, 897.

[8] G. Xing, N. Mathews, S. Sun, S. S. Lim, Y. M. Lam, M. Graẗzel, S. Mhaisalkar, T. C. Sum. *Science* **2013**, 342, 344.

[9] Y. Wang, T. Mahmoudi, H. Y. Yang, K. S. Bhat, J. Y. Yoo, Y. B. Hahn. *Nano Energy* **2018**, 49, 59.

[10] Best Research-Cell Efficiency Chart | Photovoltaic Research | NREL. https://www.nrel.gov/pv/cell-efficiency.html, accessed: 13 February 2025.

[11] Y. Cheng, L. Ding. *Energy Environ. Sci.* **2021**, 14, 3233.

[12] M. I. Saidaminov, J. Kim, A. Jain, R. Quintero-Bermudez, H. Tan, G. Long, F. Tan, A. Johnston, Y. Zhao, O. Voznyy, E. H. Sargent. *Nat. Energy* **2018**, 3, 648.

[13] H. Zhu, S. Teale, M. N. Lintangpradipto, S. Mahesh, B. Chen, M. D. McGehee, E. H. Sargent, O. M. Bakr. *Nat. Rev. Mater.* **2023**, 8, 569.

[14] T. A. Chowdhury, M. A. Bin Zafar, M. Sajjad-Ul Islam, M. Shahinuzzaman, M. A. Islam, M. U. Khandaker. *RSC Adv.* **2023**, 13, 1787.

[15] L. Duan, A. Uddin. *Mater. Chem. Front.* **2022**, 6, 400.

[16] Z. Zhang, H. Wang, T. J. Jacobsson, J. Luo. *Nat. Commun.* **2022**, 13, 1.

[17] J. Zhuang, J. Wang, F. Yan. *Nano-Micro Lett.* **2023**, 15, 1.

[18] J. J. Y. W. Foong, H. A. Dewi, A. A. Zhumekenov, B. Febriansyah, A. Bruno, T. Salim, D. J. J. Tay, H. R. Abuzeid, T. M. Koh, S. G. Mhaisalkar, N. Mathews. *Sustain. Energy Fuels* **2024**, 8, 491.

[19] F. Guo, S. Qiu, J. Hu, H. Wang, B. Cai, J. Li, X. Yuan, X. Liu, K. Forberich, C. J. Brabec, Y. Mai. *Adv. Sci.* **2019**, 6, 1901067.

[20] Z. Saki, M. M. Byranvand, N. Taghavinia, M. Kedia, M. Saliba. *Energy Environ. Sci.* **2021**, 14, 5690.

[21] M. Abbas, L. Zeng, F. Guo, M. Rauf, X. C. Yuan, B. Cai. *Materials* **2020**, 13, 4851.

[22] J. Wu, S. Zhang, Q. Gu, Q. Zhang. *FlexMat* **2024**, 1, 160.

[23] L. M. Yang, E. Ganz, S. Wang, X. J. Li, T. Frauenheim. *J. Mater. Chem. C* **2015**, 3, 2244.

[24] X. Li, Q. Gao, J. Aneesh, H. Sen Xu, Z. Chen, W. Tang, C. Liu, X. Shi, K. V. Adarsh, Y. Lu, K. P. Loh. *Chem. Mater.* **2018**, 30, 5743.

[25] L. Li, Y. Zhu, N. Gong, W. Zhang, W. Peng, Y. Li, F. Zhang, X. Fan. *Int. J. Hydrogen Energy* **2020**, 45, 2689.

[26] Y. Chen, X. Luo, J. Zhang, L. Hu, T. Xu, W. Li, L. Chen, M. Shen, S. Bin Ren, D. M. Han, G. H. Ning. *J. Mater. Chem. A* **2022**, 10, 24620.

[27] S. Wang, T. Wu, J. Guo, R. Zhao, Y. Hua, Y. Zhao. *ACS Cent. Sci.* **2024**, 10, 1383.

[28] Z. Li, Z. Zhang, R. Nie, C. Li, Q. Sun, W. Shi, W. Chu, Y. Long, H. Li, X. Liu. *Adv. Funct. Mater.* **2022**, 32, 2112553.

[29] C. C. Boyd, R. C. Shallcross, T. Moot, R. Kerner, L. Bertoluzzi, A. Onno, S. Kavadiya, C. Chosy, E. J. Wolf, J. Werner, J. A. Raiford, C. de Paula, A. F. Palmstrom, Z. J. Yu, J. J. Berry, S. F. Bent, Z. C. Holman, J. M. Luther. *Joule* **2020**, 4, 1759.

[30] J. Zhang, J. Long, Z. Huang, J. Yang, X. Li, R. Dai, W. Sheng, L. Tan, Y. Chen. *Chem. Eng. J.* **2021**, 426, 130230.

[31] X. Zheng, Z. Song, Z. Chen, S. S. Bista, P. Gui, N. Shrestha, C. Chen, C. Li, X. Yin, R. A. Awni, H. Lei, C. Tao, R. J. Ellingson, Y. Yan, G. Fang. *J. Mater. Chem. C* **2020**, 8, 1972.

[32] D. Luo, R. Su, W. Zhang, Q. Gong, R. Zhu. *Nat. Rev. Mater.* **2019**, 5, 44.

[33] H. Jin, E. Debroye, M. Keshavarz, I. G. Scheblykin, M. B. J. Roeffaers, J. Hofkens, J. A. Steele. *Mater. Horiz.* **2020**, 7, 397.

[34] M. Y. Hao, H. Y. Wang, Y. Wang, Y. Qin, J. P. Zhang, X. C. Ai. *J. Power Sources* **2020**, 479, 229077.

[35] R. Garai, R. K. Gupta, P. K. Iyer. *Acc. Mater. Res.* **2023**, 4, 560.

[36] A. N. Cho, N. G. Park. *ChemSusChem* **2017**, 10, 3687.

[37] D. Zhang, D. Li, Y. Hu, A. Mei, H. Han. *Commun. Mater.* **2022**, 3, 1.

[38] H. Min, D. Y. Lee, J. Kim, G. Kim, K. S. Lee, J. Kim, M. J. Paik, Y. K. Kim, K. S. Kim, M. G. Kim, T. J. Shin, S. Il Seok. *Nature* **2021**, 598, 444.

[39] M. A. Green, E. D. Dunlop, J. Hohl-Ebinger, M. Yoshita, N. Kopidakis, K. Bothe, D. Hinken, M. Rauer, X. Hao. *Prog. Photovolt. Res. Appl.* **2022**, 30, 687.

[40] Z. Song, C. L. McElvany, A. B. Phillips, I. Celik, P. W. Krantz, S. C. Watthage, G. K. Liyanage, D. Apul, M. J. Heben. *Energy Environ. Sci.* **2017**, 10, 1297.

[41] R. F. Service. *Science* **2016**, 354, 1214.

[42] T. Wu, Z. Qin, Y. Wang, Y. Wu, W. Chen, S. Zhang, M. Cai, S. Dai, J. Zhang, J. Liu, Z. Zhou, X. Liu, H. Segawa, H. Tan, Q. Tang, J. Fang, Y. Li, L. Ding, Z. Ning, Y. Qi, Y. Zhang, L. Han. *NanoMicro Lett.* **2021**, 13, 1.

[43] P. Roy, N. K. Sinha, S. Tiwari, A. Khare. *Solar Energy* **2020**, 198, 665.

[44] T. D. Siegler, A. Dawson, P. Lobaccaro, D. Ung, M. E. Beck, G. Nilsen, L. L. Tinker. *ACS Energy Lett.* **2022**, 7, 1728.

[45] Z. Guo, A. K. Jena, G. M. Kim, T. Miyasaka. *Energy Environ. Sci.* **2022**, 15, 3171.

[46] A. Kojima, K. Teshima, Y. Shirai, T. Miyasaka. *J. Am. Chem. Soc.* **2009**, 131, 6050.

[47] H. S. Kim, C. R. Lee, J. H. Im, K. B. Lee, T. Moehl, A. Marchioro, S. J. Moon, R. Humphry-Baker, J. H. Yum, J. E. Moser, M. Grätzel, N. G. Park. *Sci. Rep.* **2012**, 2, 1.

[48] M. M. Lee, J. Teuscher, T. Miyasaka, T. N. Murakami, H. J. Snaith. *Science* **2012**, 338, 643.

[49] J. Wang, G. Wang, B. Chen. *Sustain. Energy Fuels* **2024**.

[50] M. A. Green, A. Ho-Baillie, H. J. Snaith. *Nat. Photonics* **2014**, 8, 506.

[51] M. Saliba, T. Matsui, J. Y. Seo, K. Domanski, J. P. Correa-Baena, M. K. Nazeeruddin, S. M. Zakeeruddin, W. Tress, A. Abate, A. Hagfeldt, M. Grätzel. *Energy Environ. Sci.* **2016**, 9, 1989.

[52] H. Liu, T. Liu, X. Wang, G. Hu, B. Zheng, X. Yu, Y. Wang, D. Yang. *Adv. Energy Mater.* **2024**, 2401809.

[53] M. Saliba, T. Matsui, K. Domanski, J. Y. Seo, A. Ummadisingu, S. M. Zakeeruddin, J. P. Correa-Baena, W. R. Tress, A. Abate, A. Hagfeldt, M. Grätzel. *Science* **2016**, 354, 206.

[54] M. Noman, Z. Khan, S. T. Jan. *RSC Adv.* **2024**, 14, 5085.

[55] Y. Huang, K. Yan, X. Wang, B. Li, B. Niu, M. Yan, Z. Shen, K. Zhou, Y. Fang, X. Yu, H. Chen, L. Zhang, C. Z. Li. *Adv. Mater.* **2024**, 2408101.

[56] F. Znidi, M. Morsy, Md. Nizam Uddin. *Next Nanotechnol.* **2024**, 5, 100061.

[57] R. Sharif, A. Khalid, S. W. Ahmad, A. Rehman, H. G. Qutab, H. H. Akhtar, K. Mahmood, S. Afzal, F. Saleem. *Nanoscale Adv.* **2023**, 5, 3803.

[58] W. Yu, Y. Zou, H. Wang, S. Qi, C. Wu, X. Guo, Y. Liu, Z. Chen, B. Qu, L. Xiao. *Chem. Soc. Rev.* **2024**, 53, 1769.

[59] M. Ren, X. Qian, Y. Chen, T. Wang, Y. Zhao. *J. Hazard. Mater.* **2022**, 426, 127848.

[60] J. Dou, Y. Bai, Q. Chen. *Mater. Chem. Front.* **2022**, 6, 2779.

[61] C. H. Chen, S. N. Cheng, L. Cheng, Z. K. Wang, L. S. Liao. *Adv. Energy Mater.* **2023**, 13, 2204144.

[62] A. Abate. *ACS Energy Lett.* **2023**, 8, 1896.

[63] Y. Su, J. Yang, H. Rao, Y. Zhong, W. Sheng, L. Tan, Y. Chen. *Energy Environ. Sci.* **2023**, 16, 2177.

64] M. A. Green, E. D. Dunlop, M. Yoshita, N. Kopidakis, K. Bothe, G. Siefer, X. Hao. *Prog. Photovolt. Res. Appl.* **2024**, 32, 3.

[65] Best Research-Cell Efficiency Chart | Photovoltaic Research | NREL.

[66] C. S. Pathak, H. Choi, H. Kim, J. Lim, S. K. Cho, D. S. Ham, S. Song. *Solar RRL* **2024**, 8, 2300860.

[67] S. S. Dipta, M. A. Rahim, A. Uddin. *Appl. Phys. Rev.* **2024**, 11, 21301.

[68] K. Aitola, G. G. Sonai, M. Markkanen, J. J. Kaschuk, X. Hou, K. Miettunen, P. D. Lund. *Solar Energy* **2022**, 237, 264.

[69] S. D. Stranks, H. J. Snaith. *Nat. Nanotechnol.* **2015**, 10, 391.

[70] S. Ašmontas, M. Mujahid. *Nanomaterials* **2023**, 13, 1886.

[71] Y. Li, Y. Lu, X. Huo, D. Wei, J. Meng, J. Dong, B. Qiao, S. Zhao, Z. Xu, D. Song. *RSC Adv.* **2021**, 11, 15688.

[72] J. P. Correa-Baena, A. Abate, M. Saliba, W. Tress, T. J. Jacobsson, M. Grätzel, A.

Hagfeldt. *Energy Environ. Sci.* **2017**, 10, 710.

[73] J. M. Ball, A. Petrozza. *Nat. Energy* **2016**, 1, 1.

[74] S. Bera, A. Saha, S. Mondal, A. Biswas, S. Mallick, R. Chatterjee, S. Roy. *Mater. Adv.* **2022**, 3, 5234.

[75] L. Dou, Y. M. Yang, J. You, Z. Hong, W. H. Chang, G. Li, Y. Yang. *Nat. Commun.* **2014**, 5, 1.

[76] S. Kar, N. F. Jamaludin, N. Yantara, S. G. Mhaisalkar, W. L. Leong. *Nanophotonics* **2021**, 10, 2103.

[77] S. Singh, Laxmi, D. Kabra. *J. Phys. D Appl. Phys.* **2020**, 53, 503003.

[78] X. Chen, S. Cheng, L. Xiao, H. Sun. *J. Phys. D Appl. Phys.* **2020**, 53, 373001.

[79] L. Fu, H. Li, L. Wang, R. Yin, B. Li, L. Yin. *Energy Environ. Sci.* **2020**, 13, 4017.

[80] F. Gao, Y. Zhao, X. Zhang, J. You. *Adv. Energy Mater.* **2020**, 10, 1902650.

[81] G. Li, J. Song, J. Wu, Z. Song, X. Wang, W. Sun, L. Fan, J. Lin, M. Huang, Z. Lan, P. Gao. *ACS Energy Lett.* **2021**, 6, 3614.

[82] T. Liu, J. Zhang, M. Qin, X. Wu, F. Li, X. Lu, Z. Zhu, A. K. Y. Jen. *Adv. Funct. Mater.* **2021**, 31, 2009515.

[83] Y. Huang, K. Yan, X. Wang, B. Li, B. Niu, M. Yan, Z. Shen, K. Zhou, Y. Fang, X. Yu, H. Chen, L. Zhang, C. Z. Li. *Adv. Mater.* **2024**.

[84] S. Chen, X. Zhang, J. Zhao, Y. Zhang, G. Kong, Q. Li, N. Li, Y. Yu, N. Xu, J. Zhang, K. Liu, Q. Zhao, J. Cao, J. Feng, X. Li, J. Qi, D. Yu, J. Li, P. Gao. *Nat. Commun.* **2018**, 9, 1.

[85] G. Niu, W. Li, J. Li, X. Liang, L. Wang. *RSC Adv.* **2017**, 7, 17473.

[86] Z. Liu, P. Liu, M. Li, T. He, T. Liu, L. Yu, M. Yuan. *Adv. Energy Mater.* **2022**, 12, 2200111.

[87] M. Raeisian Asl, S. F. K. Panahi, M. Jamaati, S. S. Tafreshi. *Int. J. Energy Res.* **2022**, 46, 13117.

[88] Y. Lai, Z. Lin, S. Baumann, G. E. Eperon, A. Virtuani, Q. Jeangros, D. Sulas-Kern, D. Barrit, J. Schall, W. Nie, G. Oreski, M. Khenkin, C. Ulbrich, R. Peibst, J. Stein, M. Köntges. *Energy Environ. Sci.* **2024**.

[89] T. L. Leung, I. Ahmad, A. A. Syed, A. M. C. Ng, J. Popović, A. B. Djurišić. *Commun. Mater.* **2022**, 3, 1.

[90] T. Yue, K. Li, X. Li, N. Ahmad, H. Kang, Q. Cheng, Y. Zhang, Y. Yue, Y. Jing, B. Wang, S. Li, J. Chen, G. Huang. *ACS Nano* **2023**, 17, 14632.

[91] B. Ghosh, D. J. J. Tay, M. B. J. Roeffaers, N. Mathews. *Appl. Phys. Rev.* **2023**, 10.

[92] E. Jokar, C. H. Chien, A. Fathi, M. Rameez, Y. H. Chang, E. W. G. Diau. *Energy Environ. Sci.* **2018**, 11, 2353.

[93] S. M. Hasnain. *Solar Energy* **2023**, 262, 111825.

[94] B. Parida, A. Singh, M. Oh, M. Jeon, J. W. Kang, H. Kim. *Mater. Today Commun.* **2019**, 18, 176.

[95] F. Giordano, A. Abate, J. P. Correa Baena, M. Saliba, T. Matsui, S. H. Im, S. M. Zakeeruddin, M. K. Nazeeruddin, A. Hagfeldt, M. Grätzel. *Nat. Commun.* **2016**, 7, 1.

[96] N. J. Jeon, J. H. Noh, W. S. Yang, Y. C. Kim, S. Ryu, J. Seo, S. Il Seok. *Nature* **2015**, 517, 476.

[97] Y. Rong, L. Liu, A. Mei, X. Li, H. Han. *Adv. Energy Mater.* **2015**, 5, 1501066.

[98] Y. Ming, Y. Jiang, J. Li, J. Huang, P. Xiang, C. Qiu, Y. Rong. *Chem. Inorg. Mater.* **2024**, 3, 100050.

[99] Y. Zhao, Q. Ye, Z. Chu, F. Gao, X. Zhang, J. You. *Energy Environ. Mater.* **2019**, 2, 93.

[100] F. M. Rombach, S. A. Haque, T. J. Macdonald. *Energy Environ. Sci.* **2021**, 14, 5161.

[101] K. Wang, S. Olthof, W. S. Subhani, X. Jiang, Y. Cao, L. Duan, H. Wang, M. Du, S. (Frank) Liu. *Nano Energy* **2020**, 68, 104289.

[102] W. Yu, X. Sun, M. Xiao, T. Hou, X. Liu, B. Zheng, H. Yu, M. Zhang, Y. Huang, X. Hao. *Nano Res.* **2021**, 15, 85.

[103] T. Kanlayapattamapong, W. Insri, S. Homnan, A. Gardchareon, P. Kanjanaboos, D. Wongratanaphisan, P. Ruankham. *Surf. Interfaces* **2023**, 41, 103244.

[104] P. Zhang, J. Wu, T. Zhang, Y. Wang, D. Liu, H. Chen, L. Ji, C. Liu, W. Ahmad, Z. D. Chen, S. Li. *Adv. Mater.* **2018**, 30, 1703737.

[105] S. Weber, T. Rath, J. Mangalam, B. Kunert, A. M. Coclite, M. Bauch, T. Dimopoulos, G. Trimmel. *J. Mater. Sci. Mater. Electron.* **2018**, 29, 1847.

[106] B. G. H. M. Groeneveld, M. Najafi, B. Steensma, S. Adjokatse, H. H. Fang, F. Jahani, L. Qiu, G. H. Ten Brink, J. C. Hummelen, M. A. Loi. *APL Mater.* **2017**, 5, 076103.

[107] M. Feng, M. Wang, H. Zhou, W. Li, X. Xie, S. Wang, Z. Zang, S. Chen. *ACS Appl. Energy Mater.* **2020**, 3, 9732.

[108] H. Elbohy, B. Bahrami, S. Mabrouk, K. M. Reza, A. Gurung, R. Pathak, M. Liang, Q. Qiao, K. Zhu. *Adv. Funct. Mater.* **2019**, 29, 1806740.

[109] S. Zhang, M. Stolterfoht, A. Armin, Q. Lin, F. Zu, J. Sobus, H. Jin, N. Koch, P. Meredith, P. L. Burn, D. Neher. *ACS Appl. Mater. Interfaces* **2018**, 10, 21681.

[110] J. H. Kim, P. W. Liang, S. T. Williams, N. Cho, C. C. Chueh, M. S. Glaz, D. S. Ginger, A. K. Y. Jen. *Adv. Mater.* **2015**, 27, 695.

[111] T. Ivanova, A. Harizanova, M. Shipochka, P. Vitanov. *Materials* **2022**, *15*, 1742.

[112] S. A. Akalin, M. Erol, B. Uzunbayir, S. Oguzlar, S. Yildirim, F. P. Gokdemir Choi, S. Gunes, U. D. Yilmazer Menda, M. J. Mendes. *Adv. Mater. Technol.* **2024**, 9, 2301760.

[113] J. D. Desai, S. K. Min, K. D. Jung, O. S. Joo. *Appl. Surf. Sci.* **2006**, 253, 1781.

[114] D. Koushik, M. Jošt, A. Dučinskas, C. Burgess, V. Zardetto, C. Weijtens, M. A. Verheijen, W. M. M. Kessels, S. Albrecht, M. Creatore. *J. Mater. Chem. C Mater.* **2019**, 7, 12532.

[115] S. K. Kim, H. J. Seok, D. H. Kim, D. H. Choi, S. J. Nam, S. C. Kim, H. K. Kim. *RSC Adv.* **2020**, 10, 43847.

[116] C. C. Boyd, R. C. Shallcross, T. Moot, R. Kerner, L. Bertoluzzi, A. Onno, S. Kavadiya, C. Chosy, E. J. Wolf, J. Werner, J. A. Raiford, C. de Paula, A. F. Palmstrom, Z. J. Yu, J. J. Berry, S. F. Bent, Z. C. Holman, J. M. Luther, E. L. Ratcliff, N. R. Armstrong, M. D. McGehee. *Joule* **2020**, 4, 1759.

[117] H. Wang, Z. Huang, S. Xiao, X. Meng, Z. Xing, L. Rao, C. Gong, R. Wu, T. Hu, L. Tan, X. Hu, S. Zhang, Y. Chen. *J. Mater. Chem. A* **2021**, 9, 5759.

[118] W. Chen, Y. Zhou, G. Chen, Y. Wu, B. Tu, F. Z. Liu, L. Huang, A. M. C. Ng, A. B. Djurišić, Z. He. *Adv. Energy Mater.* **2019**, 9, 1803872.

[119] K. Choi, H. Choi, J. Min, T. Kim, D. Kim, S. Y. Son, G. W. Kim, J. Choi, T. Park. *Solar RRL* **2020**, 4, 1900251.

[120] H. Liu, K. Yan, J. Rao, Z. Chen, B. Niu, Y. Huang, H. Ju, B. Yan, J. Yao, H. Zhu, H. Chen, C. Z. Li. *ACS Appl. Mater. Interfaces* **2022**, 14, 6794.

[121] J. W. Lee, H. S. Kim, N. G. Park. *Acc. Chem. Res.* **2016**, 49, 311.

[122] G. Yang, P. Qin, G. Fang, G. Li. *Solar RRL* **2018**, 2, 1800055.

[123] Y. H. Wu, X. Q. Shi, X. H. Ding, Y. K. Ren, T. Hayat, A. Alsaedi, Y. Ding, P. Xu, S. Y. Dai. *ACS Appl. Mater. Interfaces* **2018**, 10, 3602.

[124] W. Q. Wu, P. N. Rudd, Z. Ni, C. H. van Brackle, H. Wei, Q. Wang, B. R. Ecker, Y. Gao, J. Huang. *J. Am. Chem. Soc.* **2020**, 142, 3989.

[125] X. Zhou, Y. Wang, C. Li, T. Wu. *Chem. Eng. J.* **2019**, 372, 46.

[126] P. Guo, Q. Ye, X. Yang, J. Zhang, F. Xu, D. Shchukin, B. Wei, H. Wang. *J. Mater. Chem. A* **2019**, 7, 2497.

[127] R. Wang, J. Xue, K. L. Wang, Z. K. Wang, Y. Luo, D. Fenning, G. Xu, S. Nuryyeva, T. Huang, Y. Zhao, J. L. Yang, J. Zhu, M. Wang, S. Tan, I. Yavuz, K. N. Houk, Y. Yang. *Science* **2019**, 366, 1509.

[128] R. Wang, J. Xue, L. Meng, J. W. Lee, Z. Zhao, P. Sun, L. Cai, T. Huang, Z. Wang, Z. K. Wang, Y. Duan, J. L. Yang, S. Tan, Y. Yuan, Y. Huang, Y. Yang. *Joule* **2019**, 3, 1464.

[129] D. Bi, C. Yi, J. Luo, J. D. Décoppet, F. Zhang, S. M. Zakeeruddin, X. Li, A. Hagfeldt, M. Grätzel. *Nat. Energy* **2016**, 1, 1.

[130] N. Ren, B. Chen, B. Shi, P. Wang, Q. Xu, Y. Li, R. Li, X. Cui, F. Hou, T. Li, Q. Huang, Y. Li, Y. Ding, G. Hou, X. Chen, C. Zhu, Y. Zhao, A. Hagfeldt, X. Zhang. *Small* **2020**, 16, 2002887.

[131] X. Jiang, J. Zhang, S. Ahmad, D. Tu, X. Liu, G. Jia, X. Guo, C. Li. *Nano Energy* **2020**, 75, 104892.

[132] C. Y. Chang, C. C. Wang. *J. Mater. Chem. A* **2020**, 8, 8593.

[133] R. M. LoPachin, T. Gavin, A. DeCaprio. *Chem. Res. Toxicol.* **2012**, 25, 239.

[134] P. Guo, Q. Ye, X. Yang, J. Zhang, F. Xu, D. Shchukin, B. Wei, H. Wang. *J. Mater. Chem. A* **2019**, 7, 2497.

[135] S. Zhu, X. Yao, Q. Ren, C. C. Zheng, S. Li, Y. Tong, B. Shi, S. Guo, L. Fan, H. Ren, C. Wei, B. Li, Y. Ding, Q. Huang, Y. L. Li, Y. Zhao, X. Zhang. *Nano Energy* **2018**, 45, 280.

[136] F. Zhang, D. Bi, N. Pellet, C. Xiao, Z. Li, J. J. Berry, S. M. Zakeeruddin, K. Zhu, M. Grätzel. *Energy Environ. Sci.* **2018**, 11, 3480.

[137] F. Meng, K. Liu, S. Dai, J. Shi, H. Zhang, X. Xu, D. Li, X. Zhan. *Mater. Chem. Front.* **2017**, 1, 1079.

[138] A. P. Côté, A. I. Benin, N. W. Ockwig, M. O'Keeffe, A. J. Matzger, O. M. Yaghi. *Science* **2005**, 310, 1166.

[139] C. S. Diercks, O. M. Yaghi. *Science* **2017**, 355, 623.

[140] N. Huang, P. Wang, D. Jiang. *Nat. Rev. Chem.* **2016**, 1, 1.

[141] K. Geng, T. He, R. Liu, S. Dalapati, K. T. Tan, Z. Li, S. Tao, Y. Gong, Q. Jiang, D. Jiang. *Chem. Rev.* **2020**, 120, 8811.

[142] S. J. Lyle, P. J. Waller, O. M. Yaghi. *Cell* **2019**, 172, 184.

[143] X. Guan, F. Chen, Q. Fang, S. Qiu. *Chem. Soc. Rev.* **2020**, 49, 4087.

[144] H. Wang, Z. Zeng, P. Xu, L. Li, G. Zeng, R. Xiao, Z. Tang, D. Huang, L. Tang, C. Lai, D. Jiang, Y. Liu, H. Yi, L. Qin, S. Ye, X. Ren, W. Tang. *Chem. Soc. Rev.* **2019**, 48, 488.

[145] S. T. Yang, J. Kim, H. Y. Cho, S. Kim, W. S. Ahn. *RSC Adv.* **2012**, 2, 10179.

[146] L. K. Ritchie, A. Trewin, A. Reguera-Galan, T. Hasell, A. I. Cooper. *Microporous Mesoporous Mater.* **2010**, 132, 132.

[147] J. R. Hunt, C. J. Doonan, J. D. LeVangie, A. P. Côté, O. M. Yaghi. *J. Am. Chem. Soc.* **2008**, 130, 11872.

[148] K. T. Tan, S. Ghosh, Z. Wang, F. Wen, D. Rodríguez-San-Miguel, J. Feng, N. Huang, W. Wang, F. Zamora, X. Feng, A. Thomas, D. Jiang. *Nat. Rev. Methods Primers* **2023**, 3, 1.

[149] A. P. Côté, H. M. El-Kaderi, H. Furukawa, J. R. Hunt, O. M. Yaghi. *J. Am. Chem. Soc.* **2007**, 129, 12914.

[150] H. M. El-Kaderi, J. R. Hunt, J. L. Mendoza-Cortés, A. P. Côté, R. E. Taylor, M. O'Keeffe, O. M. Yaghi. *Science* **2007**, 316, 268.

[151] F. J. Uribe-Romo, J. R. Hunt, H. Furukawa, C. Klöck, M. O'Keeffe, O. M. Yaghi. *J. Am. Chem. Soc.* **2009**, 131, 4570.

[152] R. W. Tilford, W. R. Gemmill, H. C. Zur Loye, J. J. Lavigne. *Chem. Mater.* **2006**, 18, 5296.

[153] X. Wu, B. Wang, Z. Yang, L. Chen. *J. Mater. Chem. A* **2019**, 7, 5650.

[154] P. J. Waller, Y. S. Alfaraj, C. S. Diercks, N. N. Jarenwattananon, O. M. Yaghi. *J. Am. Chem. Soc.* **2018**, 140, 9099.

[155] D. Kaleeswaran, P. Vishnoi, R. Murugavel. *J. Mater. Chem. C Mater.* **2015**, 3, 7159.

[156] A. F. M. EL-Mahdy, Y. H. Hung, T. H. Mansoure, H. H. Yu, Y. S. Hsu, K. C. W. Wu, S. W. Kuo. *J. Taiwan Inst. Chem. Eng.* **2019**, 103, 199.

[157] F. J. Uribe-Romo, C. J. Doonan, H. Furukawa, K. Oisaki, O. M. Yaghi. *J. Am. Chem.*

Soc. **2011**, 133, 11478.

[158] L. Stegbauer, K. Schwinghammer, B. V. Lotsch. *Chem. Sci.* **2014**, 5, 2789.

[159] E. Jin, M. Asada, Q. Xu, S. Dalapati, M. A. Addicoat, M. A. Brady, H. Xu, T. Nakamura, T. Heine, Q. Chen, D. Jiang. *Science* **2017**, 357, 673.

[160] X. Li. *Mater. Chem. Front.* **2021**, 5, 2931.

[161] X. Li, H. Tang, L. Gao, Z. Chen, H. Li, Y. Wang, K. Yang, S. Lu, K. Wang, Q. Zhou, Z. Wang. *Polymer* **2022**, 241, 124474.

[162] E. Jin, J. Li, K. Geng, Q. Jiang, H. Xu, Q. Xu, D. Jiang. *Nat. Commun.* **2018**, 9, 1.

[163] J. Zhao, J. Ren, G. Zhang, Z. Zhao, S. Liu, W. Zhang, L. Chen. *Chem. Eur. J.* **2021**, 27, 10781.

[164] J. Huang, X. Liu, W. Zhang, Z. Liu, H. Zhong, B. Shao, Q. Liang, Y. Liu, Q. He. *Chem. Eng. J.* **2021**, 404, 127136.

[165] D. Mullangi, S. Shalini, S. Nandi, B. Choksi, R. Vaidhyanathan. *J. Mater. Chem. A* **2017**, 5, 8376.

[166] J. Guo, G. Meng, X. Zhang, H. Huang, J. Shi, B. Wang, X. Hu, J. Yuan, W. Ma. *Adv. Mater.* **2023**, 35, 2302839.

[167] J. L. Segura, M. J. Mancheño, F. Zamora. *Chem. Soc. Rev.* **2016**, 45, 5635.

[168] J. Hu, Z. Huang, Y. Liu. *Angew. Chem. Int. Ed.* **2023**, 62, e202306999.

[169] P. Kuhn, M. Antonietti, A. Thomas. *Angew. Chem. Int. Ed.* **2008**, 47, 3450.

[170] X. Guan, Y. Ma, H. Li, Y. Yusran, M. Xue, Q. Fang, Y. Yan, V. Valtchev, S. Qiu. *J. Am. Chem. Soc.* **2018**, 140, 4494.

[171] Z. Alsudairy, N. Brown, C. Yang, S. Cai, F. Akram, A. Ambus, C. Ingram, X. Li. *Precis. Chem.* **2023**, 1, 233.

[172] C. R. Deblase, K. Hernández-Burgos, K. E. Silberstein, G. G. Rodríguez-Calero, R. P. Bisbey, H. D. Abruña, W. R. Dichtel. *ACS Nano* **2015**, 9, 3178.

[173] D. D. Medina, M. L. Petrus, A. N. Jumabekov, J. T. Margraf, S. Weinberger, J. M. Rotter, T. Clark, T. Bein. *ACS Nano* **2017**, 11, 2706.

[174] J. I. Feldblyum, C. H. McCreery, S. C. Andrews, T. Kurosawa, E. J. G. Santos, V. Duong, L. Fang, A. L. Ayzner, Z. Bao. *Chem. Commun.* **2015**, 51, 13894.

[175] J. W. Colson, A. R. Woll, A. Mukherjee, M. P. Levendorf, E. L. Spitler, V. B. Shields, M. G. Spencer, J. Park, W. R. Dichtel. *Science* **2011**, 332, 228.

[176] H. R. Abuzeid, A. F. Abdelaal, S. Elsharkawy, G. A. M. Ali. *Handb. Nanosensors* **2024**, 1.

[177] X. Liu, D. Huang, C. Lai, G. Zeng, L. Qin, H. Wang, H. Yi, B. Li, S. Liu, M. Zhang, R. Deng, Y. Fu, L. Li, W. Xue, S. Chen. *Chem. Soc. Rev.* **2019**, 48, 5266.

[178] D. Zhou, X. Tan, H. Wu, L. Tian, M. Li. *Angew. Chem.* **2019**, 131, 1390.

[179] Y. X. Fang, Y. F. Lin, Z. L. Xu, D. Pandaya, S. J. Xu. *Desalination* **2024**, 588, 117977.

[180] C. Yang, S. Li, X. Lv, H. Li, L. Han, B. Su. *J. Memb. Sci.* **2021**, 637, 119618.

[181] R. Wang, X. Shi, A. Xiao, W. Zhou, Y. Wang. *J. Memb. Sci.* **2018**, 566, 197.

[182] T. Kim, J. Oh, S. C. Kim, J.-G. Ahn, S. Kim, Y. Y. Kim, H. Lim. *Small Methods* **2024**, 2400063.

[183] H. J. Bora, P. J. Boruah, P. Kalita, G. Gogoi, H. Bailung, N. S. Sarma, A. Kalita. *Chem. Eur. J.* **2023**, 29, e202300756.

[184] W. Yao, Y. Chen, T. Fang, X. Liu, X. Zhao, S. Gao, Z. Li, H. Wang, J. Wang. *J. Phys. Chem. Lett.* **2023**, 14, 8165.

[185] F. Zhang, J. Fan, S. Wang. *Angew. Chem. Int. Ed.* **2020**, 59, 21840.

[186] X. Shi, R. Wang, A. Xiao, T. Jia, S. P. Sun, Y. Wang. *ACS Appl. Nano Mater.* **2018**, 1, 6320.

[187] C. Zhang, T. Xiao, J. He, B. Lu, X. Li, J. Zhai, X. Fan. *Small* **2023**, 19, 2301512.

[188] X. Qin, X. Xu, J. Zhao, Y. Gui, H. Guo, J. Mao, Y. Wang, Z. Zhang. *Desalination* **2023**, 557, 116598.

[189] X. Sun, M. Di, J. Liu, L. Gao, X. Yan, G. He. *Small* **2023**, 19, 2303757.

[190] D. D. Medina, J. M. Rotter, Y. Hu, M. Dogru, V. Werner, F. Auras, J. T. Markiewicz, P. Knochel, T. Bein. *J. Am. Chem. Soc.* **2015**, 137, 1016.

[191] N. C. Roy, T. Kundu. *RSC Adv.* **2023**, 13, 3669.

[192] S. Hao, T. Zhang, S. Fan, Z. Jia, Y. Yang. *Chem. Eng. J.* **2021**, 421, 129750.

[193] S. S. Mundra, S. S. Pardeshi, S. S. Bhavikatti, A. Nagras. *Mater. Today Proc.* **2021**, 46, 1229.

[194] M. Liu, Y. Liu, J. Dong, Y. Bai, W. Gao, S. Shang, X. Wang, J. Kuang, C. Du, Y. Zou, J. Chen, Y. Liu. *Nat. Commun.* **2022**, 13, 1.

[195] S. I. G. P. Mohamed, S. Namvar, T. Zhang, H. Shahbazi, Z. Jiang, A. M. Rappe, A. Salehi-Khojin, S. Nejati. *Adv. Mater.* **2024**, 36, 2309302.

[196] Y.-L. Ji, B.-X. Gu, H.-Q. Huo, S.-J. Xie, H. Peng, W.-H. Zhang, M.-J. Yin, B. Xiong, H. Lu, L. F. Villalobos, Q. Zhao, C.-J. Gao, M. Elimelech, Q.-F. An. *Nat. Water* **2024**, 2, 183.

[197] Y. Zhang, S. N. Riduan. *Chem. Soc. Rev.* **2012**, 41, 2083.

[198] Y. Wen, J. Zhang, Q. Xu, X. T. Wu, Q. L. Zhu. *Coord. Chem. Rev.* **2018**, 376, 248.

[199] J. Guo, D. Jiang. *ACS Cent. Sci.* 2020, 6, 869.

[200] H. Li, Q. Pan, Y. Ma, X. Guan, M. Xue, Q. Fang, Y. Yan, V. Valtchev, S. Qiu. *J. Am. Chem. Soc.* **2016**, 138, 14783.

[201] Q. Fang, S. Gu, J. Zheng, Z. Zhuang, S. Qiu, Y. Yan. *Angew. Chem. Int. Ed.* **2014**, 53, 2878.

[202] P. Puthiaraj, Y. R. Lee, S. Zhang, W. S. Ahn. *J. Mater. Chem. A Mater.* **2016**, 4, 16288.

[203] S. Y. Ding, J. Gao, Q. Wang, Y. Zhang, W. G. Song, C. Y. Su, W. Wang. *J. Am. Chem. Soc.* **2011**, 133, 19816.

[204] W. Yu, S. Gu, Y. Fu, S. Xiong, C. Pan, Y. Liu, G. Yu. *J. Catal.* **2018**, 362, 1.

[205] Y. Yusran, H. Li, X. Guan, Q. Fang, S. Qiu. *EnergyChem* **2020**, 2, 100035.

[206] H. Fan, H. Wang, M. Peng, H. Meng, A. Mundstock, A. Knebel, J. Caro. *ACS Nano* **2023**, 17, 7584.

[207] Z. Wang, S. Zhang, Y. Chen, Z. Zhang, S. Ma. *Chem. Soc. Rev.* **2020**, 49, 708.

[208] R. Tao, T. Yang, Y. Wang, J. Zhang, Z. Wu, L. Qiu. *Chem. Commun.* **2023**, 59, 3175.

[209] M. Sajjad, W. Lu. *J. Energy Storage* **2021**, 39, 102618.

[210] L. Zhang, X. Zhang, D. Han, L. Zhai, L. Mi. *Small Methods* **2023**, 7, 2300687.

[211] T. AlHazaimeh, M. Raheem, A. Al-Othman. *Int. J. Thermofluids* **2024**, 21, 100531.

[212] X. Feng, L. Chen, Y. Honsho, O. Saengsawang, L. Liu, L. Wang, A. Saeki, S. Irle, S. Seki, Y. Dong, D. Jiang. *Adv. Mater.* **2012**, 24, 3026.

[213] L. Yao, S. Liu, L. Li, B. Ge, W. Jiao, S. Zong, X. Song, D. Zhou, Z. Liang. *CCS Chem.* **2023**, 1.

[214] N. Wang, S. Q. Ye, M. Li, H. Pan, G. W. Wang. *Solar RRL* **2024**, 8, 2300790.

[215] R. Nie, W. Chu, Z. Li, H. Li, S. Chen, Y. Chen, Z. Zhang, X. Liu, W. Guo, S. Il Seok. *Adv. Energy Mater.* **2022**, 12, 2200480.

[216] C. Wu, Y. Liu, H. Liu, C. Duan, Q. Pan, J. Zhu, F. Hu, X. Ma, T. Jiu, Z. Li, Y. Zhao. *J. Am. Chem. Soc.* **2018**, 140, 10016.

[217] M. G. Mohamed, C. C. Lee, A. F. M. EL-Mahdy, J. Lüder, M. H. Yu, Z. Li, Z. Zhu, C. C. Chueh, S. W. Kuo. *J. Mater. Chem. A* **2020**, 8, 11448.

[218] X. Gao, Z. Li, J. Guo, G. Meng, B. Wang, G. Lang, Z. Tang, J. Feng, M. Chen, X. Ling, B. Wang, J. Yuan. *Adv. Energy Sustainability Res.* **2024**, 5, 2300205.

[219] S. Xu, Q. Zhang. *Mater. Today Energy* **2021**, 20, 100635.

[220] X. Li, H. Tang, L. Gao, Z. Chen, H. Li, Y. Wang, K. Yang, S. Lu, K. Wang, Q. Zhou, Z. Wang. *Polymer (Guildf.)* **2022**, 241, 124474.

[221] Y. Li, X. Wu, J. Zhang, C. Han, M. Cao, X. Li, J. Wan. *Polymers (Basel)* **2023**, 15, 3704.

[222] Y. Yang, K. Börjesson. *Trends Chem.* **2022**, 4, 60.

[223] R. Nie, X. Chen, Z. Li, W. Chu, S. Ma, C. Li, X. Liu, Y. Chen, Z. Zhang, W. Guo. *Nano Res.* **2023**, 16, 9387.

[224] S. Jin, T. Sakurai, T. Kowalczyk, S. Dalapati, F. Xu, H. Wei, X. Chen, J. Gao, S. Seki, S. Irle, D. Jiang. *Chem. Eur. J.* **2014**, 20, 14608.

[225] A. Dey, F. A. Rahimi, S. Barman, A. Hazra, T. K. Maji. *J. Mater. Chem. A Mater.* **2023**, 11, 13615.

[226] S. Wang, L. Da, J. Hao, J. Li, M. Wang, Y. Huang, Z. Li, Z. Liu, D. Cao. *Angew. Chem. Int. Ed.* **2021**, 60, 9321.

[227] A. Ghosh, S. Menon, S. Biswas, S. Sahoo, A. Dey, R. Boomishankar, J. K. Zaręba, U. V. Waghmare, T. K. Maji. *Adv. Funct. Mater.* **2023**, 2502787.

[228] J. He, H. Liu, F. Zhang, X. Li, S. Wang. *Adv. Funct. Mater.* **2022**, 32, 2110030.

[229] C. Wu, Y. Liu, H. Liu, C. Duan, Q. Pan, J. Zhu, F. Hu, X. Ma, T. Jiu, Z. Li, Y. Zhao. *J. Am. Chem. Soc.* **2018**, 140, 10016.

[230] X. Li, Q. Gao, J. Aneesh, H. Sen Xu, Z. Chen, W. Tang, C. Liu, X. Shi, K. V. Adarsh, Y. Lu, K. P. Loh. *Chem. Mater.* **2018**, 30, 5743.

[231] M. Li, C. Gong, J. Du, D. Ding, D. Du, D. Wang, J. Jiang, T. Li, C. Zheng, Y. F. Yang, Y. She, J. Jia. *ACS Mater. Lett.* **2023**, 5, 694.

[232] N. P. Bradshaw, Z. Hirani, L. Kuo, S. Li, N. X. Williams, V. K. Sangwan, L. E. Chaney, A. M. Evans, W. R. Dichtel, M. C. Hersam. *Adv. Mater.* **2023**, 35, 2303673.

[233] M. Y. Teo, S. Kee, L. Stuart, J. Stringer, K. C. Aw. *J. Mater. Chem. C* **2021**, 9, 12051.

[234] J. J. Espada, R. Rodríguez, A. de la Peña, M. Ramos, J. L. Segura, E. M. Sánchez-

Carnerero. *J. Clean. Prod.* **2023**, 395, 136381.

[235] X. Liang, C. Han, F. Wang, J. Wu, X. Zhou, H. Lin, X. Liu, Q. Zhu, G. Li, H. Hu. *Chem. Eng. J.* **2023**, 477, 147235.

[236] S. Park, M. S. Kim, W. Jang, J. K. Park, D. H. Wang. *Nanoscale* **2018**, 10, 4708.

[237] M. G. Rabbani, A. K. Sekizkardes, Z. Kahveci, T. E. Reich, R. Ding, H. M. El-Kaderi. *Chem. Eur. J.* **2013**, 19, 3324.

[238] Y. Cao, X. Hu, C. Zhu, S. Zhou, R. Li, H. Shi, S. Miao, M. Vakili, W. Wang, D. Qi. *Colloids Surf. A Physicochem. Eng. Asp.* **2020**, 600, 125004.

[239] H. R. Abuzeid, A. F. M. El-Mahdy, M. M. Ahmed, S. W. Kuo. *Polym. Chem.* **2019**, 10, 6010.

[240] H. R. Abuzeid, A. F. M. El-Mahdy, S. W. Kuo. *Microporous Mesoporous Mater.* **2020**, 110151.

[241] X. Zhuang, W. Zhao, F. Zhang, Y. Cao, F. Liu, S. Bi, X. Feng. *Polym. Chem.* **2016**, 7, 4176.

[242] E. Jin, M. Asada, Q. Xu, S. Dalapati, M. A. Addicoat, M. A. Brady, H. Xu, T. Nakamura, T. Heine, Q. Chen, D. Jiang. *Science* **2017**, 357, 673.

[243] M. G. Rabbani, A. K. Sekizkardes, O. M. El-Kadri, B. R. Kaafarani, H. M. El-Kaderi. *J. Mater. Chem.* **2012**, 22, 25409.

[244] A. M. Evans, M. R. Ryder, W. Ji, M. J. Strauss, A. R. Corcos, E. Vitaku, N. C. Flanders, R. P. Bisbey, W. R. Dichtel. *Faraday Discuss.* **2021**, 225, 226.

[245] Roy, D. Asthana, S. D. Verma, N. Doley. *ChemPhysChem* **2024**, *25*, e202400969.

[246] S. Wan, J. Guo, J. Kim, H. Ihee, D. Jiang. *Angew. Chem. Int. Ed.* **2009**, 48, 5439.

[247] J. R. Lakowicz. *Principles of Fluorescence Spectroscopy* **1983**, 187.

[248] M. Wang, M. Wang, H. H. Lin, M. Ballabio, H. Zhong, M. Bonn, S. Zhou, T. Heine, E. Cánovas, R. Dong, X. Feng. *J. Am. Chem. Soc.* **2020**, 142, 21622.

[249] H. Ding, Y. Li, H. Hu, Y. Sun, J. Wang, C. Wang, G. Zhang, B. Wang, W. Xu, D. Zhang. *Chem. Eur. J.* **2014**, 20, 14614.

[250] B. Nath, W. H. Li, J. H. Huang, G. E. Wang, Z. H. Fu, M. S. Yao, G. Xu. *CrystEngComm* **2016**, 18, 4259.

[251] S. L. Cai, Y. B. Zhang, A. B. Pun, B. He, J. Yang, F. M. Toma, I. D. Sharp, O. M. Yaghi, J. Fan, S. R. Zheng, W. G. Zhang, Y. Liu. *Chem. Sci.* **2014**, 5, 4693.

[252] S. Wan, J. Guo, J. Kim, H. Ihee, D. Jiang. *Angew. Chem. Int. Ed.* **2008**, 47, 8826.

[253] L. Wang, B. Dong, R. Ge, F. Jiang, J. Xu. *ACS Appl. Mater. Interfaces* **2017**, 9, 7108.

[254] G. H. V. Bertrand, V. K. Michaelis, T. C. Ong, R. G. Griffin, M. Dincâ. *Proc. Natl. Acad. Sci. U.S.A.* **2013**, 110, 4923.

[255] Z. Meng, R. M. Stolz, K. A. Mirica. *J. Am. Chem. Soc.* **2019**, 141, 11929.

[256] V. Lakshmi, C. H. Liu, M. Rajeswara Rao, Y. Chen, Y. Fang, A. Dadvand, E. Hamzehpoor, Y. Sakai-Otsuka, R. S. Stein, D. F. Perepichka. *J. Am. Chem. Soc.* **2020**, 142, 2155.

[257] N. G. Park. *Adv. Energy Mater.* **2020**, 10, 1903106.

[258] S. A. Veldhuis, P. P. Boix, N. Yantara, M. Li, T. C. Sum, N. Mathews, S. G. Mhaisalkar. *Adv. Mater.* **2016**, 28, 6804.

[259] A. A. Zhumekenov, Y. Li, Y. Zhou, N. Yantara, A. Kanwat, B. Febriansyah, D. J. J. Tay, H. R. Abuzeid, Y. B. Tay, E. B. Miftahullatif, K. Hippalgaonkar, S. A. Pullarkat, J. Yin, N. Mathews. *J. Am. Chem. Soc.* **2024**, 146, 6706.

[260] S. Liu, V. P. Biju, Y. Qi, W. Chen, Z. Liu. *NPG Asia Mater.* **2023**, 15, 1.

[261] H. Chen, S. Teale, B. Chen, Y. Hou, L. Grater, T. Zhu, K. Bertens, S. M. Park, H. R. Atapattu, Y. Gao, M. Wei, A. K. Johnston, Q. Zhou, K. Xu, D. Yu, C. Han, T. Cui, E. H. Jung, C. Zhou, W. Zhou, A. H. Proppe, S. Hoogland, F. Laquai, T. Filleter, K. R. Graham, Z. Ning, E. H. Sargent. *Nat. Photonics* **2022**, 16, 352.

[262] Z. Wang, L. Liu, Y. Wang, Y. Ma, Z. Yang, M. Wan, H. Zhu, T. Mahmoudi, Y. B. Hahn, Y. Mai. *Chem. Eng. J.* **2023**, 457, 141204.

[263] L. Liu, Y. Ma, Y. Wang, Q. Ma, Z. Wang, Z. Yang, M. Wan, T. Mahmoudi, Y. B. Hahn, Y. Mai. *NanoMicro Lett.* **2023**, 15, 1.

[264] W. Chen, Y. Zhu, J. Xiu, G. Chen, H. Liang, S. Liu, H. Xue, E. Birgersson, J. W. Ho, X. Qin, J. Lin, R. Ma, T. Liu, Y. He, A. M. C. Ng, X. Guo, Z. He, H. Yan. *Nat. Energy* **2022**, 7, 229.

[265] L. Li, Y. Wang, X. Wang, R. Lin, X. Luo, Z. Liu, K. Zhou, S. Xiong, Q. Bao, G. Chen, Y. Tian, Y. Deng, K. Xiao, J. Wu, M. I. Saidaminov, H. Lin, C. Q. Ma, Z. Zhao, Y. Wu, L. Zhang, H. Tan. *Nat. Energy* **2022**, 7, 708.

[266] J. Park, J. Kim, H. S. Yun, M. J. Paik, E. Noh, H. J. Mun, M. G. Kim, T. J. Shin, S. Il Seok. *Nat.* **2023**, 616, 724.

[267] T. Yang, W. Zhao, Y. Yang, W. Huang, K. Zhao, S. F. Liu. *Adv. Mater.* **2023**, 35, 2211006.

[268] J. W. Lee, H. S. Kim, N. G. Park. *Acc. Chem. Res.* **2016**, 49, 311.

[269] Z. Yang, J. Dou, S. Kou, J. Dang, Y. Ji, G. Yang, W. Q. Wu, D. Bin Kuang, M. Wang. *Adv. Funct. Mater.* **2020**, 30, 1910710.

[270] F. Zhang, D. Bi, N. Pellet, C. Xiao, Z. Li, J. J. Berry, S. M. Zakeeruddin, K. Zhu, M. Grätzel. *Energy Environ. Sci.* **2018**, 11, 3480.

[271] D. Zhou, X. Tan, H. Wu, L. Tian, M. Li. *Angew. Chem. Int. Ed.* **2019**, 58, 1376.

[272] C. Chen, S. Zhang, S. Wu, W. Zhang, H. Zhu, Z. Xiong, Y. Zhang, W. Chen. *RSC Adv.* **2017**, 7, 35819.

[273] N. Phung, A. Abate. *Small* **2018**, 14, 1802573.

[274] D. Meggiolaro, S. G. Motti, E. Mosconi, A. J. Barker, J. Ball, C. A. R. Perini, F. Deschler, A. Petrozza, F. De Angelis. *Energy Environ. Sci.* **2018**, 11, 702.

[275] J.-W. Lee, S.-H. Bae, N. de Marco, Y.-T. Hsieh, Z. Dai, Y. Yang. *Mater. Today Energy* **2017**.

[276] J. X. Zhong, J. F. Liao, Y. Jiang, L. Wang, D. Bin Kuang, W. Q. Wu. *J. Mater. Chem. A* **2020**, 8, 9743.

[277] M. Grätzel. *Nat. Mater.* **2014**, 13, 838.

[278] H. J. Snaith. *J. Phys. Chem. Lett.* **2013**, 4, 3623.

[279] W. S. Yang, B. W. Park, E. H. Jung, N. J. Jeon, Y. C. Kim, D. U. Lee, S. S. Shin, J. Seo, E. K. Kim, J. H. Noh, S. Il Seok. *Science (1979)* **2017**, 356, 1376.

[280] B. Ding, Y. Ding, J. Peng, J. Romano-deGea, L. E. K. Frederiksen, H. Kanda, O. A. Syzgantseva, M. A. Syzgantseva, J. N. Audinot, J. Bour, S. Zhang, T. Wirtz, Z. Fei, P. Dörflinger, N. Shibayama, Y. Niu, S. Hu, S. Zhang, F. F. Tirani, Y. Liu, G. J. Yang, K. Brooks, L. Hu, S. Kinge, V. Dyakonov, X. Zhang, S. Dai, P. J. Dyson, M. K. Nazeeruddin. *Nat.* **2024**, 628, 299.

[281] R. He, Y. Wu, Z. Li, Y. Wang, W. Zhu, A. Tong, X. Chen, W. Pan, W. Sun, J. Wu. *Surfaces Interfaces* **2024**, 48, 104274.

[282] S. Liu, Y. Guan, Y. Sheng, Y. Hu, Y. Rong, A. Mei, H. Han. *Adv. Energy Mater.* **2020**, 10, 1902492.

[283] L. Zhu, S. Xu, G. Liu, L. Liu, H. Zhou, Z. Ai, X. Pan, F. Zhang. *Chem. Sci.* **2024**, 15,

5642.

[284] R. A. Afre, D. Pugliese. *Micromachines* **2024**, 15, 192.

[285] J. Lee, K. Y. Baek, J. Lee, H. Ahn, Y. Kim, H. Lim, Y. Kim, J. Woo, S. D. Stranks, S. K. Lee, H. Sirringhaus, K. Kang, T. Lee. *Adv. Funct. Mater.* **2023**, 33, 2302048.

[286] N. Phung, R. Félix, D. Meggiolaro, A. Al-Ashouri, G. Sousa E Silva, C. Hartmann, J. Hidalgo, H. Köbler, E. Mosconi, B. Lai, R. Gunder, M. Li, K. L. Wang, Z. K. Wang, K. Nie, E. Handick, R. G. Wilks, J. A. Marquez, B. Rech, T. Unold, J. P. Correa-Baena, S. Albrecht, F. De Angelis, M. Bär, A. Abate. *J. Am. Chem. Soc.* **2020**, 142, 2364.

[287] Y. Zhou, J. Chen, O. M. Bakr, H. T. Sun. *Chem. Mater.* **2018**, 30, 6589.

[288] Z. Li, C. Xiao, Y. Yang, S. P. Harvey, D. H. Kim, J. A. Christians, M. Yang, P. Schulz, S. U. Nanayakkara, C. S. Jiang, J. M. Luther, J. J. Berry, M. C. Beard, M. M. Al-Jassim, K. Zhu. *Energy Environ. Sci.* **2017**, 10, 1234.

[289] W. Zhao, Z. Yao, F. Yu, D. Yang, S. Liu. *Adv. Sci.* **2018**, 5, 1700131.

[290] H. Kanda, N. Shibayama, M. Abuhelaiqa, S. Paek, R. Kaneko, N. Klipfel, A. A. Sutanto, C. R. Carmona, A. J. Huckaba, H. Kim, C. Momblona, A. M. Asiri, M. K. Nazeeruddin. *J. Mater. Chem. A* **2020**, 8, 17113.

[291] M. H. Miah, M. U. Khandaker, M. B. Rahman, M. Nur-E-Alam, M. A. Islam. *RSC Adv.* **2024**, 14, 15876.

[292] L. Arunagiri, F. Gao. *Natl. Sci. Rev.* **2024**, 11.

[293] X. Shen, B. M. Gallant, P. Holzhey, J. A. Smith, K. A. Elmestekawy, Z. Yuan, P. V. G. M. Rathnayake, S. Bernardi, A. Dasgupta, E. Kasparavicius, T. Malinauskas, P. Caprioglio, O. Shargaieva, Y. H. Lin, M. M. McCarthy, E. Unger, V. Getautis, A. Widmer-Cooper, L. M. Herz, H. J. Snaith. *Adv. Mater.* **2023**, 35.

[294] Y. Li, H. Wu, W. Qi, X. Zhou, J. Li, J. Cheng, Y. Zhao, Y. Li, X. Zhang. *Nano Energy* **2020**, 77, 105237.

[295] J. J. Jeronimo-Rendon, S. H. Turren-Cruz, J. Pascual, D. Di Girolamo, M. A. Flatken, H. Köbler, W. Hempel, M. Li, A. Di Carlo, P. P. Boix, I. Mora-Seró, A. Abate, M. Saliba. *Adv. Funct. Mater.* **2024**, 34, 2313928.

[296] H. Zhao, Z. Xu, Y. Che, Y. Han, S. Yang, C. Duan, J. Cui, S. Dai, Z. Liu, S. Liu. *J. Power Sources* **2021**, 492, 229580.

[297] B. Wang, X. Yin, S. Iqbal, M. Que, W. Que. *Adv. Mater. Interfaces* **2022**, 9, 2200636.

[298] S. Wang, W. B. Xiao, F. Wang. *RSC Adv.* **2020**, 10, 32364.

[299] A. M. Evans, A. Giri, V. K. Sangwan, S. Xun, M. Bartnof, C. G. Torres-Castanedo, H. B. Balch, M. S. Rahn, N. P. Bradshaw, E. Vitaku, D. W. Burke, H. Li, M. J. Bedzyk, F. Wang, J. L. Brédas, J. A. Malen, A. J. H. McGaughey, M. C. Hersam, W. R. Dichtel, P. E. Hopkins. *Nat. Mater.* **2021**, 20, 1142.

[300] L. S. Xie, G. Skorupskii, M. Dincă. *Chem. Rev.* **2020**, 120, 8536.

[301] E. V. Peán, S. Dimitrov, C. S. De Castro, M. L. Davies. *Phys. Chem. Chem. Phys.* **2020**, 22, 28345.

[302] H. Li, H. Di, X. Wang, Z. Ren, M. Lu, A. A. Liu, X. Yang, N. Wang, Y. Zhao, B. Li. *Sci. China Phys. Mech. Astron.* **2023**, 66, 1.

[303] K. Ye, B. Zhao, B. T. Diroll, J. Ravichandran, R. Jaramillo. *Faraday Discuss.* **2022**, 239, 146.